The University of Canterbury

Department of Chemical and Process Engineering

PhD Thesis:

In silico modelling of soft tissue scaffolds

30th April 2020

Student: Harshal Panidepu – 81046656

Supervisor: Professor Conan Fee
Co-supervisor: Associate Professor Matt Watson.

Abstract

Globally the number of people waiting for a lifesaving organ transplant heavily outweighs the number of organs available. This work is about using computer simulations to understand how to utilize "bioprinting" technology to address this issue. Bioprinting refers to 3D printing biocompatible scaffolds that provide support to cell growth in a three dimensional shape. Despite tremendous advances in tissue engineering, vascularization remains a key unsolved challenge in these bioprinted tissues.

Previous studies have reported oxygen limitation as a major problem leading to hypoxia and cell death of bioprinted tissues. The project theme is to explore scaffolds of different architecture, shapes and thicknesses, to quantify oxygen availability in these structures. Emphasis was placed on analysing scaffolds bioprinted as Triply Periodic Minimal Surfaces (TPMS). Computational Fluid Dynamic (CFD) studies coupled with high performance computing was used to investigate oxygen diffusion through scaffolds, using the Lattice Boltzmann Method (LBM). The CFD model simulated blood flow through TPMS structures while oxygen diffusion and consumption were simultaneously occurring within the tissue-scaffold system. The LBM model was developed with an open source software '*Palabos*', which was coded in C++.

There are four distinct bodies of work presented in this thesis. In the first work, the LBM results of oxygen diffusion distances in tissues were verified with analytical model predictions (Krogh's model), for a simple capillary case. The validation was done in the radial direction of the capillary, both in the presence and in absence of hydrogel. The second focus was to identify entrance and exit effects in the TPMS scaffold systems, which were addressed by using exit lengths and improving the steady state tolerance criteria of the simulations. Mesh independence studies were performed with LBM using the Schwarz Diamond (SD) TPMS structure as a case study. Supercomputing facilities were used to accelerate computing using the Message Passing Interface framework and *slurm* job scheduling system. The third focus was to understand the nature of oxygen concentration profiles in the axial direction of TPMS scaffolds, and to analyse the effect of scaffold permeability and thickness on the profiles. New concepts such as Specific Normal Area (SNA) were defined to quantify the thickness of TPMS scaffolds. Using gradient estimation of the axial concentration profiles and linear extrapolation techniques, tissue survival lengths were estimated for these tissue scaffolds, for the first time. The fourth aspect was to understand the factors that lead to enhanced mass transfer in TPMS structures. The

Péclet number was quantified for flow through TPMS tissue shapes of different porosities, and the relative importance of advection and diffusion was analyzed. In this thesis, the mass transfer efficiency of nutrients was estimated with respect to partition coefficient, a novel way to rank scaffold shapes. In conclusion, SD is proposed as an efficient TPMS structure for i) favourable structure-induced permeation properties ii) minimum variation in its SNA and shorter diffusion paths iii) a reasonably high partition coefficient among TPMS structures. The CFD model provides a proof of concept for sustainable TPMS tissue-scaffold systems that could sustain up to 50% of the cells in a given space in the order of ~10 cm depending on the structural porosity, when the oxygen concentration in the perfused blood is $\geq$ 0.15 mM. The numerical model enables *in silico* testing of likely tissue viability, before bioprinting them in a particular shape. Thus, the LBM model reduces the time and cost involved in performing tissue vascularization studies in cell culture labs, using computational predictions to eliminate non-viable tissue scaffolds from a set of geometries under consideration.

Acknowledgements

Firstly, I would like to express my gratitude to Dr. Conan Fee, my supervisor for giving me an opportunity to do my Ph.D. with him, at the University of Canterbury. It has been a great education and a pleasure to work with you, and to absorb from you, my philosophy of scientific method. You have set a benchmark for me in terms of knowledge, inter-personal skills, professional conduct, leadership and wisdom. Your mentorship has given me the privilege to know my productivity in scientific freedom, develop new skills and nourish my persona.

I would like to acknowledge Dr. Matt Watson and Dr. Tim Huber who brought new insights to my research work. I appreciate your supervisory support and guidance that you afforded me while conducting this Ph.D. I want to acknowledge the support of Dr. Fabian Dolamore for his support in getting me started with *Palabos.* I want to extend my sincere regards to Ben Roberts at Lincoln University, for helping me navigate and find peace with the NeSI supercomputers. Thank you Dr. Daniel Clarke and Sean Feast for helping me in proof reading this thesis. Ben Reynolds and Ben Houlton, your presence in similar projects was a great motivation to me, as we discussed and solved our shared computational problems, and I am glad we never forgot to smile in achieving our common goals. A big thanks to all my CAPE colleagues who were present for those coffee chats and joining me for ping pong in the third pro office.

Finally, to my parents, grandparents, siblings and to most importantly Vasavi for joining my life during this adventurous computational PhD journey. I will forever be indebted to all of you, for your love and support throughout.

Many thanks to University of Canterbury, Chemical and Process Engineering department, the UC Centre for Entrepreneurship, Biomolecular Interaction Centre and the Sutherland Bequest for providing financial support.

Table of Contents

Nomenclature

The nomenclature used in this thesis is summarized in the table below, with variables expressed using dimensions of Length [L], Mass [M], Time [T] or [-] if dimensionless.

Symbol	***Description***	
a	Acceleration of particle in LBM	LT^{-2}
c_i	Velocity vector in i^{th} direction	LT^{-1}
c	Velocity vector used in Boltzmann equation derivation	LT^{-1}
c_s	Artificial speed of sound in lattice units	-
C_{O_2}	Symbol for oxygen concentration in Krogh model	$N\ L^{-3}$
C_{blood}	Oxygen concentration in blood phase at steady state	$N\ L^{-3}$
C_{R_c}	Oxygen concentration at radius R_c in Krogh model	$N\ L^{-3}$
C_{tissue}	Oxygen concentration in tissue phase at steady state	$N\ L^{-3}$
$\widetilde{D}$	Deviated diffusion parameter of oxygen in the blood	$L^2\ T^{-1}$
D_m	Number of lattice dimensions in LBM	-
$\widetilde{D_m}$	Modified diffusion parameter in LBM	$L^2\ T^{-1}$
D_n	Number of discrete directions in LBM	-
D_{ref}	Reference diffusion coefficient in LBM	$L^2\ T^{-1}$
D_{O_2}	Diffusion coefficient of oxygen in tissue, used in Krogh model	$L^2\ T^{-1}$
e	Energy	$M\ L^2\ T^{-2}$
f	Probability density function	-
f_j	Probability density function in the j^{th} direction	-
f_{eq}	Equilibrium probability density function	-
f_{eq_j}	Equilibrium probability density function in the j^{th} direction	-
F	Body force in LBM	$M\ L\ T^{-2}$
h	Thickness of the cylindrical hydrogel scaffold	L
l_b	Pertaining to Lattice Boltzmann Method units	-
L_c	Characteristic length of TPMS structures	L
L_{char}	Reference length of system in physical scale, to determine grid resolution in LBM	L
l_x	Length of the simulation domain in axial flow direction	L
l_y	Length of the simulation domain in transverse flow direction	L
l_z	Length of the simulation domain in transverse flow direction	L
O_2	Oxygen	-
p	Subscript pertaining to LBM variables in physical units	-
P	Partition coefficient	-
Pe	Péclet number	-
Q_n	Number of discrete velocities in LBM	-

Symbol	*Description*	
Q_s	Sink or oxygen consumption term in the advection-diffusion equation	N L^{-3} T^{-1}
r	Lattice Boltzmann Method spatial vector	-
R	Resolution	-
R_c	Radius of capillary in Krogh model	L
R_o	Distance from capillary centre where oxygen concentration is zero	L
t	Time	T
t_j	Constant term of equilibrium distribution term in j^{th} direction	-
u	Velocity vector	L T^{-1}
u_a	Advection velocity term	L T^{-1}
u_d	Diffusion velocity term	L T^{-1}
u_r	Velocity in the r^{th} direction.	L T^{-1}
u_{lb}	Fluid velocity in lattice units	-
u_p	Fluid velocity in physical units	L T^{-1}
u_n	n^{th} moment of a function	-
$u_{channel}$	Channel velocity in TPMS structures computed by estimating the average concentration in the TPMS structures at steady state.	L T^{-1}
$u'_{channel}$	Channel velocity in TPMS structures computed as a ratio of imposed perfusion velocity and TPMS structural porosity	L T^{-1}
$u_{superficial}$	Average superficial velocity of the blood in channel	L T^{-1}
x	Pertaining to the axial coordinate system (x-axis)	-
y	Pertaining to the axial coordinate system (y-axis)	-
z	Pertaining to the axial coordinate system (z-axis)	-

Greek Symbols		
Symbol	***Description***	
α	Parameter value to determine TPMS porosity	-
β	Parameter value to determine TPMS porosity	-
δ	A small increment	-
δ_t	Time conversion factor	T
δ_x	Length conversion factor	L
Δ	A change in the property	-
μ	Dynamic viscosity	$M\ L^{-1}\ T^{-1}$
ν	Kinematic viscosity in physical units	$L^2\ T^{-1}$
ν_{lb}	Kinematic viscosity in lattice units	-
ω	Collision frequency of particles.	-
ρ	Density	$M\ L^{-3}$
∂	Partial differential operator	-
d	Differential operator	-
τ	Lattice Boltzmann Method relaxation parameter	-
∇	Gradient operation.	-
ϕ	Dimensionless oxygen consumption term	-
Ω	Lattice Boltzmann Collision operator	-

Abbreviations	
Symbol	***Description***
ADE	Advection Diffusion Equation
ANSYS	Analysis Systems
bFGF	Basic Fibroblast Growth Factor
BGK	Bhatnagar-Gross-Krook
CAD	Computer Aided Design
CAGR	Compound Annual Growth Rate
CFD	Computational Fluid Dynamics
ECM	Extracellular matrix
F-RD	Fischer Kosch
FEM	Finite Element Method
GUI	Graphic User Interface
HPC	High Performance Computers
LBE	Lattice Boltzmann Equations
LGA	Lattice Gas Automaton
LBM	Lattice Boltzmann Method
MRT	Multiple Relaxation Time
MSC	Mesenchymal Stem Cells
NeSI	New Zealand eScience Infrastructure
NS	Navier-Stokes
P2GD	Primitive-Gyroid-Diamond
R&D	Research and Development
RBC	Red Blood Cells
SD	Schwarz Diamond
SG	Schoen Gyroid
SP	Schwarz Primitive
SLATE	Stereolithography Apparatus for Tissue Engineering
SWIFT	Sacrificial Writing into Functional Tissues
SNA	Specific Normal Area
SRT	Single Relaxation Time
STL	Stereolithography
TPMS	Triply Periodic Minimal Surface
TRT	Two Relaxation Time
VEGF	Vascular Endothelial Growth Factor
VTI	Visual Tool Kit Image

1. Introduction

1.1. Soft tissues

Soft tissues refer to tissues that support, connect and surround organs of the body. Muscles, nerves, fibrous tissues, mammary glands, fatty tissues, blood vessels, tendons and synovial[1] membrane contain soft tissues [1]. There is an increasing demand for soft tissues for trauma surgery and tissue reconstruction following malignancies in these tissues. The supply and demand for these tissues is mismatched, because there is a scarcity of organ and tissue donors worldwide. With development of 3D printing technology, it is possible to 3D print soft tissues in the lab. Biofabrication and bioprinting are popular terms encountered in the context of 3D printing tissues. Biofabrication refers to any process involving bioactive molecules [2] and cells while bioprinting is a manufacturing process involving a motorized dispensing system to fabricate ordered three dimensional biological constructs [3].

Vasculature[2] or blood (nutrients) flow pathway is particularly important while 3D printing soft-tissues, to ensure that cells are in close proximity to blood source, so that diffusion of essential nutrients to them is not limited. Primarily, oxygen delivery to soft tissues is crucial for cell survival and therefore, cells should be present at an appropriate diffusional distance from the oxygen supply to survive [4]. Oxygen delivery is more important in soft-tissues than in cartilaginous tissues, which have a low oxygen demand and could thrive in relatively nutrient deficient microenvironments [5]. This thesis is about efficient vasculature design for bioprinted soft tissues to overcome oxygen limitation, that will have applications in organ transplantation [6] and *in vitro* tissue bioreactors [7].

1.2. Scaffolds and oxygen limitation

The bioprinting process discussed in this thesis involves 3D printing of a biocompatible material known as a scaffold. Scaffolds are like a mould or a pattern, designed to provide support to tissues growing on them, so that the tissues occupy a desired 3-dimensional structure. The 3D printed scaffolds both embed tissues and provide a perfusion pathway (vasculature) for blood or

[1] Membrane surrounding joints.
[2] Arrangement of blood vessels in an organ or tissue.

nutrient media to flow around them. Figure 1.2-1 shows a two dimensional illustration of three phases (tissue, scaffold and blood) and their respective thicknesses (α, β and μ microns).

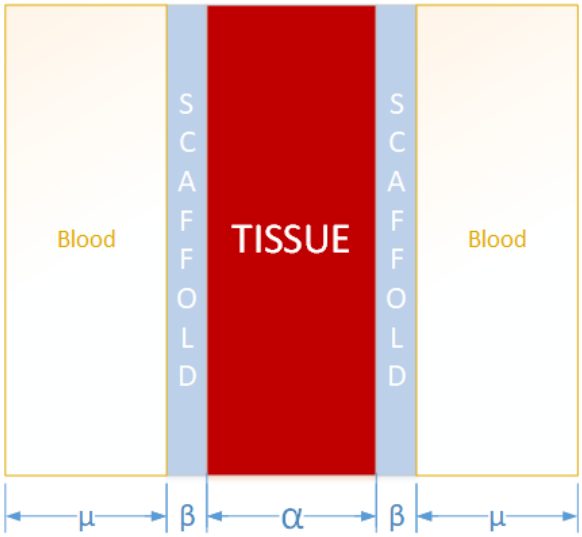

Figure 1.2-1: 2D illustration of a tissue (α μm) sandwiched between hydrogel scaffolds of thickness β μm, with a blood flow pathway of thickness μ μm.

In this thesis, 3D printed scaffolds manufactured from cellulose-based hydrogels are discussed. Therefore, the terms *scaffold* and *hydrogel* are used interchangeably in this thesis. Hydrogels are water-swollen cross-linked polymeric networks formed by reaction of monomers [8]. Previously scaffold structures were inspired by nature (biomimicry) and designed as dendritic patterns i.e. mimicking capillary networks, as shown in Figure 1.2-2 [9, 10]. In these designs, the vasculature or the blood perfusion pathway is laid out as branched patterns around the tissue cells. However, oxygen deficient zones were found to develop at a certain distance from the vasculature in such designs, which hindered cell growth. Many observations were made on oxygen scarcity, for instance, Miller [11] noted that cells packed at high densities change their trajectory of differentiation and die rapidly in unfavourable microenvironments. Niklason and Langer [12] found in their experimental study that the cells seeded on a gel scaffold did not reach the densities found in functional organs, due to poor oxygen diffusion. Wittenberg and Wittenberg [13] noted that below critical oxygen partial pressure, mitochondrial respiration would be in jeopardy. Karande [14] worked on scaffold porosity and permeability, and studied how oxygen influenced the *in vitro* cell viability and concluded that reduced oxygen availability decreased cell viability. Similarly, Ball, Nguyen, Placone and Fisher [15] reported that fabricating a scaffold beyond the oxygen diffusional limit leads to formation of necrotic cores or oxygen deficient regions. Therefore, in order to 3D print soft tissues successfully, oxygen

deficiency must be alleviated. Table 1.2-1 summarizes several concepts that frequently occur in medical science to describe oxygen deficiency. These concepts are also important to understand the bioprinting of tissues.

Table 1.2-1: Physiological terms describing oxygen scarcity

Terms	Description	Reference
Ischemia	Restriction or reduced blood supply, resulting in inadequate transport of nutrients.	[16]
Anaemia	Decrease in the red blood cells, resulting in lower oxygen carrying capacity of blood.	[17]
Anoxia	Complete lack of oxygen.	[18]
Hypoxia	Reduced supply of oxygen.	[19]
Hypoxemia	Abnormally low oxygen concentration in arterial blood.	[20]

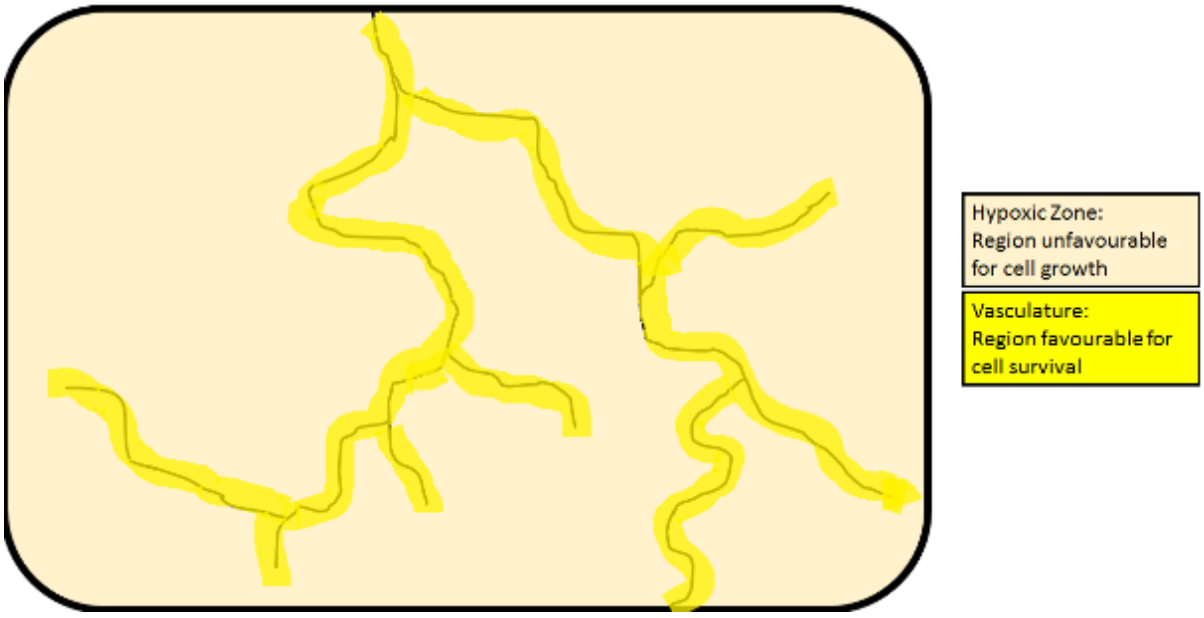

Figure 1.2-2: Illustration of dendritic vasculature.

This thesis describes the use of Computational Fluid Dynamics (CFD) studies with the Lattice Boltzmann method (LBM), to design hydrogel scaffold shapes, inspired by Triply Periodic Minimal Surfaces (TPMS). Specifically, scaffolds designed in the shape of sheet TPMS structures are analysed in this thesis because they have the potential to provide oxygen

supply to the cells within the distance needed and ensure an intimate and uniform distribution of blood supply in a tissue-scaffold system [21]. Figure 1.2-3 shows an example of a sheet gyroid[3] structure and Appendix A contains a table describing the shapes and properties of other TPMS structures investigated in this thesis [22].

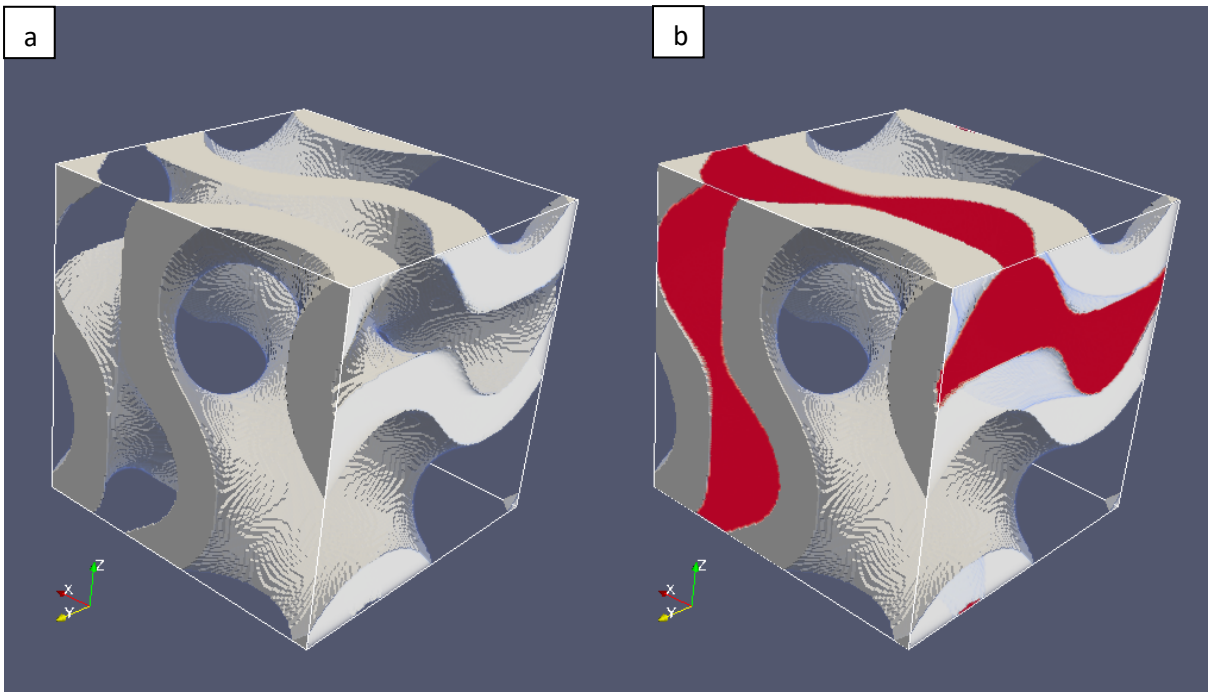

Figure 1.2-3: a) A 3D model of hydrogel-derived sheet gyroid b) A sheet gyroid separating tissue (red) and the blood perfusion space.

TPMS structures are mathematically determined based on complex trigonometric equations. Therefore, there are multiple possibilities to change a TPMS structure by subtle variation in the equations. To determine and quantify the oxygen mass transfer efficiency of all 3D printed TPMS structures in a cell culture lab is time consuming. Therefore, in this thesis CFD studies are sought as an alternative methodology to screen TPMS scaffolds *in silico*, to assess their mass transfer efficiency and to explore the prospect of bioprinting them. Specifically, this thesis contains oxygen diffusion simulations around TPMS hydrogel scaffolds of various shapes and sizes. The scaffold dimensions and the dimensional interdependencies between $\alpha, \beta,$ and μ variables (Figure 1.2-1) are explored in detail. Structural and chemical properties of hydrogel scaffolds such as porosity, thickness and oxygen

[3] A TPMS structure.

diffusivity values are investigated, to understand how the design of a scaffold structure affects oxygen diffusion.

1.3. Thesis outline:

Chapter 2 contains a summary of current state-of-the-art technology used in 3D printing soft tissues, across tissue engineering labs worldwide. TPMS structures and the mathematical basis of these structures are described in detail. The TPMS structures explored in this thesis are: gyroid, Schwarz Diamond, P2GD, IWP, Lidinoid, D', Double Schoen gyroid, Schwarz primitive, Fischer Kosch, and Double Diamond (Appendix A). The chapter also describes the fundamental theory behind CFD with LBM. The fundamental equations of fluid motion were derived from LBM first principles, and compared with the Navier Stokes equation. Details on *Palabos* software are discussed, which is an open source C++ software package used to perform LBM simulations. The robustness of the LBM model is described, and its applicability to study tissue vascularization is justified.

Chapter 3 contains the implementation details of the LBM model. It begins with details of modelling tissues, hydrogel and void space in the simulation domain. The Schwarz Diamond TPMS structure was used as a case study to implement the LBM model and to explain the methodology to trigonometrically define the three phases (tissue, hydrogel and blood). The chapter provides details on the specific equations used in the LBM model implementation. It contains details on the BGKW model that was used for velocity lattice, and Perko-Patel model used for the concentration lattice. The chapter contains a description of the consumption kinetics used in the LBM model, a zero-order consumption term to replicate the metabolic demand of oxygen in tissues. The numerical model developed with *Palabos* was used to measure oxygen diffusion distances in tissues at steady state. These diffusion distances were compared with the distances obtained from Krogh's analytical solution, for the case of a simple capillary. Next, a hydrogel layer was placed between capillary and tissue with an appropriate permeability, and the oxygen diffusion distances in tissue were analysed at steady state. The LBM model was later employed to study oxygen diffusion in large three-dimensional TPMS scaffolds. In 3D simulations, oxygen accumulation in the tissue was quantified in terms of average oxygen concentration in scaffold slices in the blood flow direction. Such axial concentration profiles were modelled for different TPMS scaffolds and hydrogel thicknesses at steady state. It was observed that the computational requirements for simulations in 3D were enormous, and therefore the chapter contains details of the computational capabilities of the New Zealand eScience Infrastructure (NeSI) supercomputers and how they were utilized to

perform CFD simulations in this thesis. Details of scale up of computation speed with the High Performance Computers (HPC) are mentioned. The scaffold systems had regions of little relevance where entrance and exit effects were dominant, and therefore ways to counteract these effects by introducing exit lengths is discussed in the chapter. Mesh independence studies were also performed to identify the optimum resolution for conducting simulations. The main crux of the chapter was to identify TPMS unit cells that could be considered approximately periodic, in the axial blood flow direction.

In Chapter 4, the application of the developed LBM model to run simulations in scaffolds of 3D printable size is described. The non-uniformity of TPMS scaffold thickness is discussed and quantified in the concept of Specific Normal Area (SNA). The oxygen accumulation in tissues was estimated for different scaffold thicknesses (25 μm, 100 μm and 200 μm) and the sensitivity of oxygen concentration profiles was estimated. Similar sensitivity studies were performed on scaffolds of constant thickness but with varying oxygen permeability. These studies were performed to get an insight on oxygenation gain of tissue and the cost of improving scaffold permeability. Oxygen perfusion was simulated through an axial domain of size 7 mm, given the computational limitation involved to simulate a scaffold size spanning centimetres. Different oxygen concentrations were perfused through the scaffold segment, to understand oxygenation in a larger scaffold. Substantial emphasis was placed on identification of the shape and nature of the concentration profiles along the scaffold. Curve fitting, gradient measurement and linear extrapolation techniques were employed to understand the oxygen concentration profiles in the TPMS tissue scaffolds. The survival length of a bioprinted scaffold is defined as a concept and estimated for different TPMS structures. The survival length estimate gave an indication about the approximate length of the scaffold that is sustainable/normoxic for a given set of conditions.

Chapter 5 contains details about the mass transfer efficiency of TPMS scaffolds in terms of partition coefficient. Partition coefficient as a concept was used to estimate oxygen accumulation and distribution between tissue and blood phases at steady state. Furthermore, the TPMS structures were ranked according to their partition coefficients, representing the mass transfer efficiency of TPMS structures. Next, the Péclet number was calculated in TPMS structures and it was correlated with the partition coefficient to understand the causal factors leading to enhanced oxygen accumulation in tissue. Factors such as advection and diffusion were analysed in TPMS structures to understand which effect is more or less dominant in these structures. The Péclet number was calculated using two approaches in this chapter, by

considering different definitions for average velocity in TPMS scaffolds. In conclusion, diffusion was identified as a dominant effect in TPMS structures. It is proposed that Schwarz Diamond structures is an ideal structure for 3D printed scaffolds, that provides an optimum balance between mass transfer efficiency and relatively easy bioprintability.

Finally, in Chapter 6, conclusions are summarized and recommendations for future work are provided.

2. Literature Review

2.1. 3D tissue printing

3D tissue printing refers to a computer aided process in which cells or cell compatible material are precisely placed as aggregates, which then serve as building blocks to be further processed into a functional 3D organ [23]. Developing a fully functional organ by this process relies on three main technologies namely cell technology, biomanufacturing technology and *in vivo* integration technologies. Cell technology refers to obtaining cells at the level required for clinical applications. Biomanufacturing technology includes combining cells and biomaterials in a functional 3D configuration. *In vivo* integration technologies refers to the immunological acceptance of the biomanufactured construct. These technologies must come together for the safety, efficacy and integrity of a fully functional 3D printed organ [23].

An additively manufactured organ would normally be designed to contain a network of hierarchically branched vascular segments similar to a native organ tissue. Visconti et al. stated that a naturally occurring branched vascular system is essential to create a functional intra-organ vascular system [24]. However, the level of multiscale organisation or the biomimetic design required for producing both micro and macro vasculature, is not practical with most printing technologies, due to manufacturing time and printer spatial resolution limitations. Scalability and cost effectiveness are associated challenges that must be overcome for successful organ printing [24]. It is also noteworthy that 3D printing speeds and resolution continue to improve, but they still lag behind the optimal levels [25]. One of the first noteworthy milestones in organ printing was achieved by the Wake Forest Institute for Regenerative Medicine, where a biodegradable scaffold in the shape of a urinary bladder was 3D printed and transplanted into a human body. The scaffold was created using inkjet printing technique, but the cartridges were filled with patient specific cells instead of ink. The scaffold shape was designed in the shape of the patient's bladder which was obtained from a CT scan [26].

2.2. Bioprinting techniques

Bioprinting requires scaffolds that can be derived from natural or synthetic polymers or a combination of both. Hydrogels as scaffold materials have been discussed in numerous studies as they have structural similarity to the extracellular matrix of tissues [27, 28]. Hydrogel

tissue scaffolds can be made from many materials, including but not limited to: collagen, cellulose, atelocollagen, alginate, gelatin, chitosan, collagen/glycosaminoglycan, collagen/hyaluronan and poly-l-lactic acid. Further details on the chemical and physical properties of the materials can be found in the works of Chan et al. [29].

Four common methods of bioprinting are inkjet printing, stereolithography, laser bioprinting and extrusion bioprinting. In inkjet printing, bioink droplets (scaffold and cell material together) are ejected through a thermal or piezoelectric actuator which are combined and patterned in the required shape [30]. In laser-assisted bioprinting, a beam of laser is pulsed on a cell layer, which causes it to bubble through local heating and propels it to fall. This bubble is allowed to fall over a scaffold layer which encapsulates it and thus bioink could be patterned in the required shape [31]. In the stereolithography technique, a digital light projection in the shape of the desired pattern is focused on a bioink plane and this causes the polymer scaffold to crosslink according to the pattern of light, through photo-polymerisation [32]. In extrusion bioprinting, pneumatic or manual force is used to force the hydrogel material through the nozzle, which solidifies into a scaffold of a desired shape [33].

Sacrificial Writing into Functional Tissue (SWIFT) is a new technique that emerged in 2019. The technique is intended to 3D print large vascularized organ building blocks, which are high density cells derived from stem cells. In this technique, blood vessels are 3D printed, which is different to other techniques, wherein only tissue cells are 3D printed. First, target cells, which are dense and exhibit a viscoplastic rheology, are mixed with Extra Cellular Matrix (ECM) to make a living matrix. Into this matrix, a thin nozzle is inserted and strands of a special type of gelatin ink are laid down in the desired vasculature pattern. The temperature is gradually increased from 0℃ to 37℃ to allow the matrix to stiffen, while the gelatin melts and is washed away to leave an empty perfusion pathway. Currently, the blood vessel diameters designed with SWIFT technology are in the range of 400 μm to 1 mm. A cardiac tissue patch was developed by this method, which successfully pulsated for about a week; and efforts are continuing to make this fabrication technique more efficient [34].

Another advancement in bioprinting was an improvement to the stereolithography technique in 2019, an open source bioprinting technique known as SLATE (Stereolithography Apparatus for Tissue Engineering). In this technique, hydrogel solutions are solidified when exposed to blue light, to fabricate scaffolds in the desired shape. This technique also involves photo-polymerization, which requires photoabsorbers, to focus the light at a particular location.

Currently known photoabsorbers are toxic to the cells and the SLATE technique is different from simple stereolithography in regards to the photoabsorber. In the SLATE technique, biocompatible food dyes such as tartrazine, curcumin and anthocyanin are used as the photoabsorber. Using this technique, lung mimicking structures and liver like constructs were fabricated and successful oxygen mass transfer has been demonstrated [35].

The bioinks used for bioprinting are also rapidly evolving and improving with innovation. In 2019, Noor et al. synthesized a bioink to generate heart cells that are personalized for each individual. In this method, the omentum tissue[4] is extracted from a patient, which contains both the cells and the ECM. The cells and ECM are centrifuged and separated, following which the ECM is processed into a personalized thermoresponsive[5] hydrogel. These hydrogels were fluid-like at room temperature, but become stiffer at body temperature (37℃). The cells that were separated from ECM were reprogrammed to become pluripotent[6], and then differentiated to become cardiomyocytes[7] and endothelial cells. These cells were later encapsulated into the thermoresponsive hydrogel derived from omentum tissue, to generate the bioink. These bioinks are now considered autologous[8] and can be transplanted back into the patient [36]. Another biocompatible ink that has lately been explored for its superior material properties is *Pluronic* F127. This ink is known for its unique phase behaviour at critical micelle concentration. The thermoresponsive properties of the ink also make it an attractive gel to 3D print scaffolds for tissue engineering [37].

A vascularized biocompatible scaffold is a prerequisite in most of the bioprinting strategies. However, the efficient shape and architecture of a 3D printed scaffold is not addressed properly in the bioprinting literature. Previously vascularization attempts include biomimicking as fractal patterns in which the vascular branching was designed according to fractal algorithms, based on Murray's equation [38]. The cell densities were found to increase up to the 6th level of branching complexity, but remain constant beyond that [39]. Fractal surface models were also used to design biomedical device surfaces to investigate contact properties and enhance cell integration [40].

Vascularization also requires growth factors to promote emergence of new blood vessels in addition to a biocompatible scaffold. Growth factors such as Vascular Endothelium Growth

[4] Fatty tissue stretching over abdomen.
[5] Hydrogels displaying a discontinuous change in their physical properties with change of temperature.
[6] Cells able to give rise to different cell types (stem cell technology).
[7] Heart cells.
[8] Obtained from the same individual.

Factor (VEGF) and Basic Fibroblast Growth Factor (bFGF) are typically delivered as recombinant proteins or via gene vectors. Another approach is to directly inject progenitor cells[9] such as endothelium progenitor cells and mesenchymal stem cells into the tissue. These cells will differentiate into new blood vessels and connect to existing vessels. Using these growth factors, a multiscale vasculature network was developed by combining ~1 mm fluid channels to adjacent capillary networks through a natural maturation process [41]. Studies have also reported implanting endothelial cells into the conduits of the biocompatible scaffold [24, 42-44]. Certain polyethylene glycol-based hydrogels have also been explored as a biocompatible scaffold material. These hydrogels have bioactive ligands, which are cross-linked by specific reactions. They have sites for cell adhesion, cleavable peptides and tethered growth factors attached to them and thus, these matrices can induce new blood vessel development [45, 46]. These techniques involve both 3D printing and take advantage of the natural biological maturation process. Cellulose is another polysaccharide used to synthesize hydrogels that is popular for being renewable[10] and biodegradable [47]. The molecular structure of cellulose has abundant hydroxyl groups in it, which makes it a potential material for 3D printing hydrogels [48]. Cellulose-derived scaffolds are the focus in this thesis and therefore the scaffold parameter values such as oxygen diffusion coefficient used for CFD modelling were based on the properties of cellulose.

Other attempts to make organs in the lab rely extensively on stem cell technology such as blastocyst complementation. In this technique, human stem cells are transferred into genetically engineered animal embryos. These embryos are grown in a host animal to produce organs that should be compatible with the human genotype, that are intended to be harvested for organs as needed. Some of these techniques are considered controversial in some nations, from an animal rights point of view. However, in 2019 the Japanese government approved the use of stem-cell technology to create hybrid embryos in animals. There are challenges to be overcome in this research, such as minimizing the existing genetic distances between humans and animals. Regardless, the science of stem cell technology is rapidly progressing to address the issue of soft tissue and organ shortages [49, 50]. Stem cells offer a promising solution for the need to have an unlimited supply of cells, however the differentiation process must be fine-tuned for targeted tissue development with the desired phenotype[11] [51].

[9] Cells that are able to differentiate into specific type of cells.
[10] Present in plant wood.
[11] Observable traits of an individual resulting from interaction of their genotype with the environment.

The advantages of bioprinting include efficient control over tissue geometry across wide scales, while producing scaffolds with precise material and cell patterns. Typically, the minimum feature sizes of 3D printers are between 10 μm and 500 μm [52]. However, 3D printing tiny capillaries requires a minimum feature size less than 5 μm. Therefore, bioprinting has disadvantages such as reduced cell viability occurring due to inadequate oxygen availability to remote cells. Also for some bioprinting techniques, the potential scaffold material choices are limited, due to absence of a binding cross-linker for all range of materials. However, in future these limitations could potentially be eliminated with improvement in the resolution of the 3D printers.

2.3. Tissue bioreactor designs

There are interesting tissue bioreactor designs intended to specifically nurture cells in a lab environment. Hollow fiber systems are a type of configuration, which consists of a shell side and tube side. In this method, the shell is traversed by a large number of small diameter tubes [53]. The cells are placed within the fibres or on the shell side of the extra-capillary space (Figure 2.3-1). The compartment that does not contain the cells is perfused with nutrient culture medium. Typically, the cells are placed in the lumen of the small fibers, as the diffusional distance between the shell and cells is essentially equal to the fiber thickness. These systems are generally substrate or mass transfer limited, because of the diffusional limitations associated with the fiber wall [54, 55].

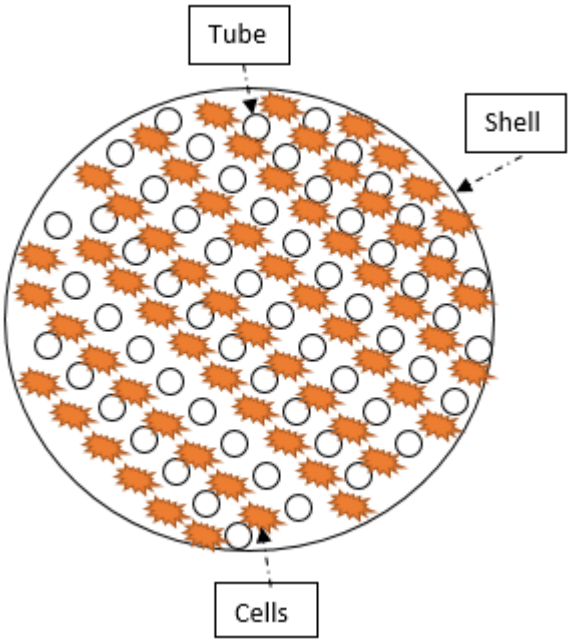

Figure 2.3-1: Cross-sectional view of a shell and tube bioreactor.

Parallel plate systems are another type of bioreactor configuration based on a flat surface geometry [56]. In these systems, nutrient flow distribution is controlled and cells are adequately perfused as shown in Figure 2.3-2). However, these systems have disadvantages such as having insufficient cell concentrations. It is possible to customize the flat-plate geometry by reducing the channel height. However, this forces the fluid through a small channel space, which increases the shear force experienced by the cells. Studies indicate that a shear force of >5 $dyne/cm^2$ could have deleterious effects on the cells [57, 58]. Therefore, alternatives such as grooved surfaces have been designed to reduce shear stress. In such systems, the cells are lodged into the groves, such that shear stresses are minimized. However, these configurations increase the fluid hold-up volume.

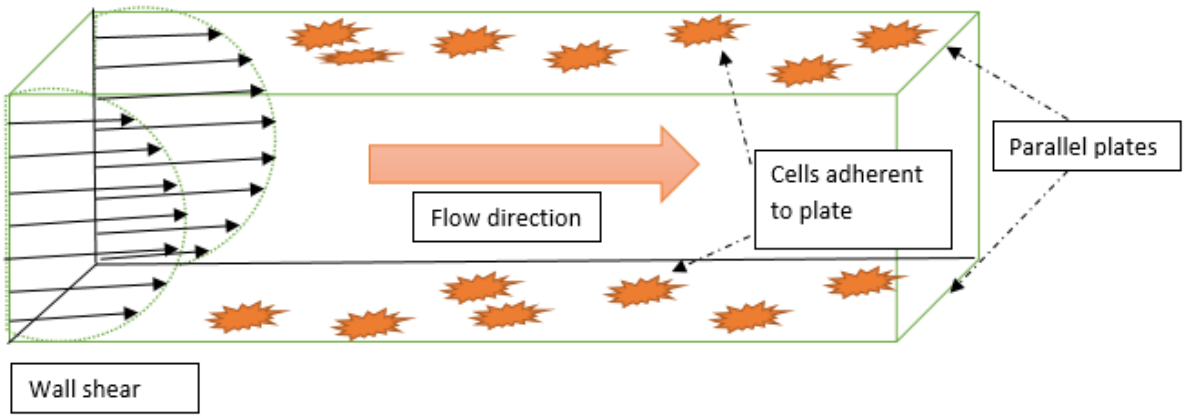

Figure 2.3-2: Lateral view of a parallel plate tissue bioreactor.

Microfluidic channels are another way to sustain cells and in this configuration, semipermeable channels mimic a vascular network [59]. The channels are laid out in the desired pattern and after printing each microfluidic channel layer, tissue spheroids (cells) are deposited between these channels (Figure 2.3-3). The channels facilitate perfusion media transport as well as oxygenate the adjacent cells through the membrane. Cells are typically embedded in spheroidal shapes as it reduces the shear stress experienced by them [60]. This method also allows bioprinting multiple cell types between the microfluidic channels.

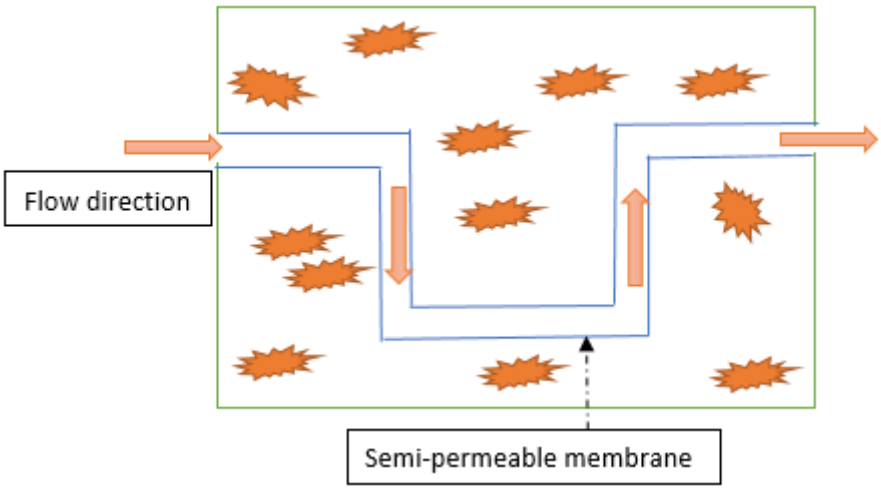

Figure 2.3-3: Top view of a simple microfluidic device.

However, these bioreactor design are mainly *in vitro* tissue bioreactor strategies. These designs also have limitations such as inadequate oxygenation due to large diffusion distances between the nutrient supply and cell location. Therefore, functional capacity of these designs is also limited due to inability to sustain large cell concentrations.

2.4. Triply periodic minimal surfaces

TPMS structures are periodic along the three Cartesian axes (x, y and z) and are classified as minimal surfaces. This is because in a given fixed boundary these structures tend to have a zero mean curvature and extremal surface areas [61]. All points on these structures are saddle points[12], which makes the core of the structure appear hyperbolic [62, 63]. These structures are identified by the Bonnet transformations involved in their Weierstrass-Enneper parameterization, which is a parametric set of equations to describe TPMS surfaces using complex numbers [64]. TPMS structures are an interesting phenomenon in number theory and topological studies, and research is ongoing to discover more of these structures. Figure 2.4-1 show the basic TPMS structures (Schwarz Primitive, Schwarz Diamond and Schoen Gyroid). However in the past decade, there has been an explosion in the discovery of new TPMS structures (Appendix A), and they are classified under *genus* and *family* definitions of the parent TPMS structures. Software packages such as the SURFACE EVOLVER aid in numerically defining new TPMS structures [65].

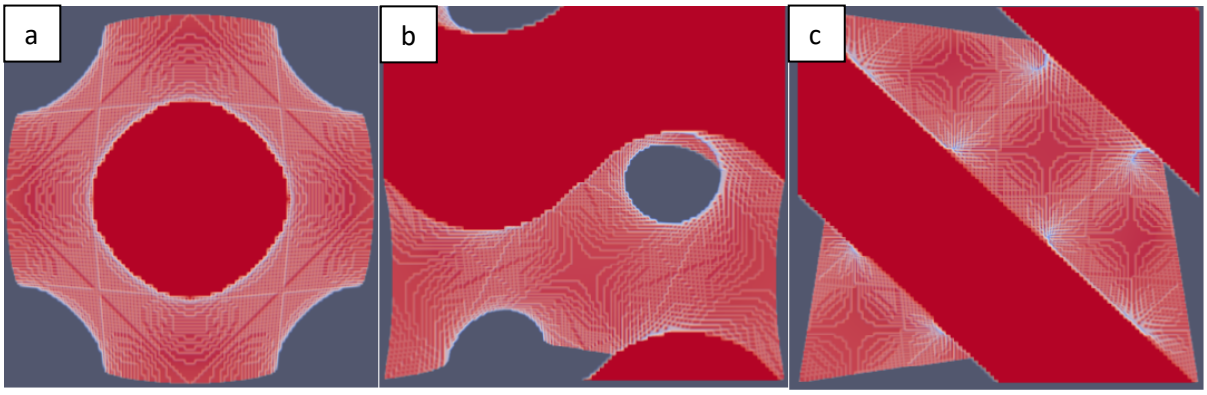

Figure 2.4-1: a) 50% Schwarz Primitive b) 50% Schoen Gyroid c) 50% Schwarz Diamond

Traditionally, cubic and simple lattice shaped scaffolds are constructed by additive manufacturing techniques. However, the straight edges and sharp turns, or spheres and cylinders that emerge from these respective methods are not ideal for cell attachment, migration and proliferation. This is because such shapes are in contrast to the natural ECM, which is separated by curved partitions [22]. Rajgopalan et al. reports that surfaces with a small radius of curvature relative to cell size[13] enhance cell migration, because the cytoskeleton of cells is not oriented parallel to the edge [66]. He noted that cell adhesion and proliferation increases by a factor of six in a 3D matrix compared to a 2D substrate [67]. The curvy and intertwined

[12] Also known as minimax point, where the slopes in orthogonal directions are zero, but which is not a local extremum of a function.
[13] Less flat and more round edges.

nature of TPMS structure could therefore be an attractive candidate to enhance soft tissue matrix development.

TPMS structures are reported to have higher permeability, low stress concentration and higher surface to volume ratio than a sphere and have found utility in various science and engineering applications [68]. Another advantage of TPMS structures is that they can be closely approximated by analytical trigonometric equations and a single parameter value can be used to define the relative proportions of different phases in a printed structure. This alleviates the need to define and design each TPMS phase, thereby minimizing the pre-processing time. For instance, the tissue phases (red) in Figure 2.4-1 were created using a single parameter as shown in Table 2. Similarly, parameter values can be appropriately chosen to create sheet TPMS structures mathematically, transforming them into CAD files and eventually 3D printing them.

Table 2: Trigonometric equations representing the TPMS structures modelled in Figure 2.4-1

TPMS structures	Equations
Schwarz Primitive	$\cos(x) + \cos(y) + cos(z) = parameter$
Schoen Gyroid	$\sin(x)\cos(y) + \sin(y)\cos(z) + sin(z)\cos(x) = parameter$
Schwarz Diamond	$sin(x)\,sin(y)\,sin(z) + \sin(x)\cos(y)\cos(z) + \cos(x)\sin(y)\cos(z) + \cos(x)\cos(y)\sin(z) = parameter$

TPMS structures are currently being used to fabricate bone scaffolds, because they enable porosity controlled designs [69, 70]. However, the potential of using sheet TPMS structures for soft tissue 3D printing has not been tested yet. There are many computational studies performed on TPMS structure applications in areas such as: mechanical testing with Finite Element Method (FEM) software ABAQUS [71-73], electrical and thermal conductivity testing with FEM [74], elastic moduli and mechanical isotropy investigations with FEM [75], and Poisson's ratio investigations of TPMS structures [76]. However, there have been limited computational studies analysing mass transfer phenomena in TPMS structures. Fernandes et al. in 2019 studied the TPMS structures: Gyroid, Schwarz Primitive and Schwarz Diamond, to examine their potential application as bone scaffolds and to observe the macroscopic flow permeability through these scaffolds in the axial direction. It was noted that gyroid had the highest permeability followed by Schwarz Primitive and Schwarz Diamond. However, this

study did not investigate the simulation of oxygen diffusion and consumption within these TPMS scaffolds. In this thesis, this gap is identified and addressed by designing a more comprehensive CFD model that simulates blood advection, oxygen diffusion and consumption through scaffolds designed as sheet TPMS architectures [77]. The TPMS structures investigated in this project are: Gyroid, F-RD, I-WP, Schwarz-Diamond, P2GD, Fisher-Koch, Lidinoid, D' surface, Double Schoen Gyroid (DSG) and Double Diamond [78, 79] (Appendix A).

2.5. Computational fluid dynamics

Computational fluid dynamics (CFD) is a science of quantitative predictions of fluid-flow phenomena based on conservation laws of mass, momentum and energy using computers [80]. CFD studies are performed to obtain numerical solutions to systems in steady or transient state. Typically, CFD models require the fluid domain to be represented by small elements (grid points/mesh) and calculations are performed on these interacting elements. The meshing process could be refined (high resolution) or crude (low resolution) which are computationally expensive and cheap respectively. Traditionally, the Navier Stokes equation is employed to perform CFD studies. However, in this thesis the Lattice Boltzmann method is used to perform CFD as this approach scales well on graphic processing units and supercomputers through parallelisation [81].

2.5.1. Navier Stokes equation

The Navier Stokes (NS) equation was derived by Navier, Poisson, Saint Venant and Stokes (1827 – 1845)[82]. The NS equation is a mathematical description of physics governing the flow field and was derived by applying Newton's[14] second law of motion to a fluid element. Hence, it is also called the momentum equation [83, 84]. Equation [1] represents the NS equation for compressible Newtonian fluids.

$$\rho\left\{\frac{\partial u}{\partial t} + u.\nabla u\right\} = -\nabla p + \nabla.\left(\mu(\nabla u + (\nabla \mathrm{u})^T) - \frac{2}{3}\mu(\nabla.u)I\right) + F \qquad [1]$$

; where I is the Identity matrix[15], μ is the dynamic viscosity of fluid $[\mathrm{ML^{-1}T^{-1}}]$, u is the fluid velocity $[\mathrm{LT^{-1}}]$, $\rho\left\{\frac{\partial \mathrm{u}}{\partial \mathrm{t}} + \mathrm{u}.\nabla \mathrm{u}\right\}$ represents the inertial forces, $\nabla \mathrm{p}$ represents the pressure

[14] Force is equivalent to rate of change of momentum.
[15] Diagonal of a matrix has value 1, other elements are 0.

forces, $\nabla.\left(\mu(\nabla u + (\nabla u)^{T}) - \frac{2}{3}\mu(\nabla.u)I\right)$ represents the viscous forces and F represents the external force $[MLT^{-2}]$.

The NS equation is conventionally solved in conjunction with the conservation of mass or the continuity equation (Equation [2]). Therefore, for an incompressible fluid, Equations [2] and [3] are solved together.

$$\nabla.u = 0 \qquad [2]$$

$$\frac{\partial u}{\partial t} + (u.\nabla)u = \mu\nabla^2 u - \frac{1}{\rho}\nabla P + \frac{F}{\rho} \qquad [3]$$

2.5.2. Boltzmann equation

The Boltzmann equation is a statistical description of the movement of gases. It is an integro-differential equation proposed by Ludwig Eduard Boltzmann (1844-1906), who was a renowned scientist in the field of statistical mechanics [85]. The Boltzmann equation is the culmination of an attempt to understand the macroscopic[16] properties of matter such as viscosity, temperature and diffusion coefficients from microscopic properties of atoms including the atom's position and its microscopic velocity. Boltzmann proposed a probability distribution function to understand the microscopic properties of particles (Appendix C) [86].

2.6. Derivation of Boltzmann equation

The particle distribution[17] (f) at any given time (t) is defined by its position (r), velocity (c) and time (t). In a time interval (dt), the particle distribution function for a unit mass changes to $f\left(r + cdt, c + Fdt^{18}, t + dt\right)$, when the particles are acted upon by a force (F). If no collision between molecules is assumed, the number of particles would remain constant. This process is mathematically represented by Equation [4].

$$f(r + cdt, c + Fdt, t + dt)drdc - f(r, c, t)drdc = 0 \qquad [4]$$

However, if collision between particles is assumed, molecules may stream in different directions post the collision process. This rate of change of molecules between the initial and final status of the particle distribution function is by a collision operator[19](Ω) which can be mathematically described by Equation [5].

$$f(r + cdt, c + Fdt, t + dt)drdc - f(r, c, t)drdc = \Omega(f)drdcdt \qquad [5]$$

[16] Also known as phenomenological properties.
[17] It is a function used to represent the property/behavior of collection of particles.
[18] $Fdt = \frac{kgm}{s^2}.s = \frac{m}{s}$.
[19] Used with collision parameter interchangeably.

Dividing Equation [5] on both sides by $(drdcdt)$ and taking a limit to this function as $(dt \rightarrow 0)$ yields Equation [6], which by construction represents the change in the probability distribution function (Ω).

$$\frac{df}{dt} = \Omega(f) \quad [6]$$

Because f is implicitly dependent on r, t and c, the principles of partial differentiation may be used to obtain Equation [7], using the partial differentiation rule.

$$df = \frac{\partial f}{\partial r}dr + \frac{\partial f}{dc}dc + \frac{\partial f}{\partial t}dt \quad [7]$$

Dividing Equation [7] by dt and substituting into Equation [6] yields

$$\frac{df}{dt} = \frac{\partial f}{\partial r}.\left(\frac{dr}{dt}\right) + \frac{\partial f}{dc}.\left(\frac{dc}{dt}\right) + \frac{\partial f}{\partial t} = \Omega(f) \quad [8]$$

Or

$$\frac{\partial f}{\partial r}.(c) + \frac{\partial f}{dc}.(a) + \frac{\partial f}{\partial t} = \Omega(f) \quad [9]$$

Since acceleration (a) is rate of change of velocity, it could be written as the ratio of force, *F*, and mass, *m*, from Newton's second law. Thus, the collision parameter evaluates to Equation [10].

$$\Omega(f) = \frac{\partial f}{\partial r}.(c) + \frac{\partial f}{dc}.\left(\frac{F}{m}\right) + \frac{\partial f}{\partial t} \quad [10]$$

In the absence of external force $(F = 0)$, Equation [10] simplifies to Equation [11].

$$c.\nabla(f) + \frac{\partial f}{\partial t} = \Omega(f) \quad [11]$$

Equation [11] is the fundamental Boltzmann equation, which is an integro-differential equation[20] and mathematically challenging to solve. A parallel can be drawn between the macroscopic properties such as density (ρ), internal energy (e) and velocity (u) to microscopic features such as particle velocity and molecular mass(m). This mathematical connection between the macro and micro scales is reflected in Equation [12], Equation [13] and Equation [14], which correlates to conservation of mass, momentum and energy respectively.

$$\rho(r,t) = \int mf(r,c,t)dc \quad [12]$$

[20] Containing both integration and differentiation terms.

$$\rho(r,t) * u(r,t) = \int mcf(r,c,t)dc \quad [13]$$

$$\rho(r,t) * e(r,t) = \int \frac{1}{2} m{u_r}^2 f(r,c,t)dc \quad [14]$$

;where u_r is the particle velocity relative to the fluid velocity $(c-u)$. Based on the derivation of the conservation equations LBM is proving to be a potential alternative to Navier Stokes equations. Further details on the similarity between Boltzmann algorithm and Navier Stokes can be found in the books by Mohamad et al. [87] and Sukop et al. [88]. Although this is a simplified derivation of the Boltzmann equation, assuming the absence of an external force term, an additional source term for force could be added to yield a more comprehensive equation. However, in the CFD cases simulated in this thesis an external force term is also included and the Perko-Patel model discussed in Chapter 3 includes the theory behind its implementation.

2.7. Lattice Boltzmann method

The LBM is inspired by the Lattice Gas Automata method (LGA) [89]. The LGA method has a hexagonal or square lattice with nodes or grid points. Particles are present at these nodal points and they move between them (Figure 2.7-1) [90]. The structure of the lattice constrains the specificity and movement of the factious[21] particles [91]. When two gas particles reach the same site, the collision rules are enforced such that they are collided away, and the position and velocity of each individual particle is recorded at each iteration or time step. The LGA method became popular when the NS equations could be derived from it. However, the LGA method had issues of statistical noise[22][92] and was limited to square and hexagonal lattices, which made handling three dimensional simulation problems challenging.

[21] Colliding particles.
[22] Unexplained variation in a sample.

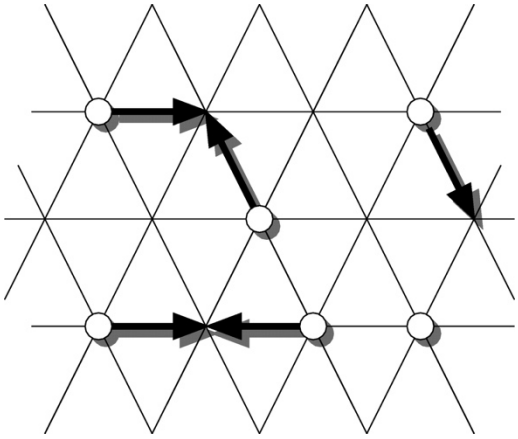

Figure 2.7-1 Hexagonal lattice in LGA method.

LBM emerged as an alternative to LGA, due to the numerical problems observed in the latter. CFD with LBM envisages a lattice of spherical particles, which are in random motion, with inelastic collisions between them [93]. LBM limits space to a lattice structure and the velocity space to a discrete set of microscopic velocities (Figure 2.7-2 and Figure 2.7-3). However, there are more lattice choices in the LBM method in comparison to LGA. The lattice nomenclature in LBM is denoted by $D_m Q_n$, where D_m indicates the number of dimensions and Q_n represents the number of discrete velocities [94]. For instance, the D2Q9 is a two dimensional lattice with one central particle and eight neighbouring particles (Figure 2.7-2). Similarly, a D3Q19 lattice is a three dimensional lattice with one central particle and 18 neighbours (Figure 2.7-3). The lattice positions relative to the central node are assigned weightings according to the Gauss-Hermite[23] quadrature formulae. The choice of lattice in LBM depends on the physics being modelled and higher dimensional lattices allow recovery of more accurate data from the moments of the velocity distribution (Appendix C) [95].

[23] Used in numerical analysis as a method to calculate integral values.

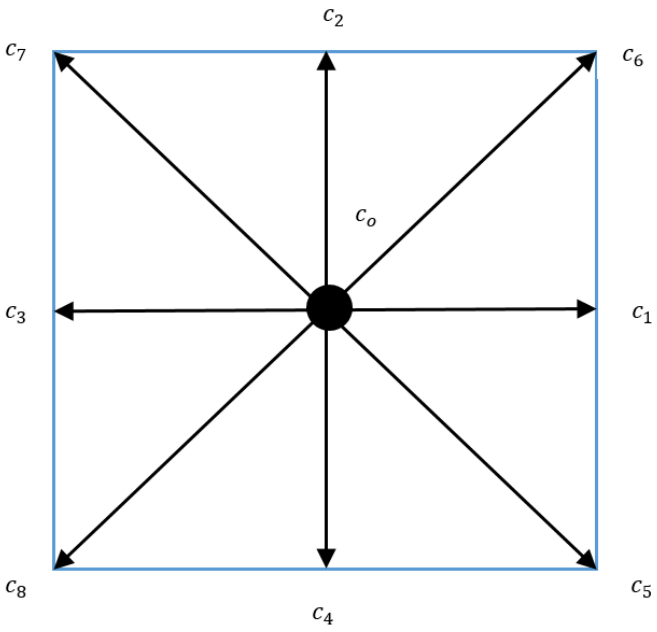

Figure 2.7-2: D2Q9 LBM lattice with c_i representing the velocity vector (reproduced from [96]).

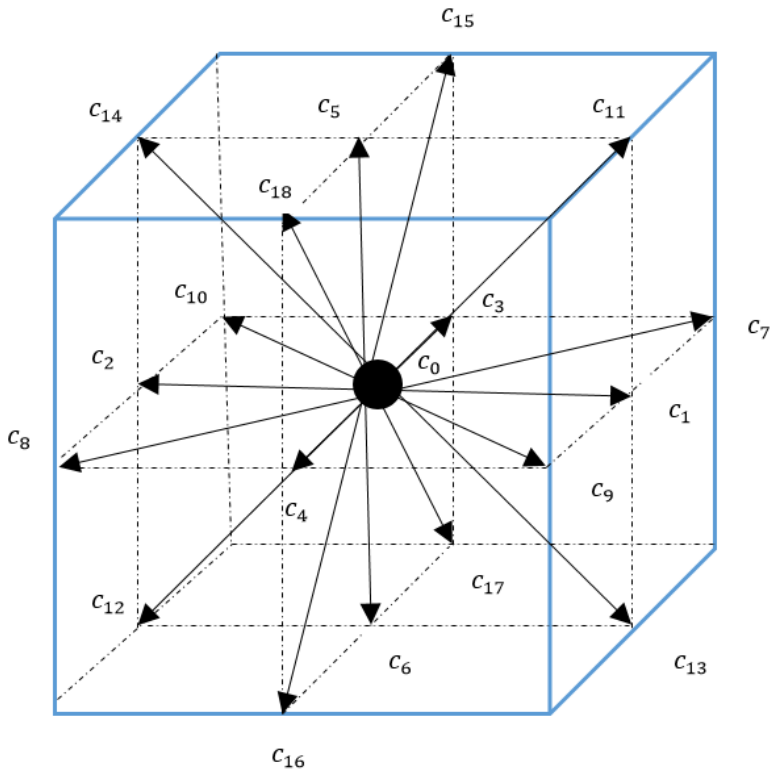

Figure 2.7-3: D3Q19 LBM lattice with c_i representing the velocity vector (reproduced from [96]).

LBM uses a probability distribution function, unlike the LGA methodology to track individual particles. The probability distribution function corresponds to the particle density at each node and time step. The particle density at a node is estimated based on the probability that a particle has arrived to that node, in the previous streaming step. In LGA, the presence or

absence of each particle at a node is characterized by a Boolean function[24]. Contrarily in LBM, the Boolean function is replaced by the probability of a particle streaming in a certain direction. The probability distribution methodology allocates any value between 0 and 1 to a particle, and thus allows virtual splitting of particles (theoretically). This flexibility diminishes the statistical noise in LBM and outcompetes the LGA methodology [97].

2.8. Collision Parameter

To solve the Boltzmann equation, Ω must be quantified. It has been found that in the hydrodynamic limit[25], the fluid molecules are close to being in an equilibrium state. This idea was used by Bhatnagar, Gross and Krook [98] to delineate Ω in a linear form, as shown in Equation [15].

$$\Omega(f) = \omega\left(f_{eq} - f\right) = \frac{1}{\tau}(f_{eq} - f) \qquad [15]$$

; where ω refers to the collision frequency of the particles, τ is the relaxation factor[26] and f_{eq} is the local equilibrium distribution function or Maxwell equilibrium distribution function (Appendix D) [99]. The BGK model is also referred to as the Single Relaxation Time (SRT) model, because the velocity distribution function is relaxed to the local equilibrium by using a single relaxation parameter. Amending the Boltzmann equation (Equation [11]) with the BGKW[27] approximation of the new collision parameter yields Equation [16].

$$c.\nabla(f) + \frac{\partial f}{\partial t} = \frac{1}{\tau}(f_{eq} - f) \qquad [16]$$

Equation [16] can be represented in Einstein notation for any direction in the Cartesian space. Thus, for the j^{th} direction[28], the representation is given by Equation [17].

$$c_j.\nabla\left(f_j\right) + \frac{\partial f_j}{\partial t} = \frac{1}{\tau}(f_{eq_j} - f_j) \qquad [17]$$

Equation [17] is the workhorse of LBM and replaces the NS equation in CFD simulations. It can be discretized to Equation [18], which can be converted to Equation [19] based on the relationship between ω and τ.

$$f_j\left(r + c_j.\Delta t, t + \Delta t\right) = f_j(r, t) + \omega\left(f_{eq_j}(r, t) - f(r, t)\right) \qquad [18]$$

[24] [0,1] or [True, False] or [Yes, No].
[25] Systems of infinite size.
[26] Used interchangeably as relaxation time or relaxation parameter.
[27] The Bhatnagar, Gross, Krook approximation was validated by Welander. Therefore, the model is also acronymed as BGKW.
[28] j is always less than or equal to the maximum number of directions allowed in the LBM lattice.

$$f_j\left(r + c_j.\Delta t, t + \Delta t\right) = f_j(\,r,t) + \frac{\Delta t}{\tau}(f_{eq}{}_j(r,t) - f(r,t)) \quad [19]$$

Equation [17] is a linear partial differential equation, with the left hand side of the equation resembling the streaming/advection term and the right side of the equation resembling the collision or source term. f_{eq} is approximated in literature as represented in Equation [20] [87].

$$f_{eq}{}_j = \rho t_j\left(1 + \frac{c_j.u}{c_s^2} + \frac{1}{2c_s^4}\left(c_j.u\right)^2 - \frac{u^2|u|^2}{c_s^2}\right) \quad [20]$$

; where t_j is a constant providing a weighting dependent on the lattice chosen, and c_s is the speed of sound in lattice units. The role of τ in the LBM equation is to push the system towards the equilibrium distribution of particles, during the streaming process. In other words, when particles coming from different directions collide, the particles are virtually adjusted, such that their movements resemble the equilibrium distribution. The inclusion of τ comes from the statistical nature of the method, and the gradual movement of particles towards an entropy state. Depending on the physical process, $f_{eq}{}_j$ may or may not vary with time. This allows LBM to solve different problems in physics by merely varying f_{eq} and τ. Every simulation needs a set of initial conditions such as ρ, u and the appropriate boundary conditions. The boundary conditions could be either constant or changing with time, depending on the simulation. CFD with LBM stands out for its ability to simulate complex systems such as multiphase flows, flow through porous media and resolve complex fluid-solid interactions at pore-scale and efficiently solve for multiphase boundaries [100] [101]. However, LBM is not as mature as the Navier Stokes equation and suffers from issues such as compressibility and inability to solve turbulent flow without further modification [102]. Its memory requirements could be intense depending upon on D_mQ_n lattice. But LBM can solve laminar and Stokes flow such as those present in blood capillaries.

2.9. Palabos

Currently software packages such as ANSYS, COMSOL and ABAQUS are popular for performing CFD studies. ANSYS is commercially available as ANSYS parametric design language and its solvers are based on finite element discretization methods. Stress-strain analysis and other multiphysics problems are commonly simulated with ANSYS. ABAQUS assists in performing non-linear finite element analysis, which is primarily used in automotive

and aerospace engineering. MATLAB also provides simplified toolboxes to perform certain CFD simulations. These software packages provide a Graphic User Interface (GUI), however the user does not have complete control over the back end algorithms. Thus, GUI-based CFD packages provide limited options to the users in terms of code customization and versatility. Open source software packages are an alternative to GUI based CFD solvers. These software packages allow the users to customize the code and specifically define the reaction kinetics. OpenFOAM[103], SU^2[104], PyFR[105], Code_Saturn[106] and *Palabos* are some of the popular open source CFD packages. These solvers have also emerged as being superior due to their solver and support capabilities [107].

Most of the CFD packages are based on the NS equations except few such as XFLOW from the Dassault systems group which is GUI based and *Palabos* by Flowkit which is an open-source C++ library [108]. In this thesis, CFD studies are performed with *Palabos* which has an extensive back end library encoding the Lattice Boltzmann algorithm. The software has well-defined namespaces[29] and classes[30] inclusive of complex chemical engineering phenomena. For example, choosing the D_nQ_m lattice in *Palabos* automatically takes care of the lattice weight constants corresponding to that lattice. "Dynamic Objects" is an exceptional feature of *Palabos* software whereby each fluid cell can be associated with its local collision step (Section 2.8). *Palabos* offers the ability to solve the collision and streaming phenomena in a single step, which saves computational time. Other LBM solvers typically tackle collision (Equations [21]) and streaming and (Equation [22]) in two steps, to avoid overwriting of particle populations. However, the *Palabos* solver integrates the collision and streaming process in a computationally efficient way by avoiding storage of populations in temporary memory locations. Therefore, the user of the *Palabos* library need not explicitly code for the particle colliding and streaming steps, thus making it an efficient LBM solver.

$$f_j^{out}(x,t) = (1-\omega)f_j^{\text{in}}(x,t) + \omega f_j^{eq}(x,t) \quad [21]$$

$$f_j^{\text{in}}(x+c_i,t+1) = f_j^{out}(x,t) \quad [22]$$

Implementing the *Palabos* LBM code however requires deeper understanding of its library such as header files, source files and functions. In particular, understanding the backend implementation of LBM algorithms in C++ as well as knowing how to call or include these functions in the main CFD file, requires experience and expertise. The *Palabos* solver also

[29] Concept in C++.
[30] Concept in C++.

provides the advantage of accelerated computing as it is easily parallelizable. Parallelization is a process where a computational task is fragmented into smaller tasks and each task is performed by different central processing unit or graphical processing unit cores[31]. Task fragmentation is an important concept in computing architectures and in this thesis, task fragmentation was done by the Message Passing Interface (MPI) standard [109]. It has been reported that '*n'* cores can achieve a reduction in computation time by a factor close to *n*, at least in principle. The divergence of computation time from an exact factor of *n* is attributed to overheads such as inter-core communication associated with parallelized computational problems. The LBM algorithm works by computing the distribution functions locally and therefore the computation can be conveniently parallelized, because multiple cores can be allocated to perform these local calculations. Previously, laminar flow through different porous media structures were performed to study adsorption robustly using *Palabos,* in the works of Fee et al. [110] and Khirevich et al. [111]. Therefore, reliability, efficiency and simplicity to model sheet TPMS structures are the major reasons behind using LBM *Palabos* simulations to achieve the objectives [112, 113].

[31] Processing unit that receives information and performs calculations based on those instructions.

3. LBM model development

3.1. Introduction

In this chapter, the LBM model development for tissue vascularization is described. Modelling of tissues, blood and hydrogel in various shapes is explained, followed by details of the diffusion model depicting oxygen mass transport. Other important CFD aspects such as boundary conditions are also explained. Zero-order kinetics was used to model oxygen consumption in this work and the choice of consumption rate is discussed in detail. Multiscale modelling was implemented to simulate oxygen diffusion and consumption in tissues, and its effectiveness is discussed briefly. After LBM model development, the model was tested on thin capillary slices by varying the capillary radius, hydrogel thickness and oxygen diffusivity in hydrogel and tissue. The oxygen penetration distances in these slices were checked against analytical solutions of oxygen diffusion profiles for the case of cylindrical capillary. Krogh's model is extensively discussed in this chapter to generate preliminary insights on the effect of parameters such as scaffold void space, oxygen concentration and tissue diffusivity on the oxygen concentration profiles. After verifying the 2D model, the model was scaled up longitudinally to examine oxygen concentration profiles in 3D space of TPMS structures. Computational resources were found to be inadequate for this and therefore high performance computers were used to achieve steady state solutions in reasonable time frames. Mesh independence studies and the usage of NeSI computational nodes were optimized for efficient scalability. Entrance and exit effects were observed in the implemented 3D LBM model which were addressed using exit lengths. The chapter concludes by identifying the location/subset of the computational domain, where the results are representative of large periodic tissue scaffolds.

3.2. Modelling tissue, hydrogel and blood with *Palabos*

To distinguish between tissue, hydrogel and blood phases, tags were assigned to each node with numerical values of '1', '0.5' and '0'respectively. These numerical tags were stored in corresponding 'pointers[32]' for convenient accessibility throughout the C++ code. There

[32] Pointer in C++ refers to a data variable that holds the memory address of the value it holds.

could be other ways to define phases, however number tagging and pointer accessibility simplifies Boolean operations, when converted into '*scalarfields*'[33].

Equation [23] was used to model a capillary of radius R_c, in the x, y and z Cartesian directions.

$$\left(y - \frac{ly}{2}\right)^2 + \left(z - \frac{lz}{2}\right)^2 = {R_c}^2 \qquad [23]$$

; where ly and lz are lengths in the directions orthogonal to the blood perfusion direction (x). By placing bounds and limits on the radii, distinct cylinders could be created and superimposed on each other. It is important to ensure that the three phases (blood, tissue and hydrogel) have their exclusive mathematical domains, so that their radii do not overlap. For instance, to model a capillary as shown in Figure 3.2-1 with hydrogel thickness h, Equation [24] was used.

$$if \begin{Bmatrix} r \leq r_p & , & \text{blood} \\ r_p + h > r > r_p & , & \text{hydrogel} \\ r \geq r_p + h & , & \text{tissue} \end{Bmatrix} \qquad [24]$$

Mathematically, the radial limits are: blood $\in (0, r_p)$, hydrogel $\in (r_p, r_p + h)$ and tissue $\in (r_p + h, l_z \; or \; l_y)$. In the axial direction, all the three phases are present in the $y - z$ plane in $x \in (0, l_x)$.

[33] A concept in Palabos that facilitates arithmetic.

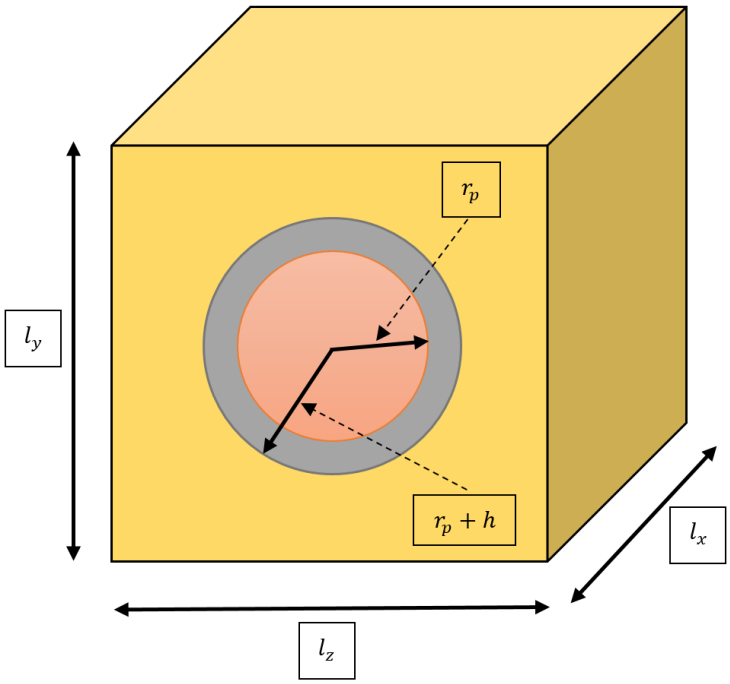

Figure 3.2-1: Illustration of blood/capillary phase (orange), tissue phase (yellow) and scaffold phase (grey).

To model a TPMS structure, trigonometric level-set equations were used to distinguish between the three phases (tissue, blood and hydrogel/scaffold). For instance, the trigonometric equation to model a Schwarz Diamond is given by Equation [25].

$$\begin{aligned} &\sin(x).\sin(y).\sin(z) \; + \\ &\sin(x).\cos(y).\cos(z) + \\ &\cos(x).\sin(y).\cos(z) + \\ &\cos(x).\cos(y).\sin(z) = isovalue \; (\alpha \; or \; \beta) \end{aligned} \qquad [25]$$

Equation [25] can be equated to any value between α and β, to create TPMS structures of varying structural porosities. α and β are also referred to as inequality values or isovalues; and they are always equal to or between '-1' and '+1' (i.e. $\alpha,\beta \in$ [-1,+1]). This is because the output of trigonometric functions such as $sin\,\theta$ and $cos\,\theta$ is always between -1 and $+1$. Equation [26] is the generic form to define TPMS structures. The value of α dictates the percentage occupied by tissue and β values dictate the percentage occupied by the hydrogel scaffold. The volume that is left unoccupied after the choice of α and β is the void or capillary space.

$$if \begin{cases} \text{Equation [25]} \leq \alpha & , \quad \text{tissue} \\ \beta > \text{Equation [25]} > \alpha & , \quad \text{hydrogel} \end{cases} \qquad [26]$$

The choice of α and β should be such that the phases remain exclusive, contiguous and do not overlap on each other. Table 3.2-1 shows how the choices of α and β affect the structural porosity of the Schwarz Diamond TPMS. The left column of Table 3.2-1 shows the inequality values, from where α and β are chosen. The right column corresponds to the structural porosity, which range from 0 to 1 (or 0% to 100%). The table was generated with a MATLAB program that iterates over Equation [25], changing the value of α between -1 and $+1$, while tabulating the TPMS porosity at every iteration. There are numerous ways to define the three phases of TPMS structures [114], but the methodology used in this thesis is as follows.

➔ Locate the desired tissue percentage in the right column (Table 3.2-1). The 'α' value corresponding to the tissue percentage should be noted in the left column.

➔ After choosing 'α', the 'β' values is chosen such that it is greater than the 'α' value.

Table 3.2-1: Porosity table for Schwarz Diamond mapping the inequality value (α) to its structural porosity

Isovalue	Porosity
-1	0.9201
-0.9	0.8753
-0.8	0.832
-0.7	0.7894
-0.6	0.7472
-0.5	0.7054
-0.4	0.664
-0.3	0.6228
-0.2	0.5818
-0.1	0.5409
0	0.5
0.1	0.4591
0.2	0.4182
0.3	0.3772
0.4	0.336
0.5	0.2946
0.6	0.2528
0.7	0.2107
0.8	0.168
0.9	0.1246
1	0.0799

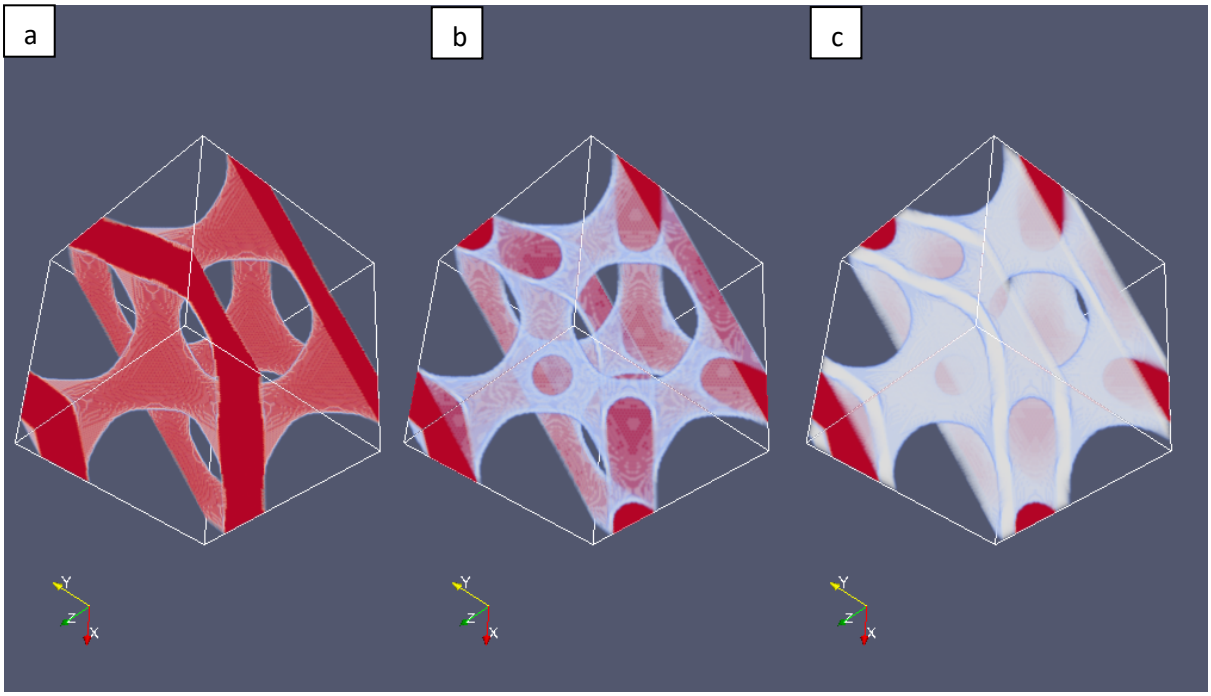

Figure 3.2-2: Schwarz Diamond structure of a) 80% b) 75% and c) 60% structural porosity.

Table 3.2-2: α and β values for the Schwarz diamond structures shown in Figure 3.2-2.

a) 20% Tissue, 0% hydrogel	b) 20% Tissue, 5% hydrogel	c) 20% Tissue, 20% hydrogel
$\alpha = -0.72$	$\alpha = -0.72$	$\alpha = -0.72$
$\beta = 0$	$\beta = -0.6$	$\beta = -0.25$

Figure 3.2-2 represents Schwarz Diamond scaffolds rendered by parameters mentioned in Table 3.2-2. It can be observed in the table that all the β values are greater than α values. The α value of '-0.72' assigns the structural porosity to 80% (20% attributed to tissue). The β value of '0' does not simulate the hydrogel scaffold material, while the β value of '-0.6' and '-0.25' models a hydrogel scaffold occupying 5% (0.8-0.75) and 20% (0.8-0.6) respectively in the void space. Appendix B contains porosity tables for other TPMS structures from which α and β values can be chosen, to define a structure with desired porosity.

3.3. Implementing LBM for tissue vascularization studies

Two D3Q19 lattices were included in the LBM simulations to model blood flow and tissue oxygenation, one for the velocity lattice and the other for concentration lattice. The first step in LBM simulations is to perform pre-processing that involves discretizing space and time. Space was discretized by calculating the length conversion factor (δ_x) using a characteristic

length (L_{char}), which is also known as the reference length. For LBM simulations, L_{char} was chosen as 200 μm because most of the simulations in this work dealt with phase thicknesses (hydrogel/tissue/blood) in the range of (100 μm-1000 μm). The number of nodes that are used to represent L_{char} is known as resolution (R), in the context of LBM. Resolution of the lattice is an important parameter in LBM simulations, because it determines the number of quadrature points, i.e. the number of nodes pre-allocated to allow particle collision and streaming. The higher the R (quadrature points), the more accurate but slower the simulation will be. Therefore the correct resolution should be identified for an optimal trade-off between accuracy of results and computation speed [115]. After choosing R, the length conversion factor is calculated by Equation [27].

$$\delta_x = \frac{L_{char}}{R - 1} \quad [27]$$

Discretizing 'time' involves computing the time conversion factor (δ_t). δ_t is related to δ_x by Equation [28], and it is function of velocity in lattice system (u_{lb}) as well as velocity in physical system (u_p).

$$\delta_t = \delta_x * \left(\frac{u_{lb}}{u_p}\right) \quad [28]$$

For the velocity lattice to replicate a laminar flow such as those present in the blood capillaries, τ should be equal to unity while implementing the BGKW model (section 2.6 and section 2.7). The computed δ_x and δ_t are the conversion factors between variables in the physical and lattice system.

Physical system (p) $\xrightarrow{variable \times\ conversion\ factors}$ Lattice system (d)

Lattice system (d) $\xrightarrow{variable \times \left[\frac{1}{conversion\ factors}\right]}$ Physical system (p)

The dimensionless numbers such as Reynolds number[34] and Péclet number[35] should be consistent between physical and lattice systems, which is ensured with Equation [28]. Thus, the flow consistency is maintained between the lattice scale and physical scale.

Equation [28] has two unknown variables δ_t and u_{lb}. In Dolamore's work [116], u_{lb} and δ_t were guessed in a manner to yield an appropriate lattice kinematic viscosity (ϑ_{lb}), such that the τ evaluates to '1'. In this thesis, the trial and error calculation has been avoided by

[34] The ratio of inertial to viscous forces.
[35] The ratio of advective and diffusive mass transfer.

rearranging the conversion equations. Firstly, ϑ_{lb} was computed with Equation [29] by setting τ = 1 (where c_s is equivalent to lattice speed of sound in a D3Q19 LBM model which is obtained from Boltzmann distribution as $\frac{1}{\sqrt{3}}$) [117].

$$\vartheta_{lb} = \left(\frac{1}{\tau} - 0.5\right) * c_s^2 \quad [29]$$

The calculated ϑ_{lb} was later utilized to calculate δt from the kinematic viscosity of the fluid/blood (ϑ) with Equation [30]. This rearrangement was a time saving step, because it minimized the simulation set up time as well as avoiding interpretation errors. δt was later used to calculate u_{lb} with Equation [28] and thus the first step in LBM pre-processing was completed.

$$\delta t = \left(\frac{\vartheta_{lb}}{\vartheta} * \delta x^2\right) \quad [30]$$

Defining tissue and hydrogel morphology (Section 3.2), followed by defining boundary conditions for velocity and concentration lattices, completes the simulation setup. A configuration file (*.xml* file[36]) contained all the simulation parameters, which were read into the main C++ code.

3.4. Modelling advection-diffusion of oxygen

The oxygen advection-diffusion was simulated with a D3Q19 concentration lattice whose domain size was equal to that of the velocity lattice. Oxygen was treated as a scalar dissolved solute and its concentration was tracked at each time step. The concentration lattice emulated the advection diffusion equation of oxygen transport, and it was based on a modified SRT method developed by Perko and Patel [118, 119]. In the Perko-Patel model, the diffusion term is modified ($\widetilde{D_m}$) and it is a combination of deviated diffusion term ($\widetilde{D}$) and reference diffusion parameter (D_{ref}) (Equation [31]). The deviated diffusion term was included to minimize the numerical instabilities that arise due to the existence of two lattices in SRT models.

$$\widetilde{D_m} = D_{ref} + \widetilde{D} \quad [31]$$

The advection-diffusion equation is given by Equation [32], where Q_s is the sink term representing the oxygen consumption rate and u_a is the advection velocity. The modified

[36] Written in Extensible Mark-up language (XML).

diffusion parameter of Equation [31] was substituted in the general advection diffusion equation (Equation [32]), to yield Equation [33].

$$\frac{\partial C}{\partial t} = \nabla.\left(\widetilde{D_m}\nabla C\right) - \nabla.(u_a C) + Q_s \quad [32]$$

$$\frac{\partial C}{\partial t} = \nabla.\left((D_{ref} + \widetilde{D})\nabla C\right) - \nabla.(u_a C) + Q_s \quad [33]$$

The flux of the deviation term was converted to Equation [34] by including a diffusion velocity (u_d).

$$\widetilde{D}\nabla C = u_d C \quad [34]$$

u_d was obtained by first-order Chapman-Enskog expansion of the deviation term [120]. After substitution, the advection-diffusion equation was converted to Equation [35], which was rearranged to give Equation [37].

$$\frac{\partial C}{\partial t} = \nabla.\left((D_{ref}\nabla C + u_d C)\right) - \nabla.(u_a C) + Q_s \quad [35]$$

$$\frac{\partial C}{\partial t} = \nabla.\left(D_{ref}\nabla C\right) + \nabla.(u_d C) - \nabla.(u_a C)) + Q_s \quad [36]$$

$$\frac{\partial C}{\partial t} = \nabla.\left(D_{ref}\nabla C\right) + \nabla.C(u_d - u_a)) + Q_s \quad [37]$$

D_{ref} was chosen as the kinematic viscosity of blood ($3.036\times 10^{-6}\ m^2\ s^{-1}$) [80], and it ensures that relaxation time is '1' in both the velocity and the concentration lattice. This imposition makes the D_{ref} approximately 1000 times more than the molecular diffusivity of oxygen in the tissue ($2.1\times 10^{-9}\ m^2\ s^{-1}$) which is within the stability boundaries of Perko-Patel LBM model [121]. Thus momentum transport and diffusion transport are modelled simultaneously in this work.

3.5. Boundary conditions

Figure 3.5-1 illustrates the simulation domain and the boundary conditions for the velocity and concentration lattices. In both lattices, a Dirichlet boundary condition was imposed at the entrance point of the blood flow; and a Neumann boundary condition was

imposed at the exit of the blood flow. A Dirichlet boundary condition in the context of the velocity lattice implies a constant creeping velocity profile applied at the scaffold entrance [122]. The Neumann velocity boundary condition was imposed at the scaffold exit such that the axial velocity gradient was zero. In the void space for the velocity lattice, bounce-back conditions were enabled to confine the blood flow to the channel space and therefore restricting bulk blood flow permeation into the hydrogel or tissue.

For the advection-diffusion/concentration lattice, a Dirichlet boundary condition implied a fixed concentration value was applied at the entrance of the scaffold. As the velocity and concentration lattices are coupled, the imposed solute concentration was transported through the scaffold at the assigned velocity. At the scaffold exit, the Neumann boundary condition was imposed such that the axial concentration gradient was zero. Periodic boundary conditions were placed on the lateral boundaries of velocity and concentration lattices. This was based on the premise that there is no physical containment in lateral directions for the 3D printed soft tissue. These boundary conditions make the simulations in a small block of tissue representative of a larger tissue implant. For the internal boundary conditions on the advection-diffusion lattice, bounce-back conditions were enabled, if oxygen diffusion in tissue was to be restricted. The bounce back conditions were turned off, if oxygen diffusion in tissue was allowed.

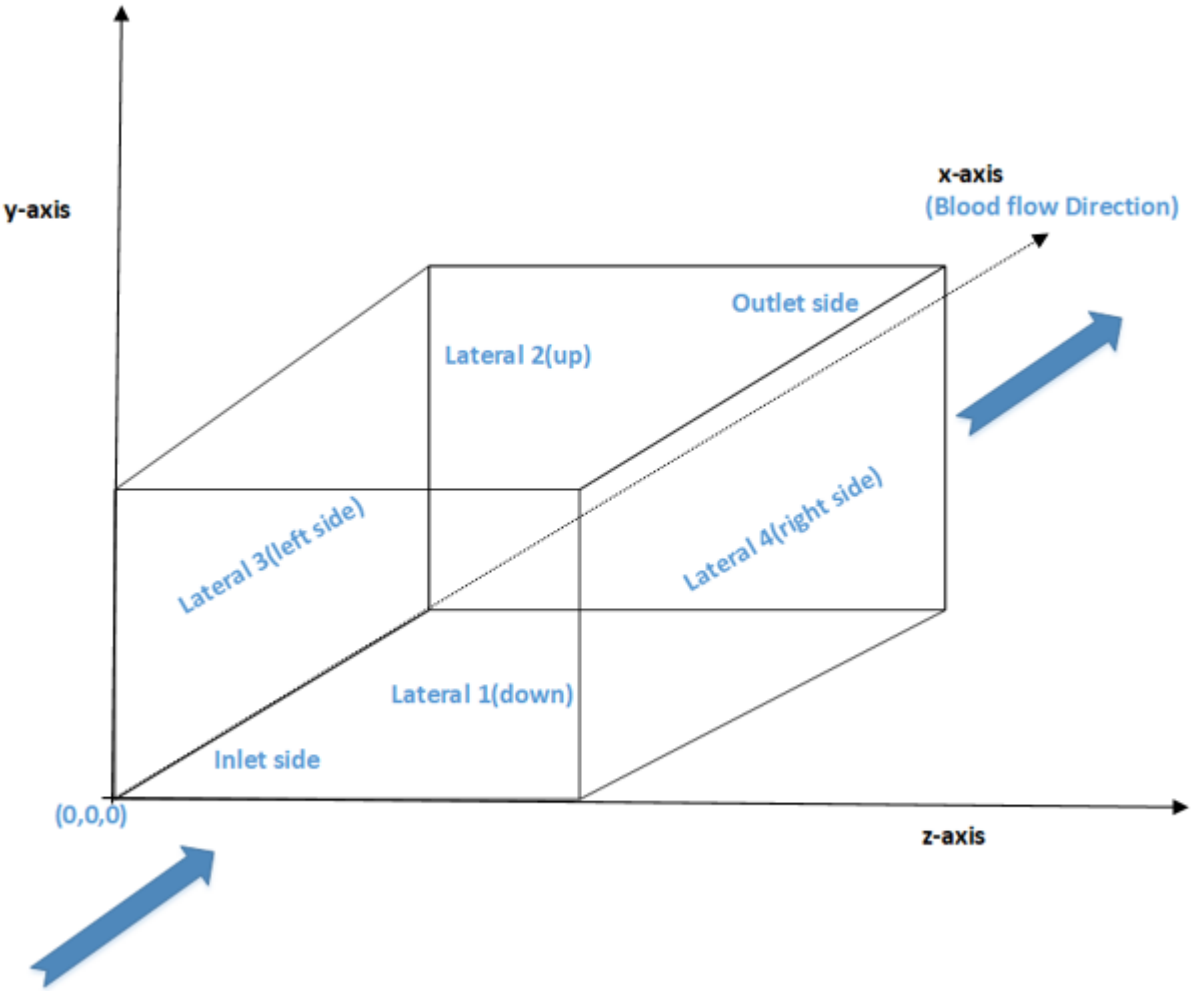

Figure 3.5-1: The cuboidal domain in which different TPMS structures have been modelled, showing the six faces where the boundary conditions were imposed.

3.6. Oxygen consumption and multiscale modelling

Oxygen consumption in the tissues has been modelled as zero-order kinetics i.e. a specified amount eliminated constantly from the tissues until steady state is achieved [123, 124]. Steady state was checked with the L1 norm, which in the LBM context refers to the difference between average concentration of the concentration lattice between successive iterations. The simulation was considered to reach steady state, if the $L1$ norm fell below a threshold value of 10^{-5} mM.

In the developed LBM model, both the lattices (velocity and concentration) are solved under the same global iteration scheme, meaning there are no separate time scales for the velocity and concentration lattice ($'\delta t'$ is same for both time lattices). However, given the fact the oxygen diffusion occurs over a longer time scale than its advection rate, a scaling factor was

introduced in the concentration lattice to make the oxygen diffusion phenomena faster. The speed increase was realized by 'skipping' time-steps in the concentration lattice equivalent to a scale factor. To compensate for the missing time-steps, the diffusion rate and consumption rate were multiplied by the scale factor. This adjustment meant that the deviated diffusion term was altered, although the reference diffusion term was kept constant to maintain the relaxation parameter equal to '1'. Previously Dolamore [125] found a scale factor of 10 (~around 10 iterations) to be sufficient to skip and thus make the computation faster, without compromising solution accuracy. At higher scale factors, the virtual time step becomes too large to accurately capture the system behaviour, and therefore solution accuracy decreases.

Table 3.6-1 shows different values of tissue oxygen consumption rates found in literature. It can be seen that the numbers are quite varied, differing by orders of magnitude. One common reason for this difference was due to measurement of consumption rates in different cell lines at varied densities. Some measurements were made when cells were under metabolic stress, which pushed the consumption rate upwards. With the LBM model, a range of consumption values were analysed, and the sensitivity of concentration profiles to different oxygen consumption rates was tested, to assess the difference in tissue oxygenation.

Table 3.6-1: Oxygen consumption rates of tissues found in literature.

Literature Values	**Conversion to $mol\,m^{-3}s^{-1}$**	**Literature Reference**
$3.72\times 10^{-8}\ \ gmol\ cm^{-3}s^{-1}$	3.72×10^{-2}	[126]
$3.5\times 10^{-4}\ \ mol\ m^{-3}s^{-1}$	3.72×10^{-4}	[127]
$2.78\times 10^{-8}\ \ mol\ L^{-1}s^{-1}$	2.78×10^{-5}	[101]
$3.4\pm 1.6\ \times 10^{-8}\ \ mol\ m^{-3}s^{-1}$	$3.4\pm 1.6\ \times 10^{-4}$	[128]
$0.0196\ mol\ m^{-3}s^{-1}$	1.96×10^{-2}	[129]
$9.8\times 10^{-9}\ \ mol\ L^{-1}s^{-1} - 8.8\times 10^{-7}\ \ mol\ L^{-1}s^{-1}$	$9.8\times 10^{-6} - 8.8\times 10^{-4}$	[4]
$5.44\times 10^{-2}\ \ nmol\ cm^{-3}s^{-1}$	5.44×10^{-5}	[36]

Blood flow velocity is a crucial aspect to consider for tissue vascularization. Table 3.6-2 indicates the range of blood velocities that exist in physiology. However, vascularization occurs only when capillaries transport nutrients to every corner of the body. Therefore,

capillary velocity was taken as reference velocity for simulating advection of blood through TPMS structures (≤ 1 mm s^{-1}).

Table 3.6-2: Blood velocities at different locations in human body.

Location	Blood velocity	Conversion (mm s^{-1})	Reference
Aorta	40 cm s^{-1}	400	[130]
Hepatic artery	10-80 cm s^{-1}	100-800	[131]
Portal Vein	20-40 cm s^{-1}	200-400	[131]
Veins	15 cm s^{-1}	150	[130]
Capillaries	0.3 mm s^{-1}	0.3	[130]

3.7. LBM model verification with Krogh's 2D capillary model

The developed LBM model was tested on a thin slice of cylindrical capillary that was surrounded by tissue. The LBM capillary model was made geometrically similar to Krogh's conceptualization of a capillary with radius R_c, surrounded by tissue (Figure 3.7-1) [132].

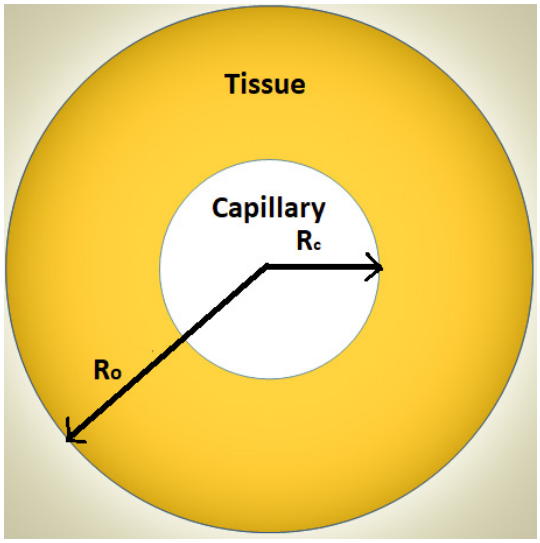

Figure 3.7-1: Krogh's conceptualization of a capillary (radius = R_C) that is surrounded by a tissue (> R_C), which is oxygenated between R_C and R_O.

The Krogh model is primarily a mass balance on nutrients entering in and exiting out of a capillary. It solves for steady state one dimensional oxygen diffusion from capillary into the tissue, such that the rate of oxygen consumption in the tissue is equal to oxygen supply from the capillary. Thus, for a given supply or diffusion rate of oxygen, the tissue would only be oxygenated within a certain radius (R_o). Therefore, R_o in Krogh's model was defined as the distance from the capillary centre to where the oxygen concentration is zero. This

simplification in Krogh's model comes from the assumption that a soft tissue/skeletal muscle consists of cylindrical capillaries that are parallel to muscle fibres. He imagines the capillaries to be connected to arterioles on one end and draining into venules at the other end. Krogh also assumes uniform capillary spacing in his model, although realistically the spacing between capillaries is non-uniform. The Krogh model also considers zero order kinetics of oxygen consumption in the tissue, similar to the LBM model implemented in this thesis.

Equation [38] represents the fundamental mass-balance equation in polar cylindrical coordinates.

$$\frac{D_{O_2}}{r}\frac{d}{dr}\left(r\frac{dC_{O_2}}{dr}\right) = Q_s \qquad [38]$$

; where D_{O_2} is the diffusion coefficient of oxygen in tissue; C_{O_2} is the oxygen concentration at a distance, r, from the centre of the capillary and Q_s is the oxygen consumption rate in the tissue. Solving Equation [38] by equating oxygen concentration at the capillary-tissue surface to that of oxygen concentration in blood, and imposing a no flux boundary condition on oxygen transport beyond R_o, yields Equation [39].

$$C_{O_2} = C_{\mathrm{Rc}}\left[1 + \emptyset\left[\left(\frac{\mathrm{r}}{R_o}\right)^2 - \left(\frac{Rc}{R_o}\right)^2 - 2\ln\left(\frac{r}{Rc}\right)\right]\right] \qquad [39]$$

; where $\mathrm{C_{Rc}}$ is the oxygen concentration at the blood-tissue interface/wall concentration, Rc is the radius of the blood vessel and $\emptyset$ is a dimensionless number quantifying the metabolism of cells (which is a function of Q_s).

Equation [39] gives the concentration at any radial distance 'r' from the capillary centre and it is a non-linear equation with an unknown value R_o. This equation was iteratively solved in MATLAB for different values of r, to identify an r value where C_{O_2}would be 0. This value of r was noted and defined as R_o, following from the definition of Krogh's model. After determining R_o, Equation [39] was solved again to get the concentration C_{O_2} at every 'r' between $\mathrm{R_c}$ and R_o. Thus, the analytical oxygen concentration profiles in the radial direction were generated. The LBM numerical solution was validated with the analytical solution to analyse how the oxygen concentration profiles compare with each other, for the same set of assumptions and parameters (R_c, D_{O_2} and Q_s).

Figure 3.7-2.a shows a 2D view of capillary and tissue with a black line running across. Subsets of the black line at the blood-tissue interface were analysed for oxygen concentration

along the line. The axisymmetry property of capillary was exploited to substitute it with a quadrant simulation, to reduce computation time and to focus on the region of interest (Figure 3.7-2.b).

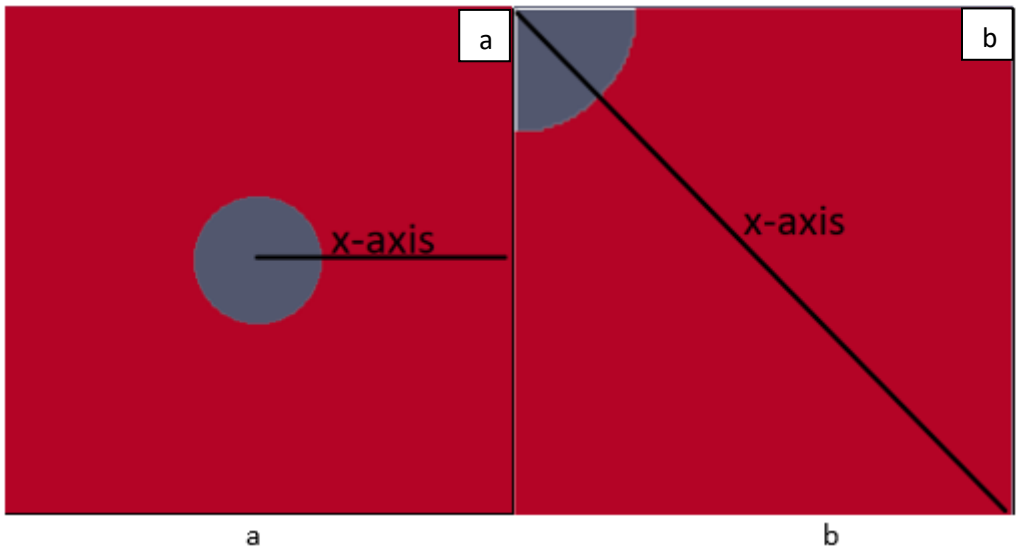

Figure 3.7-2: a) Cross-sectional view of capillary (dark-grey) surrounded by tissue (red). b) A quadrant of capillary simulated with LBM to examine diffusion at a higher resolution. The black line represents the x-axis location, over which oxygen concentration was evaluated (Figure 3.7-3).

Table 3.7-1: Parameters used for LBM model validation.

Parameters	**Figure 3.7-3 a)**	**Figure 3.7-3 b)**	**Figure 3.7-3 c)**	**Figure 3.7-3 d)**
Oxygen concentration in capillary (mM)	1	1	1	1
Diffusion coefficient of oxygen in tissue ($cm^2\ s^{-1}$)	2.1×10^{-5}	2.1×10^{-5}	1.6×10^{-5}	2.1×10^{-5}
Capillary radii (μm)	250	30	250	250
Oxygen consumption rate ($mM\ s^{-1}$)	0.01	0.01	0.01	0.03

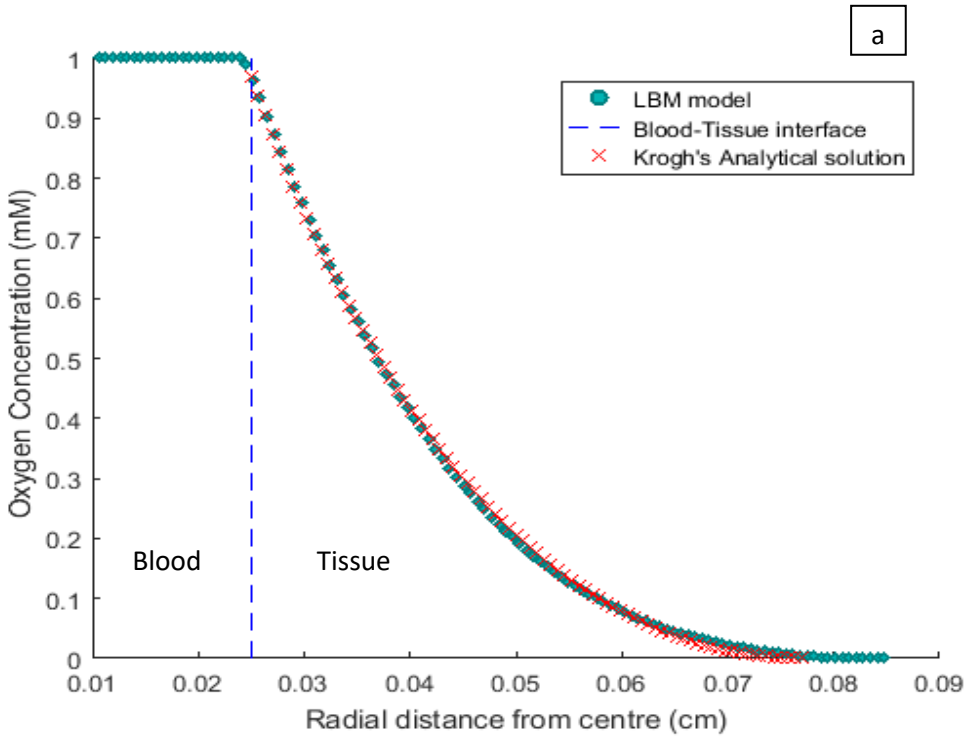
a
LBM model
Blood-Tissue interface
Krogh's Analytical solution
Oxygen Concentration (mM)
Radial distance from centre (cm)
Blood
Tissue
0
0.1
0.2
0.3
0.4
0.5
0.6
0.7
0.8
0.9
1
0.01
0.02
0.03
0.04
0.05
0.06
0.07
0.08
0.09

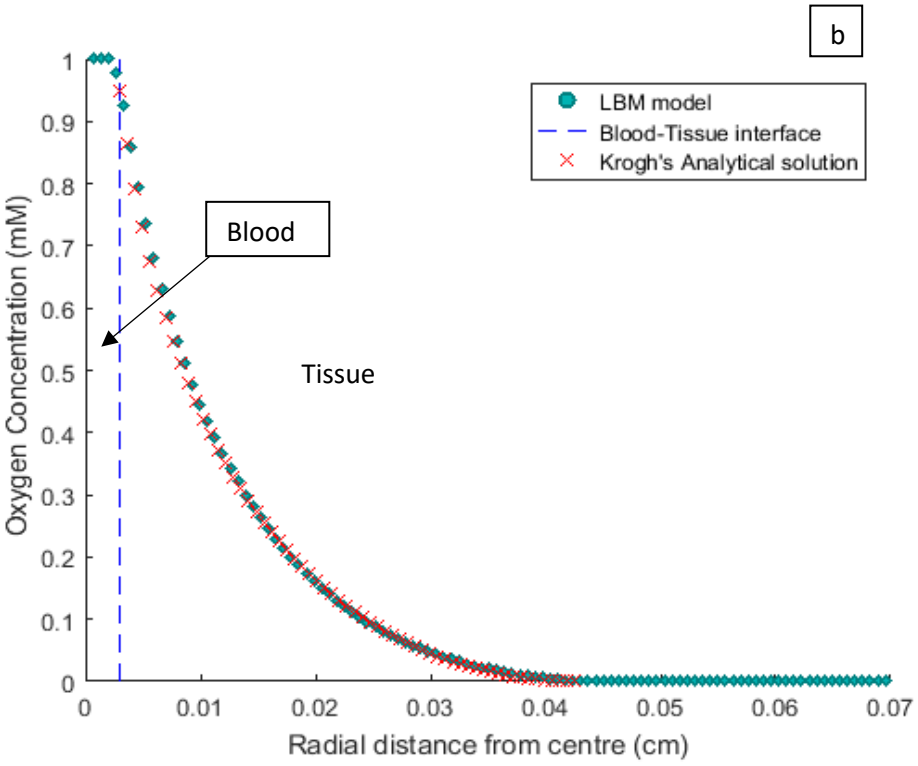
b
LBM model
Blood-Tissue interface
Krogh's Analytical solution
Oxygen Concentration (mM)
Radial distance from centre (cm)
Blood
Tissue
0
0.1
0.2
0.3
0.4
0.5
0.6
0.7
0.8
0.9
1
0
0.01
0.02
0.03
0.04
0.05
0.06
0.07

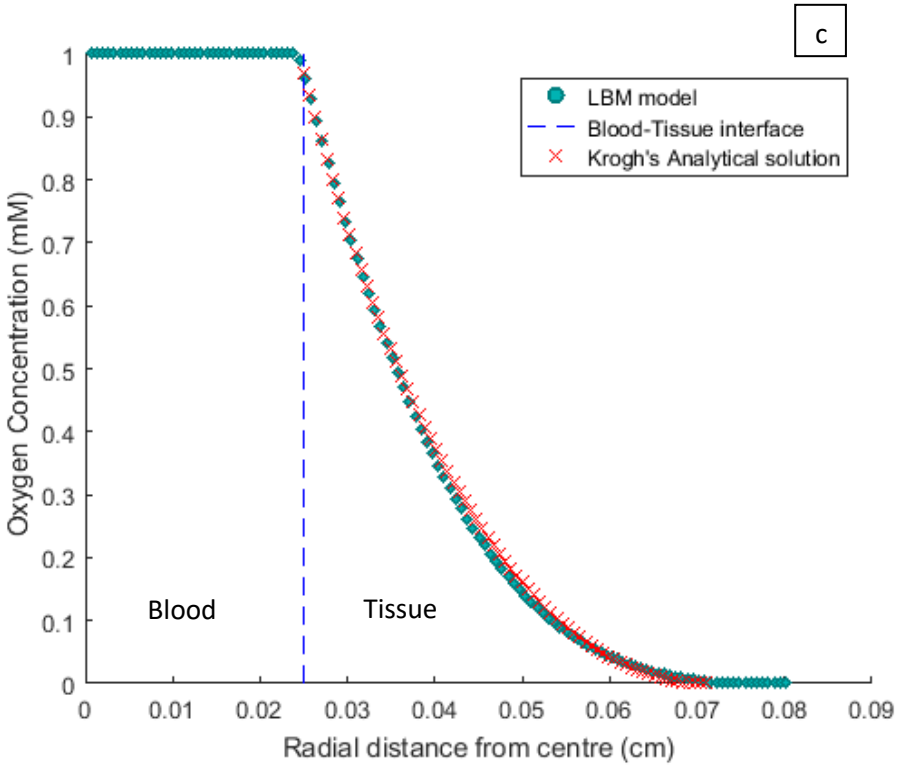
c
LBM model
Blood-Tissue interface
Krogh's Analytical solution
Oxygen Concentration (mM)
Radial distance from centre (cm)
Blood
Tissue
0
0.1
0.2
0.3
0.4
0.5
0.6
0.7
0.8
0.9
1
0
0.01
0.02
0.03
0.04
0.05
0.06
0.07
0.08
0.09

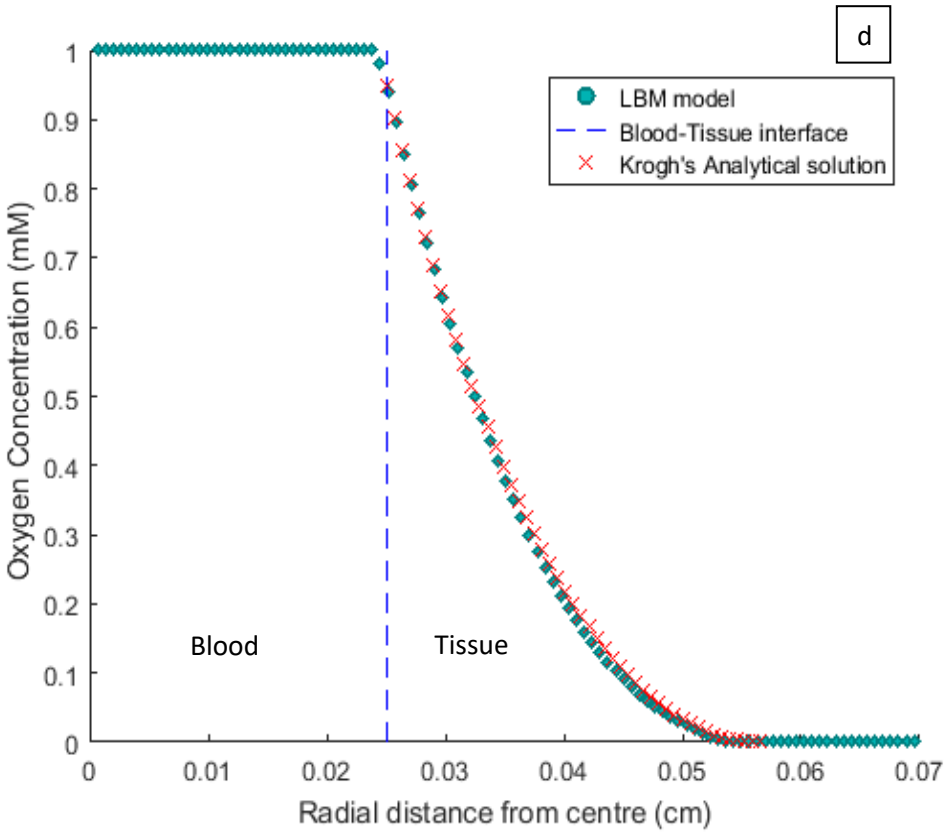

Figure 3.7-3: LBM model validation with Krogh's analytical solution showing similar concentration profiles in the tissue. The key parameters pertaining to the specific figures are shown in Table 3.7-1. The x-axis corresponds to the black line shown in Figure 3.7-2 and y-axis represents the corresponding oxygen concentration along the line. The dashed blue line marks the capillary-tissue interface, with tissue being at higher x-values and oxygenated blood at lower x-values.

Figure 3.7-3 shows a close agreement between the oxygen concentration profiles in LBM and the Krogh model at steady state. The diffusion distances of oxygen in the tissue was found to be comparable between the two models for the same set of parameters and assumptions. The oxygen concentration at the blood-tissue interface for the numerical model was chosen to match the analytical model because the later does not solve the diffusion on the blood side. The tail of the numerical model was observed longer than the analytical model because the radial size of the domain simulated in the numerical model was larger than R_o, hence zero concentration scatter points were observed beyond R_o. In summary, higher oxygen consumption rate in tissue, lower tissue permeability to dissolved oxygen and lower oxygen concentration in the blood side decreased the oxygen diffusion distance from the blood into the tissue.

3.8. LBM model verification in the presence of hydrogel scaffolds in a capillary model

The LBM was subsequently employed to solve for O_2 concentration profiles, with hydrogel scaffold sandwiched between capillary and tissue (Figure 3.8-1). This study was done to understand the impact of hydrogel thickness and diffusivity on the oxygen concentration profiles in the tissue, and to verify the resistivity of hydrogel layers. Table 3.8-1 shows the parameter values of the graphs in Figure 3.8-2.

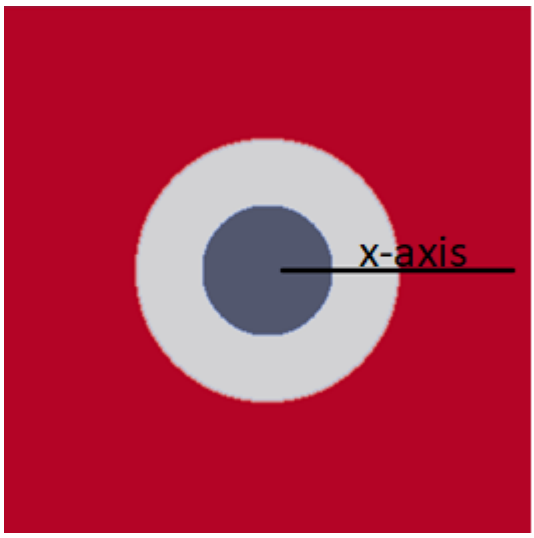

Figure 3.8-1: Cross-sectional view of hydrogel scaffold (white) separating the capillary lumen (dark-grey) and the tissue (red), rendered in Paraview. The image shows the x-axis location over which the oxygen concentrations were evaluated in Figure 3.8-2.

In Figure 3.8-2 a) - d), two types of oxygen concentration profiles are plotted; one with hydrogel (Figure 3.8-1) shown by red squares and one without hydrogel shown by blue crosses (Figure 3.7-2). These two cases were plotted on the same graph to emphasize how the resistivity of hydrogel layers affects oxygen diffusion.

Table 3.8-1: Parameters used in model verification cases in the presence of hydrogel.

Parameters	**Figure 3.8-2 a)**	**Figure 3.8-2 b)**	**Figure 3.8-2 c)**	**Figure 3.8-2 d)**
Oxygen concentration in capillary (mM)	1	0.0405	0.0405	0.0405
Diffusion coefficient of oxygen in tissue ($cm^2\ s^{-1}$)	2.1×10^{-5}	2.1×10^{-5}	2.1×10^{-5}	2.1×10^{-5}
Hydrogel thickness (μm)	250	125	125	250
Diffusion coefficient of oxygen in hydrogel ($cm^2\ s^{-1}$)	1.9×10^{-5}	1.9×10^{-5}	1.9×10^{-4}	1.9×10^{-4}
Capillary radii (μm)	250	250	250	250
Oxygen consumption rate ($mM\ s^{-1}$)	0.01	0.01	0.01	0.01

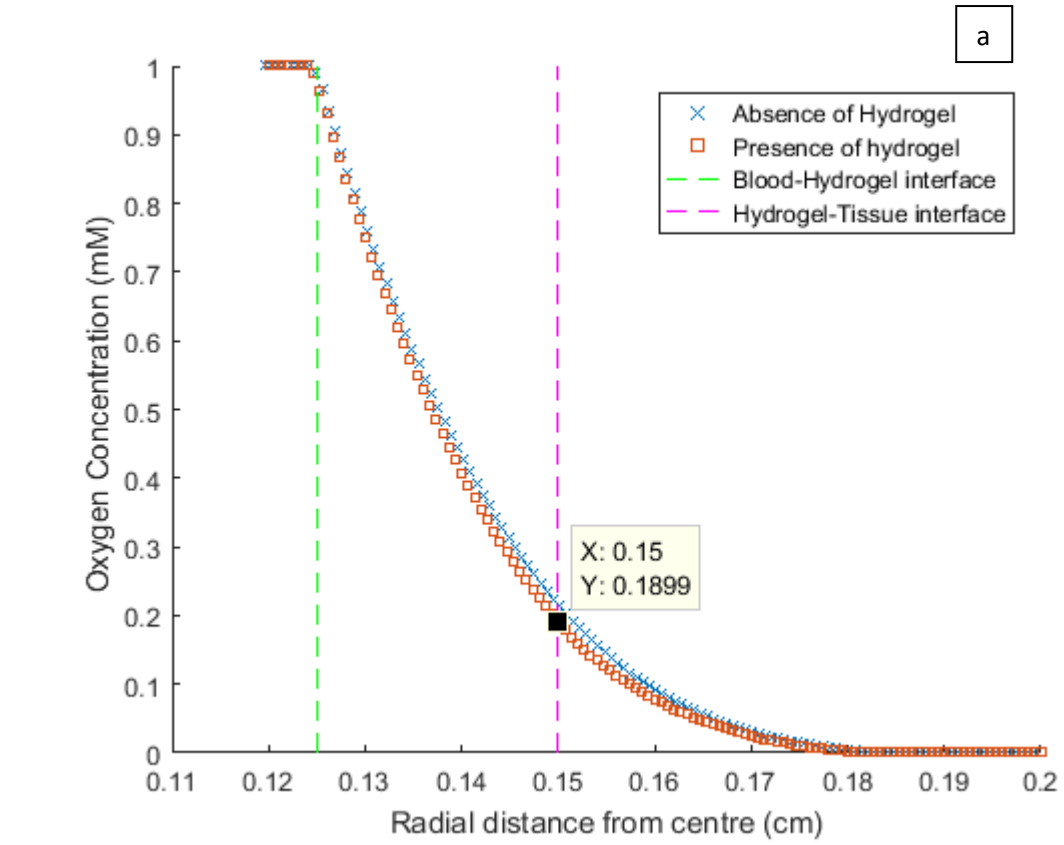
a
Absence of Hydrogel
Presence of hydrogel
Blood-Hydrogel interface
Hydrogel-Tissue interface
X: 0.15
Y: 0.1899
Oxygen Concentration (mM)
Radial distance from centre (cm)
0
0.1
0.2
0.3
0.4
0.5
0.6
0.7
0.8
0.9
1
0.11
0.12
0.13
0.14
0.15
0.16
0.17
0.18
0.19
0.2

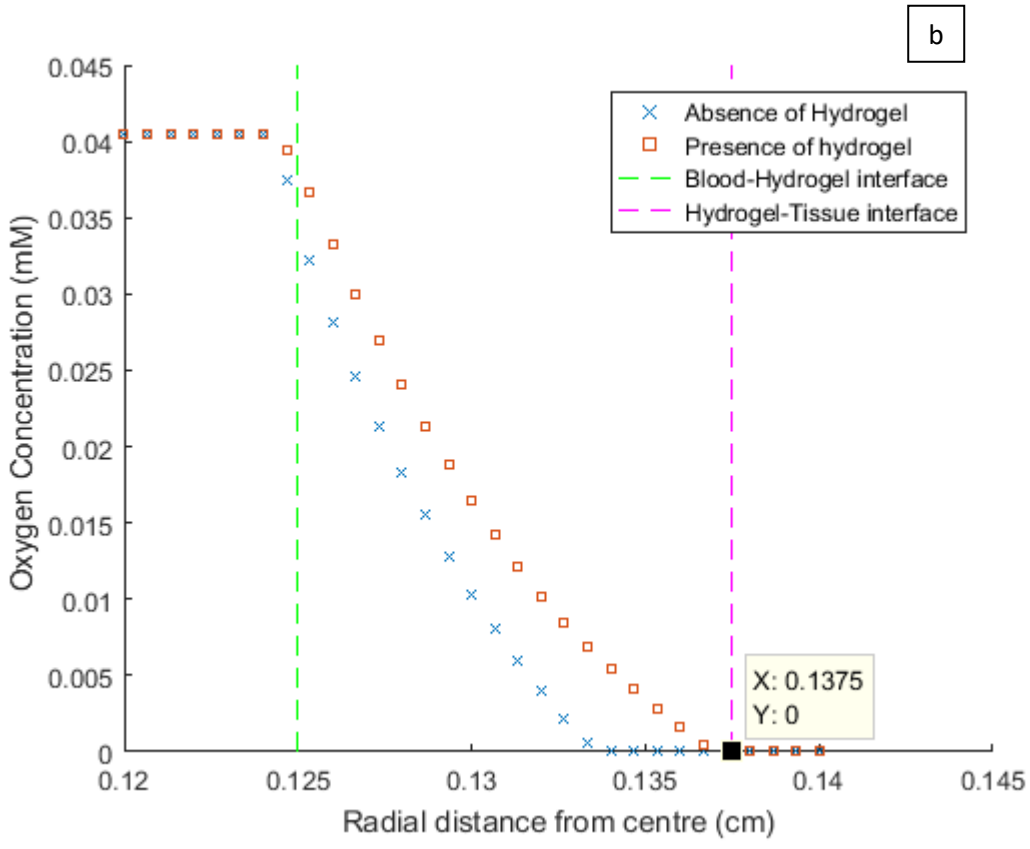
b
Absence of Hydrogel
Presence of hydrogel
Blood-Hydrogel interface
Hydrogel-Tissue interface
X: 0.1375
Y: 0
Oxygen Concentration (mM)
Radial distance from centre (cm)
0
0.005
0.01
0.015
0.02
0.025
0.03
0.035
0.04
0.045
0.12
0.125
0.13
0.135
0.14
0.145

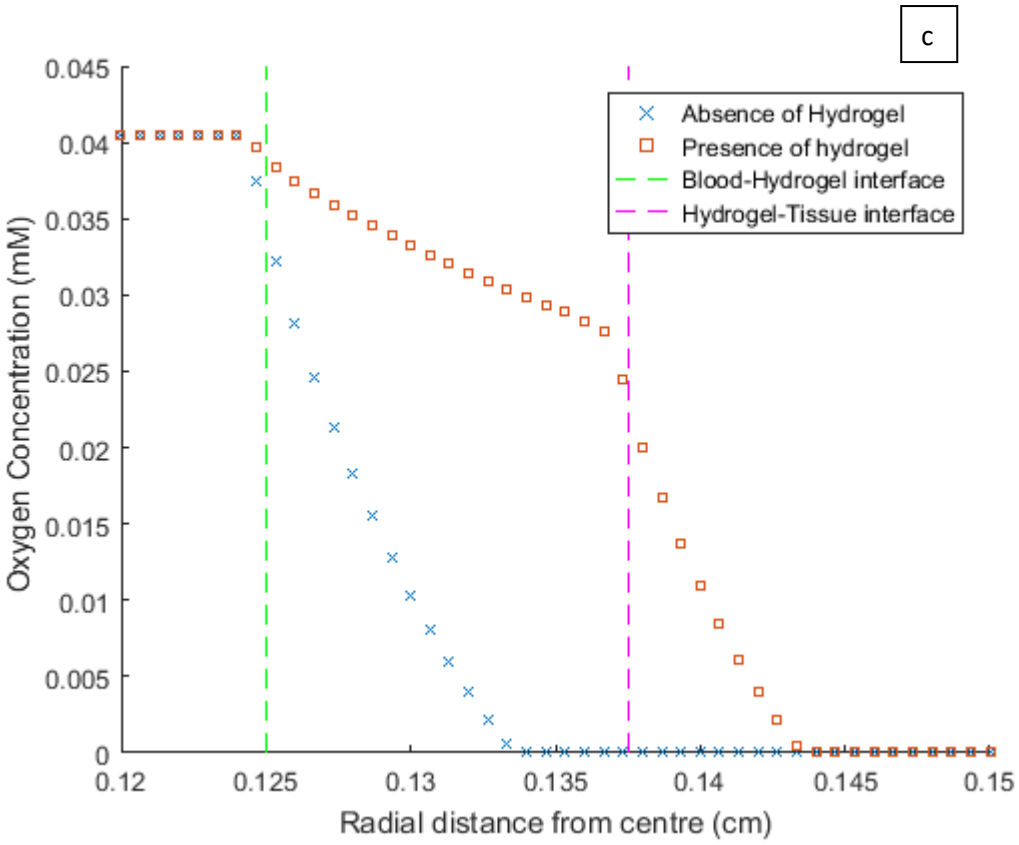
c
Absence of Hydrogel
Presence of hydrogel
Blood-Hydrogel interface
Hydrogel-Tissue interface
Oxygen Concentration (mM)
0.045
0.04
0.035
0.03
0.025
0.02
0.015
0.01
0.005
0
0.12
0.125
0.13
0.135
0.14
0.145
0.15
Radial distance from centre (cm)

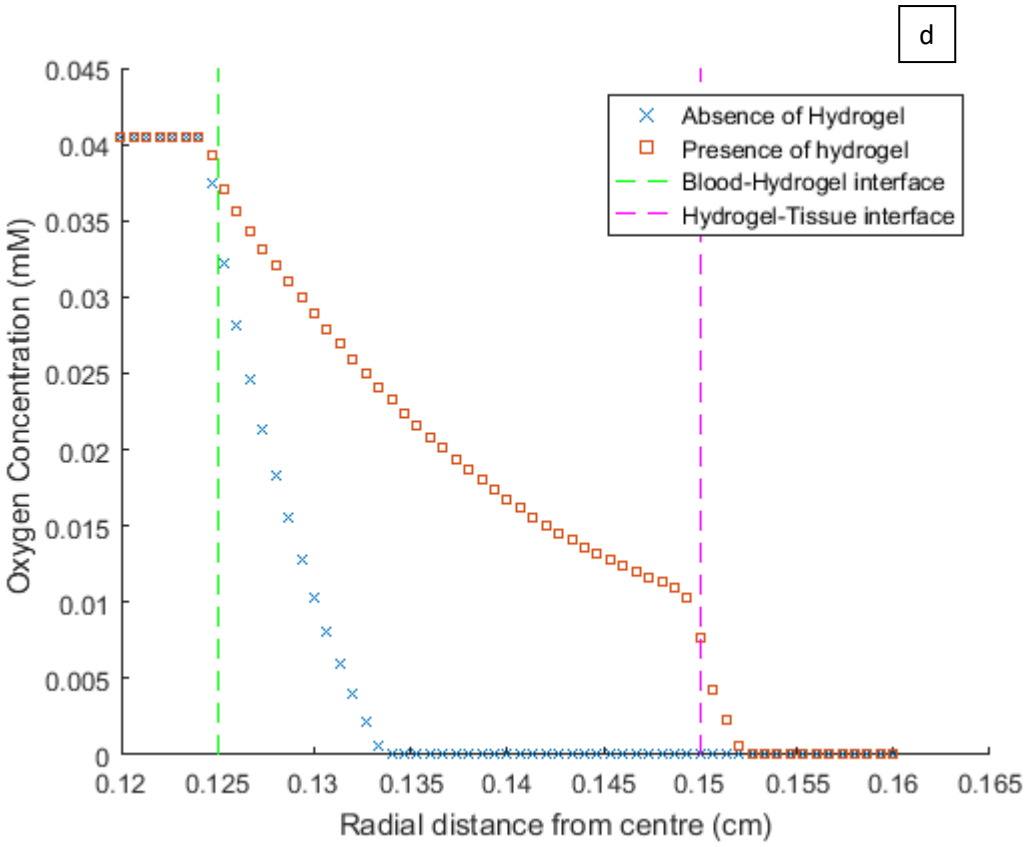

Figure 3.8-2: Oxygen diffusion profiles by LBM in the presence and absence of hydrogel. The key parameters pertaining to the specific figures are shown in Table 3.8-1. The x-axis corresponds to the black line (Figure 3.8-1) and the y-axis corresponds to the oxygen concentration along the line. The region between dashed green and magenta lines indicates the hydrogel thickness with red squares indicating the oxygen concentrations in that scenario (Figure 3.8-1). Blue crosses indicate the oxygen concentrations in the absence of hydrogel i.e. when the whole region right of dashed green line is just tissue (Figure 3.7-2).

It was found that the thickness of oxygenated tissue decreases in the presence of hydrogel scaffold and the numerical model shows the decay pattern of the oxygen concentration profiles in hydrogel and tissue. It was found that thicker hydrogels with less permeability decrease the oxygen penetration distances in the tissue as anticipated.

3.9. Case for TPMS structures for tissue vascularization

The Krogh's equation (Equation [39]) was iteratively solved by changing the oxygen concentration at the wall, to estimate the oxygen penetration distances in tissue (R_o) (Figure 3.9-1). Wall refers to the hydrogel-tissue interface or blood-tissue interface depending on the presence or absence of hydrogel. The other parameters used in the Figure 3.9-1 are: oxygen diffusion coefficient in tissue (2.1×10^{-9} m^2s^{-1}), capillary radius (300 μm) and inlet oxygen concentration (0.15 mM). Figure 3.9-1 emphasizes the sensitivity of oxygen diffusion distances to wall concentration at steady state. This correlation was not drawn in previous studies and it was found useful to observe the plateauing effect, which showed that the oxygen penetration distances in tissue are more sensitive when the wall oxygen concentration is relatively low.

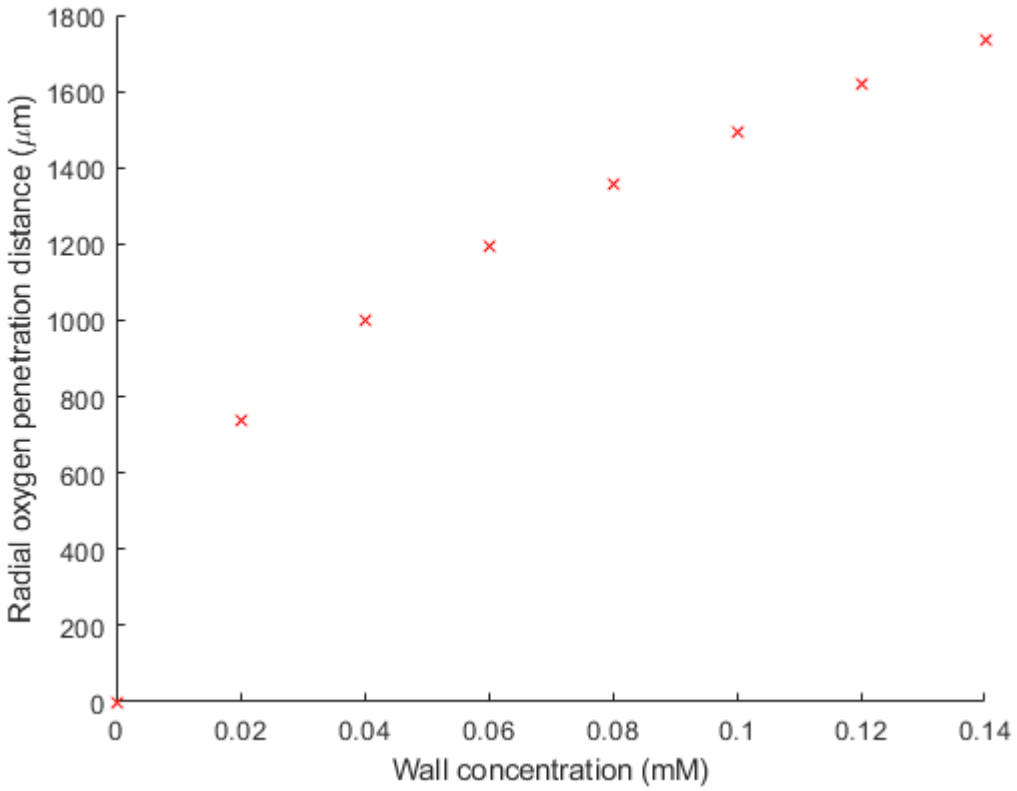

Figure 3.9-1: Oxygen concentration at the blood-tissue interface vs oxygen penetration distance in the tissue.

Figure 3.9-2 compares a 25% structurally porous capillary with a gyroid of equal porosity. It can be seen that TPMS structures provide multiple perfusion pathways, which allows for multilateral diffusion, thus enhancing mass transfer at any given location in the tissue. Correlating wall concentration and oxygen penetration distances analytically is a challenging mathematical task in TPMS structures, unlike a capillary case. Therefore, CFD

studies are performed to analyse the details of oxygen concentration profiles in TPMS structures and observe the 3D concentration maps at steady state.

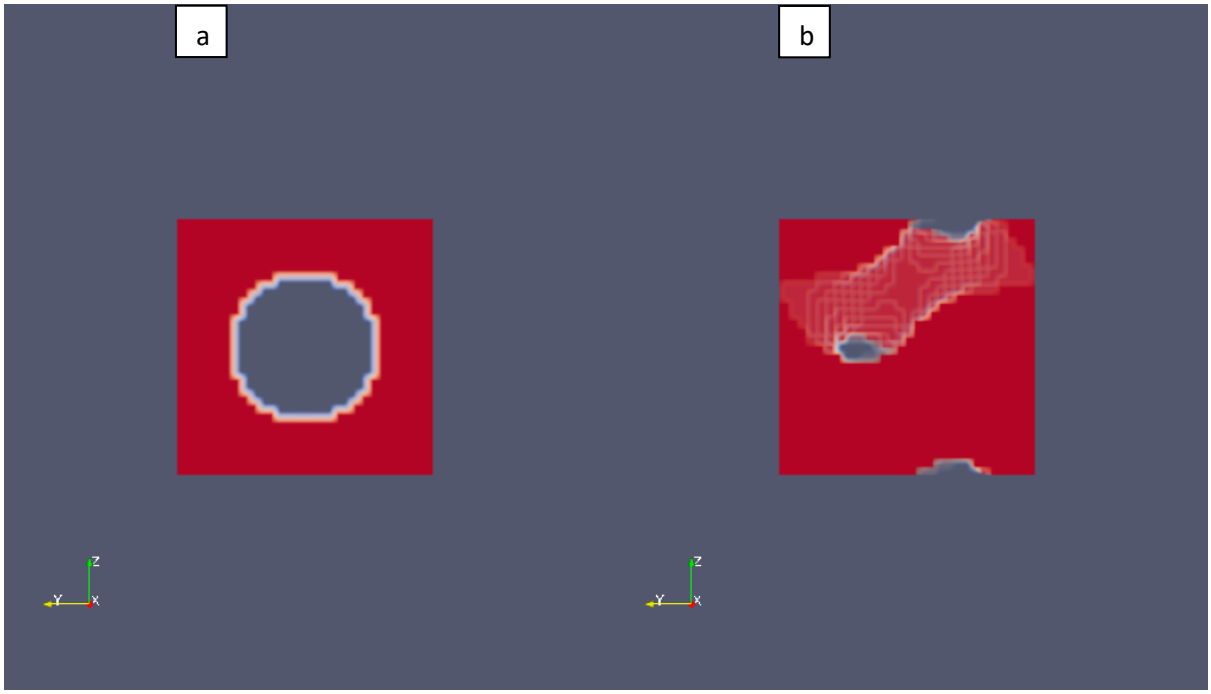

Figure 3.9-2: a) 25% structurally porous capillary (single flow pathway) and b) 25% structurally porous gyroid (two flow pathways)

3.10. Parallelization of LBM simulations in *Mahuika*

3D simulations in this thesis had an enormous demand for computation time, therefore they were subject to parallel computation on high performance computers. The LBM simulations were run on the NeSI *Mahuika* cluster, with 32 Broadwell cores, operating at 2.1 GHz, with 128 GB RAM. This project was allotted 6000 core hours per month on the *Mahuika* platform of the NeSI infrastructure [133], to perform the simulations. Eventually, this limit was increased to 97000 core hours annually to accommodate for the increased computation needs. The Linux work-flow chart to utilize this infrastructure in 2018-19 is appended in Appendix E [134, 135]. Prior to running the simulations, the optimum number of cores required to perform a certain simulation job was identified, to benchmark a standard for future work. Figure 3.10-1 compares the relative computation speed between simulations, when performed by employing 2, 4, 8, 16, 32 and 64 *Mahuika* cores in parallel. The computational speed was assessed by noting the simulation time required to reach steady state for all cases, and normalizing it by the simulation time of the case requiring the longest computation time (2 cores for this case). It was observed that computation time required to reach steady state decreased with an increase

in the deployed cores. However, there were diminishing returns in terms of computation speed beyond 16 cores. Therefore, 16 cores were employed for subsequent simulations in this work.

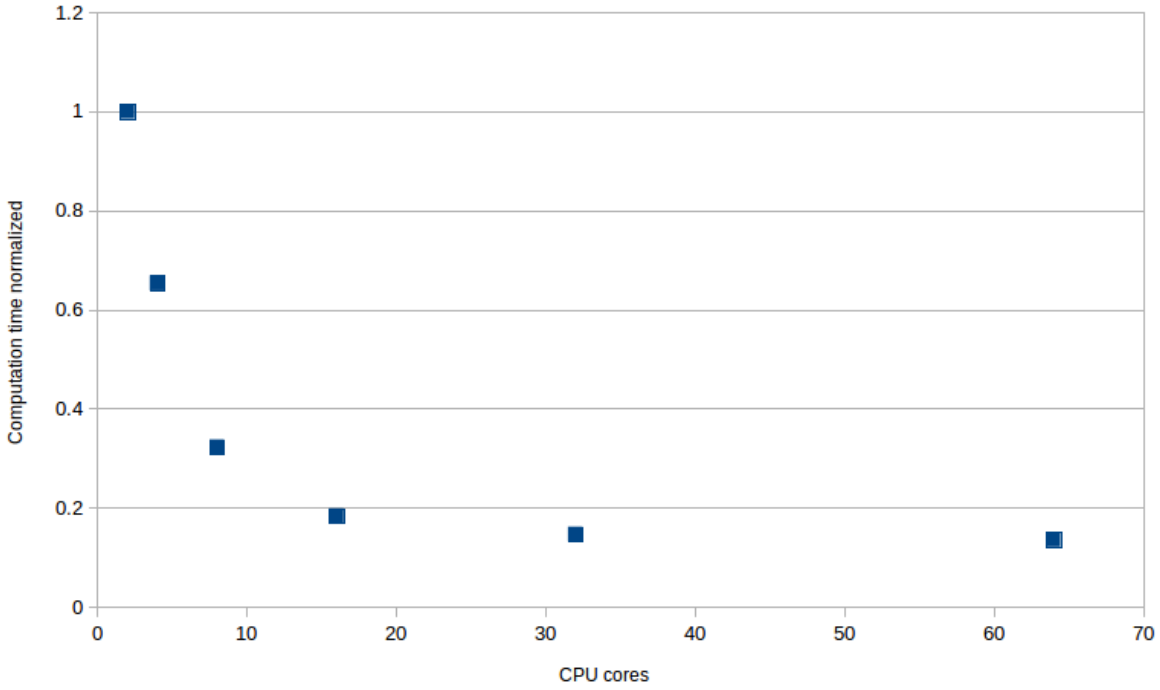

Figure 3.10-1: Normalized simulation time vs NeSI computing cores

3.11. Mesh independence studies

Resolution refers to the spatial discretization of the domain, and it could be either crude, refined or intermediate. High resolution/refined grids are desirable but they come at a computation cost. Computation is faster in low resolution/crude grids, but the inaccuracy in the CFD solution is higher. Therefore, mesh independence studies were performed to identify the optimum number of nodes to make the numerical result independent of mesh/grid/node spacing [136, 137]. Figure 3.11-1 shows an 80% porous Schwarz Diamond (SD80%) that was chosen as a case-study to examine O_2 diffusion profiles with changing spatial resolution. The TPMS structure was perfused with a velocity of 1 $mm\ s^{-1}$ at 0.15 mM oxygen concentration, and while diffusion was allowed in the tissue, oxygen consumption in tissue was set to zero.

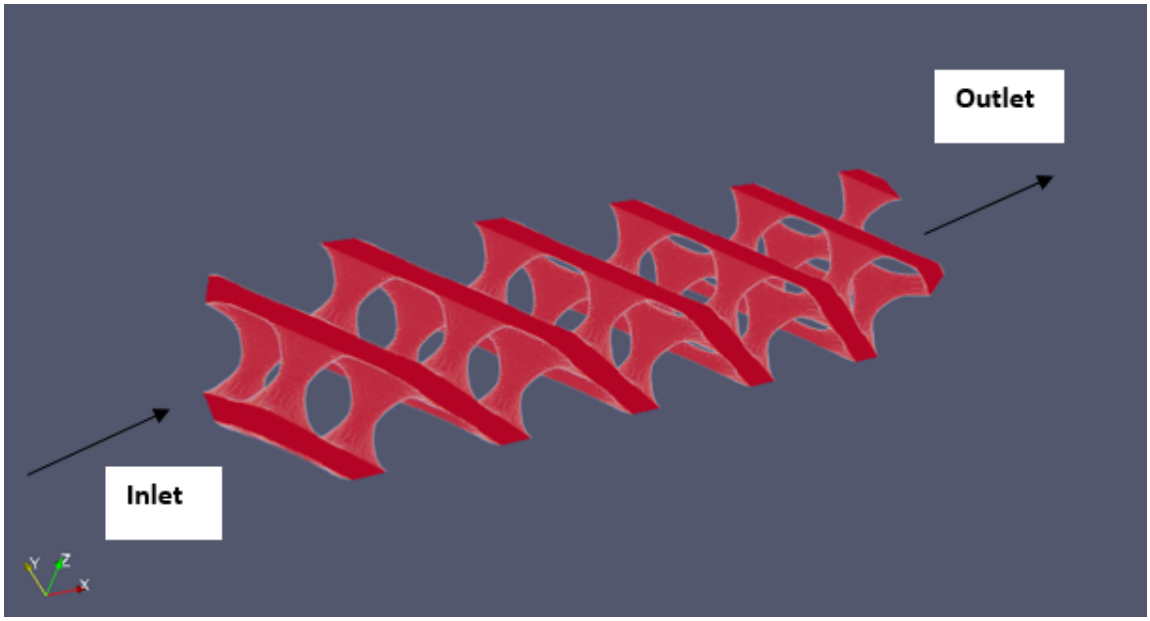

Figure 3.11-1: An 80% porous Schwarz Diamond TPMS structure (1000, 200, 200) μm in x, y, z directions.

The mesh independence studies were carried out by changing the number of nodes representing L_{char} (200 μm). Figure 3.11-2 indicates cases where L_{char} was represented by 11, 21, 31, 41, 51 and 61 nodes respectively. The data-points in the figure represent the average oxygen concentration in slices separated by 100 μm. The magnitude of the data-point is an average oxygen concentration in a slice that includes both tissue and blood sides. After getting the steady state O_2 concentration profiles, the solution accuracy and computation time was compared for simulations run at different resolutions.

A dip in the oxygen concentration profiles was noted along the blood flow axis (Figure 3.11-2) which was unanticipated given that the O_2 consumption was zero. It was also observed that increasing the spatial resolution did not counteract this effect. One of the reasons identified for this dip was the non-rigorous concentration tolerance criteria. It was observed that decreasing the tolerance criteria reduced the dip as shown in Figure 3.11-3. However, an increase in time cost was associated with decrease in tolerance criteria as shown in Figure 3.11-4. Therefore 10^{-5} mM[37] was considered as an optimum value to declare steady-state as a trade-off between speed and accuracy.

[37] Difference between average concentration of the concentration lattice between successive iterations.

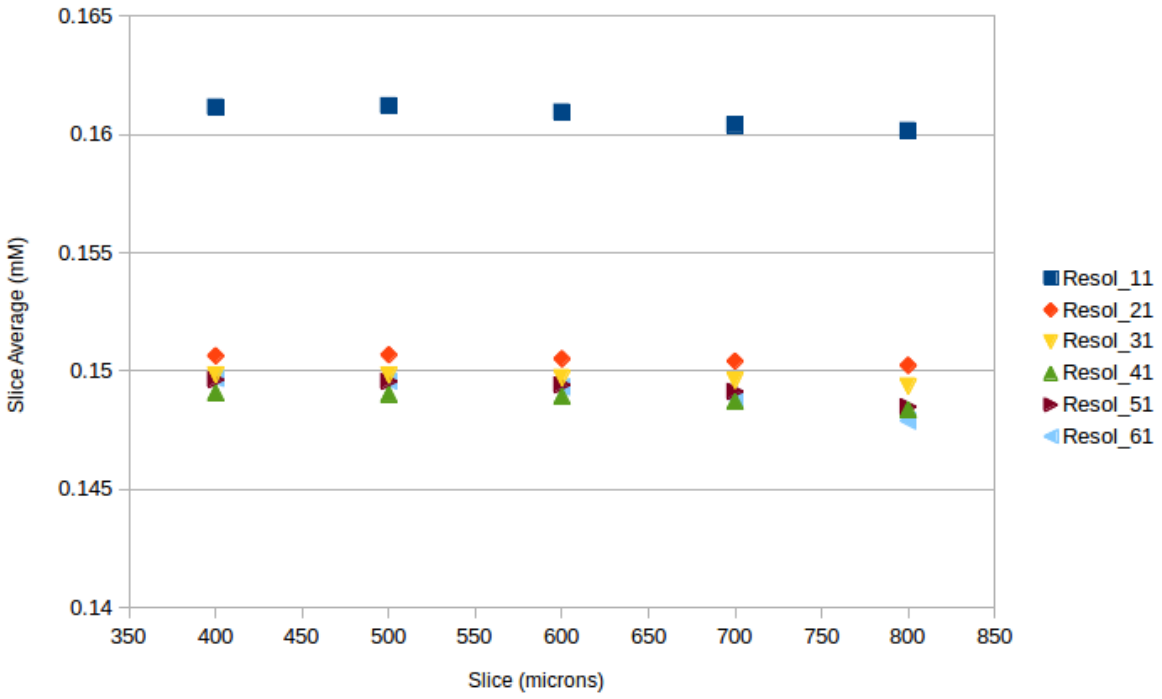

Figure 3.11-2: Average oxygen concentration in SD80% slices separated by 100 μm

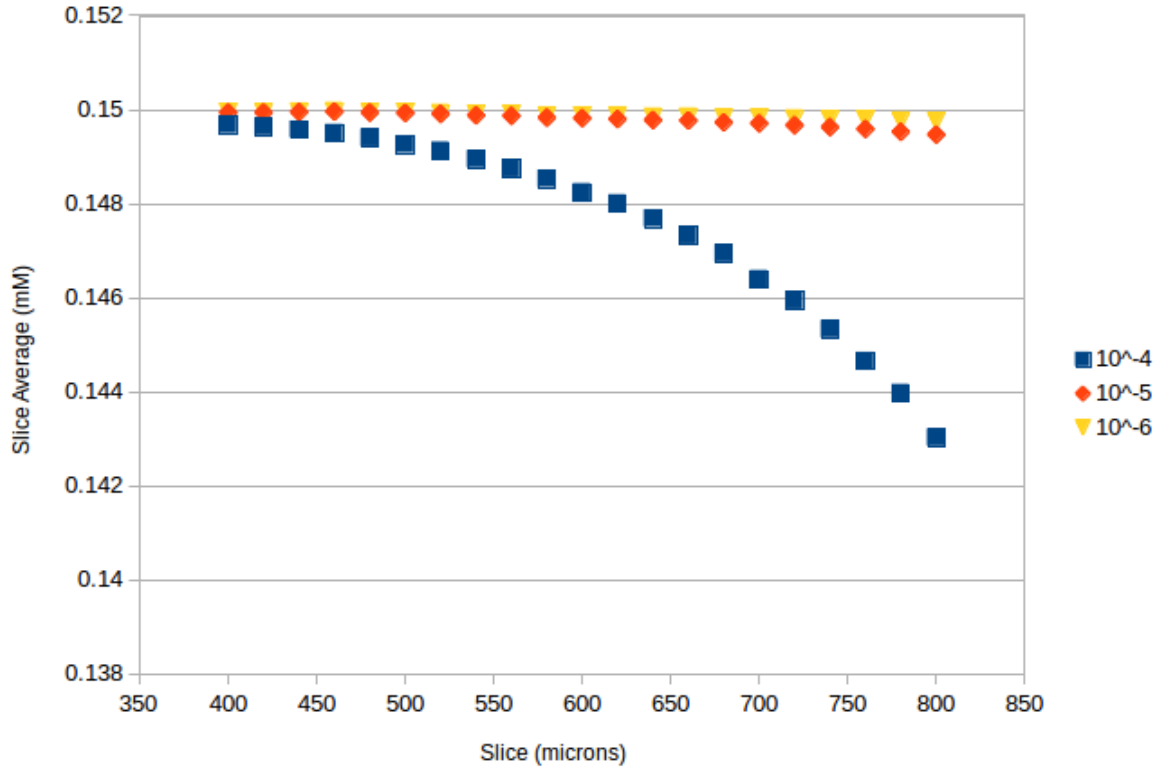

Figure 3.11-3: Effect of concentration tolerance criteria on O_2 diffusion profiles at steady state.

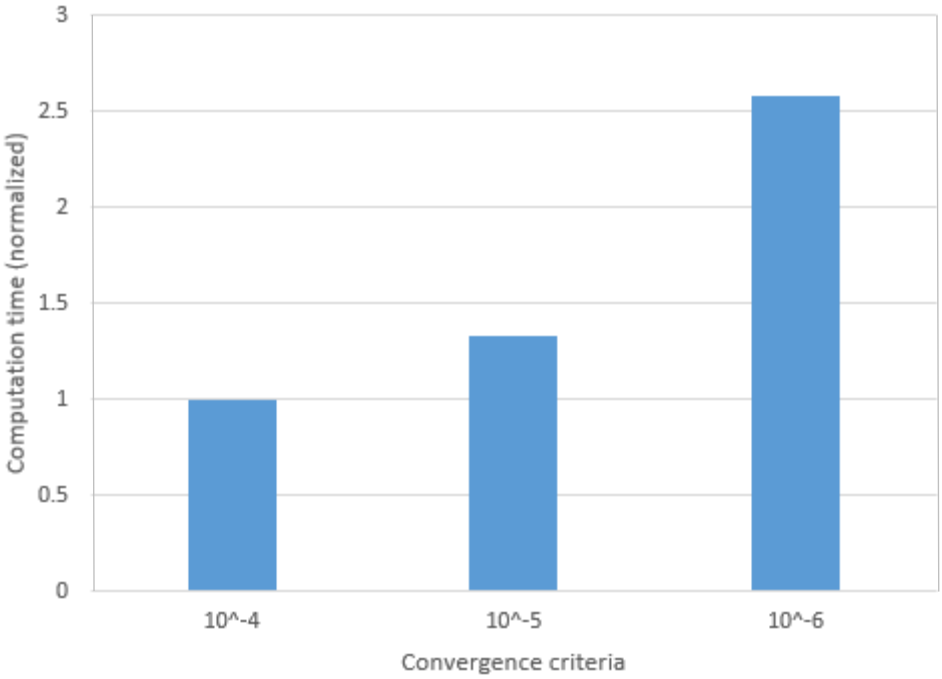

Figure 3.11-4: Normalized computation time required to reach steady-state with changing concentration tolerance.

Figure 3.11-5 compares the computation time required to reach steady state for six different resolution cases. An exponential increase in computation time was observed with increasing resolution. Resolution-61 simulations were found to be ~1100 times slower than resolution-12 and ~15 times slower than resolution-31. Therefore, L_{char} was represented by 31 nodes and identified as an optimal resolution as a trade-off between solution accuracy and time cost (Figure 3.11-2 and Figure 3.11-5). This was regarded as a reasonable compromise, because the oxygen concentration profiles for resolutions greater than 31 were found converging (Figure 3.11-2).

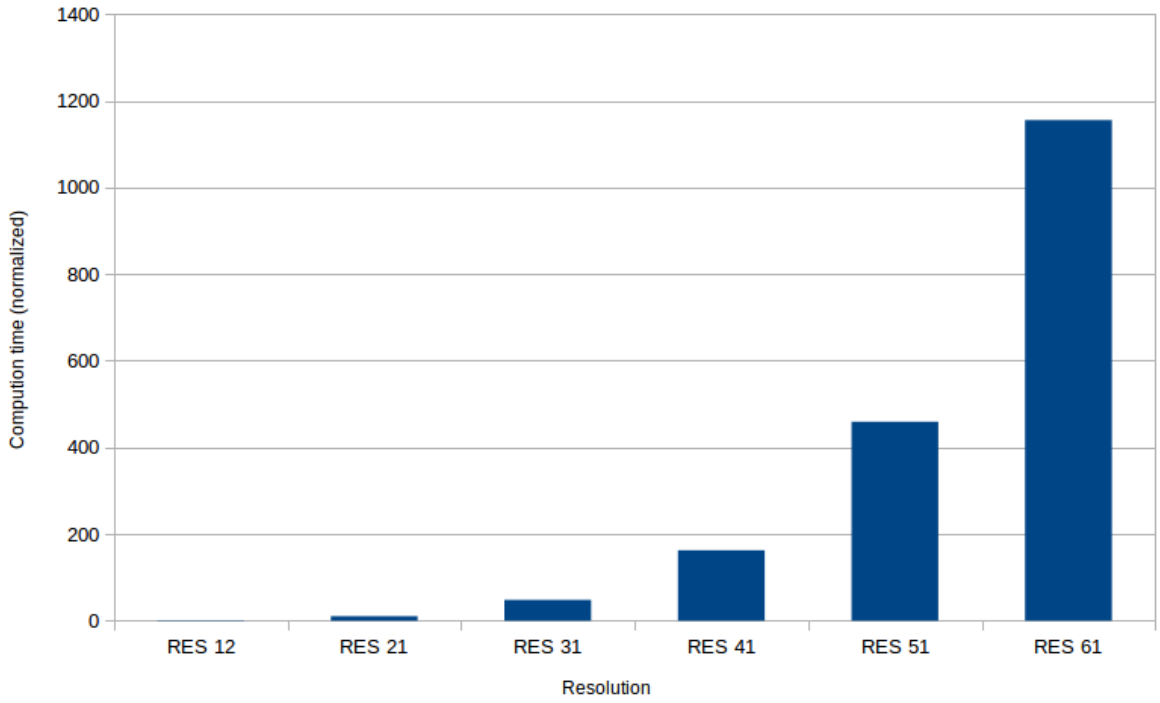

Figure 3.11-5: Normalized computation time required to reach steady-state with changing spatial resolution.

3.12. Exit effects

Figure 3.11-2 shows a dip that occurred in the slice average oxygen concentrations, in the blood exit region. Exit effects were identified as a reason for this effect in addition to concentration tolerance criteria. Exit effects emerged due to the Neumann concentration boundary condition imposed at the scaffold exit, where the axial concentration gradient was set to zero. This imposition meant an abrupt change in the concentration profiles in the exit unit cells, which distinguished these profiles from those present in the middle unit cells [138, 139]. This effect is elaborated by considering a 2-D view of SD80% TPMS unit cell, of edge length 200 μm (Figure 3.12-1). 5-10 such unit cells were stacked back to back and oxygenated blood with 0.15 mM concentration was perfused at 1 $mm\ s^{-1}$ through the scaffold. Oxygen diffusion in the tissue was enabled in the simulation but consumption was set to zero. This set up was conceptualized to ignore the consumption effect and focus on the stability of the diffusion model. At steady-state, the average oxygen concentration in the slices (separated by 20 μm) was estimated as shown in Figure 3.12-2. It should be noted that the oxygen concentration profiles of the cases with 5, 6, 7, 8, 9 and 10 TPMS unit cells are present in the first 1000 μm, 1200 μm, 1400 μm, 1600 μm and 2000 μm respectively. The results show that the concentration profiles at the blood entrance and exit regions differ significantly to those in

the middle unit cells. Exit effects were found to drastically change the concentration profiles in the last ~2 TPMS unit cells, where the imposed Neumann boundary condition limits the oxygen diffusion in the peripheral unit cells, in order to maintain a zero concentration gradient in the axial direction and to ensure mass conservation. Therefore, a dip in slice average oxygen concentration was observed at steady state as relatively less amount of oxygen diffused in the exit tissue region. Figure 3.12-3 is a close-up image of Figure 3.12-2, but focussing only on the first 1000 μm from the blood entrance point. The figure emphasizes that the concentration profiles in the middle unit cells are more stable and established than those at the blood entrance and exit regions. Therefore, the middle unit cells of the simulations were considered as periodic unit cells, because the O_2 concentration profiles in them were found to be homogeneous.

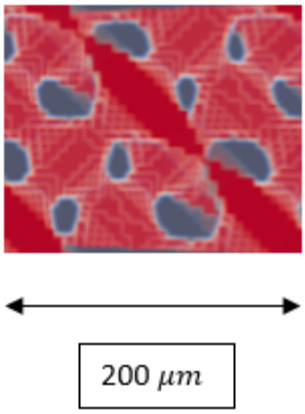

Figure 3.12-1: 2D view of a single TPMS unit cell (SD80%) of edge length 200 μm, assuming blood perfusion from left to right.

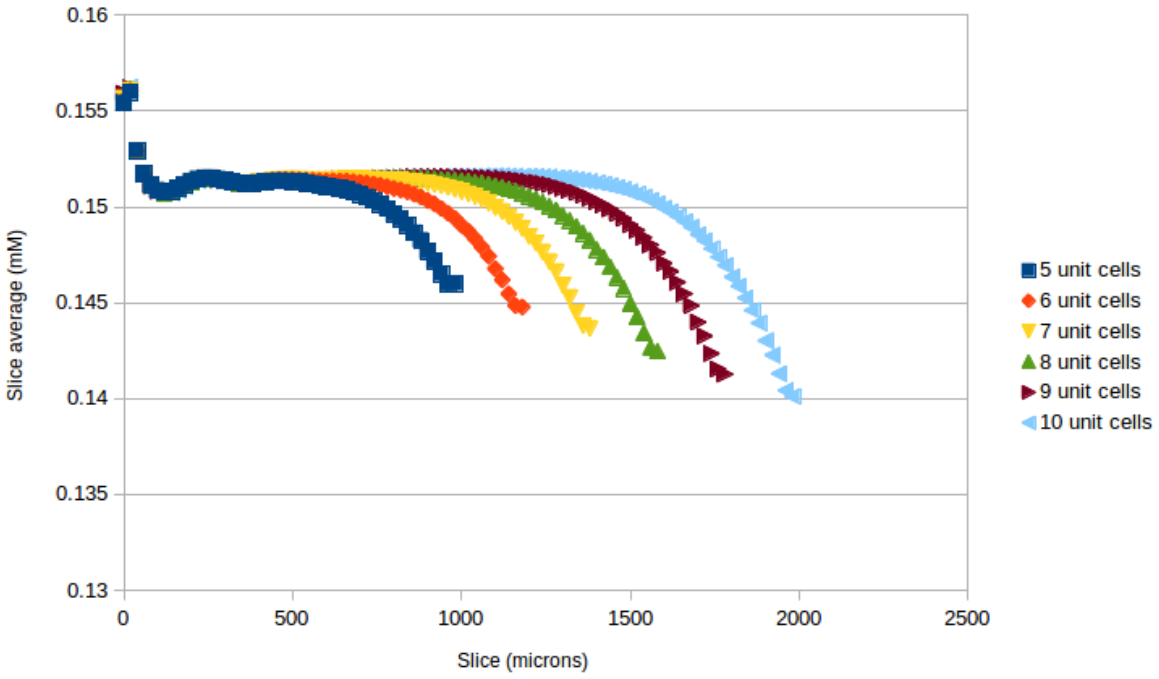

Figure 3.12-2: Exit-effects in the posterior unit cells.

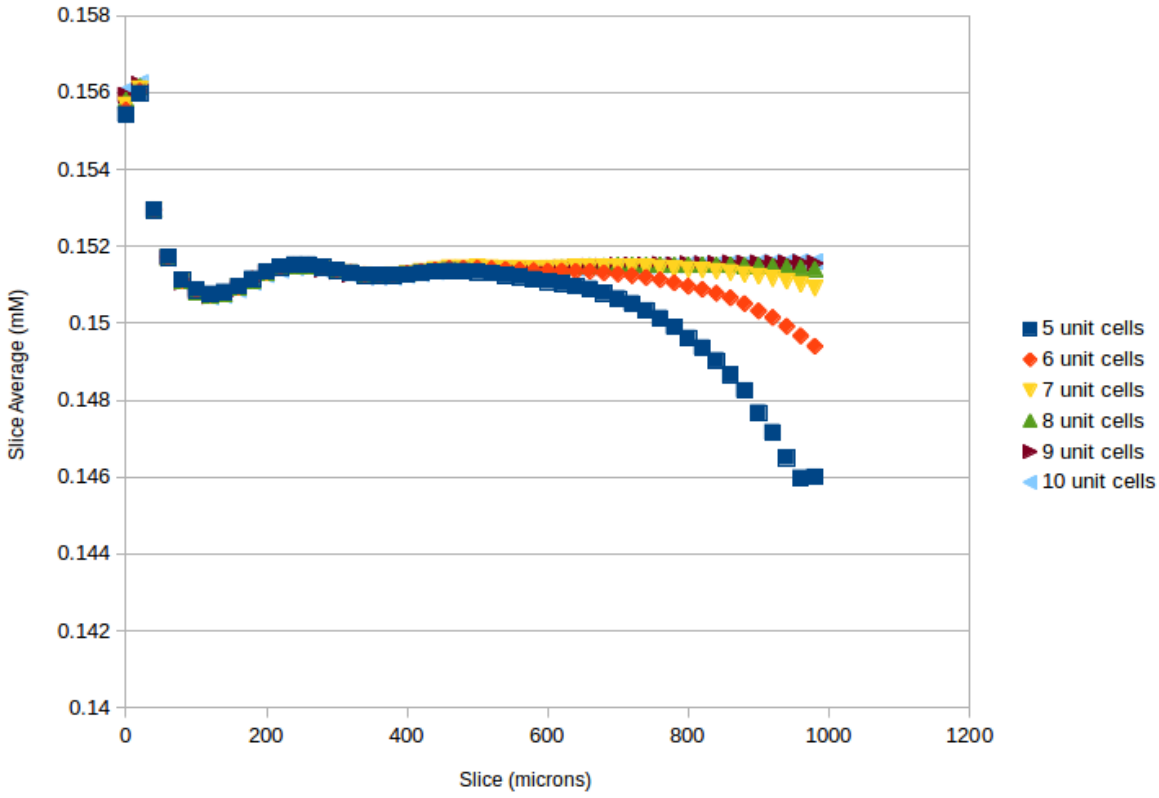

Figure 3.12-3: Close-up of Figure 3.12-2 with focus on front 1000 μm or first 5 unit cells.

3.13. Minimizing exit effects

There are multiple ways to counter exit-effects such as improving boundary conditions at the exit or having an infinitely long scaffold, such that the concentration profiles in the posterior unit cells can be ignored. An alternative approach considered in the LBM simulations was to have empty spaces at the scaffold exit, referred to as exit-length. This approach minimized the exit effects because the Neumann boundary condition was now applied at the exit of the exit-length and thus minimizing the concentration profile distortion in the rear unit cells. Figure 3.13-1 shows a 2D side view of an 80% porous SD juxtaposed by an empty unit cell of equal size. Exit-length was encoded such that, it could be enlarged and elongated in multiples of the predefined unit cell size in the C++ code. Exit-lengths also come at an increased computation cost and therefore need to be optimized to realize a trade-off between solution accuracy and computation time.

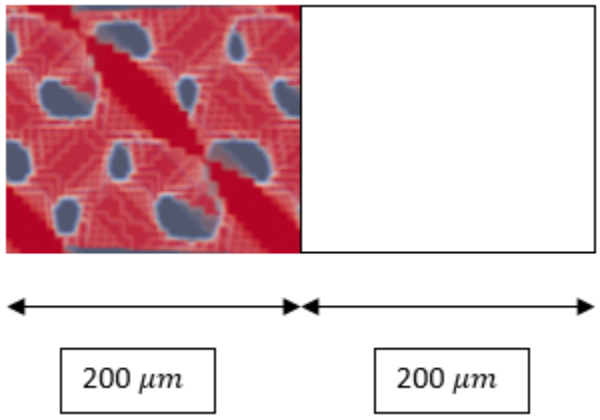

Figure 3.13-1: Illustration of exit-length at the rear TPMS unit cell.

Figure 3.13-2 shows steady state oxygen concentration profiles in SD80% slices, when the perfused inlet concentration was 0.15 mM, transported at 1 mm s^{-1}. Similar to the previous approach, O_2 diffusion in tissue was allowed, but O_2 consumption was set to zero in these simulations. The data points represent cases with no exit length (Exit_0) to exit lengths measuring about 5 unit cells (Exit_5), when stacked behind 5 TPMS unit cells that are placed between 0 and 1000 μm. It was observed that the exit-length was necessary to get stable concentration profiles in the middle unit cells, and its absence made the concentration profiles appear inconsistent. Overall it was found that exit-length of '2' decreased the exit effects adequately, stabilized the concentration profiles in the middle unit cells and the simulations were also found to reach steady-state in reasonable computation time. Figure 3.13-3 is a close-

up image of Figure 3.13-2 suggesting stable concentration profiles in the middle unit cells for exit length ≥ 2.

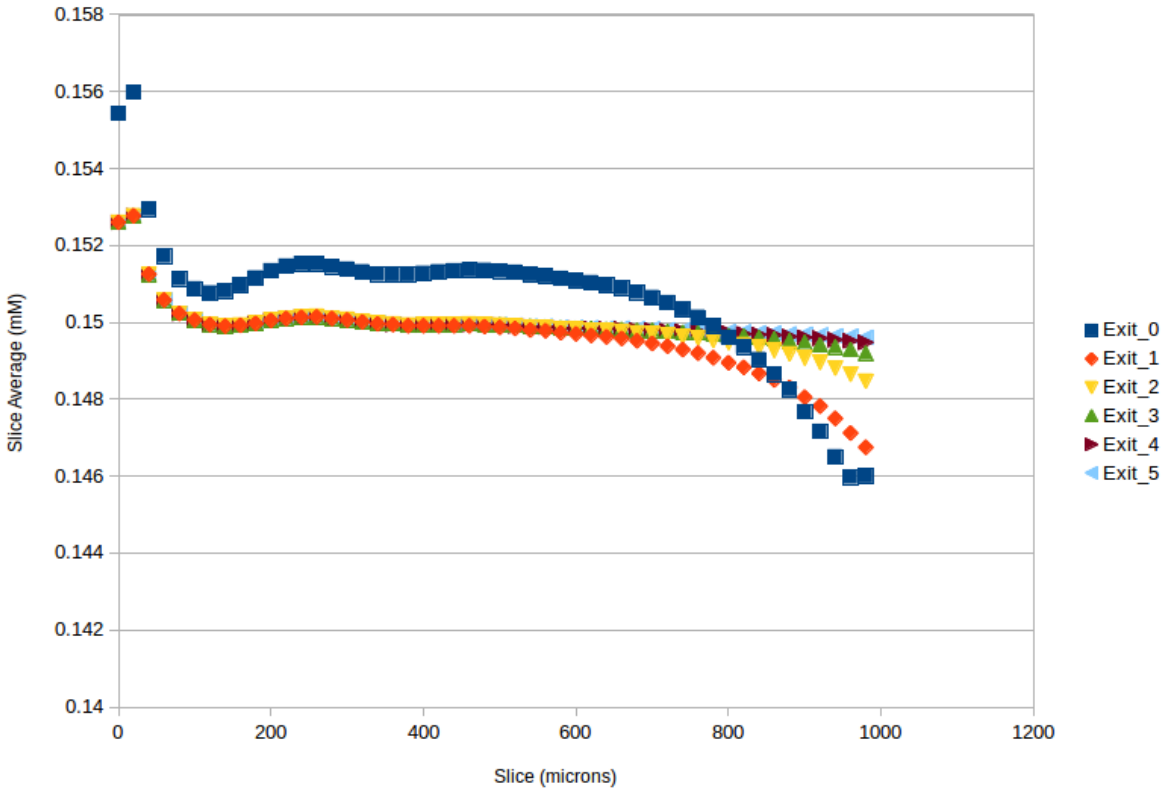

Figure 3.13-2: Oxygen concentration profiles along scaffold length in SD80%, at varying exit lengths.

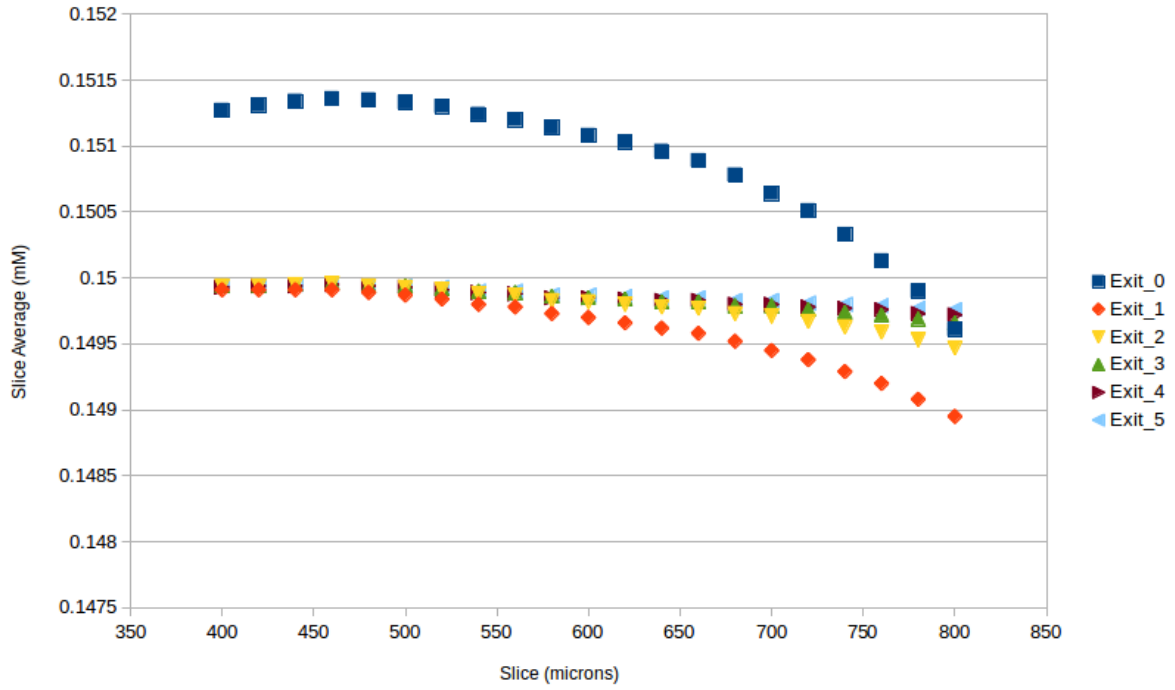

Figure 3.13-3: Close-up of Figure 3.13-2, showing stable oxygen concentration profiles in the middle unit cells at steady state.

3.14. Entrance effects

Figure 3.13-2 shows unusual concentration profiles in the anterior TPMS unit cells (0-200 μm). The data points representing average oxygen concentration in these slices were hypothesized as entrance effects, where the velocity profiles did not mature. Entrance effects occur in a finite length at the entrance of the scaffold where the velocity profile is different to the rest of the scaffold region [140]. To investigate the entrance effects, random sampling of radial velocity profiles at 33 μm, 300 μm, 700 μm, and 1100 μm was done along the flow axis of the SD80% scaffold. The velocity profiles of these different slices were superimposed on the same figure as shown in Figure 3.14-1. The velocity profiles in these slices are different because each slice of a TPMS structure is different, and therefore entrance effects were not clearly visible. The gaps in these velocity profiles indicate zero velocity or presence of tissue in the region. To understand entrance effects, the capillary architecture was revisited, and the radial velocity profiles were sampled along the flow-axis as shown in Figure 3.14-2. It could be observed that the velocity profiles appear homogenized and developed beyond 300 μm of the flow-axis. Entrance effects were dominant in the region < 300 μm i.e. roughly 2 unit cells, where the velocity profiles were found developing.

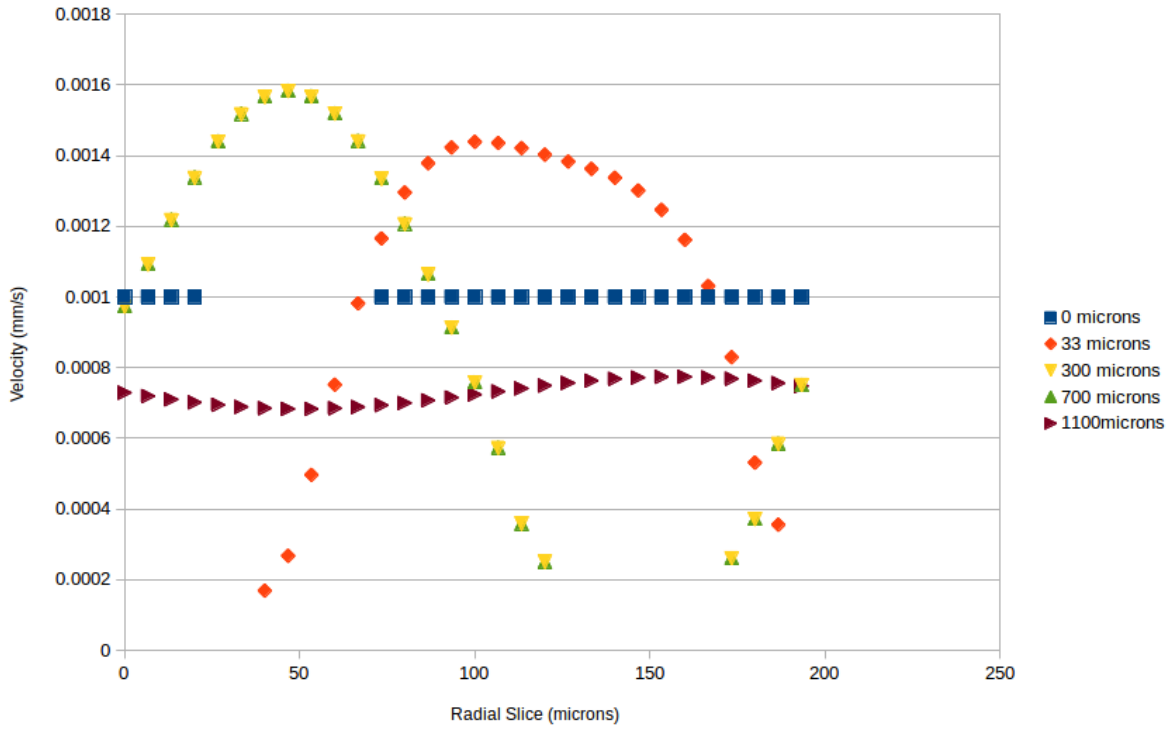

Figure 3.14-1: Velocity profiles along the length of the SD80% scaffold.

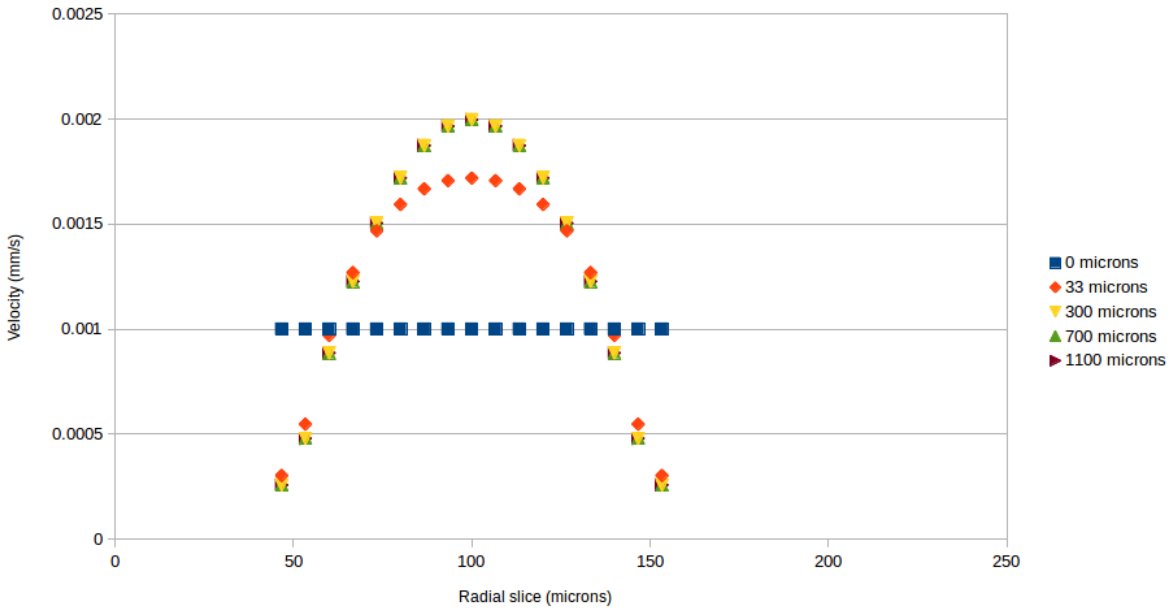

Figure 3.14-2: Velocity profiles in capillary slices (radius = 50 μm) along the scaffold.

After examining the slice average oxygen concentrations, it was concluded to exclude two unit cells at the scaffold entrance, two unit cells at the scaffold exit while having an exit

length of two unit cells. The remaining unit cells in the middle of the scaffold were considered periodic, reliable, stable and considered for further evaluation.

3.15. Validation of LBM model

After accounting for entrance and exit effects, the LBM model was tested on four test cases which are described in Table 4.2-1. An 80% porous Schwarz Diamond tissue, without hydrogel scaffold on the top, was examined for oxygen accumulation. The other parameters used in Table 4.2-1 are: oxygen diffusion coefficient in tissue ($2.1\times 10^{-9}\ m^2\ s^{-1}$), perfusion velocity ($1\ \text{mm s}^{-1}$) and perfused inlet O_2 concentration (0.15 mM). The "Nodiff/Consump" case refers to the case when oxygen diffusion and consumption in the tissue was restricted. The "Diffusion_only" case refers to the case when oxygen diffusion was allowed in the tissue but consumption set to zero. The "Large_consump" case refers to the case when the oxygen consumption rate in the tissue was higher than the "Small_consump" case, while oxygen diffusion into the tissue was allowed.

Table 3.15-1: Summary of major parameters depicted in Figure 3.15-1

Legend	Oxygen diffusion in tissue	Oxygen consumption rate
Nodiff/Consump	☒	☒
Diffusion_only	☑	☒
Large_consump	☑	$0.01\ \text{mM s}^{-1}$
Small_consump	☑	$0.0001\ \text{mM s}^{-1}$

Figure 3.15-1 shows that the diffusion only case exhibited higher oxygen accumulation at steady state than the other cases, which was anticipated as the consumption effect was turned off. The case with smaller consumption rate accumulated the next highest oxygen concentration, followed by the case with larger consumption rate. Furthermore, the case where the tissue diffusion and consumption terms were disabled, displayed the lowest slice average

oxygen concentration, considering the fact that tissue was non-permeable to oxygen, thus pushing down the slice average concentration value.

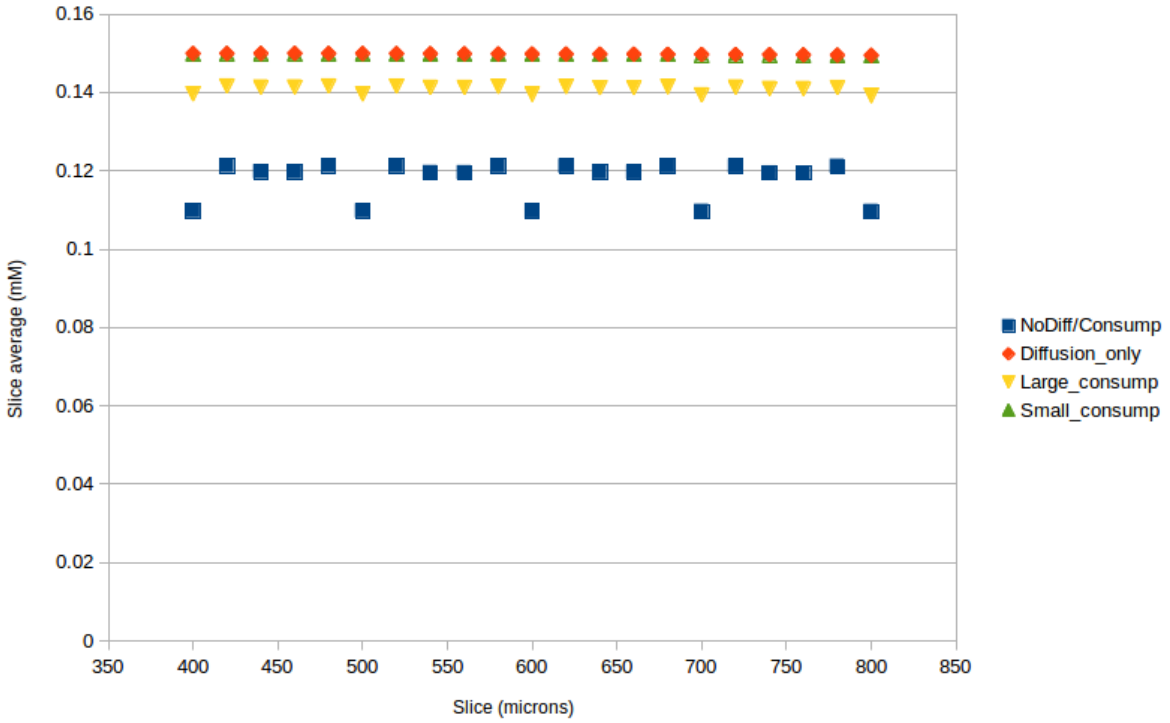

Figure 3.15-1: Slice average oxygen concentration along the length of the SD80% scaffold (including the blood and tissue side).

The average oxygen concentration in the tissue side of the slices was also investigated for all the cases mentioned in Table 3.15-1. The oxygen concentration profiles of diffusion only case and the case with small O_2 consumption rate superimposed on each other (Figure 3.15-2) because the consumption rate was not high enough to cause any distinguishable effect in the observed scale. The average concentration in tissue for the no diffusion case was null as expected, because oxygen diffusion into the tissue was restricted. The concentration profile for the large oxygen consumption rate appeared bounded in between these two cases, due to the higher metabolic rate in the tissue side.

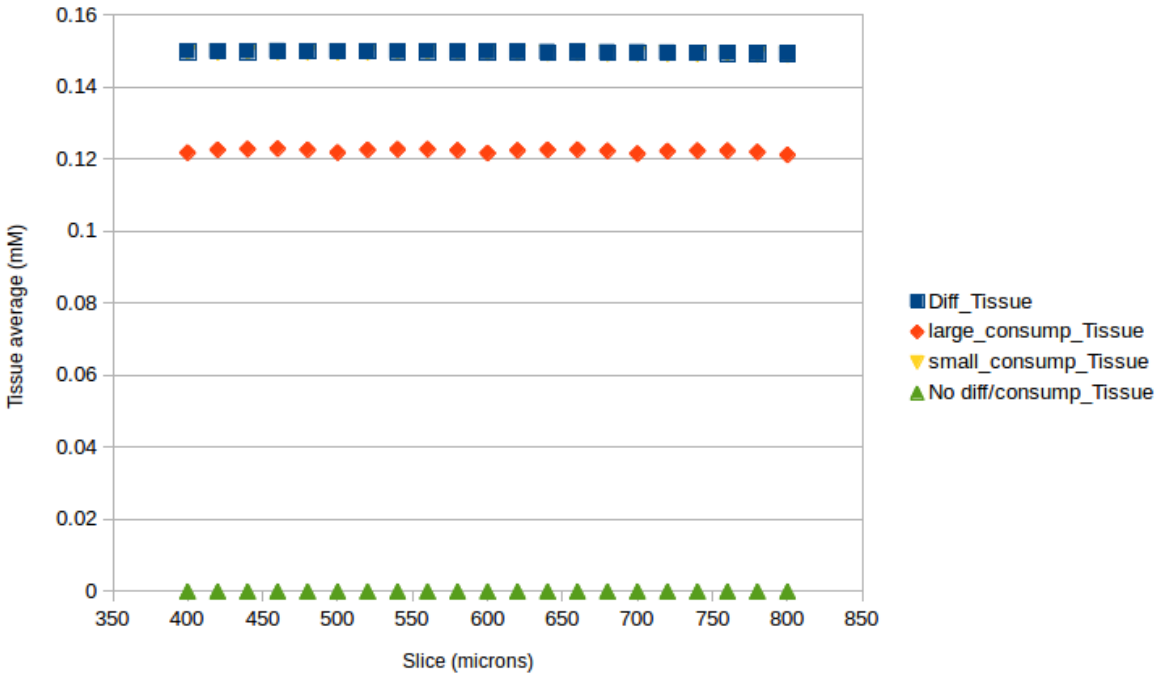

Figure 3.15-2: Average oxygen concentration in the tissue region of SD80% slices.

Figure 3.15-1 also shows fluctuations in the average oxygen concentration between the slices. These fluctuations were found to be more prominent in the case where the oxygen diffusion in tissue was disabled and the consumption set to zero (Figure 3.15-3). The concentration map of two of these contrasting slices were investigated closely at 400 μm and 420 μm (Figure 3.15-4 and Figure 3.15-5).

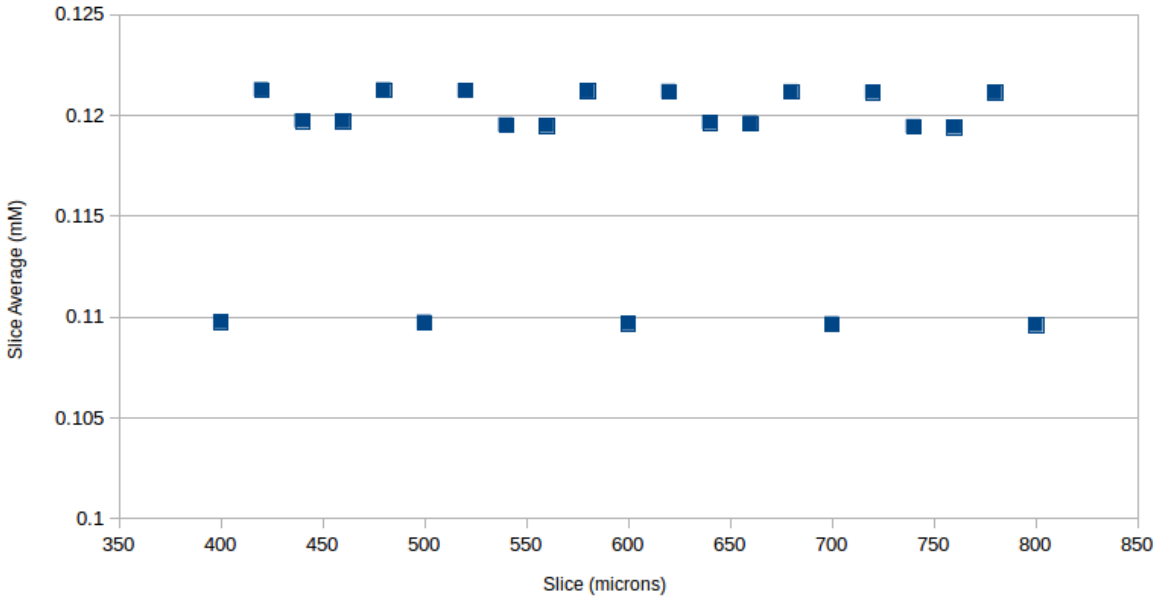

Figure 3.15-3: Average oxygen concentration in SD80% slices, when oxygen diffusion in tissue is disabled and consumption set to zero.

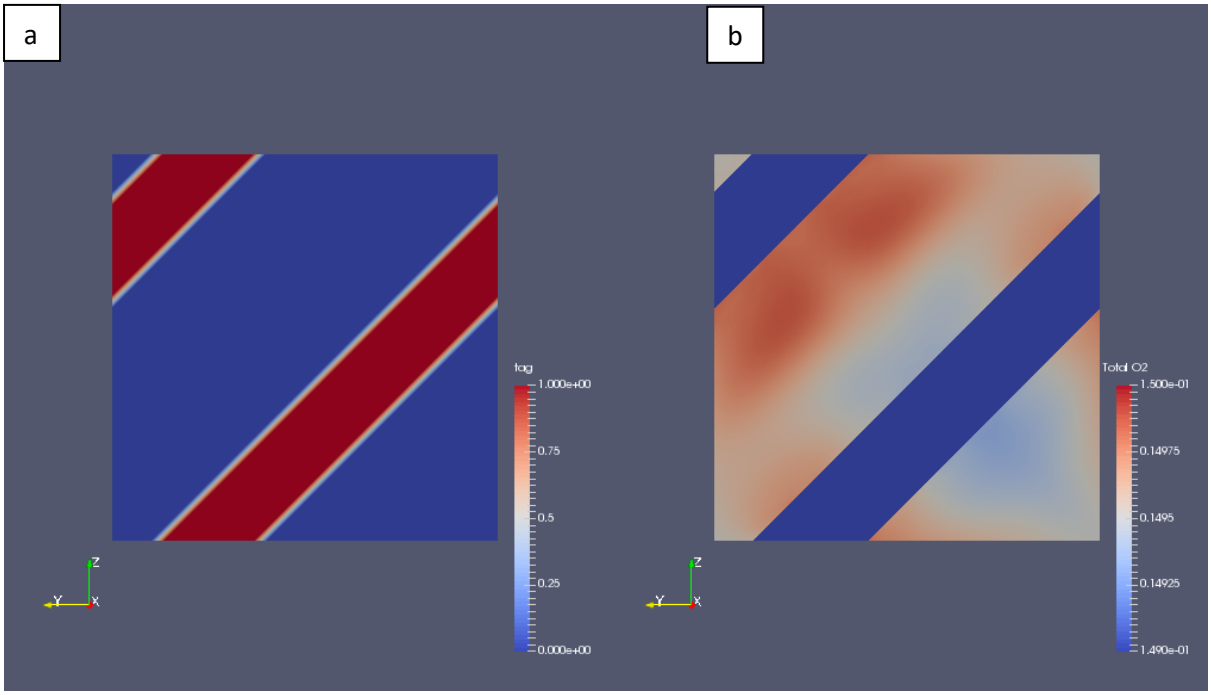

Figure 3.15-4: VTI images of SD80% slice at 400 µm when the oxygen diffusion and consumption in the tissue was turned off. a) Image showing tissue (red) and blood (blue) b) Oxygen concentration map of the corresponding slice. (Oxygenated blood is perfusing into the plane (x-direction))

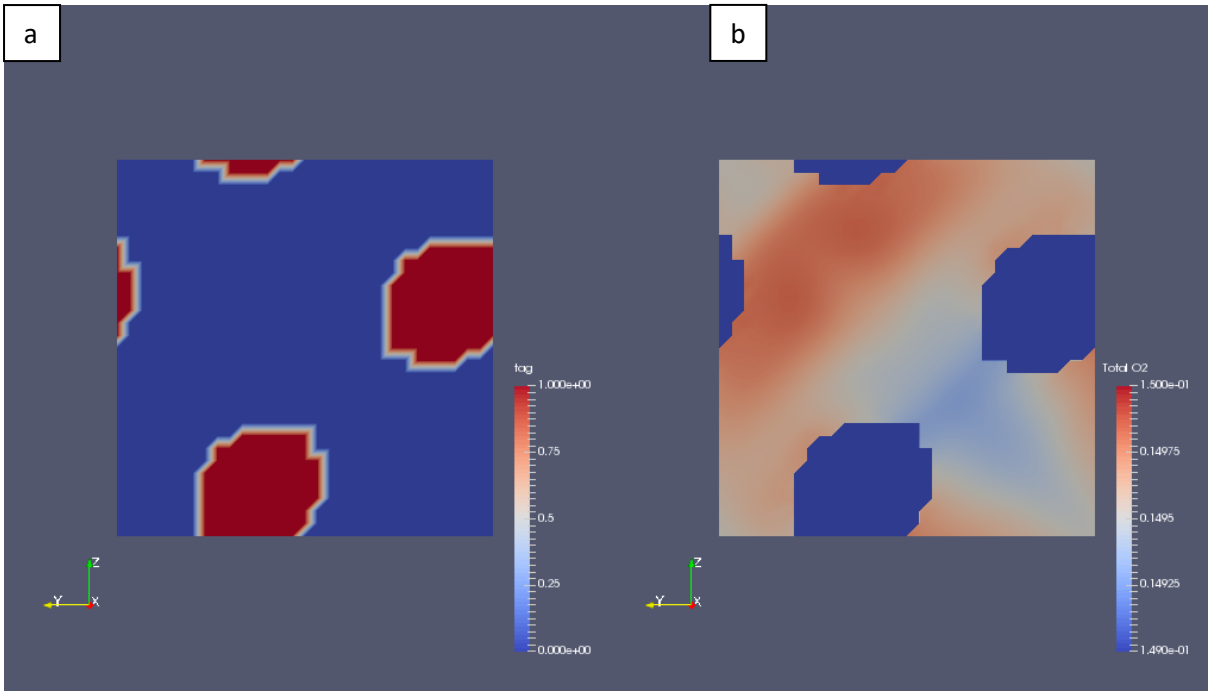

Figure 3.15-5: VTI images of SD80% slice at 420 μm when the oxygen diffusion and consumption in the tissue was turned off. a) Image showing tissue (red) and blood (blue) b) Oxygen concentration map of the corresponding slice. (Oxygenated blood is perfusing into the plane (x-direction))

The right side images of Figure 3.15-4 and Figure 3.15-5 show a non-uniform distribution of oxygen concentration within TPMS slices at steady state, depending upon the velocity profiles that developed at steady state in these structures. The left side images of Figure 3.15-4 and Figure 3.15-5 indicate that there is a difference in the number of tissue pixels (red) and the blood side pixels (blue). Assuming cell size is constant in both cases, it appears that the number of tissue cells at 400 μm is higher than at 420 μm. This information was also validated in Figure 3.15-6 where the number of tissue pixels were enumerated along the blood flow axis. This information about number of tissue cells was correlated with the average oxygen concentration in the corresponding slices (Figure 3.15-3).

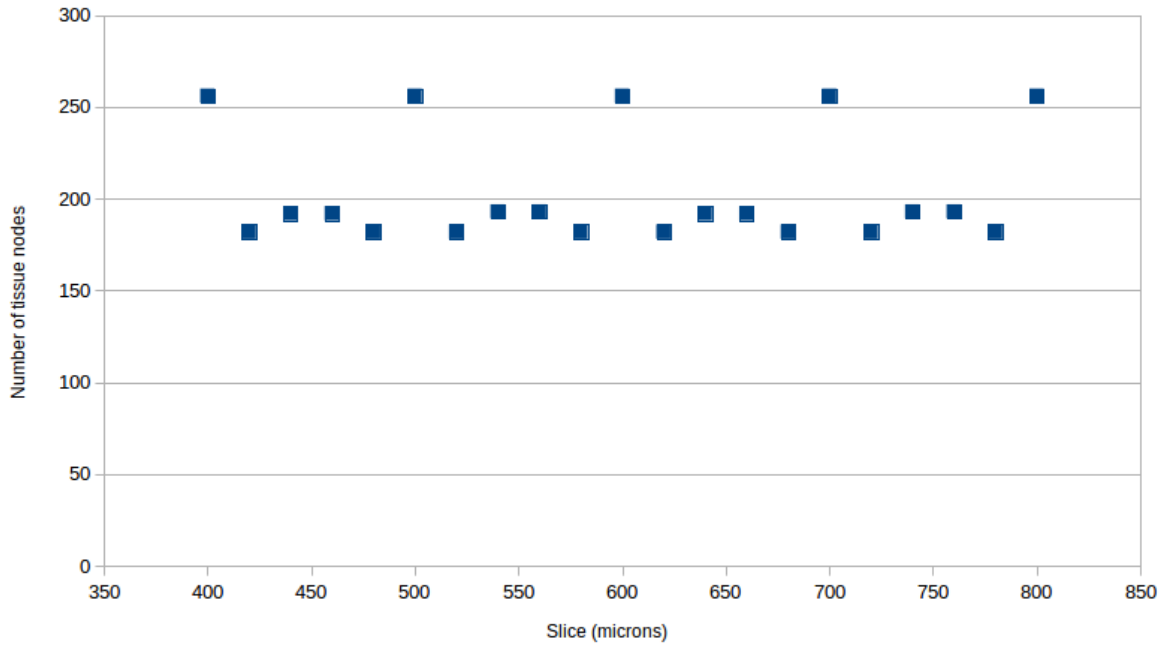

Figure 3.15-6: Enumeration of tissue cells in axial slices of SD80%.

It was concluded that higher oxygen concentration existed in slices with more blood side space (less tissue side space). This indicated that the space distribution between blood and tissue phases significantly influenced the oxygen concentration distribution and the slice average concentration in any given TPMS slice. This variation in cross-sectional area was found to be a reason for fluctuations in slice average O_2 concentration.

The fluctuation effect was found relatively less in the case with diffusion turned on, and it was hypothesized that the diffusion in tissue dissipated the fluctuations by acting as a local storage buffer, negating the strong dips (Figure 3.15-1). The slices and concentration maps of SD80% at 400 μm and 420 μm are shown in Figure 3.15-7 and Figure 3.15-8, where the oxygen diffusion in tissue was allowed but consumption set to zero. The concentration map reflects that the oxygen concentration in the blood side is higher than the tissue side at steady state, although the concentration distribution within any given phase was not necessarily uniform.

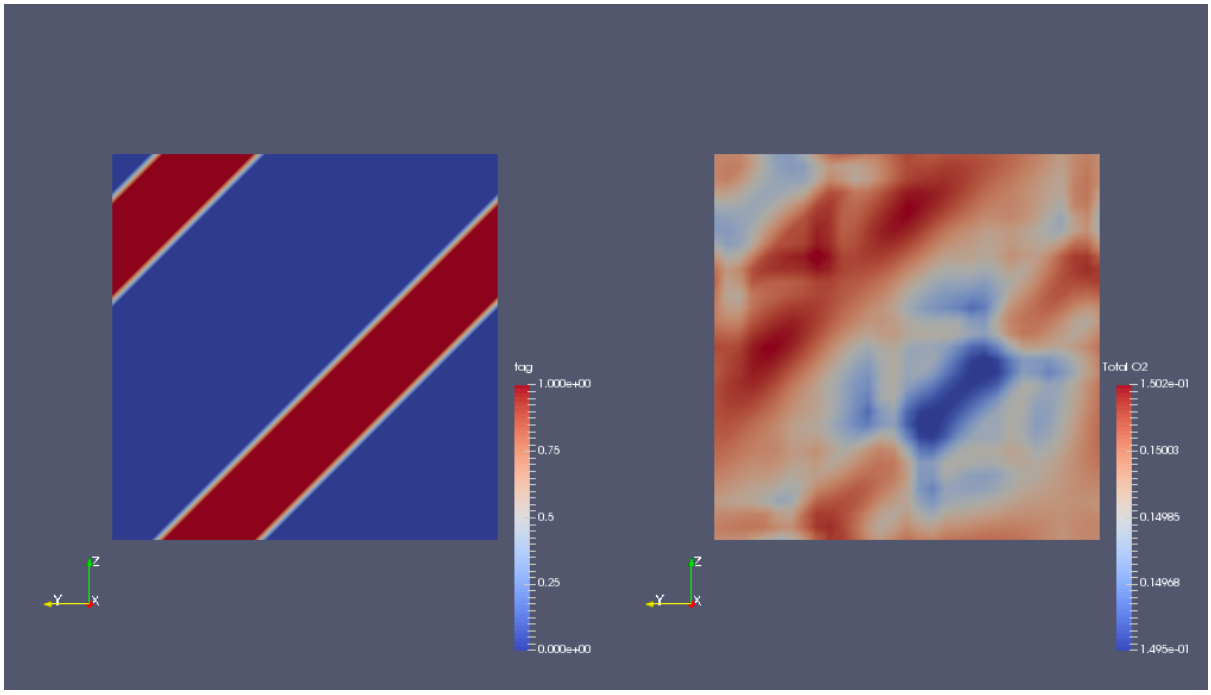

Figure 3.15-7: VTI images of SD80% slice at 400 μm when the oxygen diffusion in tissue was allowed but consumption set to zero. a) Image showing tissue (red) and blood (blue) b) Oxygen concentration map of the corresponding slice. (Oxygenated blood is perfusing into the plane (x-direction))

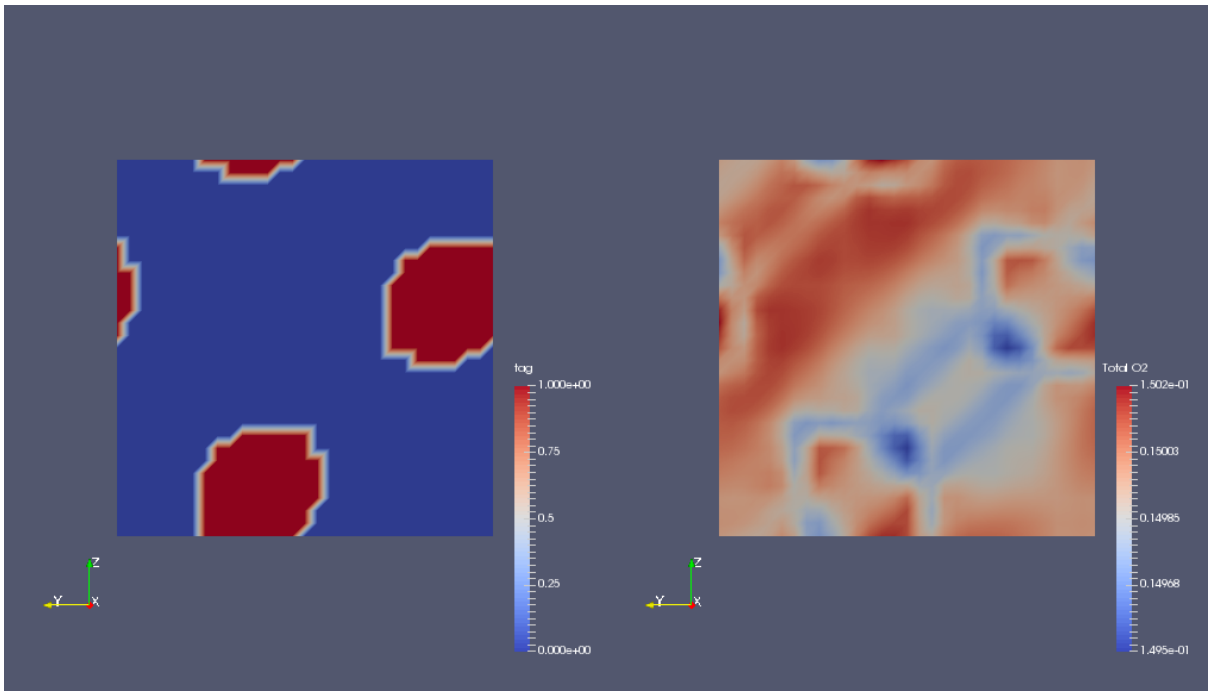

Figure 3.15-8: VTI images of SD80% slice at 420 μm when the oxygen diffusion in tissue was allowed but consumption set to zero. a) Image showing tissue (red) and blood (blue) b) Oxygen concentration map of the corresponding slice. (Oxygenated blood is perfusing into the plane (x-direction))

3.16. Effect of perfusion velocity and structural porosity on tissue vascularization

The impact of changing structural porosity and blood flow velocity was analysed to understand its effect on the average axial oxygen concentration in the slices. It was observed that, more porous structures accumulated higher oxygen concentration in the slices, as shown in Figure 3.16-1.

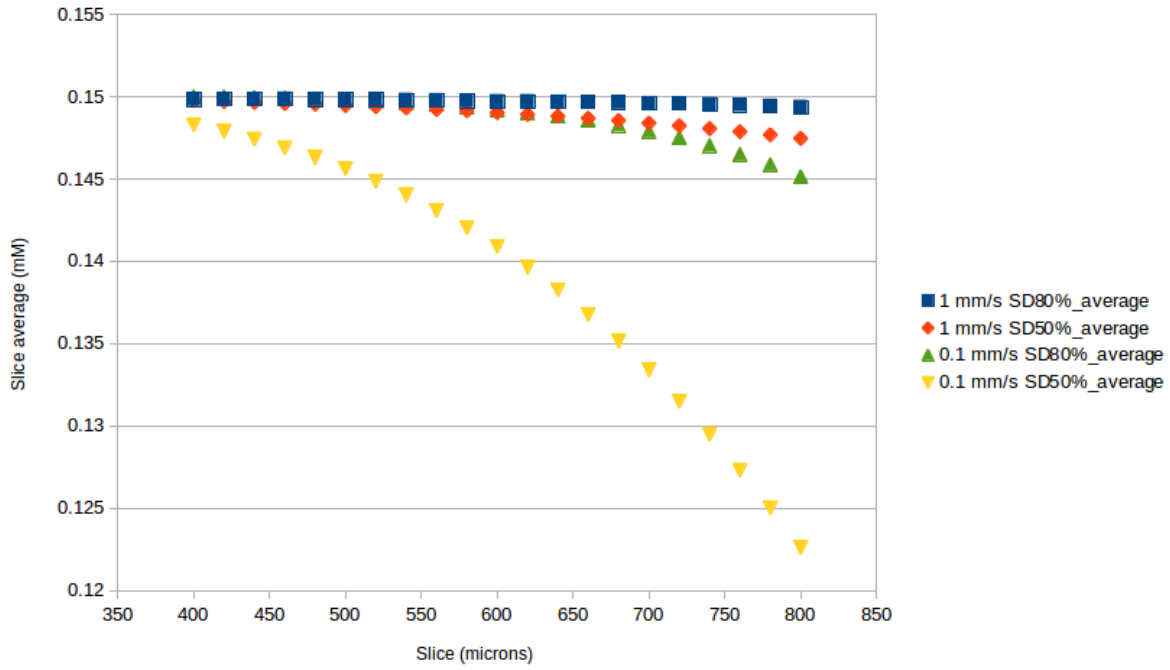

Figure 3.16-1: Average oxygen concentration along the length of the Schwarz Diamond scaffolds, at varying structural porosities and blood flow velocities.

Higher oxygen accumulation in tissue is due to higher oxygen permeability in the tissue. This observation was found in sync with literature findings suggesting increased nutrient permeability with increasing structural porosity of TPMS structures [141]. This occurs because the metabolic demand of more porous structures is less, given the fact that there is less tissue. Highly porous structures however have a lower specific tissue volume i.e. they have less amount of tissue in a given volume.

Lower perfusion velocity also affected the concentration profiles significantly as was observed in early onset of downward trajectory of the concentration profiles. It was concluded that higher perfusion velocities positively enhance mass transfer in tissues because the solute influx per unit time is higher. However, there is an upper limit to which maximum velocity can be increased; the physiological limitation is that blood velocities in capillaries which are primarily responsible for tissue vascularization are less than 1 $mm\ s^{-1}$ [142]. The computation limitation was the challenge involved in investigating diffusion phenomena beyond 1 $mm\ s^{-1}$,

because it was found that the BGKW implementation of LBM restrained the velocity field to converge within a preset tolerance criterion.

Figure 3.16-2 and Figure 3.16-3 correspond to the average oxygen concentration computed on tissue and blood/void regions respectively. It can be analysed from Figure 3.16-1 that a downward trajectory of oxygen concentration profiles is inevitable in the axial direction (in posterior slices), when the tissue is actively consuming oxygen. This information is crucial in designing scaffolds because the dip in the axial concentration profiles will also be affected due to the presence of an additional resistance layer such as a scaffold.

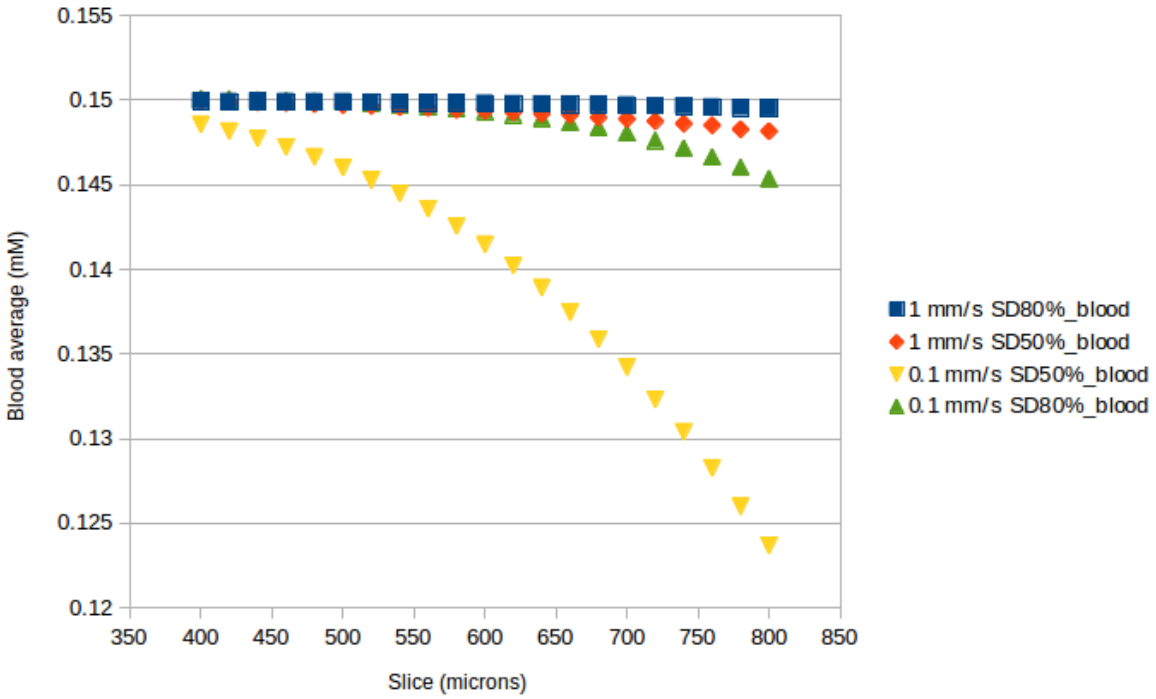

Figure 3.16-2: Average oxygen concentration in the blood side of Schwarz Diamond scaffolds, at varying structural porosities and blood flow velocities.

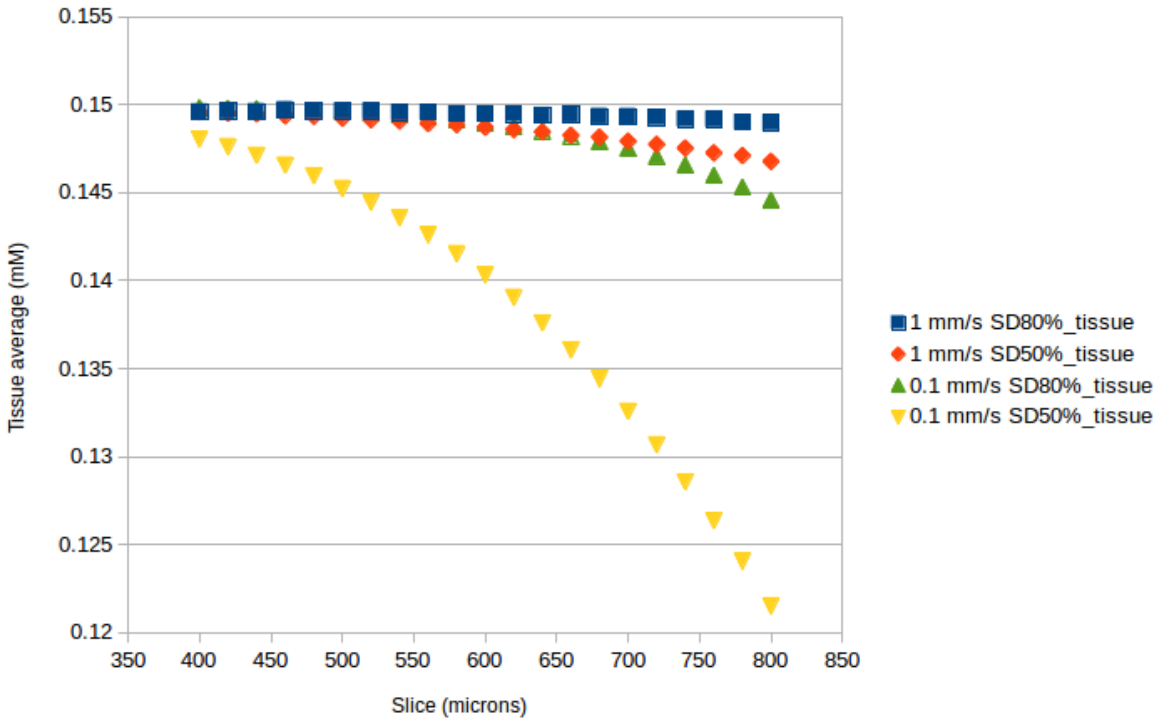

Figure 3.16-3: Average oxygen concentration in the tissue side of Schwarz Diamond scaffolds, at varying structural porosities and blood flow velocities.

The concentration dip in axial direction can be further explained with the insights gained from Krogh's capillary model. In this regard, the relationship between wall concentration and oxygen penetration distance in the tissue was at steady state was revisited (Section 3.9). Figure 3.16-4 shows an illustration of concentration losses occurring due to hydrogel scaffold and boundary layer, at a slice closer to the oxygenated blood entry point. Figure 3.16-5 shows an illustration of concentration losses occurring at a slice further towards the scaffold exit. In these figures, it is demonstrated that the scaffold and boundary losses would be higher in the posterior slices, when compared to anterior slices. This is because in the posterior slices, there is relatively higher decrease in wall concentration, which decreases the oxygen penetration distance in the tissue. The wall concentration in posterior slices is less because the oxygen concentration in the blood side of these slices would be less, due to the consumption that occurred in the tissue until that point.

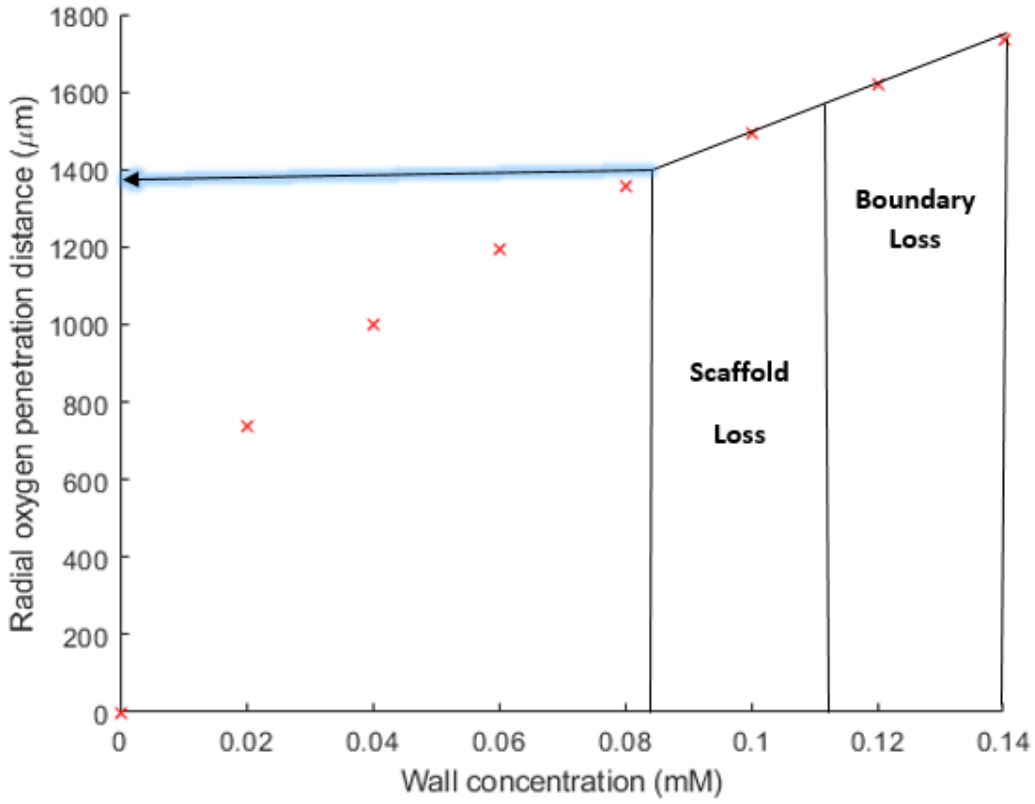

Figure 3.16-4: Illustration of concentration losses occurring due to hydrogel scaffolds and boundary layers in the anterior slices (towards the entrance of the scaffold).

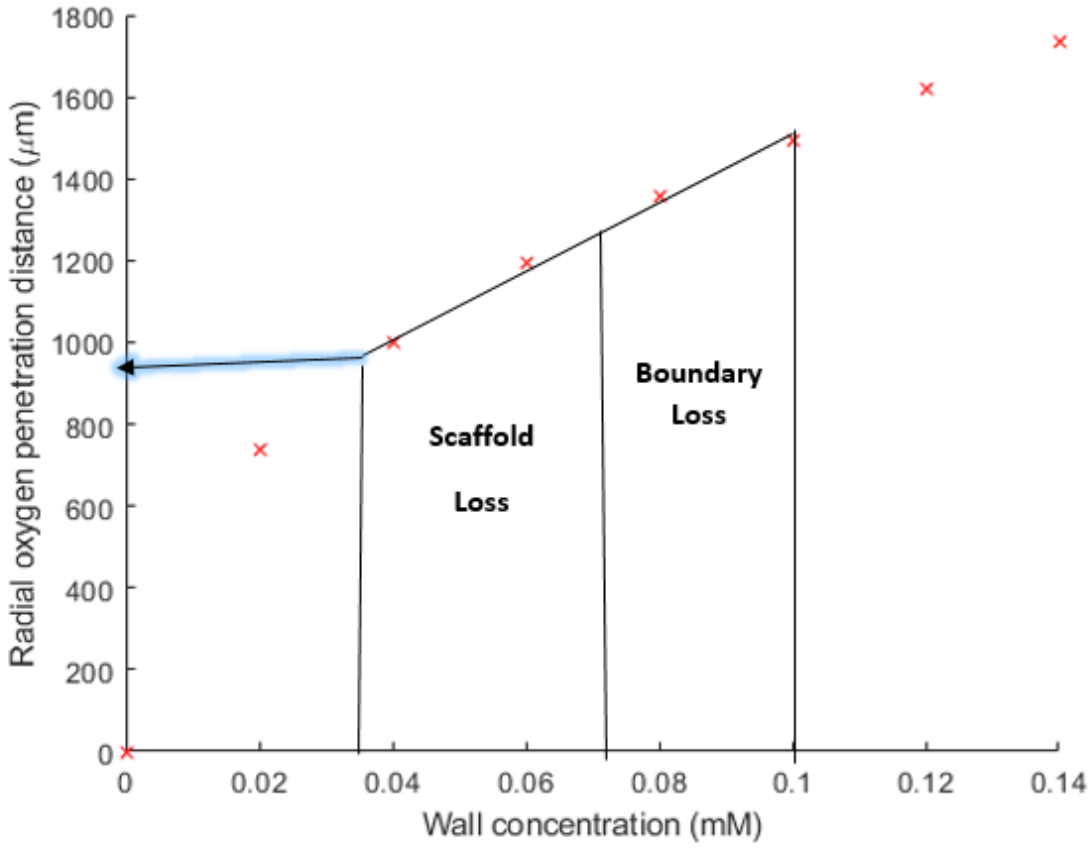

Figure 3.16-5: Illustration of concentration losses occurring due to hydrogel scaffolds and boundary layers in the posterior slices (towards the exit of the scaffold).

3.17. Summary

This chapter describes the methodology by which tissue oxygenation was explored with LBM method. It contains details on the algebraic and trigonometric equations that create different phases with TPMS architectures. The specifics of the Perko-Patel advection-diffusion model were discussed, including the choice of relaxation parameter and multi-scale modelling by including a virtual time-step. After model set-up, the LBM method was verified against Krogh's analytical solution by changing the tissue's oxygen consumption rate and diffusivity and comparing the oxygen penetration distances. Mesh-independence studies were performed with the LBM model and 31 nodes were found adequate to represent the characteristic length ($200\mu m$), for a trade-off between accuracy and speed. The Neumann concentration boundary condition caused a different pattern of slice average oxygen concentration profiles at the scaffold exit due to the zero gradient condition in the axial direction. This effect was

counteracted by using an exit-length (about 2 TPMS unit cell length) and by having a rigorous concentration tolerance criterion for simulation convergence (10^{-5} mM). The *Mahuika* platform of the NeSI high performance computers were used for simulating flow through large scaffolds that was found to reduce the simulation time. Sixteen computation cores of NeSI were identified as an optimum choice to run the simulations, as a trade-off between speed and core usage. Due to entrance and exit-effects, the data from two unit cells at the front and back end of the scaffolds were ignored, and an exit length of 2 units cells were designed at the scaffold exit. The data from middle unit cells of the scaffold were considered representative of periodic unit cells, as the oxygen concentration profiles in them were considered relevant, stable and reproducible. Furthermore, the oxygen concentration profiles were analysed in these middle unit cells for 4 different scenarios: Oxygen diffusion in tissue only case, No oxygen diffusion or consumption in tissue case, Oxygen diffusion and a small consumption rate in tissue case and oxygen diffusion and a large consumption rate in tissue case. These tests were performed to validate and compare the sensitivity of the diffusion and consumption model. The area effect in the TPMS slices was found to cause fluctuations in the computed slice average concentrations and it was noted that the presence of more blood side phase caused a local maxima in the figures and vice-versa. Additionally, the effect of structural porosity and perfusion velocity on slice average concentration was calculated and compared. It was found that higher perfusion velocity enhanced the slice average oxygen concentration due to increased oxygen advection rate. Similarly, higher structural porosity increased the oxygen accumulation in tissue region due to a lower oxygen metabolic demand.

4. Functional tissue scaffolds

4.1. Introduction

In this chapter, the LBM model was used to study oxygen diffusion in tissue scaffolds of implantable and 3D printable sizes. The domain size envisaged was 1 mm in the radial direction and 7 mm along the axial direction. There were 5 TPMS unit cells in the domain, each with an edge length of 1 mm, and blood was perfused through these unit cells that were stacked back-to-back[38]. Based on the findings of the previous chapter, the middle unit cells (3rd and 4th) were considered representative of periodicity, where there is minimum noise from entrance and exit effects. Therefore, the axial oxygen concentration profiles were analysed only in these unit cells at steady state (i.e. between 2000 μm – 4000 μm). Additionally, the simulations include concentration profiles in the presence of TPMS hydrogel scaffolds.

In this chapter, TPMS scaffold designs that are likely to be functional/normoxic are explored for a given set of parameters and assumptions. Secondly, the effect of hydrogel properties (thickness and oxygen diffusivity) on concentration profiles are explored in detail. Thickness of TPMS scaffolds is difficult to quantify as a single number as these structures are not axisymmetric [143]. Therefore, thickness of any layer of the TPMS structure depends on the 2D-slice under examination and its magnitude varies depending upon the choice of plane in 3-dimensional space ($\mathbb{R}^3$). However, it was found that the scaffold thickness in the slices of TPMS structures such as Schwarz Diamond and gyroid had minimal variation. Figure 4.1-1 and Figure 4.1-2 show the slice images in Schwarz Diamond and gyroid slices at 50% porosity, where the yellow regions (tissue) and blue regions (blood) were found homogeneous in terms of thickness.

[38] Exit length spanning 2 TPMS unit cells (~2 mm).

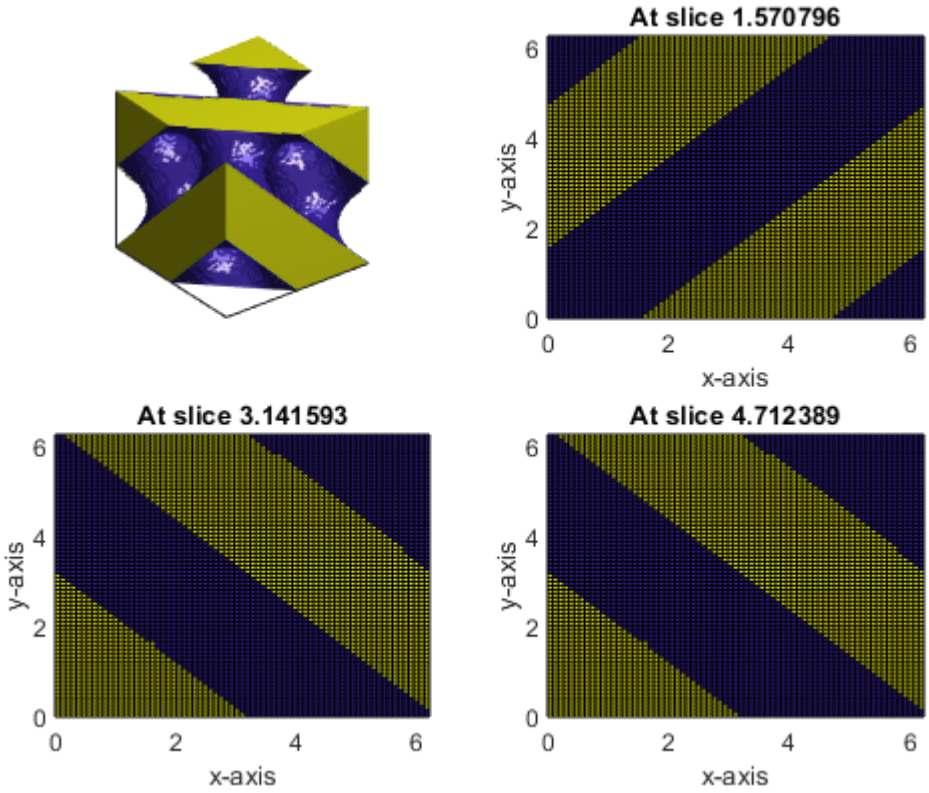

Figure 4.1-1: SD50% slices at $\frac{\pi}{2}$, π and $\frac{3\pi}{2}$ radians from the base, when the edge length was 2π.

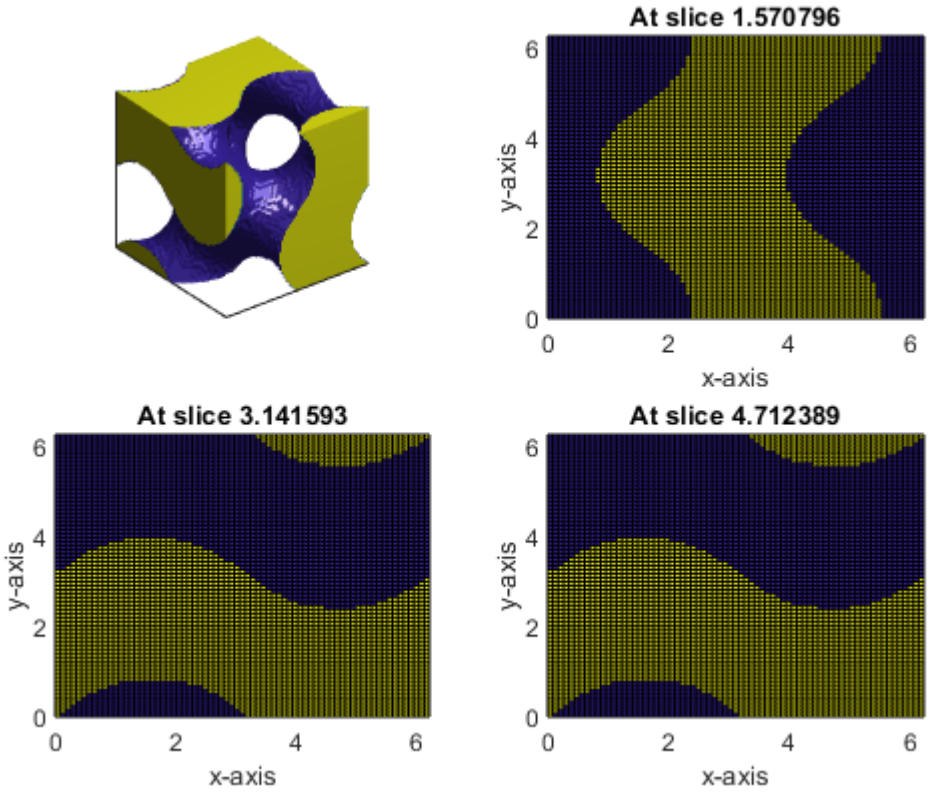

Figure 4.1-2: Gyr50% slices at $\frac{\pi}{2}$, π and $\frac{3\pi}{2}$ radians from the base when the edge length was 2π.

The variation in area could be estimated if the tissue area normal to the blood flow is quantified and plotted along the flow-axis. Accordingly, 'Specific Normal Area' (SNA) as a term was defined as the ratio of area of tissue slice and the total cross-sectional area (which is a square in these cases). The SNA for Schwarz Diamond and gyroid was plotted for 50% and 80% structural porosity (Figure 4.1-3) and it was observed that the SNA in 50% structures had lesser variation than the 80% structures.

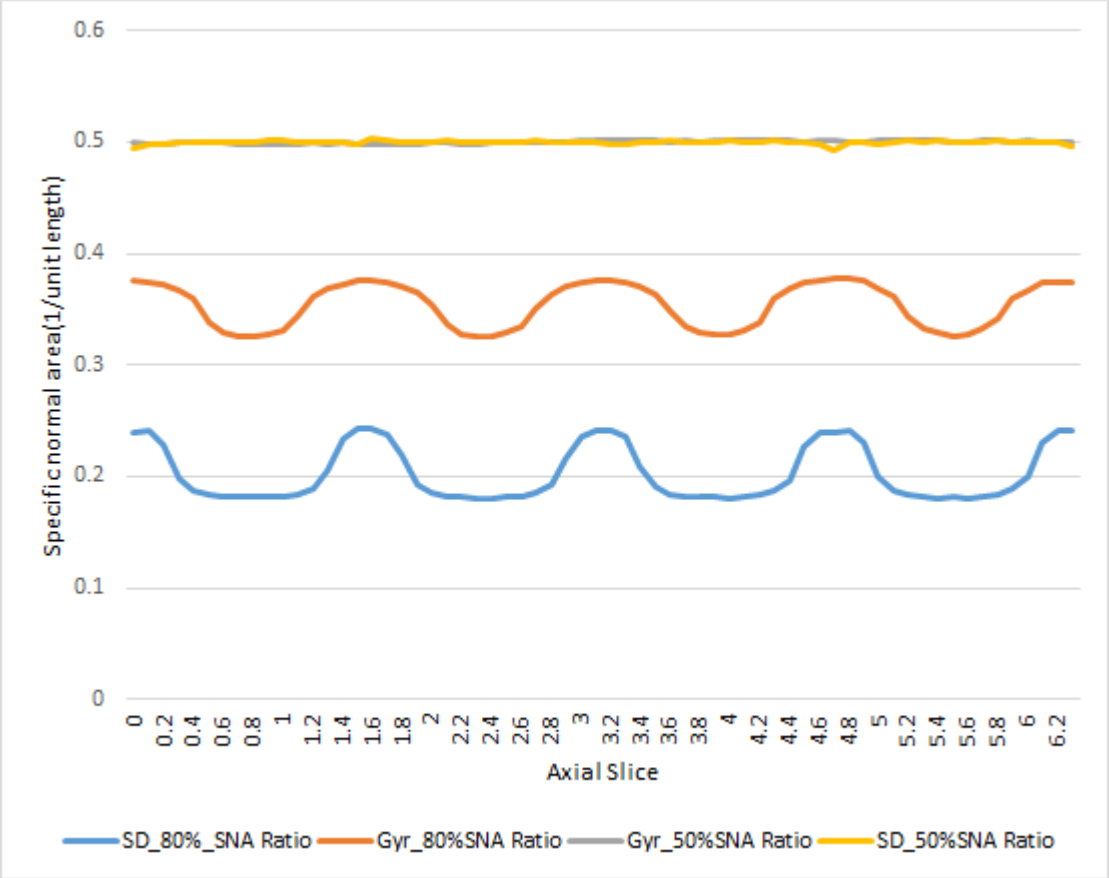

Figure 4.1-3: Specific normal area of Schwarz Diamond and Gyroid structures at 50% and 80% porosity.

In all the TPMS structures, scaffold thickness was assumed to vary proportionately with the volume occupied by the scaffold phase, as an approximation. For instance, a 60% porous Schwarz Diamond TPMS structure of 1 mm edge length, comprising of 20% tissue volume and 20% hydrogel volume was assumed to have 200 μm tissue and scaffold thickness. The hydrogel thickness was further assumed to be halved (100 μm), because the scaffold phase embeds the tissue on both sides in equal proportion as shown in Figure 4.1-4.

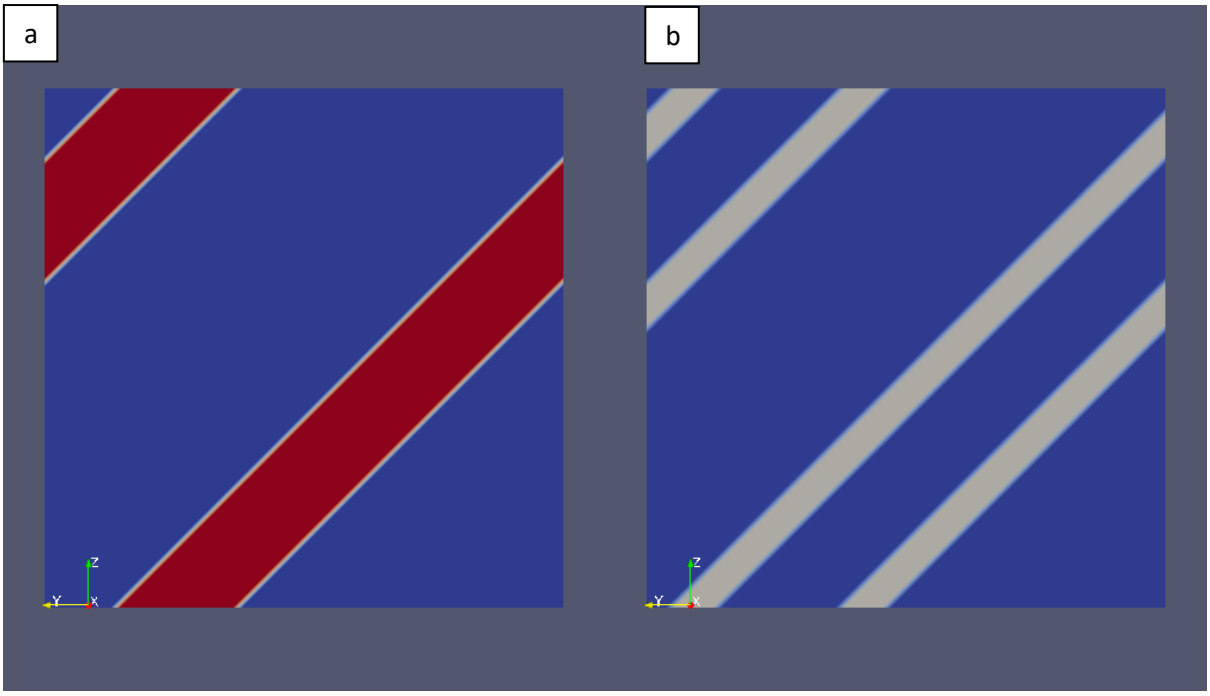

Figure 4.1-4: Thickness approximation in SD60% structure where a) Tissue (red) thickness is ~200 μm and void space (blue) thickness is ~600 μm. b) Hydrogel scaffold thickness is ~100μm.

This assumption on the scaffold thickness is relatively inaccurate as can be seen in the SNA of other TPMS structures (Figure 4.1-5). However, SNA and scaffold thickness were assumed to vary proportionately in all TPMS structures, to facilitate placing an approximate number on the TPMS phase thickness and for further analysis.

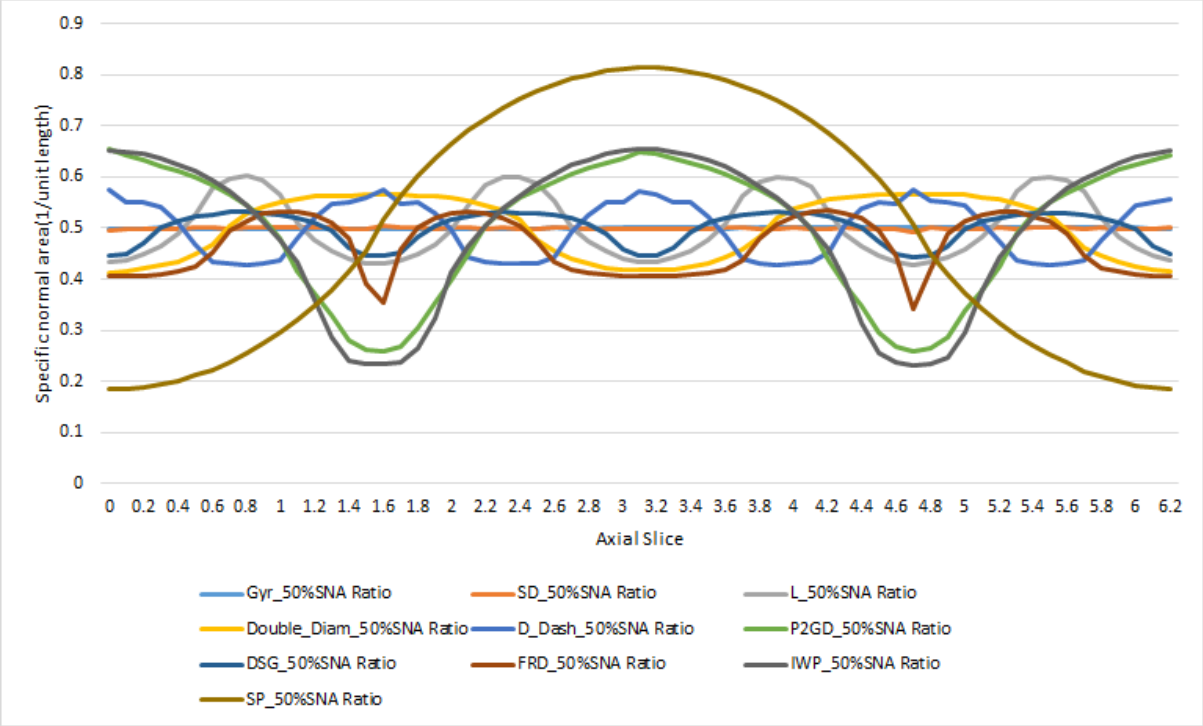

Figure 4.1-5: Specific normal area in TPMS structures at 50% porosity.

4.2. Effect of hydrogel layer thickness on tissue vascularization

The Schwarz Diamond structure was chosen as a case study to compare oxygen diffusion profiles in scaffolds at different porosities (60%, 75% and 80%), as indicated in Table 4.2-1. The tissue volume in all the cases was kept constant, while the hydrogel thickness was increased at the expense of perfusion space. The edge length of the TPMS unit scaffold was 1000 μm and by SNA analysis, the scaffold thickness in 5% and 20% hydrogel occupied volume was approximated as 25 μm and 100 μm respectively. This setup was conceptualized to quantify the effect of hydrogel scaffold thickness on axial O_2 concentration profiles, while keeping other parameters constant. The average oxygen concentration in the slices along the blood flow-axis was calculated and plotted as shown in Figure 4.2-1.

Table 4.2-1: Parameters used in Figure 4.2-1, Figure 4.2-2, Figure 4.2-3 and Figure 4.2-4, by varying the hydrogel thickness.

TPMS structure	Hydrogel wall thickness (μm)	Inlet oxygen concentration	Tissue (%)	Hydrogel/ Scaffold (%)	Blood/ Porosity (%)
SD_control	0	0.15 mM	20	0	80
SD_25	25	0.15 mM	20	5	75
SD_100	100	0.15 mM	20	20	60

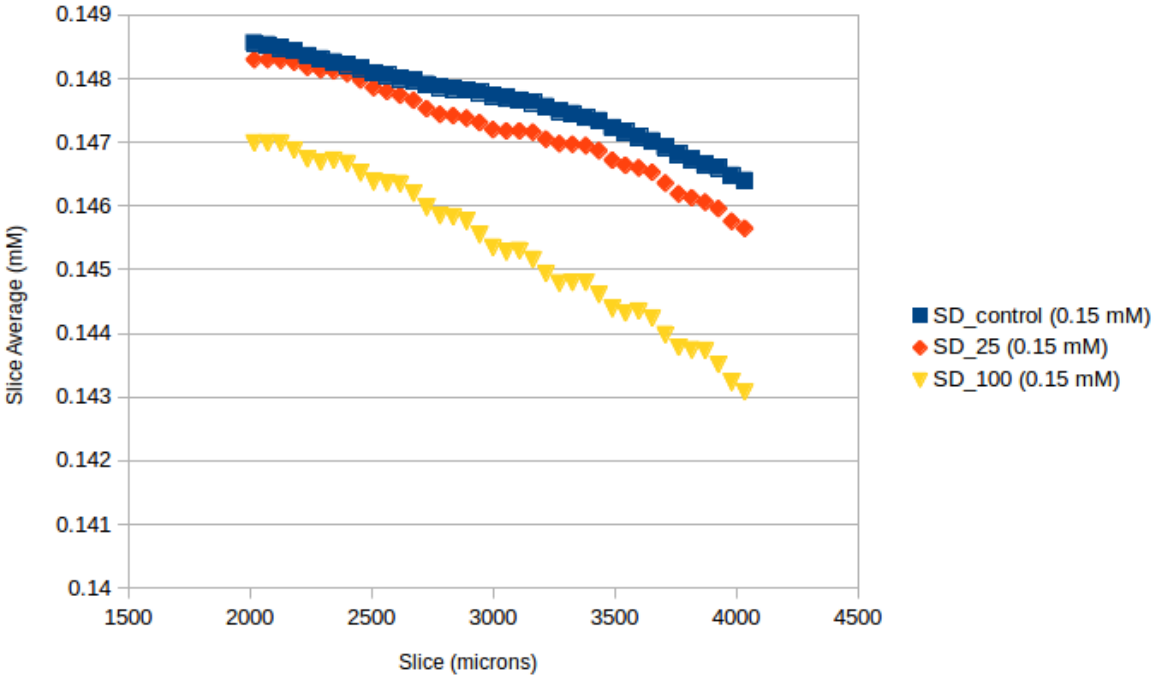

Figure 4.2-1: Average accumulated oxygen concentration in scaffold slices of thicknesses (0, 25, 100 µm) at 0.15mM inlet oxygen concentration.

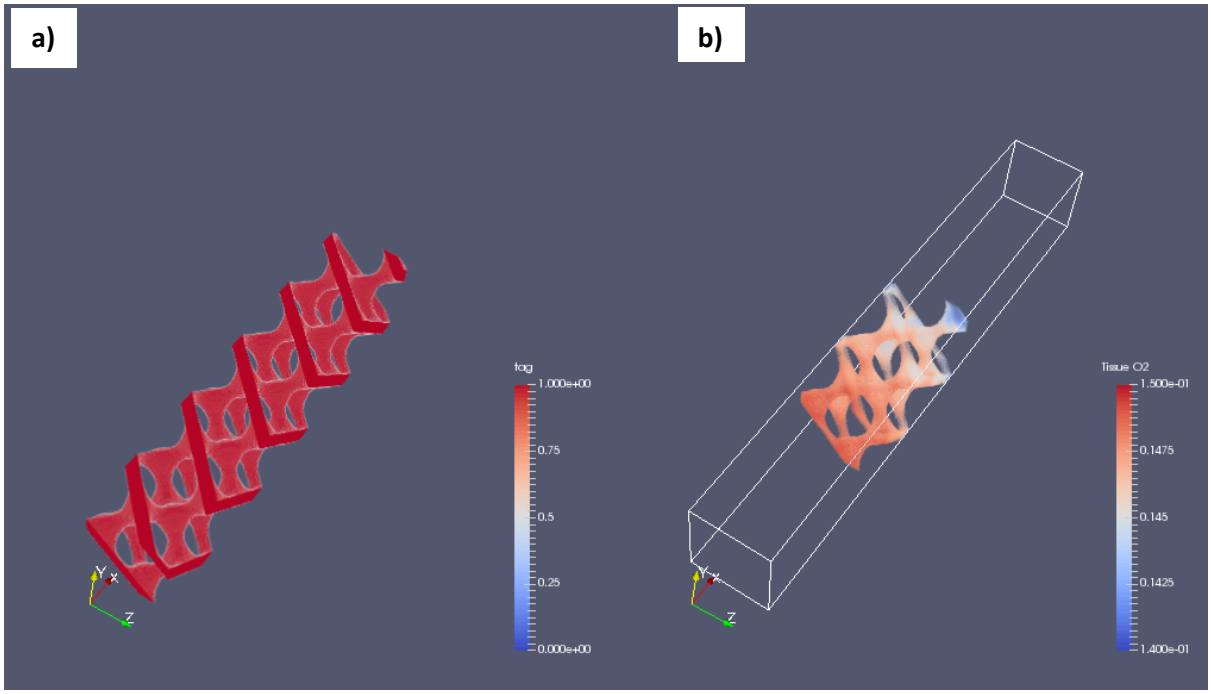

Figure 4.2-2: a) 80% porous Schwarz Diamond (no hydrogel scaffold). b) Corresponding 3D oxygen concentration map in tissue.

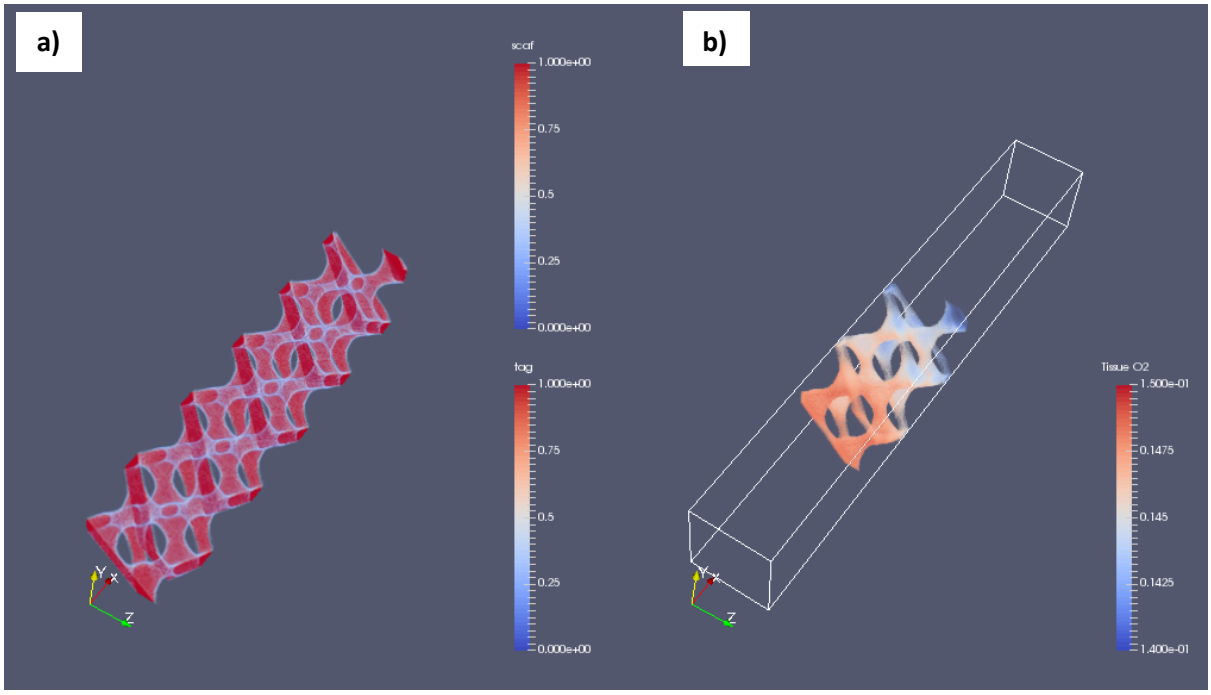

Figure 4.2-3: a) 75% porous Schwarz Diamond (20% tissue, 5% hydrogel scaffold). b) Corresponding 3D oxygen concentration map in tissue.

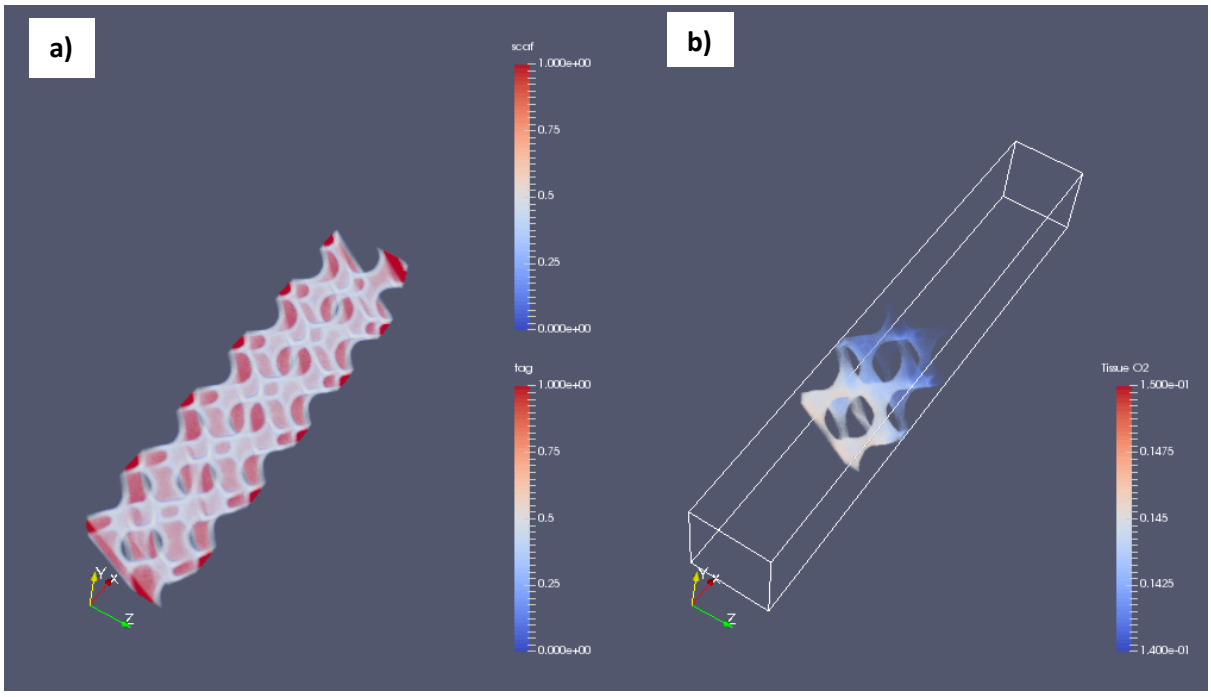

Figure 4.2-4: a) 60% porous Schwarz Diamond (20% tissue, 20% hydrogel scaffold). b) Corresponding 3D oxygen concentration map in tissue.

It was observed that the oxygen accumulation in tissues decreases as the scaffold thickness increases (Figure 4.2-1). To examine the effect of changing inlet O_2 concentration on

the axial concentration profiles, the inlet O_2 concentration was decreased progressively from 0.15 mM to 0.09525 mM and 0.0405 mM. It was found that the average oxygen accumulation in slices decreased with increasing hydrogel scaffold thickness irrespective of the inlet O_2 concentration (Figure 4.2-5 and Figure 4.2-6). These simulations were conducted on the scaffold geometries mentioned in Table 4.2-1, without changing the diffusion and consumption parameters[39].

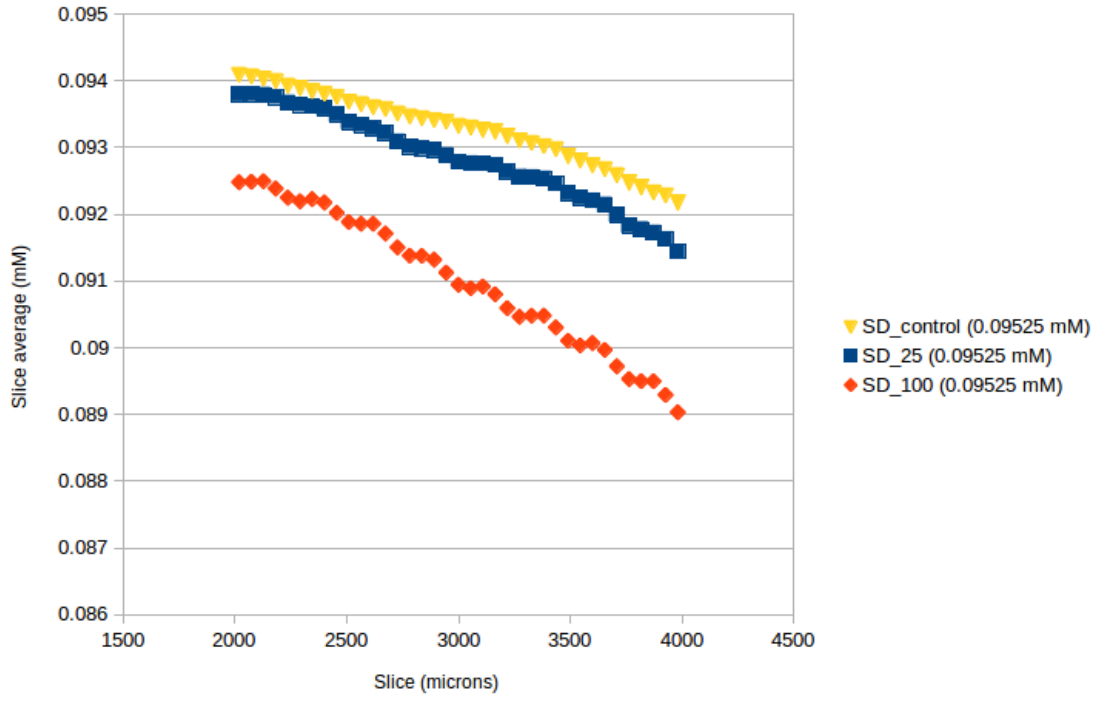

Figure 4.2-5: Average accumulated oxygen concentration in scaffold slices of thicknesses (0, 25, 100 µm) at 0.0925 mM inlet oxygen concentration.

[39] Oxygen diffusion coefficient in tissue = $2.1 \times 10^{-9} \frac{m^2}{s}$; Oxygen consumption rate in tissue = $0.0001 \frac{mM}{s}$

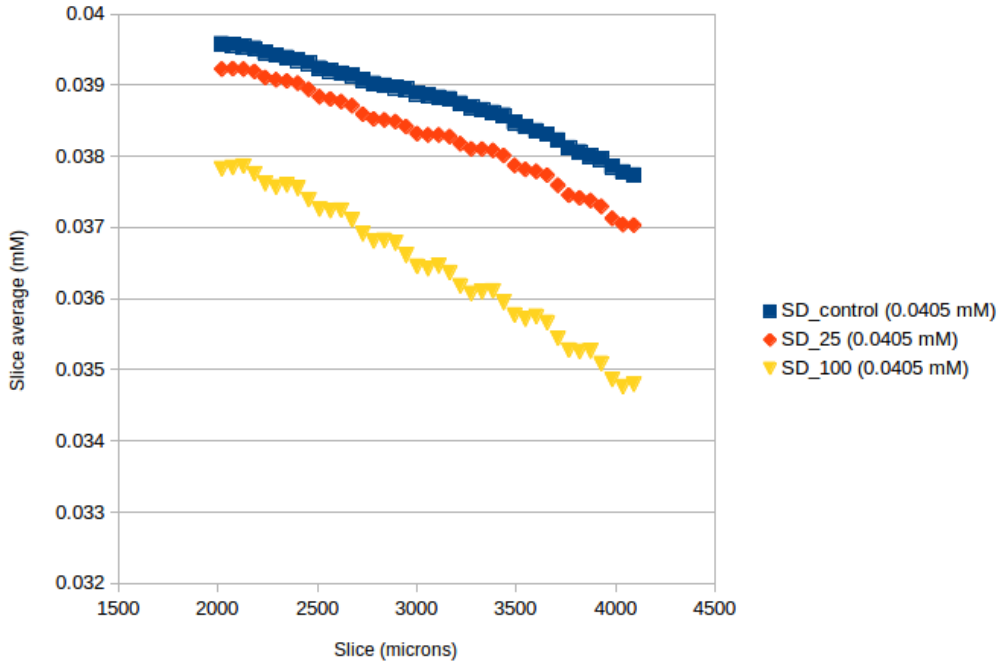

Figure 4.2-6: Average accumulated oxygen concentration in scaffold slices of thicknesses (0, 25, 100 µm) at 0.0405 mM inlet oxygen concentration.

4.3. Effect of oxygen diffusion coefficient on tissue vascularization

Figure 4.3-1 represents the average oxygen concentration along scaffold slices, when the oxygen diffusion coefficient in hydrogel is altered. The profiles correspond to a 100 μm hydrogel thickness embedding a 20% SD tissue by volume (Figure 4.2-4). The oxygen diffusion coefficient in hydrogel has been reported in literature as approximately around $1.9 \times 10^{-9}\, m^2 s^{-1}$ [144, 145]. The value of diffusion coefficient is likely to be different depending on the base material of hydrogel and its concentration. For investigative purpose, a range of oxygen diffusion coefficient values were tested, to observe its effect on tissue vascularization. The oxygen diffusion coefficient value was changed by an order of magnitude in both directions of its approximate value (i.e. $1.9 \times 10^{-8}\, m^2 s^{-1}$ and $1.9 \times 10^{-10}\, m^2 s^{-1}$). Subtle changes to the diffusion coefficient were also investigated ($1.8 \times 10^{-9}\, m^2 s^{-1}$ and $2.0 \times 10^{-9}\, m^2 s^{-1}$). The results indicated lesser oxygen accumulation in the slices as the oxygen diffusivity in scaffold decreases. The concentration profile of the case with least scaffold permeability ($1.9 \times 10^{-10}\, m^2 s^{-1}$) is analogous to Figure 3.15-3 where the oxygen diffusion in tissue was disabled and both these graphs have similarity in terms of exaggerated fluctuations. Some of the diffusivity values tested were hypothetical for instance, $1.9 \times 10^{-8}\, m^2\, s^{-1}$ is an unlikely diffusivity value, because it implies oxygen diffusivity in hydrogel scaffold is higher than blood ($2.1 \times 10^{-9}\, m^2 s^{-1}$). This model therefore has an

advantage in terms of providing a numerical method to test oxygen concentration profiles at critical and extreme diffusivity values and to correlate oxygenation gain with scaffold permeation properties. Consequently, it is possible to foresee the extent of tissue oxygenation based on the physical and chemical properties of the synthesized scaffold.

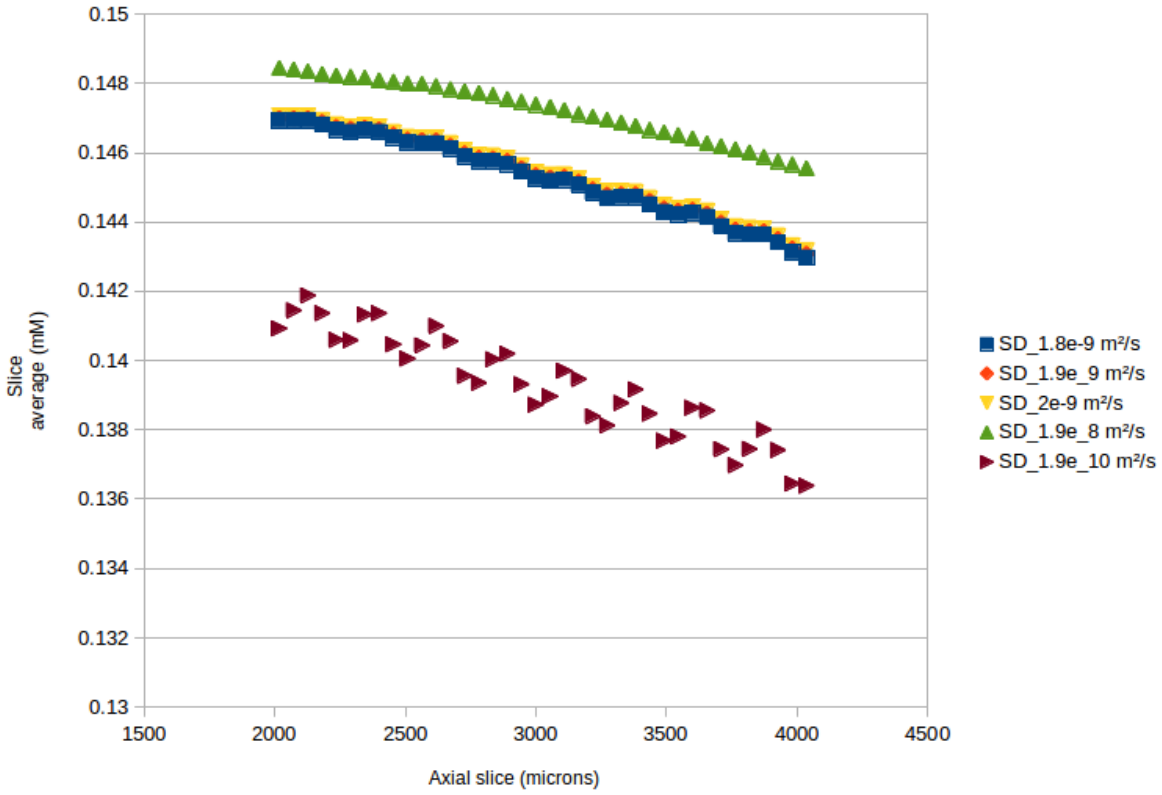

Figure 4.3-1: Average oxygen concentration in Schwarz Diamond slices at different hydrogel diffusivity values ($1.8 \times 10^{-9}\ m^2s^{-1}$, $1.9 \times 10^{-9}\ m^2s^{-1}$, $2 \times 10^{-9}\ m^2s^{-1}$, $1.9 \times 10^{-8}\ m^2s^{-1}$, $1.9 \times 10^{-10}\ m^2s^{-1}$).

Figure 4.3-2 represents the transversal concentration map at a slice 2000 μm ahead from the blood entry point. The concentration map shows the diminishing presence of oxygen in the tissue as the oxygen diffusivity in tissue decreases.

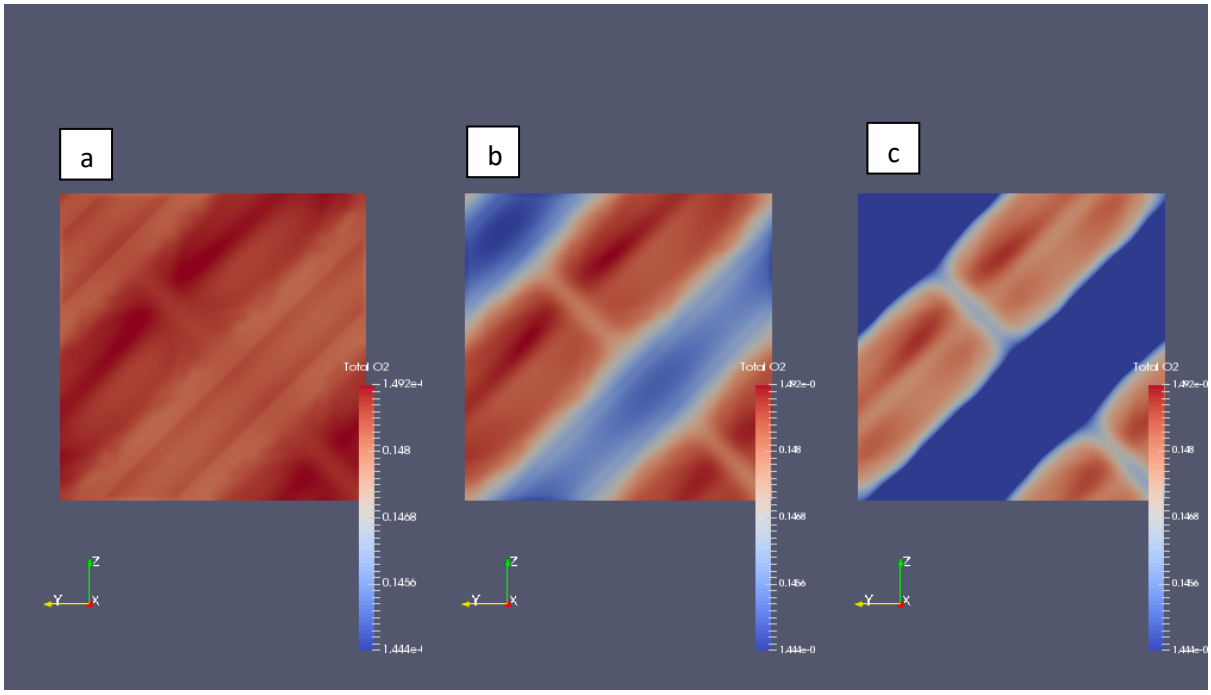

Figure 4.3-2: Concentration map at the 2000 μm slice with oxygen diffusivity of a) $1.9 \times 10^{-8}\ m^2 s^{-1}$ b) $1.9 \times 10^{-9}\ m^2 s^{-1}$ and c) $1.9 \times 10^{-10}\ m^2 s^{-1}$, when oxygenated blood is perfusing into the plane (x-direction)

4.4. Shape of oxygen concentration profiles in axial direction of tissue scaffold

To understand the nature of oxygen concentration profiles along the length of a scaffold, a 60% porous Schwarz Diamond (SD60%) comprising of 20% tissue and 20% hydrogel scaffold was considered as a case-study (Figure 4.2-4). Simulations were performed by sequentially decreasing the perfused inlet oxygen concentration, and the average concentration in the slices was analysed at steady state. This experiment was intended to simulate and understand concentration profiles in smaller scaffold segments, which are samples/subsets of a large scaffold. This is in light of the fact that oxygen concentration along the scaffold length decreases, and therefore, lesser perfused inlet oxygen concentration is representative of posterior ends of the scaffolds. This was considered necessary because simulating blood flow through a large scaffold (spanning centimetres) was an impractical computational task. The inlet O_2 concentrations perfused through the SD60% scaffold are 0.15 mM which was considered as a high concentration (Figure 4.4-1), 0.09525 mM that was considered as a low concentration (Figure 4.4-2) and 0.0405 mM which represented a further low concentration (Figure 4.4-3). Linear curve fitting was done on the data points representing slice average O_2 concentrations as shown in the figures. The fitted linear curve was also examined in the bounds of 95% confidence interval [146].

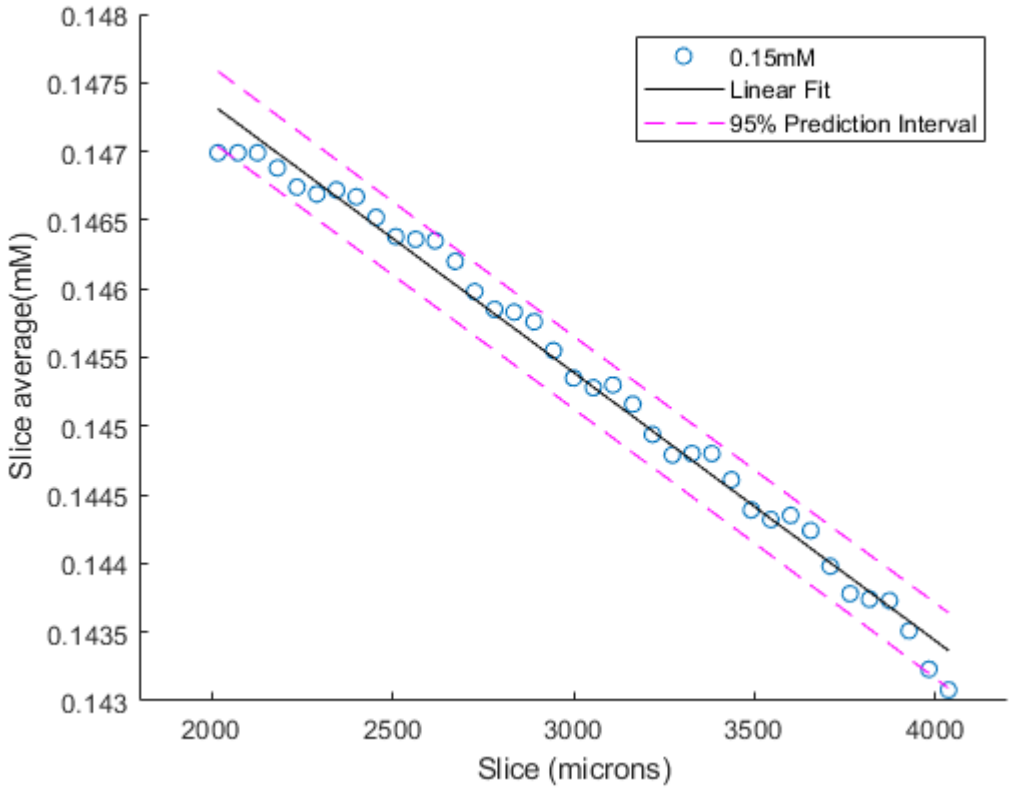

Figure 4.4-1: Average accumulated oxygen concentration in scaffold slices (SD60% 100μm hydrogel thick) when the perfused oxygen concentration is 0.15 mM.

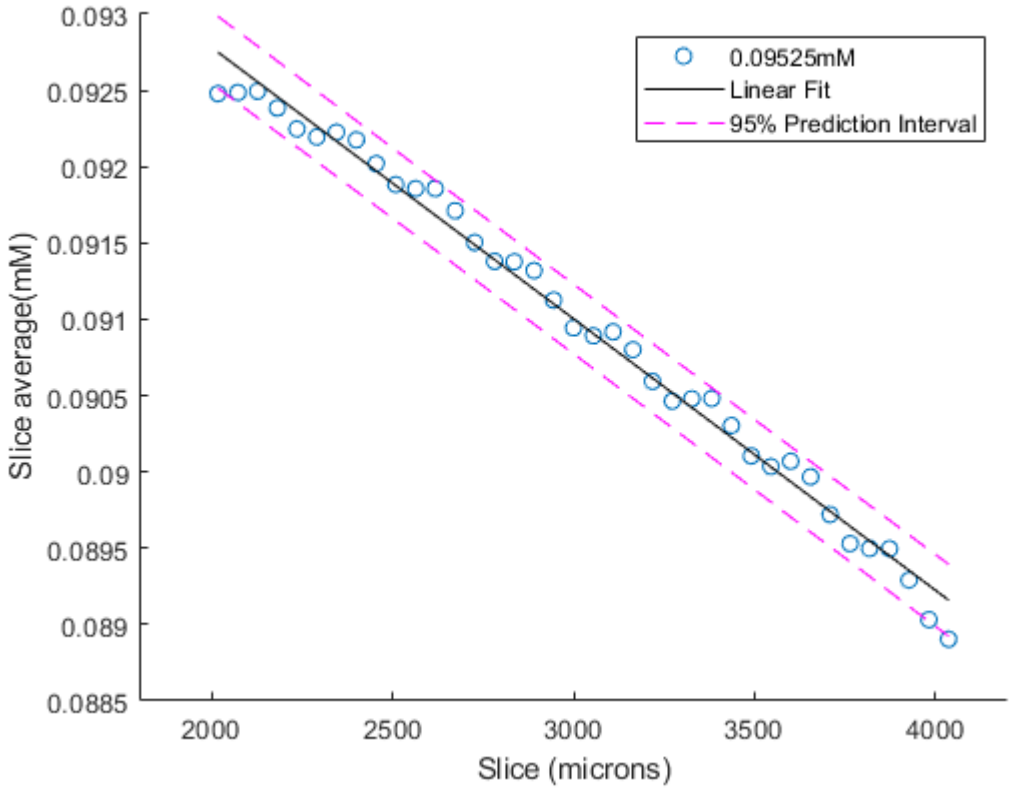

Figure 4.4-2: Average accumulated oxygen concentration in scaffold slices (SD60% 100μm hydrogel thick) when the perfused oxygen concentration is 0.09525 mM.

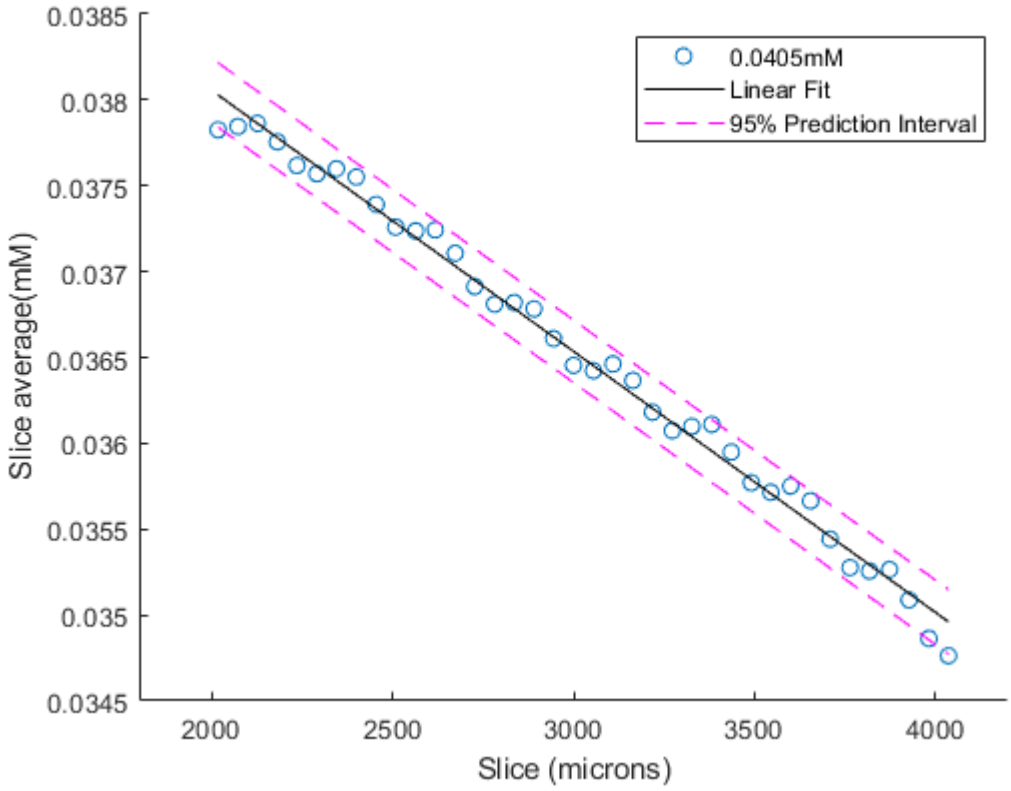

Figure 4.4-3: Average accumulated oxygen concentration in scaffold slices (SD60% 100μm hydrogel thick) when the perfused oxygen concentration is 0.0405 mM.

Subsequently, the slope of the fitted curve was calculated and plotted against perfused oxygen concentration values as shown in Figure 4.4-4. The data points correspond to the slope of the curves estimated in Figure 4.4-1, Figure 4.4-2 and Figure 4.4-3.

It was noticed in Figure 4.4-4, that the slope of the fitted curve was negative and the slope was found to increase (become less negative) with decreasing perfused oxygen concentration. These gradient values indicate that the oxygen concentration profiles in a tissue scaffold are concave upward or decay in an exponential fashion (Figure 4.4-5). This result corresponds well with the anticipated decrease in axial oxygen concentration profiles discussed in chapter 3 (Section 3.16). Such a concentration decline pattern was also previously established in the axial direction of capillaries [147] and it is an interesting coincidence to observe this pattern in TPMS structures as well.

Figure 4.4-4 represents the whole scaffold length and proves that O_2 concentration will eventually extrapolate to zero, after a certain slice in the posterior scaffold region (because the slope was observed to tend towards zero). While Figure 4.4-4 indicates the shape of O_2 concentration profile along the scaffold, it is difficult to provide the precise scaffold slice at

which a particular O_2 concentration will occur. Therefore, the estimated gradient values are arbitrarily placed on an x-axis which has no length units (bottom), although appropriately mapped to the perfused inlet oxygen concentration shown on the secondary x-axis (top).

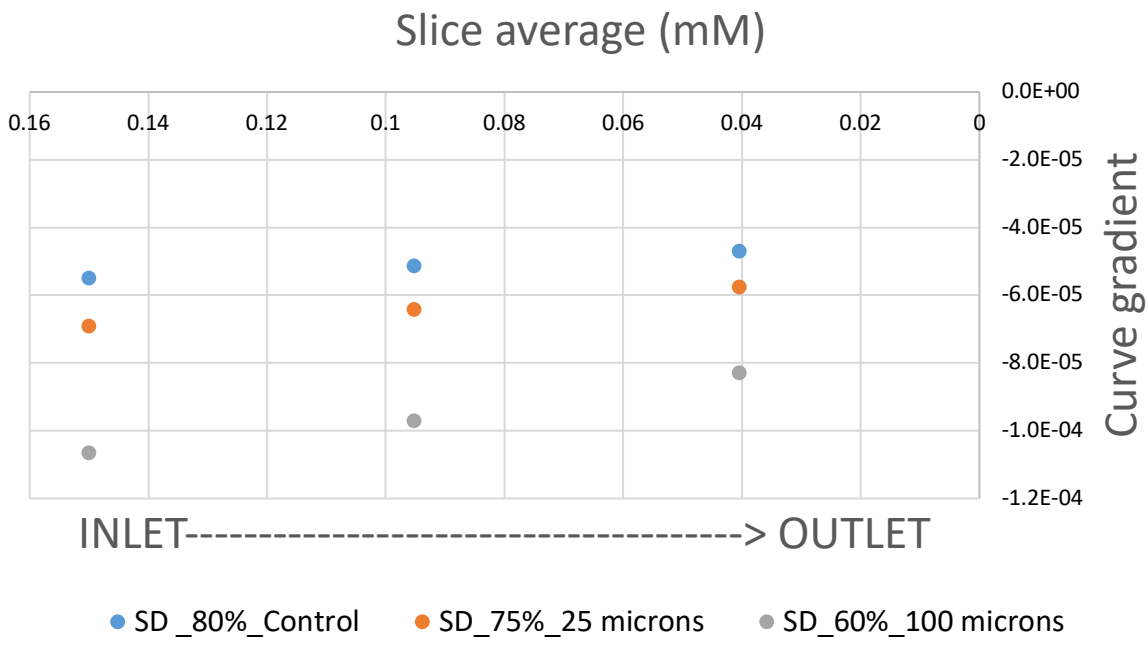

Figure 4.4-4: Estimated gradient of oxygen concentration profiles at different locations in Schwarz Diamond scaffold, with changing inlet concentrations and at different structural porosities (varying hydrogel thickness but constant tissue volume of 20%).

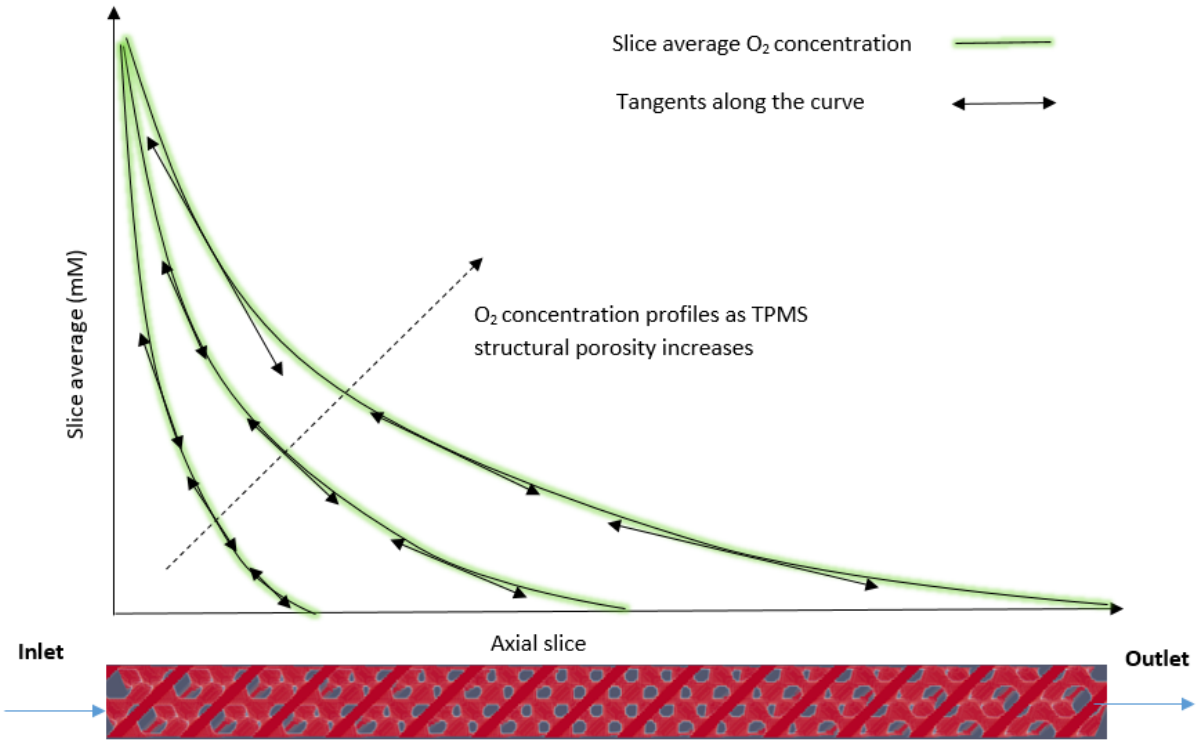

Figure 4.4-5: Illustration of concave nature of oxygen concentration profiles along the TPMS scaffold.

Figure 4.4-4 also shows that as porosity increases in Schwarz Diamond from 60% to 80%, the slope becomes less negative. This aspect is illustrated in Figure 4.4-5 where the slice average O_2 concentrations are positive over a longer scaffold length, as TPMS porosity increases.

4.5. Estimated tissue survival lengths in TPMS structures

The next endeavour was to obtain a crude estimate of the possible length over which oxygen concentration remains positive. This length was defined as 'survival length' given the fact that cells survive only in regions where there is a minimum threshold O_2 concentration. The threshold concentration was defined as the minimum perfusion O_2 concentration necessary to avoid development of anoxic regions in the radial or transverse direction. The threshold concentration was identified by trial and error by reducing the perfusion concentration repeatedly by small amounts. It was observed that when the perfused inlet O_2 concentration was reduced to 0.005 mM, anoxic regions developed in the tissue-scaffold system at steady state (Appendix H).

Next, linear extrapolation was done between the upper limit of perfused O_2 concentration (0.15 mM) and the minimum threshold concentration (0.005 mM), using the slopes estimated in Figure 4.4-1, Figure 4.4-2 and Figure 4.4-3 (Appendix G). Extrapolation

on either sides with three different slopes for the same scaffold gave three estimates of survival length as shown in Figure 4.5-1. It was observed in the figure that the extrapolated survival length increases, when estimated with the slope of the case with lower perfused oxygen concentration. This finding reemphasizes the concave upward nature of oxygen concentration profiles in TPMS scaffolds (Figure 4.4-5). The estimates of tissue survival length for different perfused O_2 concentrations are different, because the gradient values with which linear extrapolations were done are different. Concave curves have different estimates of instantaneous slope depending on the point at which the tangent is drawn. However, to attribute a single slope value to scaffolds and to allow performance comparison between them, the survival length estimate with the maximum perfused oxygen concentration (0.15mM) was considered as the benchmark. This was envisaged because the extrapolated length with 0.15 mM was a conservative estimate and also because 0.15mM is the concentration that is typically found in blood plasma at the arterial discharge end [148, 149]. However, the flipside with this extrapolation approach is that it underestimates the real survival length of a tissue and it overlooks the concave concentration profile (Figure 4.5-2).

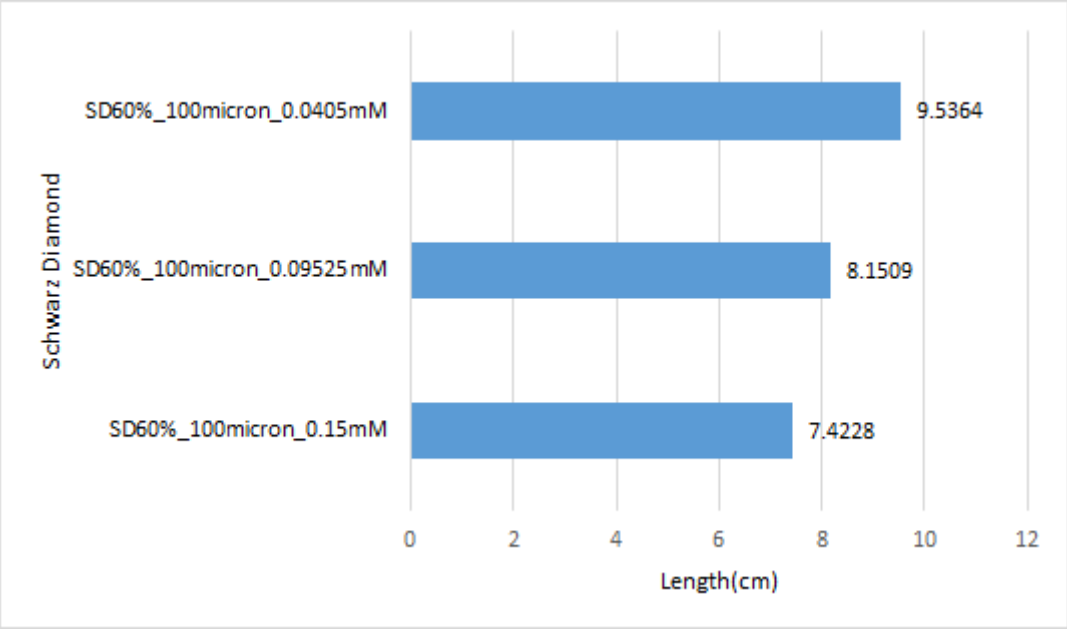

Figure 4.5-1: Estimated survival length in Schwarz Diamond structure with 100 μm thick hydrogel, at different inlet oxygen concentrations: 0.15 mM concentration case (SD60%_100micron_0.15mM), 0.09525 mM concentration case (SD60%_100micron_0.09525mM) and 0.0405 mM concentration (SD60%_100micron_0.0405mM).

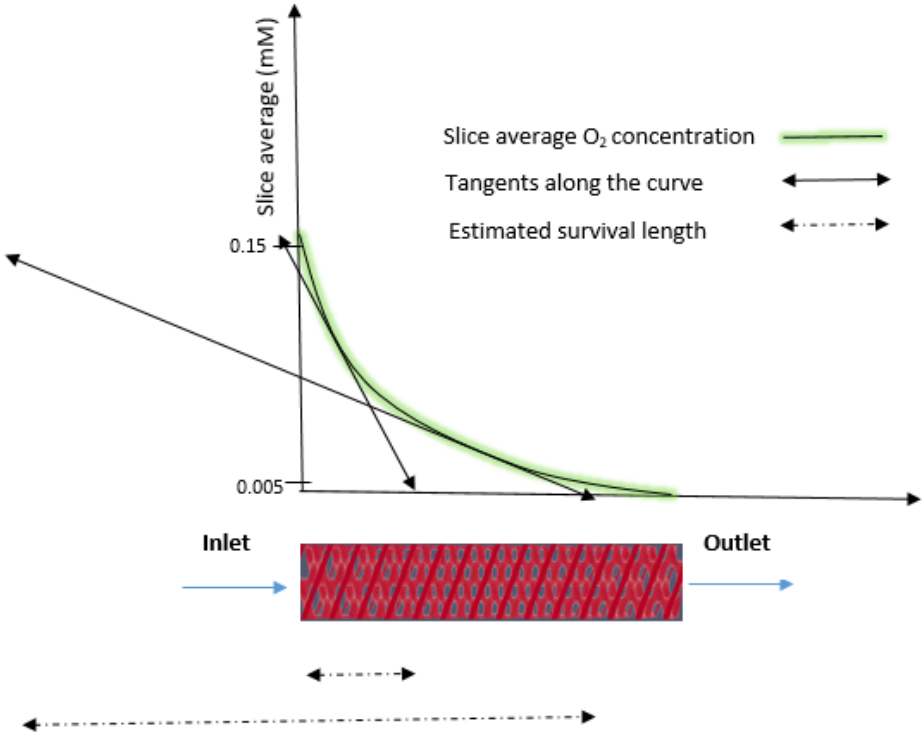

Figure 4.5-2: Estimated survival length when extrapolated between the upper limit (0.15 mM) and lower limit (0.005 mM) with different slope values.

This methodology was repeated on test cases with varying hydrogel scaffold thickness, where the survival length estimate with a 100 μm hydrogel (SD60% Figure 4.2-4) was compared to a control case with no hydrogel (SD80% Figure 4.2-2) and the case with 25 μm thick hydrogel (SD75% Figure 4.2-3). The slope estimates of these cases are shown in Figure 4.4-4 for the three different perfused O_2 oxygen concentrations (0.15 mM, 0.09525 mM and 0.0405 mM). The survival length estimates for these cases are shown in Figure 4.5-3, and it was found that the estimated surviving length was ~7.4cm in SD60% case, ~11.4 cm in SD75% case and ~14.4 cm in SD80% case. While there is no equivalent number in literature to compare the survival length estimates given the novelty of this study, these estimates were found to increase with increasing porosity as was anticipated. This is because as porosity increases, there is less hindrance to mass transfer and oxygen is transported over longer distances in the axial direction, and also presence of lesser volume of tissue implied relatively lesser oxygen demand which pushed up the survival length estimates.

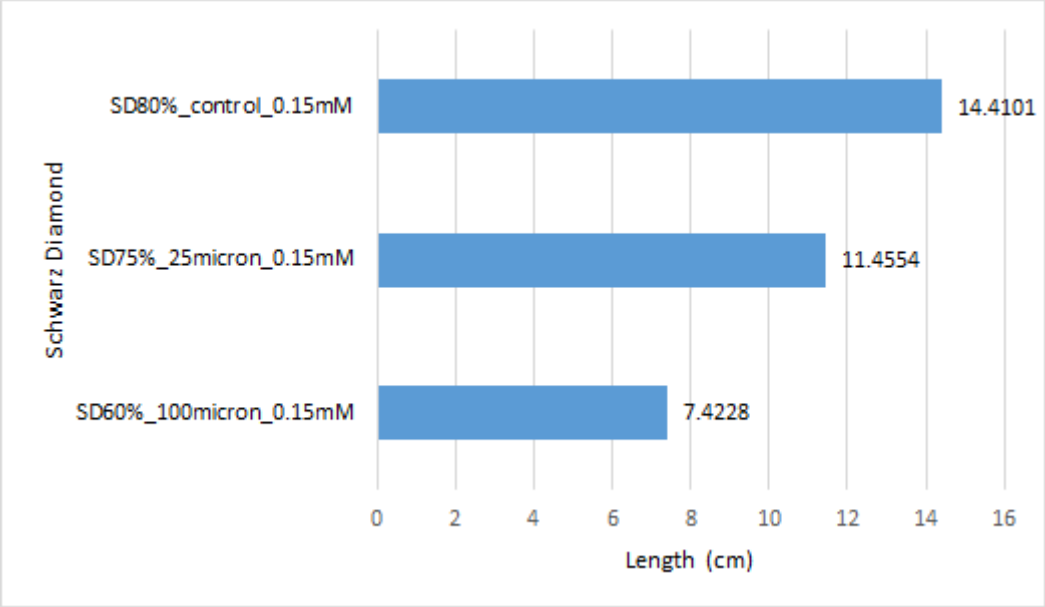

Figure 4.5-3: Estimated survival length in Schwarz Diamond structure at different porosities: 25 micron hydrogel thickness case (SD75%_25micron_0.15mM), 100 micron hydrogel thickness case (SD60%_100micron_0.15mM) and control/no hydrogel (SD80%_control_0.15mM).

Similar analysis was performed on different TPMS structures with varying porosities as shown in Figure 4.5-4. Schwarz Diamond and Double Schoen Gyroid were modelled at 30% porosity such that tissue occupied 50% volume and void space occupied 20%. Gyroid, Lidinoid and Schwarz Diamond structures were modelled as 60% porous structures, such that tissue and hydrogel occupied 20% volumetric space each. The estimated gradients at different perfused O_2 oxygen concentrations also confirm the exponential decay nature of oxygen concentration profiles in these TPMS scaffolds. The slopes of the encircled data points were used for linear extrapolated between 0.15 mM and 0.005 mM, to estimate the tissue survival length (Figure 4.5-5). Figure 4.5-6 shows the estimated tissue survival lengths in these structures when the hydrogel wall thickness is 200 μm. These lengths were shorter than the estimated survival lengths of Figure 4.5-5, where the hydrogel wall thickness in TPMS structures was 100 μm. These findings confirm the decrease in tissue survival length due to increased wall thickness and resistance to O_2 diffusion.

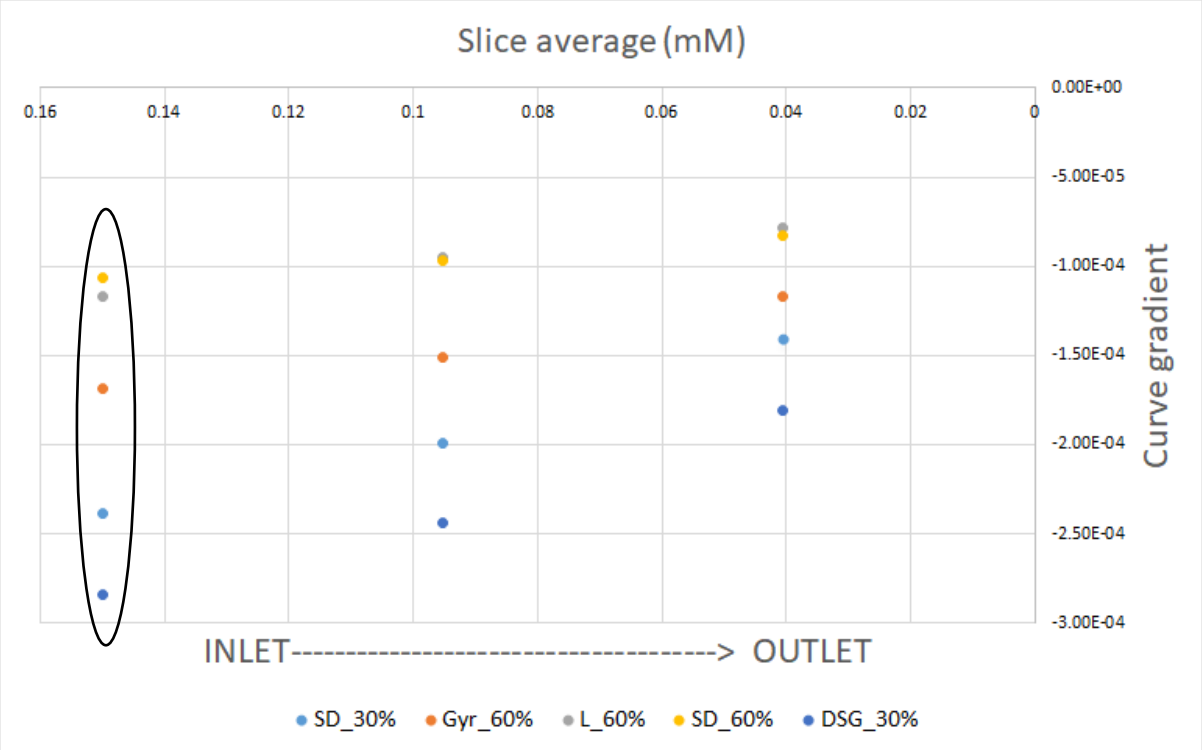

Figure 4.5-4 : Estimated gradient of oxygen concentration profiles at different locations in Schwarz Diamond scaffold, with changing inlet concentrations and different structural porosities (varying tissue volume but constant hydrogel thickness of 100 μm).

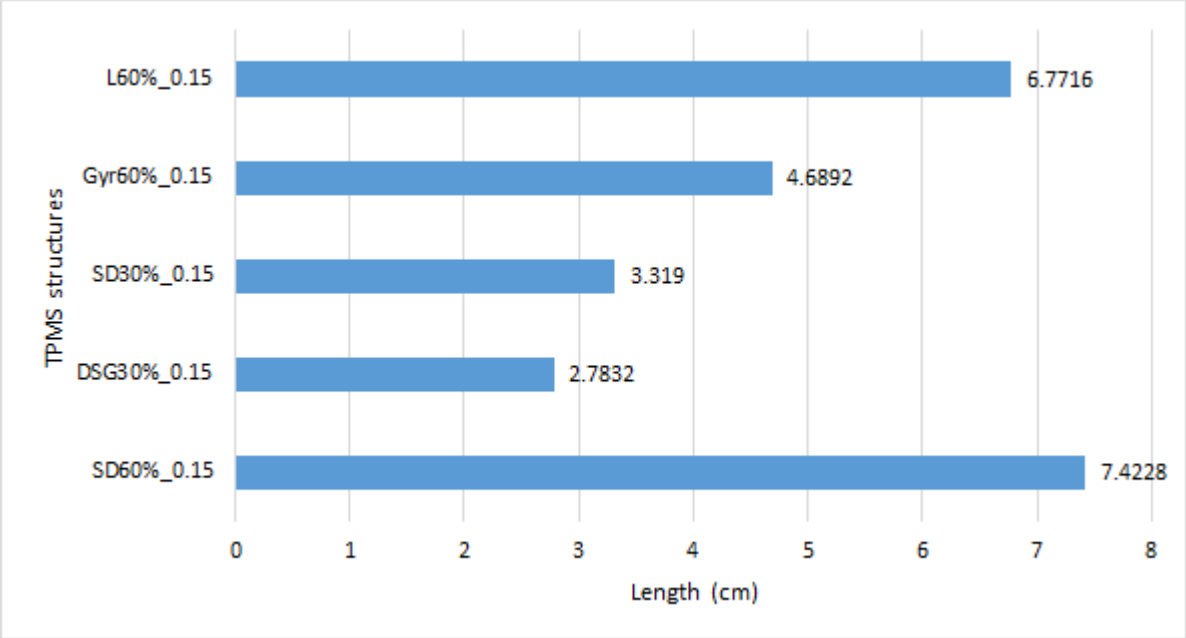

Figure 4.5-5: Estimated survival length of TPMS structures with 100 μm hydrogel wall thickness.

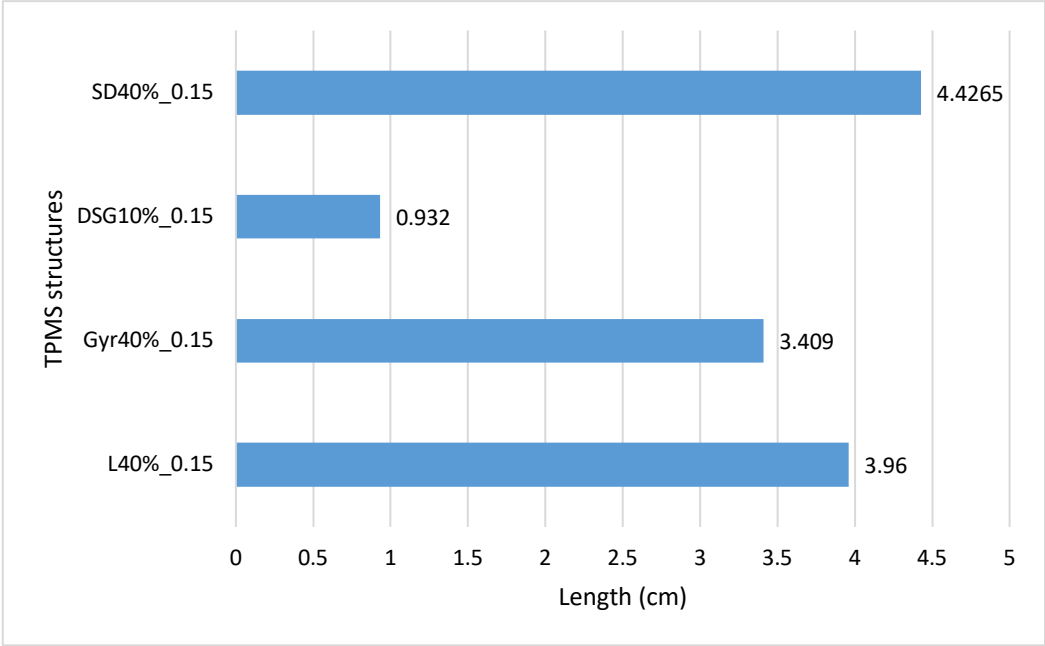

Figure 4.5-6: Estimated survival length of TPMS structures with 200 μm hydrogel wall thickness.

Figure 4.5-7 shows the accumulated oxygen concentration in Schwarz Diamond slices, where the volume occupied by phases are alternated between 30% and 40%. Typically, it is difficult to anticipate survival length in such cases where the volume occupied by phases are close in magnitude. In this regard, the LBM simulations can be used to populate a ternary diagram with survival lengths and that information can be used to interpolate the outcome with different combinations of tissue, hydrogel and porosity percentages. For instance, Figure 4.5-8

is a ternary plot showing the estimated tissue survival lengths of some cases represented in Figure 4.5-7. Representing tissue survival lengths as ternary plots is a novel representation in bioprinting science, which can be used to screen for survivable tissue scaffolds, prior to 3D printing them. These plots could potentially serve as a guiding map for biofabricators to guide manufacturing and experimental design with any scaffold shape and property.

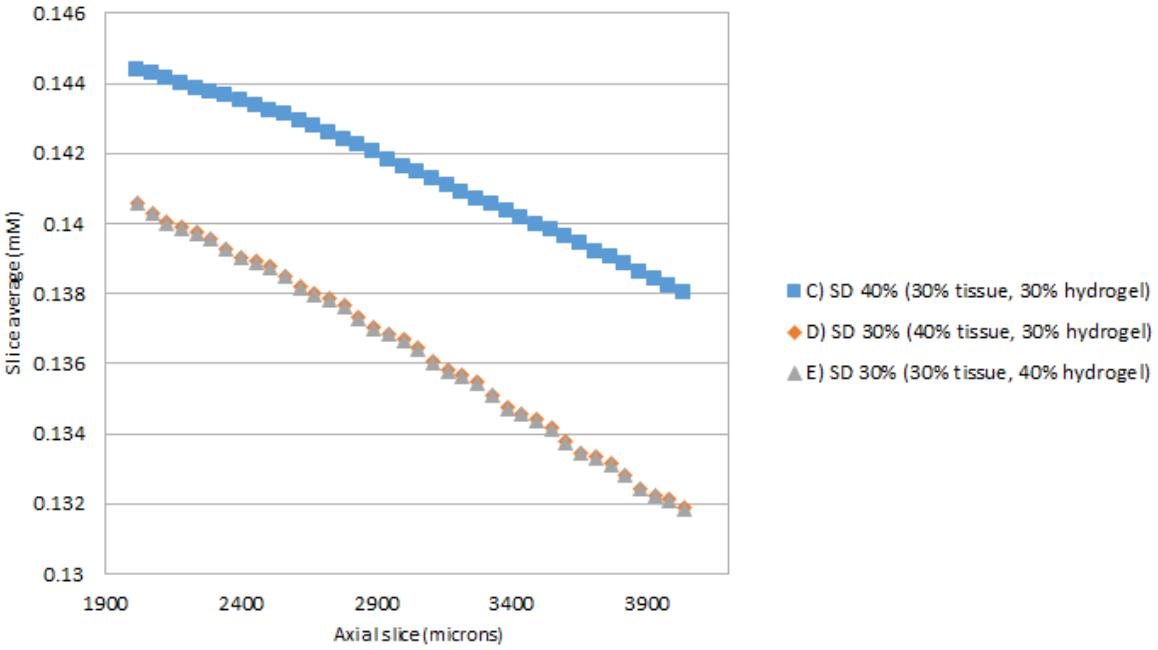

Figure 4.5-7: Average accumulated oxygen concentration in Schwarz Diamond scaffold slices.

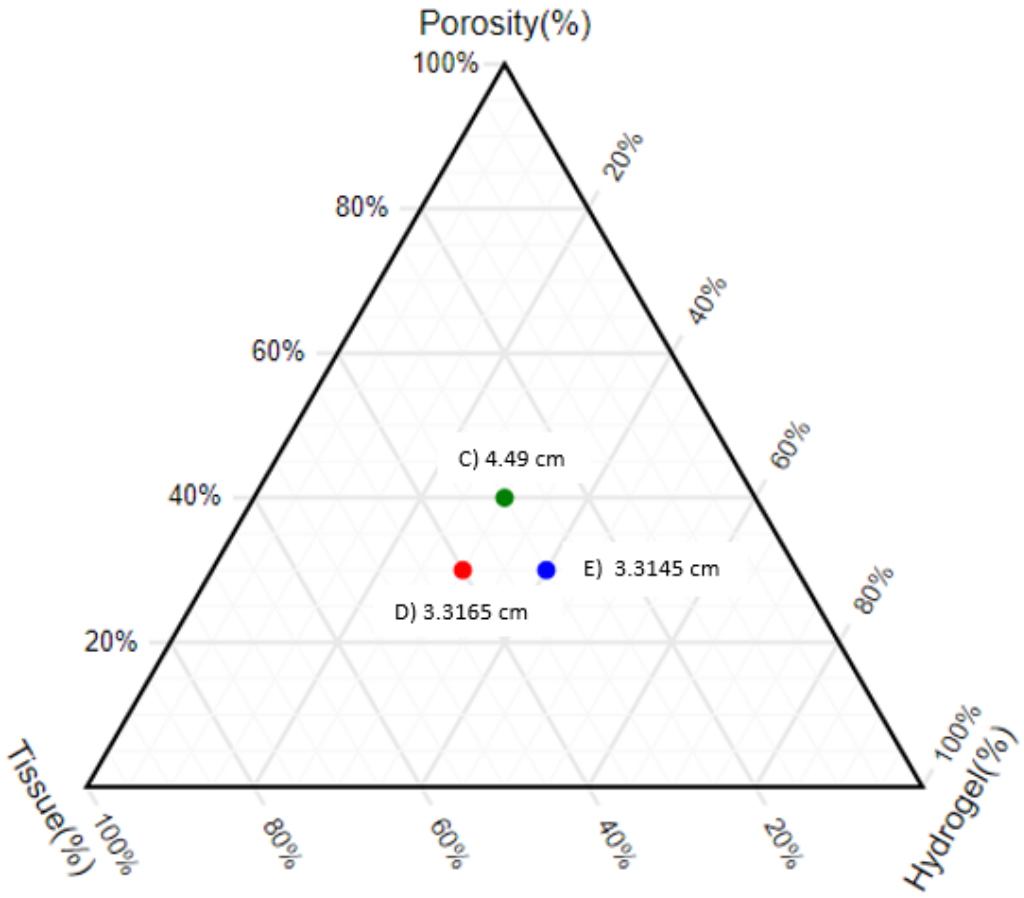

Figure 4.5-8: Estimated survival length in Schwarz Diamond structures of Figure 4.5-7

4.6. Summary

This chapter is an extension of the previous chapter that analyses oxygen concentration profiles in the periodic region of TPMS structures, ignoring data from two unit cells of the front and rear due to entrance and exit effects. In this chapter, TPMS hydrogel scaffolds of practical size are simulated (~100 - 200 μm), that are feasible to 3D print with the existing technology. The CFD simulations were also performed with parameters that are biologically relevant. The average oxygen concentration in scaffold slices was analysed with changing perfused concentrations and at different structural porosities at steady state.

Firstly, hydrogel layers were added on top of different TPMS shaped tissues and the oxygen accumulation in tissues was analysed by changing the O_2 permeability of hydrogel scaffolds. It was observed that accumulated oxygen varied depending on the hydrogel thickness and permeability. Thicker and resistive hydrogels minimized oxygen diffusion through hydrogel scaffolds, which led to a decrease in oxygen accumulation in tissue side. It was also

observed that there was no significant difference in the accumulated oxygen, if the O_2 diffusion coefficients in hydrogel were similar in magnitude. However, the axial O_2 concentration profiles were found to be sensitive to variation of diffusion coefficients by orders of magnitude.

SNA as a concept was defined in this chapter to examine how the cross-sectional area of TPMS structures was different between various slices. This exercise was undertaken to estimate the thickness of hydrogels in a given slice, which was found to vary across the slices. The SNA plots established that porosity and scaffold thickness vary proportionately only in gyroid and Schwarz Diamond TPMS structures, but not in the other TPMS structures. However, scaffold thickness was assumed to vary proportionately with the volume it occupied as an approximation.

As it was challenging to model a full-scale scaffold containing tissue and blood spanning centimetres, only segments of the large scaffold were analysed. This was done to get a qualitative idea about the shape and nature of O_2 concentration profiles. Next, the LBM simulations were conducted on the domain (length in millimetres), by decreasing the oxygen concentration in the perfusion source (blood). This was done to represent oxygen concentration profiles in a large scaffold, as it was computationally expensive to simulate a scaffold that measures centimetres. The O_2 concentration profiles in these segments was estimated at steady state and were fitted with a linear curve, and analysed in the limits of 95% confidence interval. The slopes of the fitted linear curves were calculated in different TPMS structures and at different perfusion concentrations. It was found that slopes increased (become less negative) as perfused oxygen concentration decreased. This proved the exponential decay nature of oxygen concentration profile along TPMS scaffolds. The estimated slopes on TPMS structures of different porosities, showed a steep decrease in slope with decreasing porosity, suggesting a sharp decline in oxygen concentration to zero along the scaffold.

'Survival length' as a concept was defined in this chapter, where extrapolation of the oxygen concentration curve was done between 0.15 mM (maximum concentration at the scaffold entrance) and 0.005 mM (minimum threshold concentration required to avoid anoxia in transverse direction). The linear extrapolation technique was envisaged to get an approximate length estimate over which the oxygen concentration profile shall remain above the anoxic limit to ensure cell viability. The survival length calculation for the case with maximum perfused oxygen concentration (0.15 mM) was taken as the reference simulation, because of its conservative estimate.

Table 4.6-1 summarizes TPMS scaffolds that are likely to be functional as predicted by the LBM model. All the survival length estimates of the tabulated TPMS structures are based on blood perfusion rate of 1 $mm\,s^{-1}$, carrying 0.15 mM oxygen. The porosity percentage indicated in the table comprises of the void space left after accounting for tissue and hydrogel.

Table 4.6-1: Sustainable TPMS scaffolds with blood perfusion rate of 1$mm\,s^{-1}$ carrying 0.15mM oxygen

TPMS structure	TPMS	Parameters	Survival length
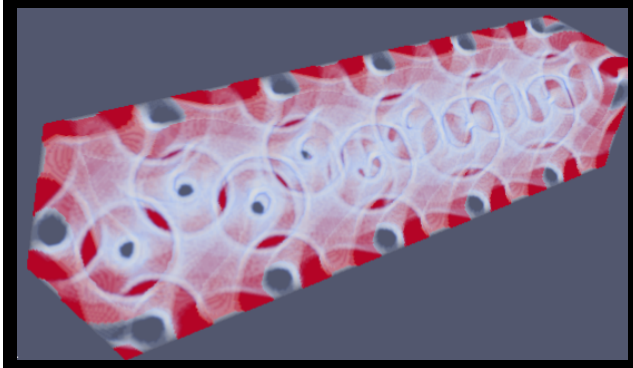	DSG	30% porous; 100 μm hydrogel. (20% hydrogel, 50% tissue)	2.7 cm
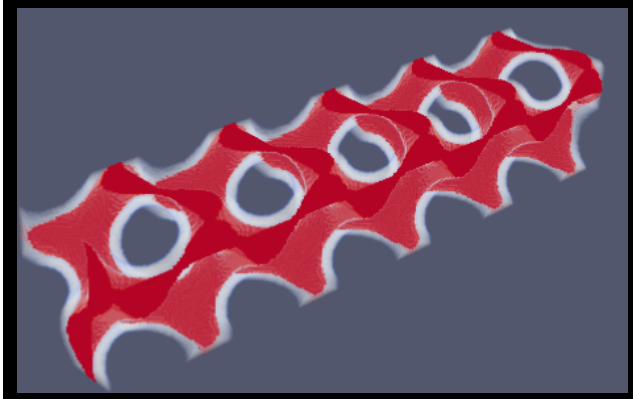	Gyroid	60% porous; 100 μm hydrogel. (20% hydrogel, 20% tissue)	4.6 cm
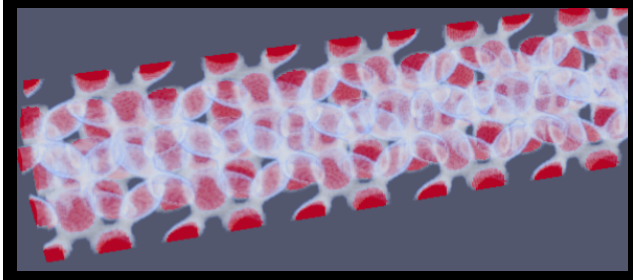	Lidinoid	60% porous; 100 μm hydrogel. (20% hydrogel, 20% tissue)	6.7 cm

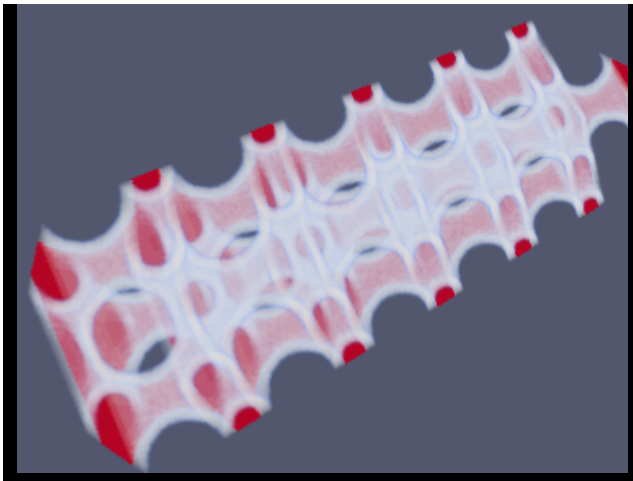	SD	60% porous; 100 μm hydrogel. (20% hydrogel, 20% tissue)	7.4 cm
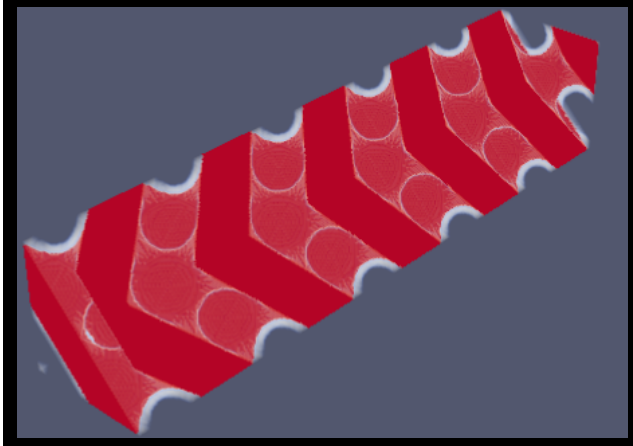	SD	30% porous; 100 μm hydrogel. (20% hydrogel, 50% tissue)	3.3 cm
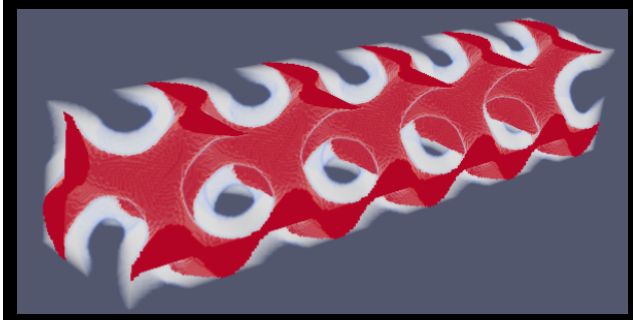	Gyroid	40% porous; 200 μm hydrogel. (40% hydrogel, 20% tissue)	3.4 cm
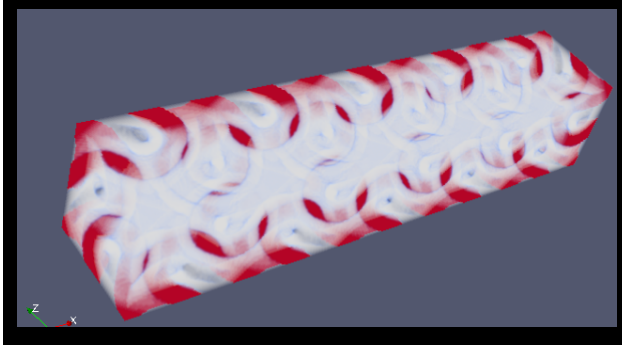	DSG	10% porous; 200 μm hydrogel. (40% hydrogel, 50% tissue)	0.93 cm

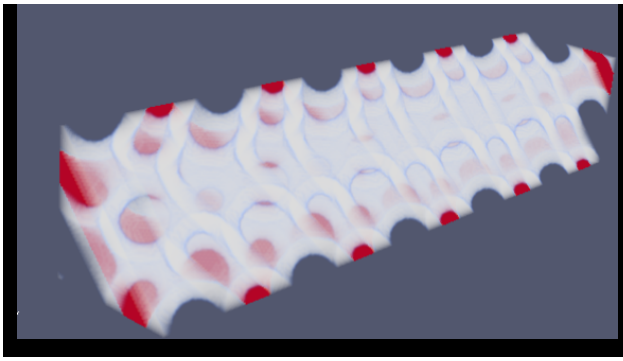	SD	40% porous; 200 μm hydrogel. (40% hydrogel, 20% tissue)	4.4 cm

5. Mass transfer efficiency in TPMS structures

5.1. Introduction

In this chapter, the mass transfer efficiency of TPMS structures is evaluated in terms of partition coefficient (P). Partition coefficient is a dimensionless number which quantifies the proportion in which a solute is distributed between phases [150]. In this chapter, the phases under consideration are blood and tissue, and P is calculated as the ratio of accumulated oxygen concentration in tissue to that of blood, at steady state (Equation [40]).

$$P = \frac{C_{tissue}}{C_{blood}} \quad [40]$$

First, the accumulated oxygen concentration is calculated as the average oxygen concentration in the blood and tissue slices respectively. The slices considered are in the periodic region of the TPMS scaffolds, where the exit and entrance effects are negligible. Next, the area under these curves was calculated by the trapezoidal rule of integration, integrating concentration values in the tissue/blood slices, along the scaffold length. Figure 5.1-1 shows the average blood/tissue oxygen concentrations in Schwarz Diamond slices at 50% porosity. For this analysis, 5 unit cells each measuring 200 μm were stacked back to back and exit lengths measuring 2 unit cells (~400 μm) were kept at the scaffold exit. Blood was perfused through the scaffold at 1 $mm\ s^{-1}$ carrying oxygenated blood at 0.15 mM concentration. The oxygen accumulation in the middle unit cells (3rd and 4th) between 400 and 800 μm was analysed at steady state.

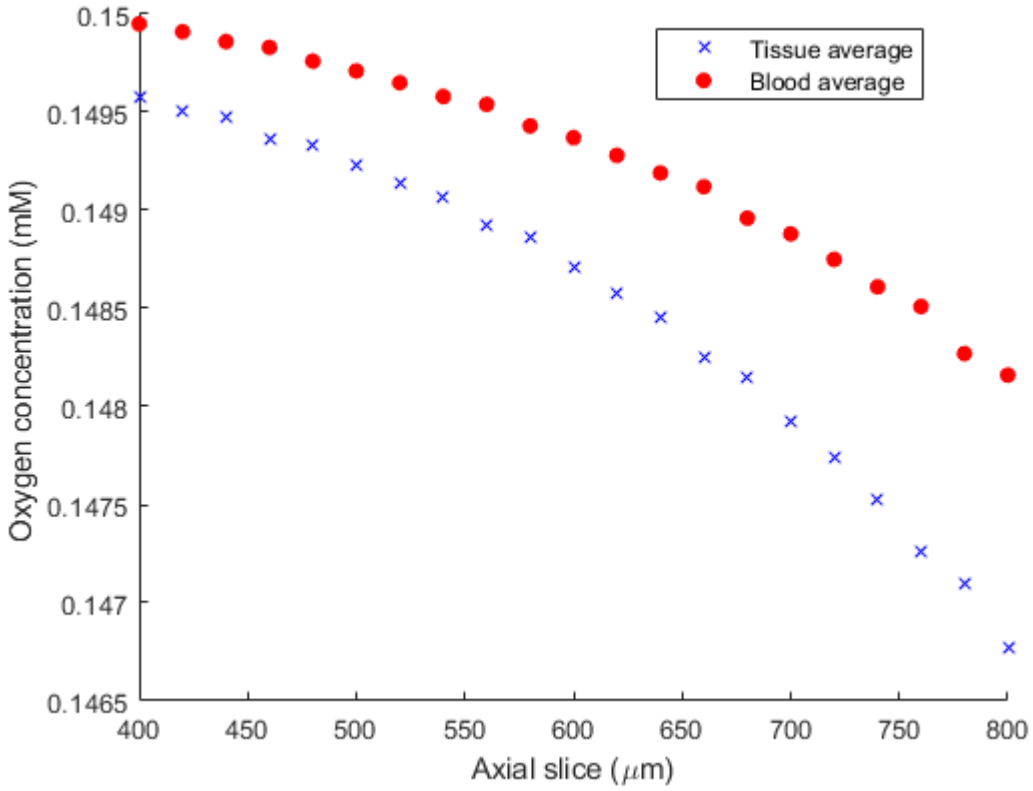

Figure 5.1-1: Average oxygen concentration in blood and tissue slices in 50% porous SD structure.

The TPMS structures shown on the x-axis of Figure 5.1-2 were perfused with a superficial flow velocity of 1 $mm\ s^{-1}$, and their partition coefficient was evaluated and ranked. Appendix F shows the average oxygen concentration in tissue and blood slices of the other TPMS structures, for which the partition coefficient was quantified. The percentage value suffixed at the end of the structures indicate the structural porosity of the structure. For instance, L_80% stands for a Lidinoid that is 80% porous containing 20% tissue by volume. The variation in oxygen accumulation in the middle TPMS unit cells arises due to difference in volumetric space occupied by tissue and blood cells, internal blood flow pattern, flow velocity and the interfacial area. While the P value was found comparable among all the analysed TPMS structures, it is a reasonable assertion that a relatively higher partition coefficient indicates a structure that favours higher oxygen accumulation in tissue over blood.

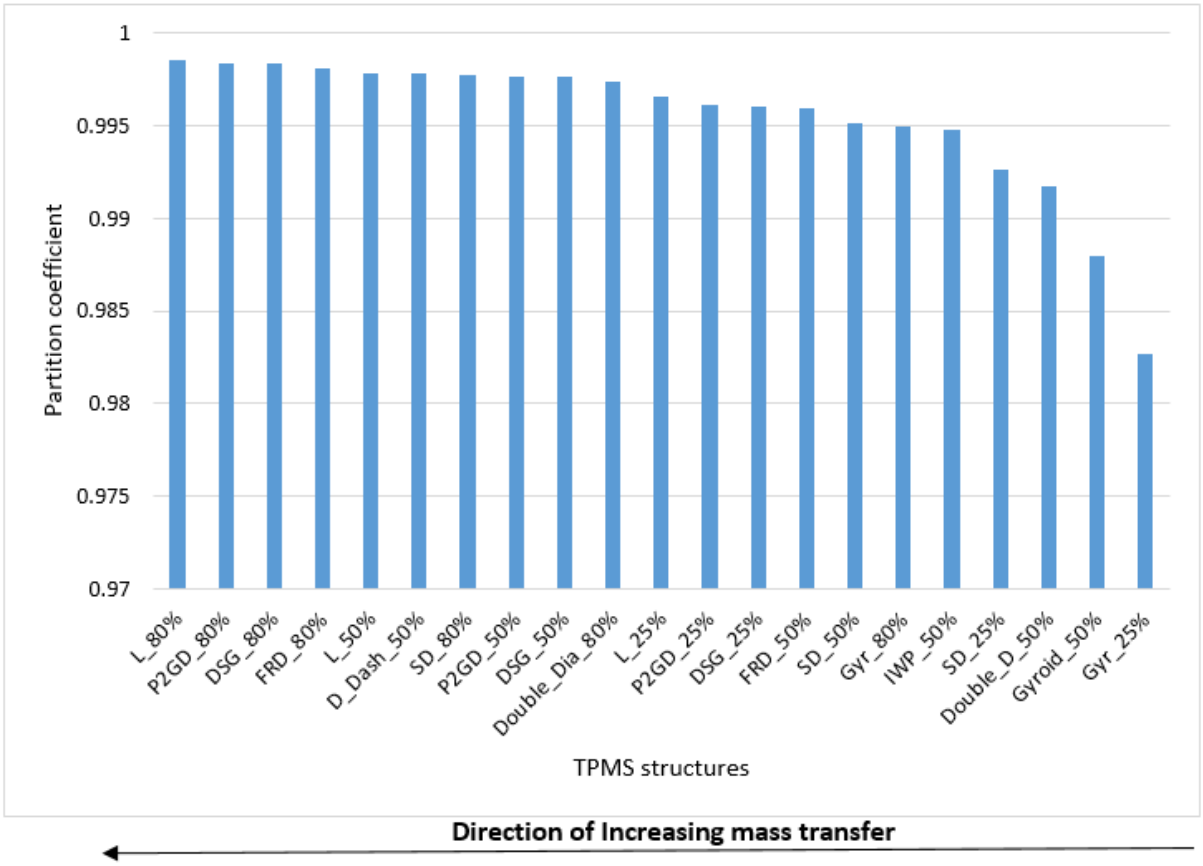

Figure 5.1-2: TPMS structure ranking according to partition coefficient at different porosities.

It was found that more porous structures were generally associated with higher partition coefficient (Figure 5.1-2). The difference in P could occur due to various reasons, for instance: more porous structures have lesser tissue percentage in a given volume, which means lower O_2 consumption per unit volume and therefore higher accumulation of oxygen in the tissue. Secondly, more porous structures also implies higher mass influx into the scaffold as the flow-rate would be higher in more porous structures. This is because the average cross-sectional area in more porous structures is large, while the superficial velocity[40] is constant across all the structures. Thirdly, there is no accumulation limit to oxygen in tissues, which means simulations proceed towards steady state possibly bypassing the maximum physiological limits of oxygen accumulation. There is insufficient literature data on the upper-limit to oxygen accumulation at the cellular level. In this thesis, however this limitation is overlooked because oxygen deficiency is the major identified problem to be overcome while 3D printing soft-tissues in the lab. In Figure 5.1-2, gyroid structures were found exhibiting least partition coefficient in all the categories (25%, 50% and 80%) which distinguishes it as an unfavourable

[40] Used interchangeably with perfusion velocity 1 $mm\ s^{-1}$.

structure for oxygen accumulation in the tissue. While the difference between maximum partition coefficient (0.998) and the minimum (0.982) does not appear significant, it could still be a crucial difference, considering the sensitivity of cells to concentrations in picomolar range. Therefore, partition coefficient was envisaged as a promising tissue scaffold ranking parameter, to quantify mass transfer efficiency.

5.2. Effect of Péclet number on mass transfer in TPMS structures

The TPMS structures of Figure 5.1-2 were also evaluated for Péclet number (Pe) to understand the nature of oxygen mass transfer with respect to advection and diffusion. Péclet number is a commonly used dimensionless parameter that quantifies the relative importance of diffusion and advection, with higher Pe indicating advection [151, 152]. The Péclet number for all TPMS structures was calculated according to Equation [41].

$$Pe = \frac{channel\ velocity \times (L_c)}{D_{O_2}} \qquad [41]$$

In this thesis, the Péclet number was calculated by two different approaches with two different interpretations of channel velocity. In the first approach, the channel velocity was considered as the average velocity that develops inside the scaffold voids, when perfused with a constant superficial velocity (1 $mm\,s^{-1}$) and defined as $u_{channel}$. To approximate the velocity in the scaffold voids, the average velocity in the axial scaffold slices was calculated in the periodic region. Figure 5.2-1, Figure 5.2-2 and Figure 5.2-3 show the average blood velocity in slices of Schwarz Diamond, gyroid and lidinoid at different porosities. The simulation set up consisted of 5 unit cells of edge length 200 μm with two empty unit cells at the back to account for exit-length (400 μm). The figures indicate that the flow rate in these structures is different due to differences in the cross-sectional area at the blood entrance location in TPMS structures of different porosities. The average channel velocities inside the TPMS unit cells were also found to fluctuate periodically due to this area effect. Similarly, in the exit-length/empty space region, it was noted that the average velocities fall below the imposed velocity at the inlet, because the flow rate in this region decreases due to the sudden increase in cross-sectional area, in order to conserve mass. For a similar reason, the structures with higher porosities displayed higher channel velocity in the exit region, proportional to porosity.

However, the average slice velocity rankings within the TPMS scaffold region had no particular pattern. This effect was observed due to variation in the *norm* of the velocity vectors computed within the slices besides differences in the blood flow rate entering the system and area effect of the TPMS slices. The channel velocity was calculated by taking the average of the average velocity calculated in the periodic region slices (400 μm-800 μm), and substituted in Equation [41] to calculate Pe.

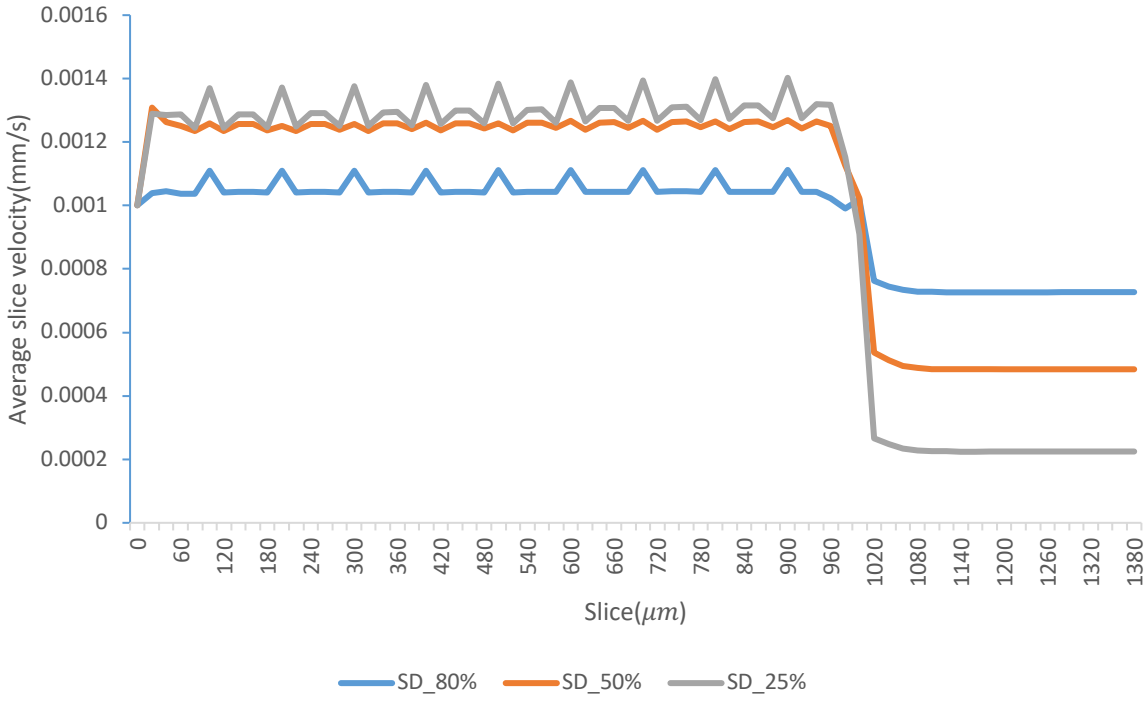

Figure 5.2-1: Average velocity in Schwarz Diamond slices along the axial direction, when the superficial blood flow velocity was 1 $mm\ s^{-1}$.

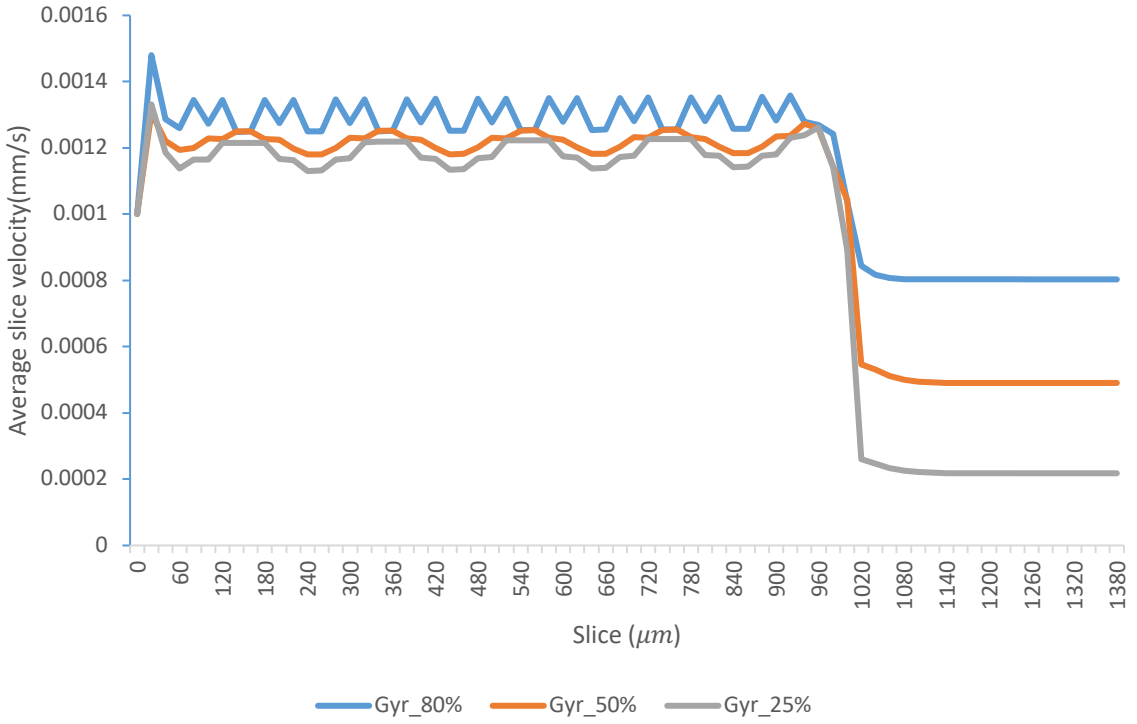

Figure 5.2-2: Average velocity in gyroid slices along the axial direction, when the superficial blood flow velocity was 1 $mm\ s^{-1}$.

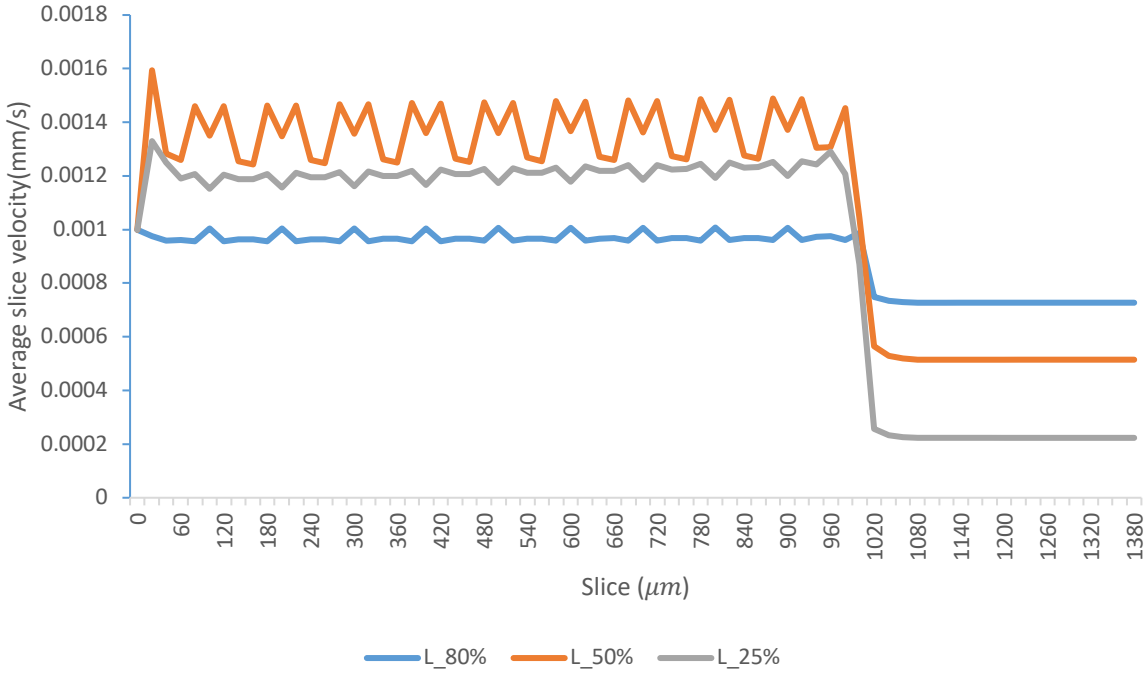

Figure 5.2-3: Average velocity in lidinoid slices along the axial direction, when the superficial blood flow velocity was 1 $mm\ s^{-1}$.

The characteristic length, L_c, is an important variable in dimensionless analysis, that includes the structure effect to explain the effect of flow behaviour on mass transfer. The variable is relatively straightforward to establish in other geometries such as cylinder, wherein the channel diameter is considered as L_c. For a packed bed of spheres, the diameter of the spheres is taken as L_c, although it may not be an accurate representation, because the spatial arrangement of spheres could be different. L_c is challenging to identify in TPMS structures, given the structural complexity and the spatial variance of slices. Several literature sources have proposed the edge length of TPMS structures as L_c [116, 153], but including this definition in understanding TPMS scaffolds, precludes the effect of structural porosity and the space distribution between tissue and blood phases. In this work, L_c was defined to include the effect of TPMS structural porosity (Equation [42]). Calculation of L_c with this definition requires the estimation of specific surface area, which is the ratio of surface area of TPMS structure to its volume. The *Palabos* code contains the C++ code to calculate the surface area of TPMS structures from STL files of TPMS structures.

$$Characteristic\ length = \frac{4 * porosity}{Specific\ surface\ area} \qquad [42]$$

The partition coefficient was plotted against Péclet number as shown in Figure 5.2-4. It was found that more structurally porous scaffolds were associated with high Péclet numbers and partition coefficients in general, however structural porosity was not necessarily the only causal factor for higher partition coefficient. This is because it was found that, although some TPMS structures were less porous (sustaining more tissue), they displayed higher partition coefficients of similar magnitude. Therefore, it is hypothesized that efficient mass transfer cannot be solely attributed to advection.

Within scaffolds of equal porosities, gyroids had the lowest partition coefficient and therefore should not be a first choice of tissue scaffold. Double Schoen Gyroid, lidinoid, P2GD and D' TPMS structures at 50% porosity were found to have a higher partition coefficient in the 50% category. These TPMS structures however would be slightly challenging to fabricate, because the phase thickness could be seen to become relatively narrower (Figure 5.2-5, Figure 5.2-6, Figure 5.2-7 and Figure 5.2-8).

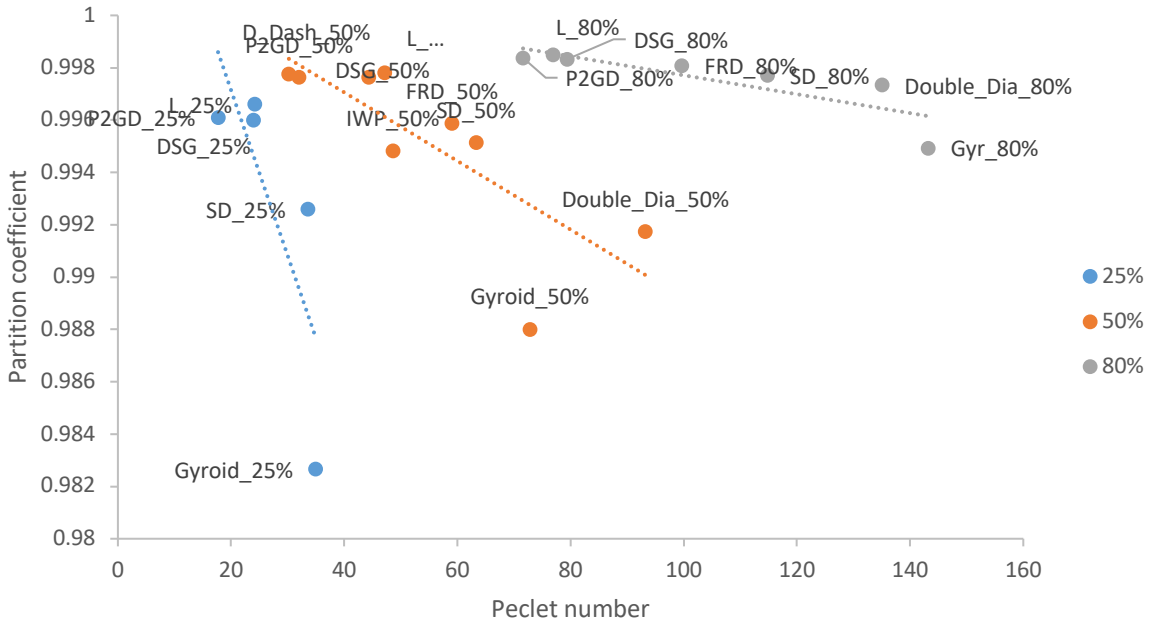

Figure 5.2-4: Partition coefficient vs Péclet number in TPMS structures.

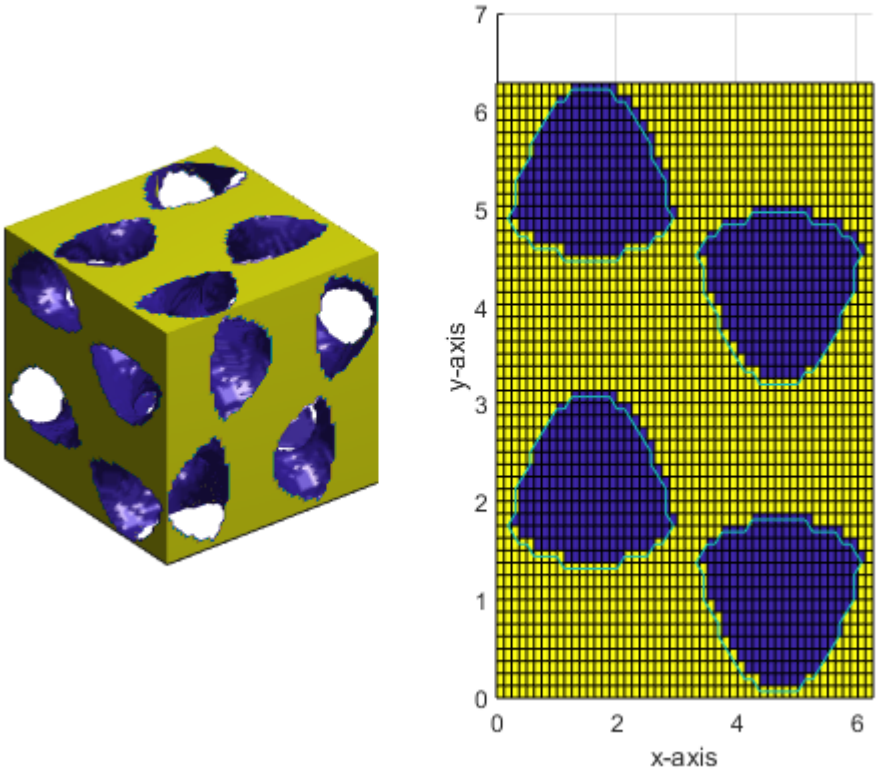

Figure 5.2-5: Middle slice composition of tissue and void space in P2GD 50%

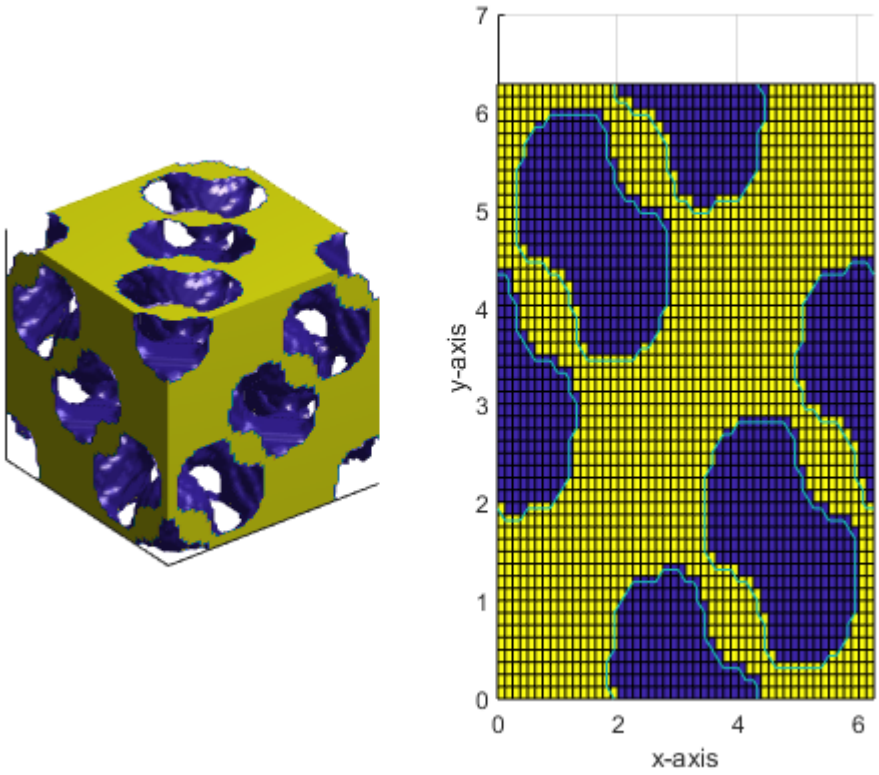

Figure 5.2-6: Middle slice composition of tissue and void space in D' 50%

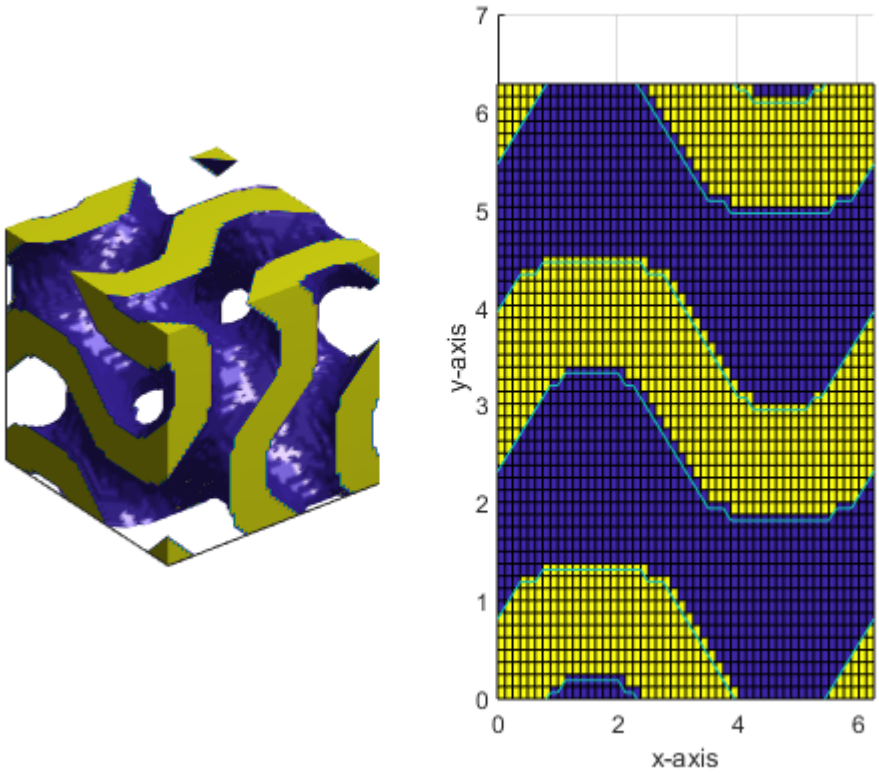

Figure 5.2-7: Middle slice composition of tissue and void space in DSG 50%

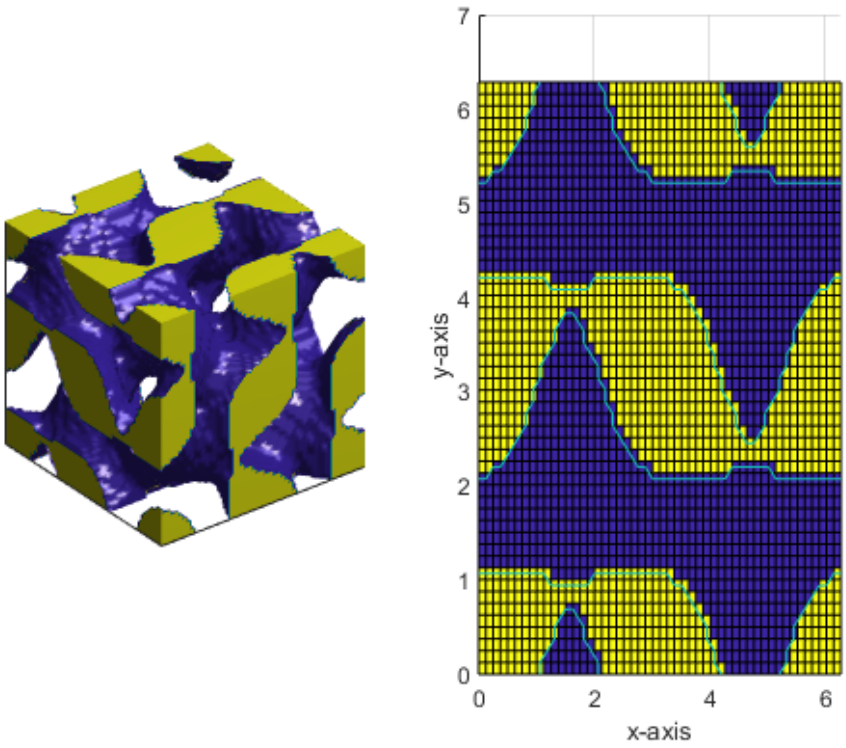

Figure 5.2-8: Middle slice composition of tissue and void space in Lidinoid 50%

In the second approach, the Péclet number was calculated by a different approximation for the channel velocity ($u'_{channel}$) in which $u'_{channel}$, superficial velocity and structural porosity are linked to each other by Equation [43]. By this definition if 80% and 60% porous scaffolds are subjected to a constant superficial flow velocity of 1 $mm\ s^{-1}$, $u'_{channel}$ evaluates to $1.225u_{superficial}$ and $1.667u_{superficial}$ respectively. Thus, more porous structures should contain lower channel velocities and vice-versa. A superficial velocity of $1\ mm\ s^{-1}$ was considered for this analysis to resemble the creeping velocity profiles present in capillaries.

$$u'_{channel} = \frac{u_{superficial}}{porosity} \qquad [43]$$

Figure 5.2-9 shows the relation between Péclet number and partition coefficient, when evaluated with the new definition of channel velocity (Equation [43]). Again, scaffolds of high porosity were generally found associated with higher partition coefficient. However, highly porous structures have lesser amount of tissue in a given volume. These structures are also challenging to 3D print, because the minimum print thickness is smaller in them and the standard deviation in SNA is higher. A lower limit to Péclet number (~70) was observed for

all TPMS structures at the considered inlet superficial velocity (1 $mm\ s^{-1}$). The structures closer to the lower limit displayed higher partition coefficient, suggesting diffusion as a predominant mass transfer phenomenon in TPMS tissue scaffolds.

In TPMS structures of equal porosity, the gyroid structures were again found to be outliers, with relatively large Péclet numbers and lower partition coefficients. This case also suggests that TPMS structures with high Péclet numbers are not necessary to enhance mass transfer, thus re-emphasizing diffusion as the primary mass transfer enhancing factor, for tissue vascularization. Double Schoen Gyroid, Lidinoid, P2GD and D' structures at 50% porosity were found to have a higher partition coefficient than other TPMS structures of equal porosity, as observed with the previous approach. The major difference in the results of the two approaches (Figure 5.2-4 and Figure 5.2-9), was in terms of the spread of the data, however, there was no difference in the general trend of partition coefficient.

In future, sophisticated 3D printers should be developed that can fabricate TPMS structures more accurately, to realize the gain in terms of partition coefficient. However, in conclusion a 50% porous Schwarz Diamond structure is proposed as a robust structure to 3D print tissue scaffolds because it provides a superior partition coefficient as well as a minimum variation in SNA and also sustains a reasonably high tissue volume (Figure 5.2-10 and Figure 4.1-5).

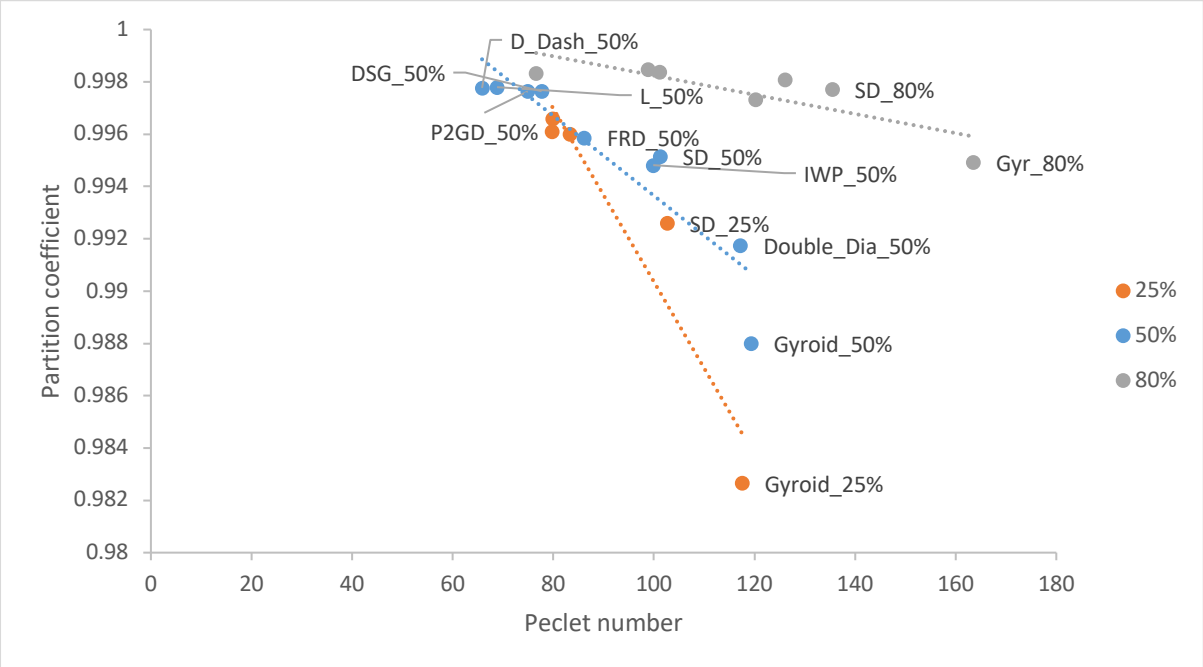

Figure 5.2-9: Péclet number vs partition coefficient ($u_{channel}$ evaluated as $\frac{u_{superficial}}{\epsilon}$)

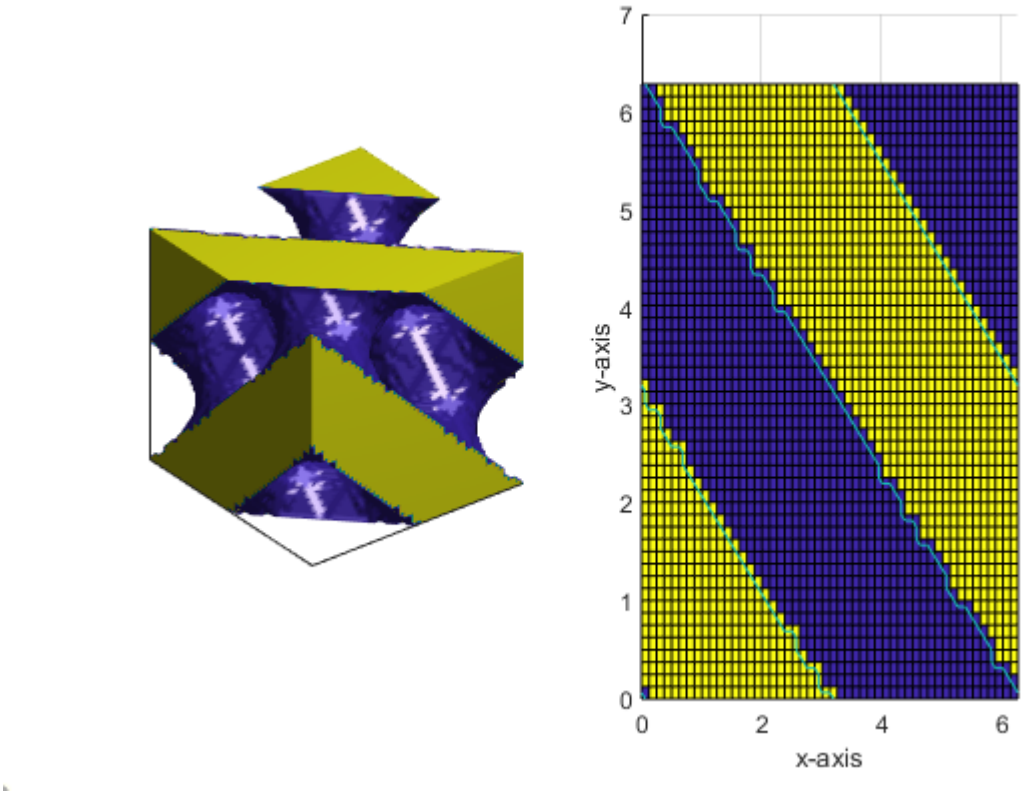

Figure 5.2-10: Middle slice composition of tissue and void space in Schwarz Diamond-50%

5.3. Summary

This chapter explored the underlying factors governing mass transfer phenomena in TPMS structures. Oxygen accumulation in tissue and blood was evaluated at steady state and was quantified as a partition coefficient. The partition coefficient $\left(\frac{C_{tissue}}{C_{blood}}\right)$ in all examined TPMS structures was found to be > 0.9. The difference in partition coefficient between TPMS structures reflected how different flow patterns affect mass transfer. Overall, more porous structures displayed higher partition coefficient, but sustained less tissue specific volume. To understand the nature of mass transfer, Péclet numbers were calculated for flow through different TPMS structures. The Péclet number was calculated by two different definitions of channel velocity: a) by assuming channel velocity to be the average velocity within the TPMS scaffold b) by assuming the channel velocity to be the ratio of superficial velocity imposed at the scaffold inlet to the structural porosity. The Péclet numbers evaluated by both the methods

were used to understand the relative importance of diffusion and advection. Low and high Péclet numbers were regarded as diffusion and advection dominated mass transfer process respectively. Furthermore, Péclet number was plotted against partition coefficient to understand the relationship between these variables. It was found that as Péclet number increased, the partition coefficient decreased in all TPMS structures of a given porosity. However, structures with higher porosity did not reflect a steep decline in the partition coefficient when the Péclet number increased. Schwarz Diamond TPMS structure at 50% porosity showed superior partition coefficient as well as minimum SNA, suggesting easier 3D printability.

6. Conclusion and Recommendations

6.1. Conclusions

Despite tremendous advances in tissue engineering, vascularization continues to remain a challenge for regeneration of clinically relevant tissues. Three-dimensional (3D) tissue engineering scaffolds face a major problem in terms of nutrient and oxygen availability to the cells after transplantation, leading to hypoxia and ultimately causing tissue necrosis. With advancement in additive manufacturing technologies such as 3D printing, it is now possible to 3D print or bioprint soft tissues in the lab. This provided the motivation to design biocompatible scaffolds, which can provide structural support for 3D organization of tissues, that can eliminate oxygen deficiency in the tissues by providing an efficient blood perfusion pathway.

This work is based on CFD with LBM that utilizes the *Palabos* open source library encoded in C++. A constant blood flow through a periodic domain of scaffold was simulated, which allowed comparisons to be made in the context of organs of appropriate scale. A fixed concentration of dissolved oxygen was coupled with blood flow and was introduced at the scaffold inlet, which diffused into the tissue through the scaffold, while oxygenated blood traversed through the scaffold. The oxygen diffusing in the tissue was modelled to undergo consumption at a zero order kinetic rate. Throughout this work, numerical modelling was used to investigate metrics at steady state, such as: oxygen concentration in tissue and blood regions, oxygen concentration in slices along the blood flow direction and maximum oxygen diffusion distance in radial direction. These metrics were evaluated with changing parameters such as: scaffold shape, scaffold thickness, blood flow velocity, oxygen consumption rate in tissues, inlet oxygen concentration at scaffold entrance, oxygen diffusion coefficient in tissue and hydrogel. *A priori*, the LBM numerical model was validated with the Krogh's analytical model for a thin capillary slice, wherein the steady state oxygen diffusion distances in the tissue were compared. Further verification was done by addition of a hydrogel layer between the capillary and tissue space, to evaluate the change in oxygen diffusion distances, upon addition of a resistive layer. The model was further verified in 3D scaffolds by accounting for entrance and exit effects after performing mesh-independence studies.

The primary objective of this work was to examine tissue oxygenation when cellulose-derived biocompatible scaffolds are 3D printed as TPMS structures. Minimal surfaces are

associated with high permeability and therefore scaffolds designed as TPMS structures were an attractive candidate to investigate for improvement in tissue oxygenation. This objective was achieved and this thesis provides a proof of concept for successful vascularization of soft tissues with TPMS structures. In particular, it was demonstrated that TPMS structures are superior to capillary structures in regard to mass transfer, because of the multidirectional nature of oxygen diffusion towards the tissue, from the blood side. It was also shown that TPMS scaffolds with wall thicknesses of ~100 or ~200 μm could sustain upto 50% of a given space with tissue in the order of ~10 cm, depending upon the structural porosity, when the perfused oxygen concentration is greater than or equal to 0.15mM.

The thesis provides the methodology for designing three intertwined TPMS phases (blood, scaffold, tissue) with a single trigonometric equation, by changing the isovalues appropriately. The design methodology and the choice of isovalues, to achieve a particular TPMS configuration was demonstrated with the Schwarz Diamond structure (Chapter 3). The same approach can be applied to create three phases of other TPMS structures, using data on structural porosities and isovalues tabulated in Appendix B.

To understand the effect of TPMS hydrogel thickness on oxygen accumulation, it was important to quantify the thickness of a TPMS phase, prior to analysing its impact. However, it was noted that these structures had variation in phase thicknesses between slices throughout a unit cell, and difficulties arose in attributing a single number to wall thickness. This was due to the fact that modelling of TPMS structures is mathematically independent of the wall thickness, and it was dependent only on the isovalues (structural porosity). This difficulty was overcome by introducing the concept of SNA, which combined wall thickness with structural porosity in a linear proportion. However, it was found that the linear proportionality assumption was most accurate in only a few TPMS structures such as the Schwarz Diamond and gyroid at 50% structural porosity and not for other TPMS structures or at different porosities. Nevertheless, within the scope of the current study, SNA was chosen as a starting point to quantify the impact of TPMS hydrogel thickness on oxygen accumulation in tissues, to maintain simplicity of TPMS modelling and 3D printing. With the definition of SNA, the wall or phase thickness of the TPMS structures explored in this thesis could be approximated by multiplying the SNA value with the corresponding edge length of a TPMS structure.

The LBM results show that porosity and perfusion velocity share an intuitive relationship with accumulated oxygen concentration in tissue, because it was found that higher

porosity and higher perfusion velocity led to an increase in the average oxygen concentration accumulated in a slice at steady state. Similarly, higher inlet oxygen concentration and thinner scaffold walls were found to accumulate higher oxygen concentration in tissue at steady state.

LBM simulations were used to estimate the survival length of TPMS scaffolds containing tissues. Survival length is a novel concept defined in this thesis, which provided an estimation about the length of a TPMS scaffold that will be normoxic. Techniques such as slope estimation of axial oxygen concentration profiles and linear curve fitting were used to establish the concave upward nature of oxygen concentration profiles and to identify the tissue survival length in TPMS scaffolds. The estimates of normoxic length could guide scaffold design by providing critical information such as the approximate length of the scaffold to be 3D printed, which could be useful to estimate for instance the volume of hydrogel material required for the 3D printing application. Thus, with this prior information on survival lengths of scaffolds, the functional capacity of a specific organ transplant can be predetermined.

The survival length estimates of TPMS structures were shown in ternary plots, which is a novel representation in bioprinting science that could be used to identify the scaffold, tissue and blood/perfusion volumes from a single chart. After identifying the phase volumes, the isovalues of the TPMS structures can be back calculated from the TPMS porosity tables mentioned in Appendix B. These isovalues and level set equations could simplify the creation of CAD and STL files, thereby reducing the process time between scaffold prototyping and 3D printing. Thus, the LBM method or CFD algorithms could be used to make bioprinting using sheet TPMS structures a robust process.

Finally, partition coefficient was proposed as a concept to determine efficiency of oxygen diffusion from the blood side to tissue side, for any given TPMS vasculature pattern. In this work, this concept was applied to estimate the ratio of concentrations at the interface of TPMS shaped blood and tissue regions at steady state (without the hydrogel). It was observed that the TPMS structural porosity shared an intuitive relationship with partition coefficient; increased porosity led to increased partition coefficient. Furthermore, partition coefficient was examined with respect to Péclet number, to understand the relative importance of advection and diffusion in enhancing mass transfer. The calculation of Péclet number required the estimation of characteristic length of a TPMS scaffold, and in this work it was calculated based on porosity and specific surface area of the tissue scaffold, to allow a consistent comparison of structures with varying porosities. Correlating the Péclet number with partition coefficient suggested that

mass transfer enhancement in TPMS structures was primarily caused by the provision of short diffusion pathlengths from blood supply to tissue, rather than enhanced convective flow on the blood side. Thus, the LBM method can be used to compute partition coefficient, which could be a potential metric to optimize tissue scaffold shapes, from the breadth of shape possibilities.

Ultimately, with all the geometries considered, Schwarz Diamond was determined as the best TPMS scaffold structure for 3D printing. This structure is recommended because it had minimum variations in SNA, suggesting easier 3D printability. The Schwarz Diamond structure also had a continuous tissue phase, unlike some other TPMS structures such as Lidinoid, I-WP and F-RD. It was observed that TPMS structures such as the Lidinoid, I-WP and F-RD displayed very high partition coefficients. However, these structures had many isolated tissue regions that were not connected to the rest of the tissue mass (Appendix A). It is suggested that this might be advantageous in terms of interfacial area between the phases, but this may impede cell signalling and work against the fundamental concept of tissue i.e. an integrated tissue mass. Therefore, partition coefficient of TPMS structures should also be analysed with the spatial organization of the scaffold.

Regardless of the rate at which 3D printer capabilities are developing or new biocompatible materials are discovered, designing efficient vasculature in the tissues remains an important issue. In this regard, this thesis puts forth the 3D printing methodology of TPMS hydrogel scaffolds, to embed soft tissues, in an attempt to minimize the limitations imposed by the current 3D printing and manufacturing techniques.

6.2. Recommendations

In this thesis, CFD analysis was limited to several TPMS structures that can be regarded as the base classes of the TPMS family, namely the Schwarz Diamond, gyroid, F-RD, I-WP, Lidinoid, Schwarz Primitive, Double Schoen gyroid, D’ surface, P2-GD and double diamond. However, in future work, similar CFD analyses could be performed on other structures derived from the TPMS family, which could be achieved by adding constants and factors to the TPMS level set equations. Furthermore, hybridization of TPMS structures using the Gaussian radial basis function or sigmoidal function should be explored, to analyse oxygenation gain [154, 155]. These structures could be examined for their potential to minimize entrance and exit effects that occur within TPMS scaffolds. Similarly, CFD studies could be performed on TPMS

structures by changing their orientation with respect to the blood flow axis, and survival length estimates should be estimated and compared at various scaffold orientation angles.

In this study, the mass transfer efficiency in TPMS structures was measured in terms of partition coefficient, a novel concept that was not explored before in the context of tissue vascularization. Many attempts were made to relate the partition coefficient to geometric properties such as tortuosity and vorticity; however, predicting mass transfer efficiency with high accuracy was not feasible with those properties. Therefore, there is a large scope for continuation of work in this area. Furthermore, the conclusions on efficiency of TPMS scaffolds was drawn on the assumption that partition coefficients of all TPMS scaffold configurations would be affected similarly, for a given volume of hydrogel scaffold. However, in future, the sensitivity of partition coefficient to scaffold thickness and permeability should be analysed to quantify the percentage decrease in partition coefficient with addition of hydrogel layers.

This dissertation is novel in terms of its attempt to provide answers about tissue survival length for scaffolds of any shape and size with a computational model. However, the extrapolation technique is not exactly precise because it overlooks the concave nature of axial oxygen concentration profiles. The extrapolation estimate is sensitive to model resolution, curve fitting technique and confidence intervals. However, this estimation could be made more precise if the complete scaffold could be the subject of a CFD study in a single simulation. While the performance comparison with scaffolds of different porosities and phase compositions[41] is still feasible with the existing methodology, there is room for further improvement to obtain precise estimates of survival lengths and to make the TPMS ternary plots more accurate.

The TPMS tissue scaffolds could also find applications in extracorporeal devices. Figure 6.2-1 shows a liver extracorporeal device that can potentially be used as a substitute to current dialysis systems [156]. In these systems, blood containing waste metabolites (analogous to portal vein) is passed through a blood warmer into a TPMS scaffold containing hepatocyte/liver cells via an oxygenator. Heparin can be supplied externally to the system to mix with the blood, to avoid blood clotting and blockage of the voids. Nutrient media (similar to hepatic artery) could be pumped in through the device containing other necessary metabolites such as glucose. To offset the deficiency of oxygen dissolved in blood, an external

[41] Blood, tissue and hydrogel volumes

supply of oxygen gas could be provided to the system, to take advantage of high diffusion coefficient of oxygen gas through the hydrogel scaffolds. This process can be made continuous at an identified flow rate and the detoxified blood can be pumped back into the body through a bubble trap. CFD studies could be performed on this set up to model 'urea' and carbon dioxide (CO_2) generation in the liver cells, as oxygen is consumed in the hepatocyte cells. Additionally, the release kinetics of the waste metabolites back into the blood stream could be simulated, which can be coupled with the velocity field.

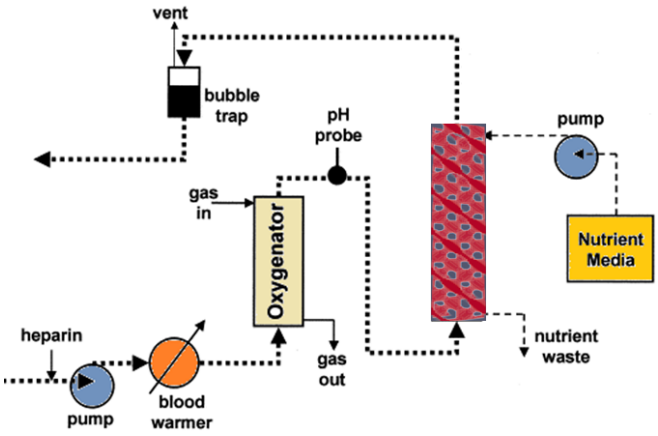

Figure 6.2-1: Schematic of a TPMS based liver extracorporeal device.

The TPMS scaffolds can also be used to embed other biological cells to make perfusion bioreactors as shown in Figure 6.2-2. The figure shows TPMS scaffolds that are periodically rotated along the perfusion direction. It would be interesting to do CFD studies to determine the angular velocity of scaffold rotation, to maximize even distribution of nutrients throughout the scaffold. It is hypothesized that this procedure will avoid one end (the anterior side) of the bioreactor to be always anoxic (relatively deoxygenated). Furthermore, when these TPMS scaffolds are used to support mammalian cell lines *in vitro*, the lumen/perfusion side could be coated with growth factors such as the VEGF[42], platelet-derived growth factor (PDGF[43]) and heparin[44]. When these growth factors are artificially delivered and supplanted on the scaffolds, they may induce angiogenesis[45]. A novel approach to induce angiogenesis could be by utilizing centrifugal force to increase mass transfer, which could potentially make the boundary layers thinner and reduce the drop in wall concentration. However, this is currently only speculation

[42] VEGF is a signal protein that a cell produces to induce new capillary formation
[43] PDGF plays a major role in cell division, growth and new blood vessel formation
[44] Heparin is an anti-coagulant to ensure smooth blood flow through the scaffold
[45] Formation of new blood vessels.

and CFD studies should be performed at various conditions on rotating TPMS scaffolds, to evaluate if there is are, in fact, advantages for such TPMS bioreactors.

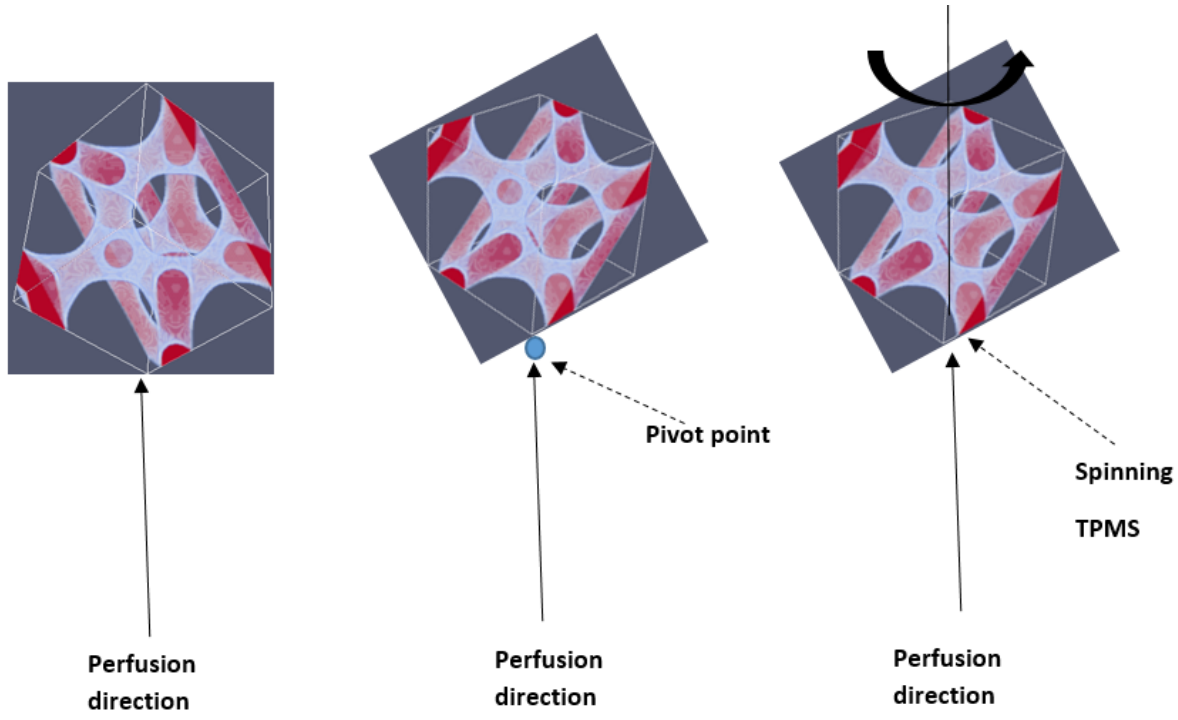

Figure 6.2-2: Schematic of spinning TPMS tissue perfusion bioreactors.

The LBM implementation in this thesis simulated only blood flow at constant velocity through the scaffolds in the Stokes regime. This was due to numerical instabilities associated with SRT method of LBM as discussed in Chapter 3. Regardless, these simulations model blood flow through capillaries more realistically, because the pulse dampens and dissipates as it reaches the peripheral end of the arterioles and empties into the capillaries. However, Two Relaxation Time (TRT) and Multiple Relaxation Time methods (MRT) could be investigated to deal with the instabilities associated with SRT, while solving the advection-diffusion equation. There is scope to extend the LBM model by implementation of these alternative relaxation time methods, which could potentially simulate turbulent and pulsatile blood flow such as those present in arteries [102]. The knowledge acquired from these simulations could be coupled with oxygen diffusion in tissues and consumption kinetics, to explore performance of TPMS perfusion bioreactors at high Reynolds number. While the choice of collision parameter may seem arbitrary with TRT and MRT simulations, it could be an interesting area of LBM application in tissue vascularization research.

Other areas of potential LBM research in tissue vascularization include coupling oxygen diffusion in tissue with the non-Newtonian rheology of the blood. This model could

take into account the varying blood viscosities at different shear rates. In this regard, the established rheology models such as Maxwell model [157] and Oldyroyd model [158] could be investigated to couple with LBM. The consumption rate implemented in the LBM model was based on zero-order kinetics; however, the consumption rate could also be modified to account for the subtle changes occurring due to cell growth on the scaffolds. The curvature effect of TPMS structures on cell growth can also be incorporated into the LBM model, by application of the Allen-Cahn equation [159]. Furthermore, the scope of LBM application could be widened to study the impact of shear forces on oxygen release from Red Blood Cells (RBCs). To make the simulations more realistic, the CFD model should also include oxygenation/deoxygenation[46] kinetics in RBCs using the Hills equation [160].

Although beyond the realms of CFD simulation, in applying the findings from this work to fabricate a real tissue scaffold, an important 3D printing challenge to overcome from a material fabrication point of view, is scaffold leakage [161]. Scaffold leakage would cause a situation similar to hematoma i.e. a blood vessel leaking directly into tissue. There are many complexities mentioned in the medical literature due to such an anomaly, including issues such as organ dysfunction and low blood pressure when implanted *in vivo*. 3D printing leak-proof biocompatible hydrogel scaffolds could however avoid this problem. Developing such scaffolds requires multiple mechanical tests such as examining the scaffolds for swelling and stability. Stress tests should be performed on scaffolds to examine if they could withstand adequate tissue weight or cell density over them. Therefore, hydrogel rheology characterization and tensile/shear stress tests should be performed on scaffolds, to check if they can provide adequate strength without compromising on nutrient delivery. Similarly, quality checks would be needed on TPMS scaffolds if they are used to make perfusion bioreactors that are subject to high flow rate perfusion media, to endure the shear force as it pumped through.

As a final comment, 3D printing in biomedical fields is projected to increase at a compounded annual growth rate of 6% during the forecast period of 2019-2025. Therefore, it reflects an increasingly important market; and the current work underpinning the design of transplant devices may in part help meet that demand.

[46] In response to local O_2 and CO_2 partial pressures

7. References:

[1] S. Lachmann, J.R. Jenner, Soft tissue injuries in sport, Blackwell Scientific Publications1994.
[2] K. Senni, J. Pereira, F. Gueniche, C. Delbarre-Ladrat, C. Sinquin, J. Ratiskol, G. Godeau, A.-M. Fischer, D. Helley, S. Colliec-Jouault, Marine polysaccharides: a source of bioactive molecules for cell therapy and tissue engineering, Marine drugs, 9 (2011) 1664-1681.
[3] A. Khademhosseini, R. Langer, A decade of progress in tissue engineering, Nature protocols, 11 (2016) 1775.
[4] R.J. McMurtrey, Analytic and Numerical Models of Oxygen and Nutrient Diffusion, Metabolism Dynamics, and Architecture Optimization in Three-Dimensional Tissue Constructs with Applications and Insights in Cerebral Organoids, (2015).
[5] D.W. Hutmacher, Scaffolds in tissue engineering bone and cartilage, Biomaterials, 21 (2000) 2529-2543.
[6] I.T. Ozbolat, Bioprinting scale-up tissue and organ constructs for transplantation, Trends in biotechnology, 33 (2015) 395-400.
[7] R. Pörtner, S. Nagel-Heyer, C. Goepfert, P. Adamietz, N.M. Meenen, Bioreactor design for tissue engineering, Journal of bioscience and bioengineering, 100 (2005) 235-245.
[8] E.M. Ahmed, Hydrogel: Preparation, characterization, and applications: A review, Journal of advanced research, 6 (2015) 105-121.
[9] M. Gelinsky, Current research directions in 3D printing in medicine, Future Medicine, 2017.
[10] D. Lei, Y. Yang, Z. Liu, B. Yang, W. Gong, S. Chen, S. Wang, L. Sun, B. Song, H. Xuan, 3D printing of biomimetic vasculature for tissue regeneration, Materials Horizons, (2019).
[11] J.S. Miller, The billion cell construct: will three-dimensional printing get us there?, PLoS biology, 12 (2014) e1001882.
[12] L.E. Niklason, R.S. Langer, Advances in tissue engineering of blood vessels and other tissues, Transplant immunology, 5 (1997) 303-306.
[13] B.A. Wittenberg, J.B. Wittenberg, Transport of oxygen in muscle, Annual Review of Physiology, 51 (1989) 857-878.
[14] T.S. Karande, Effect of scaffold architecture on diffusion of oxygen in tissue engineering constructs, 2007.
[15] O. Ball, B.-N.B. Nguyen, J.K. Placone, J.P. Fisher, 3d printed vascular networks enhance viability in high-volume perfusion bioreactor, Annals of biomedical engineering, 44 (2016) 3435-3445.
[16] N. Rajpal, E. Walters, T. Elmarsafi, T. Pittman, K. Johnson-Arbor, Use of hyperbaric oxygen therapy for tissue ischemia after breast reconstruction, Undersea & hyperbaric medicine: journal of the Undersea and Hyperbaric Medical Society, Inc, 46 (2019) 461-465.
[17] G. Minto, R. Struthers, It's not about the bike: enhancing oxygen delivery, Oxford University Press, 2017.
[18] E. Trampe, K. Koren, A.R. Akkineni, C. Senwitz, F. Krujatz, A. Lode, M. Gelinsky, M. Kühl, Functionalized Bioink with Optical Sensor Nanoparticles for O2 Imaging in 3D-Bioprinted Constructs, Advanced Functional Materials, 28 (2018) 1804411.
[19] S. Bagali, G.A. Hadimani, M.S. Biradar, K.K. Das, Introductory Chapter: Primary Concept of Hypoxia and Anoxia, Hypoxia and Anoxia, 1 (2018) 3-11.
[20] R.L. Naeye, Hypoxemia and the sudden infant death syndrome, Science, 186 (1974) 837-838.

[21] C. Fee, 3D-printed porous bed structures, Current Opinion in Chemical Engineering, 18 (2017) 10-15.
[22] S. Rajagopalan, R.A. Robb, Schwarz meets Schwann: design and fabrication of biomorphic and durataxic tissue engineering scaffolds, Medical image analysis, 10 (2006) 693-712.
[23] I.T. Ozbolat, Y. Yu, Bioprinting toward organ fabrication: challenges and future trends, IEEE Transactions on Biomedical Engineering, 60 (2013) 691-699.
[24] R.P. Visconti, V. Kasyanov, C. Gentile, J. Zhang, R.R. Markwald, V. Mironov, Towards organ printing: engineering an intra-organ branched vascular tree, Expert opinion on biological therapy, 10 (2010) 409-420.
[25] D.M. Kalaskar, 3D printing in medicine, Woodhead Publishing2017.
[26] J. Hsu, 3D Printing Aims to Deliver Organs on Demand, LiveScience, September, (2013).
[27] J.L. Drury, D.J. Mooney, Hydrogels for tissue engineering: scaffold design variables and applications, Biomaterials, 24 (2003) 4337-4351.
[28] G.Y. Huang, L.H. Zhou, Q.C. Zhang, Y.M. Chen, W. Sun, F. Xu, T.J. Lu, Microfluidic hydrogels for tissue engineering, Biofabrication, 3 (2011) 012001.
[29] B. Chan, K. Leong, Scaffolding in tissue engineering: general approaches and tissue-specific considerations, European spine journal, 17 (2008) 467-479.
[30] J.J. Ballyns, J.P. Gleghorn, V. Niebrzydowski, J.J. Rawlinson, H.G. Potter, S.A. Maher, T.M. Wright, L.J. Bonassar, Image-guided tissue engineering of anatomically shaped implants via MRI and micro-CT using injection molding, Tissue Engineering Part A, 14 (2008) 1195-1202.
[31] J. Bohandy, B. Kim, F. Adrian, Metal deposition from a supported metal film using an excimer laser, Journal of Applied Physics, 60 (1986) 1538-1539.
[32] Z. Wang, R. Abdulla, B. Parker, R. Samanipour, S. Ghosh, K. Kim, A simple and high-resolution stereolithography-based 3D bioprinting system using visible light crosslinkable bioinks, Biofabrication, 7 (2015) 045009.
[33] D.B. Kolesky, R.L. Truby, A.S. Gladman, T.A. Busbee, K.A. Homan, J.A. Lewis, 3D bioprinting of vascularized, heterogeneous cell-laden tissue constructs, Advanced materials, 26 (2014) 3124-3130.
[34] M.A. Skylar-Scott, S.G. Uzel, L.L. Nam, J.H. Ahrens, R.L. Truby, S. Damaraju, J.A. Lewis, Biomanufacturing of organ-specific tissues with high cellular density and embedded vascular channels, Science advances, 5 (2019) eaaw2459.
[35] B. Grigoryan, S.J. Paulsen, D.C. Corbett, D.W. Sazer, C.L. Fortin, A.J. Zaita, P.T. Greenfield, N.J. Calafat, J.P. Gounley, A.H. Ta, Multivascular networks and functional intravascular topologies within biocompatible hydrogels, Science, 364 (2019) 458-464.
[36] N. Noor, A. Shapira, R. Edri, I. Gal, L. Wertheim, T. Dvir, 3D Printing of Personalized Thick and Perfusable Cardiac Patches and Hearts, Advanced Science, (2019) 1900344.
[37] K.K. Moncal, V. Ozbolat, P. Datta, D.N. Heo, I.T. Ozbolat, Thermally-controlled extrusion-based bioprinting of collagen, Journal of Materials Science: Materials in Medicine, 30 (2019) 55.
[38] C.D. Murray, The physiological principle of minimum work: I. The vascular system and the cost of blood volume, Proceedings of the National Academy of Sciences of the United States of America, 12 (1926) 207.
[39] G. Vozzi, A. Previti, G. Ciaravella, A. Ahluwalia, Microfabricated fractal branching networks, Journal of Biomedical Materials Research Part A: An Official Journal of The Society for Biomaterials, The Japanese Society for Biomaterials, and The Australian Society for Biomaterials and the Korean Society for Biomaterials, 71 (2004) 326-333.

[40] A. Díaz-Lantada, A. Mosquera, J. Endrino, P. Lafont, Design and rapid prototyping of DLC coated fractal surfaces for tissue engineering applications, Journal of Physics: Conference Series, IOP Publishing, 2010, pp. 012003.
[41] V.K. Lee, A.M. Lanzi, H. Ngo, S.-S. Yoo, P.A. Vincent, G. Dai, Generation of multi-scale vascular network system within 3D hydrogel using 3D bio-printing technology, Cellular and molecular bioengineering, 7 (2014) 460-472.
[42] E.A. Phelps, A.J. García, Engineering more than a cell: vascularization strategies in tissue engineering, Current opinion in biotechnology, 21 (2010) 704-709.
[43] M. Ehrbar, S.M. Zeisberger, G.P. Raeber, J.A. Hubbell, C. Schnell, A.H. Zisch, The role of actively released fibrin-conjugated VEGF for VEGF receptor 2 gene activation and the enhancement of angiogenesis, Biomaterials, 29 (2008) 1720-1729.
[44] R. Gupta, J.r. Tongers, D.W. Losordo, Human studies of angiogenic gene therapy, Circulation research, 105 (2009) 724-736.
[45] J.J. Moon, J.E. Saik, R.A. Poche, J.E. Leslie-Barbick, S.-H. Lee, A.A. Smith, M.E. Dickinson, J.L. West, Biomimetic hydrogels with pro-angiogenic properties, Biomaterials, 31 (2010) 3840-3847.
[46] J.E. Leslie-Barbick, J.J. Moon, J.L. West, Covalently-immobilized vascular endothelial growth factor promotes endothelial cell tubulogenesis in poly (ethylene glycol) diacrylate hydrogels, Journal of Biomaterials Science, Polymer Edition, 20 (2009) 1763-1779.
[47] T. Miyamoto, S.i. Takahashi, H. Ito, H. Inagaki, Y. Noishiki, Tissue biocompatibility of cellulose and its derivatives, Journal of biomedical materials research, 23 (1989) 125-133.
[48] H. Kang, R. Liu, Y. Huang, Cellulose-Based Gels, Macromolecular Chemistry and Physics, 217 (2016) 1322-1334.
[49] A.T. Crane, J.P. Voth, F.X. Shen, W.C. Low, Concise Review: Human-Animal Neurological Chimeras: Humanized Animals or Human Cells in an Animal?, Stem Cells, 37 (2019) 444-452.
[50] J.-i. Usui, T. Kobayashi, T. Yamaguchi, A. Knisely, R. Nishinakamura, H. Nakauchi, Generation of kidney from pluripotent stem cells via blastocyst complementation, The American journal of pathology, 180 (2012) 2417-2426.
[51] S.V. Koduru, A.N. Leberfinger, D. Pasic, A. Forghani, S. Lince, D.J. Hayes, I.T. Ozbolat, D.J. Ravnic, Cellular Based Strategies for Microvascular Engineering, Stem Cell Reviews and Reports, 15 (2019) 218-240.
[52] B. Bhushan, M. Caspers, An overview of additive manufacturing (3D printing) for microfabrication, Microsystem Technologies, 23 (2017) 1117-1124.
[53] E.S. Tzanakakis, D.J. Hess, T.D. Sielaff, W.-S. Hu, Extracorporeal tissue engineered liver-assist devices, Annual review of biomedical engineering, 2 (2000) 607-632.
[54] G. Catapano, Mass transfer limitations to the performance of membrane bioartificial liver support devices, The International journal of artificial organs, 19 (1996) 18-35.
[55] J.W. Allen, T. Hassanein, S.N. Bhatia, Advances in bioartificial liver devices, Hepatology, 34 (2001) 447-455.
[56] L. De Bartolo, G. Jarosch-Von Schweder, A. Haverich, A. Bader, A novel full-scale flat membrane bioreactor utilizing porcine hepatocytes: cell viability and tissue-specific functions, Biotechnology progress, 16 (2000) 102-108.
[57] P. Kan, H. Miyoshi, K. Yanagi, N. Ohshima, Effects of shear stress on metabolic function of the co-culture system of hepatocyte/nonparenchymal cells for a bioartificial liver, ASAIO journal (American Society for Artificial Internal Organs: 1992), 44 (1998) M441-444.
[58] K. Taguchi, M. Matsushita, M. Takahashi, J. Uchino, Development of a bioartificial liver with sandwiched-cultured hepatocytes between two collagen gel layers, Artificial organs, 20 (1996) 178-185.

[59] Y. Zhang, Y. Yu, H. Chen, I.T. Ozbolat, Characterization of printable cellular micro-fluidic channels for tissue engineering, Biofabrication, 5 (2013) 025004.
[60] V. Mironov, R.P. Visconti, V. Kasyanov, G. Forgacs, C.J. Drake, R.R. Markwald, Organ printing: tissue spheroids as building blocks, Biomaterials, 30 (2009) 2164-2174.
[61] S.N. Krivoshapko, V. Ivanov, Encyclopedia of analytical surfaces, Springer2015.
[62] A. Goetz, Introduction to differential geometry, Addison Wesley Publishing Company1970.
[63] S. Yu, J. Sun, J. Bai, Investigation of functionally graded TPMS structures fabricated by additive manufacturing, Materials & Design, 182 (2019) 108021.
[64] S. Lidin, S. Larsson, Bonnet transformation of infinite periodic minimal surfaces with hexagonal symmetry, Journal of the Chemical Society, Faraday Transactions, 86 (1990) 769-775.
[65] A.H. Schoen, Reflections concerning triply-periodic minimal surfaces, Interface focus, 2 (2012) 658-668.
[66] M.N. Yousaf, B.T. Houseman, M. Mrksich, Using electroactive substrates to pattern the attachment of two different cell populations, Proceedings of the National Academy of Sciences, 98 (2001) 5992-5996.
[67] E. Cukierman, R. Pankov, D.R. Stevens, K.M. Yamada, Taking cell-matrix adhesions to the third dimension, Science, 294 (2001) 1708-1712.
[68] S. Vijayavenkataraman, L. Zhang, S. Zhang, J.Y. Hsi Fuh, W.F. Lu, Triply Periodic Minimal Surfaces Sheet Scaffolds for Tissue Engineering Applications: An Optimization Approach toward Biomimetic Scaffold Design, ACS Applied Bio Materials, 1 (2018) 259-269.
[69] A. Castro, R. Ruben, S. Gonçalves, J. Pinheiro, J. Guedes, P. Fernandes, Numerical and experimental evaluation of TPMS Gyroid scaffolds for bone tissue engineering, Computer methods in biomechanics and biomedical engineering, 22 (2019) 567-573.
[70] M. Fantini, M. Curto, F. De Crescenzio, TPMS for interactive modelling of trabecular scaffolds for bone tissue engineering, Advances on Mechanics, Design Engineering and Manufacturing, Springer2017, pp. 425-435.
[71] H.A. Almeida, P.J. Bártolo, Design of tissue engineering scaffolds based on hyperbolic surfaces: Structural numerical evaluation, Medical engineering & physics, 36 (2014) 1033-1040.
[72] A. Yánez, A. Cuadrado, O. Martel, H. Afonso, D. Monopoli, Gyroid porous titanium structures: a versatile solution to be used as scaffolds in bone defect reconstruction, Materials & Design, 140 (2018) 21-29.
[73] O. Al-Ketan, R.K.A. Al-Rub, R. Rowshan, The effect of architecture on the mechanical properties of cellular structures based on the IWP minimal surface, Journal of Materials Research, 33 (2018) 343-359.
[74] D.W. Abueidda, A.S. Dalaq, R.K.A. Al-Rub, H.A. Younes, Finite element predictions of effective multifunctional properties of interpenetrating phase composites with novel triply periodic solid shell architectured reinforcements, International Journal of Mechanical Sciences, 92 (2015) 80-89.
[75] I. Maskery, A. Aremu, L. Parry, R. Wildman, C. Tuck, I. Ashcroft, Effective design and simulation of surface-based lattice structures featuring volume fraction and cell type grading, Materials & Design, 155 (2018) 220-232.
[76] X. Zheng, Z. Fu, K. Du, C. Wang, Y. Yi, Minimal surface designs for porous materials: from microstructures to mechanical properties, Journal of materials science, 53 (2018) 10194-10208.
[77] A. Castro, T. Pires, J. Santos, B. Gouveia, P. Fernandes, Permeability versus Design in TPMS Scaffolds, Materials, 12 (2019) 1313.

[78] M. Wohlgemuth, N. Yufa, J. Hoffman, E.L. Thomas, Triply periodic bicontinuous cubic microdomain morphologies by symmetries, Macromolecules, 34 (2001) 6083-6089.
[79] A. Weyhaupt, Deformations of the gyroid and lidinoid minimal surfaces, Pacific Journal of Mathematics, 235 (2008) 137-171.
[80] P.K. Kundu, I.M. Cohen, D. Dowling, Fluid Mechanics 4th, Elsevier, 2008.
[81] L.S. Addison Snell, Intersect 360, 2017.
[82] A. Guillerme, Wood versus Iron: The strength of materials in early 19th century France, History and Technology, an International Journal, 6 (1988) 239-252.
[83] A.W. Date, Introduction to computational fluid dynamics, Cambridge University Press2005.
[84] O. Zikanov, Essential computational fluid dynamics, John Wiley & Sons2019.
[85] L. Boltzmann, Ludwig Boltzmann, Bundespressedienst1974.
[86] J. Koplik, J.R. Banavar, J.F. Willemsen, Molecular dynamics of fluid flow at solid surfaces, Physics of Fluids A: Fluid Dynamics, 1 (1989) 781-794.
[87] A. Mohamad, Lattice Boltzmann Method, Springer2011.
[88] M. Sukop, DT Thorne, Jr. Lattice Boltzmann Modeling Lattice Boltzmann Modeling, Springer2006.
[89] D.A. Wolf-Gladrow, Lattice-gas cellular automata and lattice Boltzmann models: an introduction, Springer2004.
[90] G.R. McNamara, G. Zanetti, Use of the Boltzmann equation to simulate lattice-gas automata, Physical review letters, 61 (1988) 2332.
[91] J.W. Shim, R. Gatignol, Thermal lattice Boltzmann method based on a theoretically simple derivation of the Taylor expansion, Physical Review E, 83 (2011) 046710.
[92] G. Zanetti, Hydrodynamics of lattice-gas automata, Physical Review A, 40 (1989) 1539.
[93] X. He, L.-S. Luo, Lattice Boltzmann model for the incompressible Navier–Stokes equation, Journal of statistical Physics, 88 (1997) 927-944.
[94] P.J. Dellar, Lattice Boltzmann algorithms without cubic defects in Galilean invariance on standard lattices, Journal of Computational Physics, 259 (2014) 270-283.
[95] F. Kuznik, C. Obrecht, G. Rusaouen, J.-J. Roux, LBM based flow simulation using GPU computing processor, Computers & Mathematics with Applications, 59 (2010) 2380-2392.
[96] K.N. Premnath, M.J. Pattison, S. Banerjee, An investigation of the lattice Boltzmann method for large eddy simulation of complex turbulent separated flow, Journal of Fluids Engineering, 135 (2013) 051401.
[97] S. Chen, G.D. Doolen, Lattice Boltzmann method for fluid flows, Annu. Rev. Fluid Mech., 30 (1998) 329-364.
[98] Z. Guo, B. Shi, N. Wang, Lattice BGK model for incompressible Navier–Stokes equation, Journal of Computational Physics, 165 (2000) 288-306.
[99] X. He, L.-S. Luo, A priori derivation of the lattice Boltzmann equation, Physical Review E, 55 (1997) R6333.
[100] A.A. Kanoria, Lattice Boltzmann method for applied aerodynamics problems, Indian Institute of Technology Gandhinagar, 2015.
[101] A.M. Sayed, M. Hussein, T. Becker, An innovative lattice Boltzmann model for simulating Michaelis–Menten-based diffusion–advection kinetics and its application within a cartilage cell bioreactor, Biomechanics and modeling in mechanobiology, 9 (2010) 141-151.
[102] S. Xiong, C. Zhong, C. Zhuo, K. Li, X. Chen, J. Cao, Numerical simulation of compressible turbulent flow via improved gas-kinetic BGK scheme, International journal for numerical methods in fluids, 67 (2011) 1833-1847.
[103] H. Jasak, OpenFOAM: open source CFD in research and industry, International Journal of Naval Architecture and Ocean Engineering, 1 (2009) 89-94.

[104] F. Palacios, J. Alonso, K. Duraisamy, M. Colonno, J. Hicken, A. Aranake, A. Campos, S. Copeland, T. Economon, A. Lonkar, Stanford university unstructured (su 2): an open-source integrated computational environment for multi-physics simulation and design, 51st AIAA Aerospace Sciences Meeting including the New Horizons Forum and Aerospace Exposition, 2013, pp. 287.
[105] F.D. Witherden, A.M. Farrington, P.E. Vincent, PyFR: An open source framework for solving advection–diffusion type problems on streaming architectures using the flux reconstruction approach, Computer Physics Communications, 185 (2014) 3028-3040.
[106] B. Lorendeau, Y. Fournier, A. Ribes, In-situ visualization in fluid mechanics using catalyst: A case study for code saturne, 2013 IEEE Symposium on Large-Scale Data Analysis and Visualization (LDAV), IEEE, 2013, pp. 53-57.
[107] I. Mohiuddin, H. Mathkour, Computational fluid dynamics application tools, 2015 World Congress on Information Technology and Computer Applications (WCITCA), IEEE, 2015, pp. 1-5.
[108] J. Latt, Palabos, parallel lattice Boltzmann solver, FlowKit, Lausanne, Switzerland, (2009).
[109] W. Gropp, W.D. Gropp, A.D.F.E.E. Lusk, E. Lusk, A. Skjellum, Using MPI: portable parallel programming with the message-passing interface, MIT press1999.
[110] B. Houlton, Enhancing packed bed geometry using computational fluid dynamic simulations, (2019).
[111] S. Khirevich, I. Ginzburg, U. Tallarek, Coarse-and fine-grid numerical behavior of MRT/TRT lattice-Boltzmann schemes in regular and random sphere packings, Journal of Computational Physics, 281 (2015) 708-742.
[112] R. Mei, W. Shyy, D. Yu, L.-S. Luo, Lattice Boltzmann method for 3-D flows with curved boundary, Journal of Computational Physics, 161 (2000) 680-699.
[113] M. Tian, W. Gu, J. Pan, M. Guo, Performance analysis and optimization of palabos on petascale sunway BlueLight MPP supercomputer, International Conference on Parallel Computing in Fluid Dynamics, Springer, 2013, pp. 311-320.
[114] J. Shi, L. Zhu, L. Li, Z. Li, J. Yang, X. Wang, A TPMS-based method for modeling porous scaffolds for bionic bone tissue engineering, Scientific reports, 8 (2018) 7395.
[115] J. Latt, Hydrodynamic limit of lattice Boltzmann equations, University of Geneva, 2007.
[116] F. Dolamore, C. Fee, S. Dimartino, Modelling ordered packed beds of spheres: The importance of bed orientation and the influence of tortuosity on dispersion, Journal of Chromatography A, 1532 (2018) 150-160.
[117] P.J. Dellar, Incompressible limits of lattice Boltzmann equations using multiple relaxation times, Journal of Computational Physics, 190 (2003) 351-370.
[118] K. Xu, X. He, Lattice Boltzmann method and gas-kinetic BGK scheme in the low-Mach number viscous flow simulations, Journal of Computational Physics, 190 (2003) 100-117.
[119] S. Ansumali, I.V. Karlin, Single relaxation time model for entropic lattice Boltzmann methods, Physical Review E, 65 (2002) 056312.
[120] A. Bobylev, The Chapman-Enskog and Grad methods for solving the Boltzmann equation, Akademiia Nauk SSSR Doklady, 1982, pp. 71-75.
[121] J. Perko, R.A. Patel, Single-relaxation-time lattice Boltzmann scheme for advection-diffusion problems with large diffusion-coefficient heterogeneities and high-advection transport, Physical Review E, 89 (2014) 053309.
[122] J.-D. Mueller, Essentials of computational fluid dynamics, CRC Press2015.
[123] B.A. Wagner, S. Venkataraman, G.R. Buettner, The rate of oxygen utilization by cells, Free Radical Biology and Medicine, 51 (2011) 700-712.
[124] B. Chance, Reaction of oxygen with the respiratory chain in cells and tissues, The Journal of general physiology, 49 (1965) 163-188.

[125] F. Dolamore, In Silico analysis of flow and dispersion in ordered porous media, (2017).
[126] D.D. Reneau Jr, D.F. Bruley, M.H. Knisely, A digital simulation of transient oxygen transport in capillary-tissue systems (cerebral grey matter). Development of a numerical method for solution of transport equations describing coupled convection-diffusion systems, AIChE Journal, 15 (1969) 916-925.
[127] B. Griffiths, Scaling-up of animal cell cultures, Animal cell culture. IRL Press, Oxford, (1986) 33-69.
[128] T. Schunck, P. Poulet, Oxygen consumption through metabolism and photodynamic reactions in cells cultured on microbeads, Physics in Medicine & Biology, 45 (2000) 103.
[129] X. Yan, D. Bergstrom, X. Chen, Modeling of cell cultures in perfusion bioreactors, IEEE Transactions on Biomedical Engineering, 59 (2012) 2568-2575.
[130] E.N. Marieb, Essentials of Human Anatomy and Physiology 9th ed San Francisco, Pearson Benjamin Cummings, 2009.
[131] P. Iranpour, C. Lall, R. Houshyar, M. Helmy, A. Yang, J.-I. Choi, G. Ward, S.C. Goodwin, Altered Doppler flow patterns in cirrhosis patients: an overview, Ultrasonography, 35 (2016) 3.
[132] F. Kreuzer, Oxygen supply to tissues: the Krogh model and its assumptions, Experientia, 38 (1982) 1415-1426.
[133] NeSI, Auckland, 2018.
[134] E. Nemeth, G. Snyder, T.R. Hein, T. Adelstein, B. Lubanovic, T. Limoncelli, UNIX and Linux system administration handbook, USENIX Open Access Policy, (2018) 59.
[135] A. Pletzer, W. Hayek, C. Scott, B. Corrie, G. Rae, How NeSI Helps Users Run Better and Faster on New Zealand's Supercomputing Platforms, 2017 IEEE 13th International Conference on e-Science (e-Science), IEEE, 2017, pp. 465-466.
[136] R. Gupta, D.F. Fletcher, B.S. Haynes, On the CFD modelling of Taylor flow in microchannels, Chemical Engineering Science, 64 (2009) 2941-2950.
[137] S. Prakash, C.R. Ethier, Requirements for mesh resolution in 3D computational hemodynamics, J. Biomech. Eng., 123 (2000) 134-144.
[138] R.G. Casten, C.J. Holland, Instability results for reaction diffusion equations with Neumann boundary conditions, Journal of Differential Equations, 27 (1978) 266-273.
[139] M. Gottlieb, R.B. Bird, Exit effects in non-Newtonian liquids. An experimental study, Industrial & Engineering Chemistry Fundamentals, 18 (1979) 357-368.
[140] I. Barton, The entrance effect of laminar flow over a backward-facing step geometry, International Journal for Numerical Methods in Fluids, 25 (1997) 633-644.
[141] M. Zhianmanesh, M. Varmazyar, H. Montazerian, Fluid permeability of graded porosity scaffolds architectured with minimal surfaces, ACS Biomaterials Science & Engineering, 5 (2019) 1228-1237.
[142] T. Kaully, K. Kaufman-Francis, A. Lesman, S. Levenberg, Vascularization—the conduit to viable engineered tissues, Tissue Engineering Part B: Reviews, 15 (2009) 159-169.
[143] C. Bonatti, D. Mohr, Smooth-shell metamaterials of cubic symmetry: Anisotropic elasticity, yield strength and specific energy absorption, Acta Materialia, 164 (2019) 301-321.
[144] F.C. TSE, O.C. Sandall, Diffusion coefficients for oxygen and carbon dioxide in water at 25 C by unsteady state desorption from a quiescent liquid, Chemical Engineering Communications, 3 (1979) 147-153.
[145] Y. Elsayed, C. Lekakou, P. Tomlins, Monitoring and modelling of oxygen transport through un-crosslinked and crosslinked gelatine gels, Polymer Testing, 40 (2014) 106-115.
[146] B. Ci, Confidence intervals, Lancet, 1 (1987) 494-497.
[147] A.S. Popel, Theory of oxygen transport to tissue, Critical reviews in biomedical engineering, 17 (1989) 257.

[148] R.N. Pittman, Oxygen gradients in the microcirculation, Acta Physiologica, 202 (2011) 311-322.
[149] Loligo online oxygen converter, 2019.
[150] E. Hodgson, A textbook of modern toxicology, John Wiley & Sons2004.
[151] M. Huysmans, A. Dassargues, Review of the use of Péclet numbers to determine the relative importance of advection and diffusion in low permeability environments, Hydrogeology Journal, 13 (2005) 895-904.
[152] J. Aroesty, J.F. Gross, Convection and diffusion in the microcirculation, Microvascular research, 2 (1970) 247-267.
[153] S. Nawada, S. Dimartino, C. Fee, Dispersion behavior of 3D-printed columns with homogeneous microstructures comprising differing element shapes, Chemical Engineering Science, 164 (2017) 90-98.
[154] N. Yang, Z. Quan, D. Zhang, Y. Tian, Multi-morphology transition hybridization CAD design of minimal surface porous structures for use in tissue engineering, Computer-Aided Design, 56 (2014) 11-21.
[155] D.-J. Yoo, New paradigms in cellular material design and fabrication, International Journal of Precision Engineering and Manufacturing, 16 (2015) 2577-2589.
[156] J.F. Patzer II, G.V. Mazariegos, R. Lopez, B.L.P. Investigators, Preclinical evaluation of the Excorp Medical, Inc, bioartificial liver support system, Journal of the American College of Surgeons, 195 (2002) 299-310.
[157] D. Quemada, A non-linear Maxwell model of biofluids: application to normal blood, Biorheology, 30 (1993) 253-265.
[158] H. Qi, M. Xu, Stokes' first problem for a viscoelastic fluid with the generalized Oldroyd-B model, Acta Mechanica Sinica, 23 (2007) 463-469.
[159] H.G. Lee, J. Park, S. Yoon, C. Lee, J. Kim, Mathematical Model and Numerical Simulation for Tissue Growth on Bioscaffolds, Applied Sciences, 9 (2019) 4058.
[160] M. Sharan, M. Singh, Equivalence between one step kinetics and Hill's equation, Journal of biomedical engineering, 6 (1984) 297-301.
[161] C. Tresoldi, D.P. Pacheco, E. Formenti, A.F. Pellegata, S. Mantero, P. Petrini, Shear-resistant hydrogels to control permeability of porous tubular scaffolds in vascular tissue engineering, Materials Science and Engineering: C, 105 (2019) 110035.

Appendix

A. TPMS structures (50% structurally porous)

$$F_{(100)} = \cos(x) + \cos(y) + coz(z)$$

$$F_{(110)} = \sin(x)\cos(y) + \sin(y)\cos(z) + sin(z)\cos(x)$$

$$F_{(111)} = sin(x)\,sin(y)\,sin(z) + \sin(x)\cos(y)\cos(z) + \cos(x)\sin(y)\cos(z) + \cos(x)\cos(y)\sin(z)$$

$$F_{(200)} = \cos(2x) + \cos(2y) + \cos(2z)$$

$$F_{(220)} = \cos(2x)\cos(2y) + \cos(2y)\cos(2z) + \cos(2z)\cos(2x)$$

$$F_{(222)} = \cos(2x)\cos(2y)\cos(2z)$$

$$F_{(211)} = \sin(2x)\cos(y)\sin(z) + \sin(2y)\cos(z)\sin(x) + \sin(2z)\cos(x)\sin(y)$$

$$F^{C}_{(111)} = \cos(x)\cos(y)\cos(z) + \sin(x)\sin(y)\cos(z) + \sin(x)\cos(y)\sin(z) + \cos(x)\sin(y)\sin(z)$$

$$F^{B}_{(220)} = \sin(2x)\sin(2y) + \sin(2y)\sin(2z) + \sin(2z)\sin(2x)$$

$$F^{C}_{(110)} = \sin(x)\sin(y) + \sin(y)\sin(z) + \sin(z)\sin(x)$$

A.1 Schwarz Primitive (SP)

$$SP: \quad F_{(100)} = isovalue \qquad [44]$$

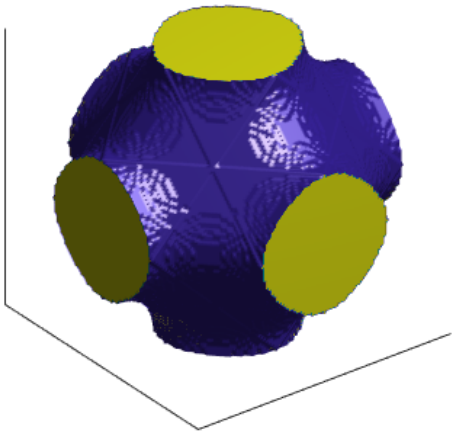

A.2 Schoen Gyroid (SG)

$$SG: \quad F_{(110)} = isovalue \qquad [45]$$

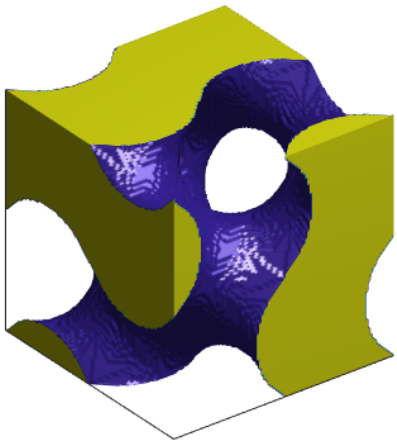

A.3 Schwarz Diamond (SD)

$$SD: \quad F_{(111)} = isovalue \qquad [46]$$

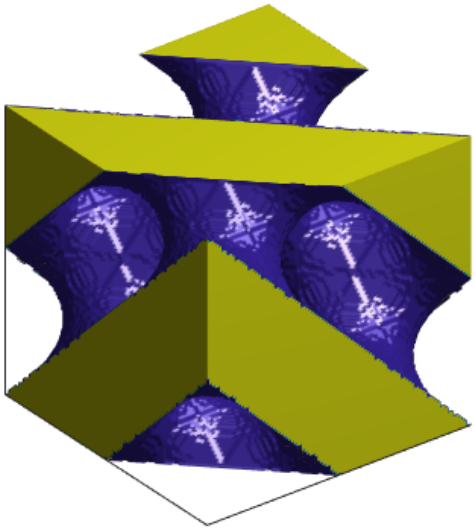

A.4 Schoen I-WP surface (IWP)

$$IWP: \quad 2F_{(110)} - F_{(200)} = isovalue \qquad [47]$$

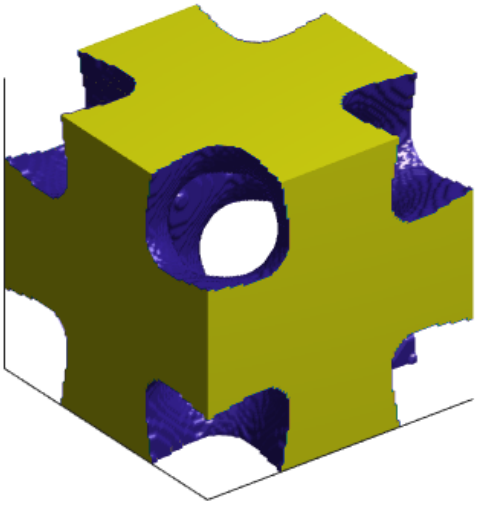

A.5 Schoen F-RD surface (F-RD)

$$FRD: \quad 0.8F_{(111)} + 0.1F_{(222)} - 0.1F_{(220)} = isovalue \qquad [48]$$

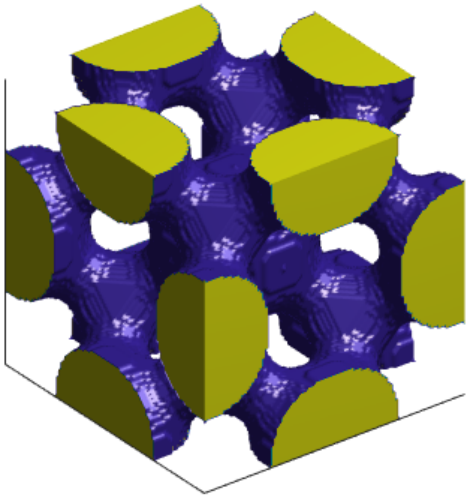

A.6 P2-GD surface (P2GD)

$$P2GD: \quad 0.7F_{(211)} - 0.1F_{(220)} - 0.2F_{(200)} = isovalue \qquad [49]$$

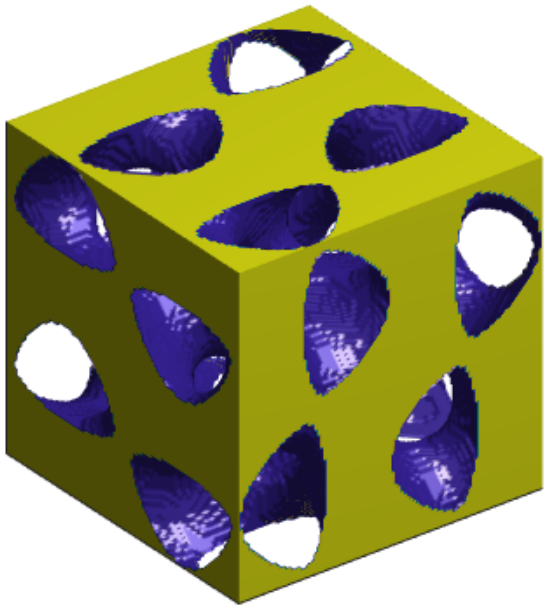

A.7 Double Schoen Gyroid (DSG)

$$DSG: \quad 0.8F_{(211)} - 0.2F_{(220)} = isovalue \qquad [50]$$

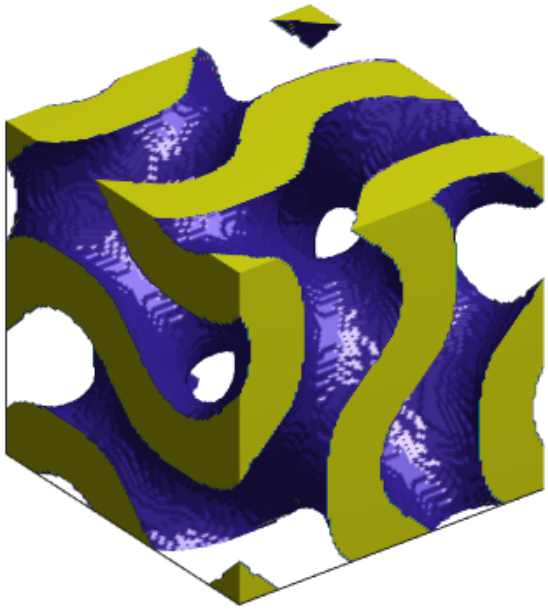

A.8 Lidinoid surface (L)

$$L: \quad 0.5F_{(211)} - 0.5F_{(220)} + 0.15 = isovalue \qquad [51]$$

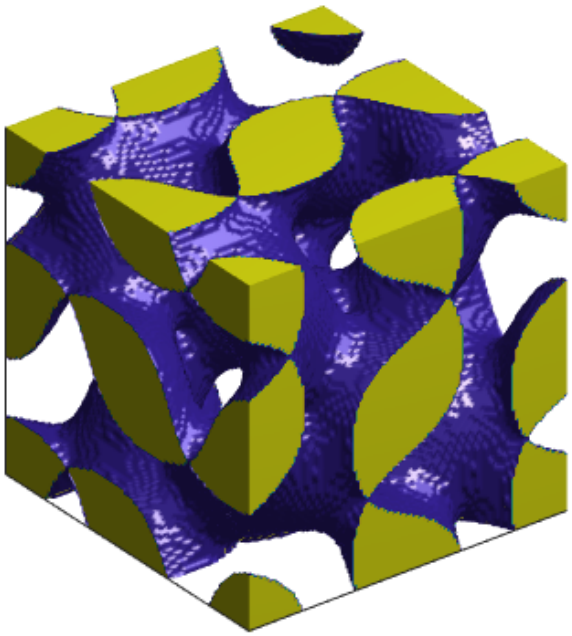

A.9 The D' surface (D)

$$D: \quad 0.5F^{C}_{(111)} - 0.5F^{B}_{(220)} = isovalue \qquad [52]$$

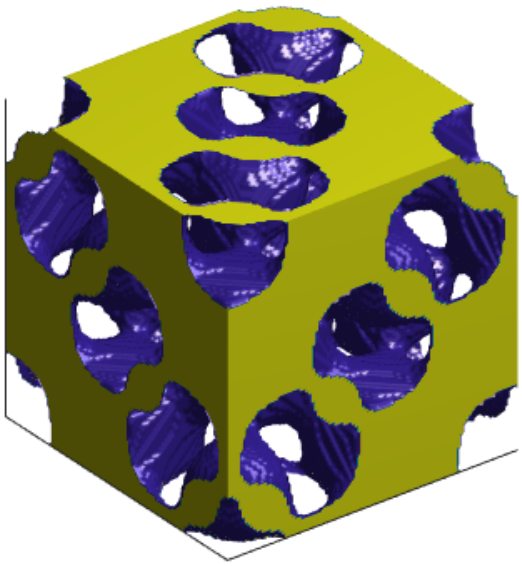

A.10 The Double diamond (DD)

$$DD: \quad 0.5FC_{(110)} + 0.5F_{(111)} = isovalue \qquad [53]$$

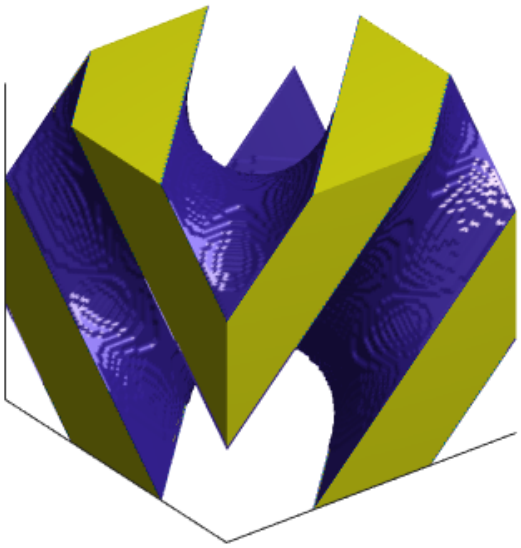

B. TPMS Porosity tables

The following table shows the relationship between isovalue[47] and TPMS structural porosities (Appendix A). All the porosity values are indicated as percentage values, in the corresponding TPMS columns. The isovalues corresponding to the TPMS structural porosity can be identified in the 1st column.

Isovalue	Schwarz Diamond	DSG	D'	IWP	P2GD	L surface	Double Diamond	F-RD	Gyroid
-1	0.9201	1	0.9296	0.6565	1	0.9752	1	1	0.8297
-0.9	0.8753	1	0.9171	0.6442	1	0.9624	1	0.995	0.7951
-0.8	0.832	1	0.903	0.6316	0.9756	0.947	1	0.9854	0.7611
-0.7	0.7894	1	0.8851	0.6192	0.934	0.9287	1	0.972	0.7275
-0.6	0.7472	1	0.8625	0.6066	0.8708	0.9069	1	0.9545	0.6944
-0.5	0.7054	0.7721	0.8343	0.5939	0.7982	0.8811	1	0.9322	0.6616
-0.4	0.664	0.6768	0.7995	0.5812	0.7294	0.85	0.741	0.9042	0.629
-0.3	0.6228	0.603	0.7613	0.5684	0.6633	0.8119	0.6329	0.8577	0.5966
-0.2	0.5818	0.5402	0.7191	0.5554	0.5995	0.7625	0.5494	0.7826	0.5643
-0.1	0.5409	0.4842	0.6718	0.5425	0.5372	0.6917	0.4784	0.6622	0.5321
0	0.5	0.4331	0.6172	0.5294	0.4764	0.6159	0.4153	0.5351	0.5
0.1	0.4591	0.3855	0.5497	0.5163	0.4167	0.5368	0.3578	0.402	0.4678
0.2	0.4182	0.3405	0.4671	0.503	0.3581	0.4596	0.3044	0.2592	0.4357
0.3	0.3772	0.2978	0.3785	0.4896	0.3002	0.3971	0.2542	0.1531	0.4034
0.4	0.336	0.2569	0.2807	0.4762	0.2479	0.3406	0.2064	0.0784	0.371
0.5	0.2946	0.2175	0.1657	0.4625	0.1998	0.2875	0.16	0.0262	0.3384
0.6	0.2528	0.1793	0.0283	0.4489	0.1541	0.2363	0.125	0	0.3056
0.7	0.2107	0.142	0	0.4349	0.1101	0.1857	0.0978	0	0.2725
0.8	0.168	0.1053	0	0.421	0.0673	0.1348	0.0753	0	0.2389
0.9	0.1246	0.0691	0	0.4067	0.0328	0.0796	0.0566	0	0.2049
1	0.0799	0.0331	0	0.3924	0.0119	0.028	0.041	0	0.1703

[47] Also referred to as inequality value.

C. Probability distribution function

Probability distribution is an important concept in the field of probability and statistics that is defined for a random variable. It provides the probability of occurrence of different possible outcomes in a random experiment. For instance, the velocity probability distribution in kinetic theory of gas provides information on the probability of gas molecules with certain velocity. A probability distribution is characterized by its moments. A moment is a specific quantitative measure of shape of a set of points. The n^{th}moment (μ_n) of a function $f(x)$ about any fixed point x_o is defined by Equation [54].

$$\mu_n = \int (x - x_o)^n f(x) dx \qquad [54]$$

These points could be any parameter. If the points represent mass, then the zeroth moment is the total mass, the first moment divided by the total mass is the centre of mass, and the second moment is the rotational inertia. If the points represent probability density, then the zeroth moment is the total probability, the first moment is the mean, the second moment is the variance (σ^2), the third moment is the skewness[48], and the fourth moment (with normalization and shift) is the kurtosis[49]. The function $f(x)$ varies according to field of study. In this thesis, $f(x)$ is the probability density function of particles that are colliding and streaming in LBM. Section 2.5 contains details on calculating macroscopic velocity, internal energy and density from the relevant moments.

D. Maxwell-Boltzmann distribution

Maxwell-Boltzmann distribution function is a probability distribution function that gives the probability distribution of speed of gas molecules. Based on this distribution, other important parameters such as the average speed and the root mean square velocity of molecules could be estimated. The Maxwell-Boltzmann distribution forms the basis for kinetic theory of gas, which heavily depends on the velocity probability distribution function. Kinetic theory of gas states that the mean free path of a molecule is the average distance travelled by molecules between successive collisions. This assumption is based on the fact that the path travelled by molecules is relatively larger than the diameter of the molecules.

[48] Asymmetry in a probability distribution
[49] Gives qualitative idea of tail of a probability distribution (heavy tailed or light tailed)

E. NeSI (*Mahuika*)

The following procedure was adopted to run simulations on the *Mahuika* platform of NeSI. The bold black font characters and words are to be typed unchanged. The blue font words are the NeSI user's login credentials and file names.

➔ To login to the lander node, the following command is used.
ssh -Y university_username**@lander02.nesi.org.nz**

The Google authenticator app of a smart phone should be used to receive the randomly generated 6 digit code, for two-factor authentication on the lander node.

➔ To login to the NeSI *Mahuika* node, the following command is used.
ssh -Y login.mahuika.nesi.org.nz

The Google authenticator app of a smart phone should be used to receive the randomly generated 6 digit code for two-factor authentication on the *Mahuika* node. This 6 digit code should be different to the lander node code, therefore sufficient time should be given for the authenticator app to regenerate a new number.

➔ There are two main folders for every NeSI user account, namely: *project* and *nobackup*

Navigate to the project folder first using command line **cd** arguments, and load the **gimkl** compiler that would allow '**make**' command to work, using the following steps.
cd /nesi/project/ NeSI_username**/progress/**
module load gimkl/2017a
make
ls - ltr

➔ Ensure that the compiled code is converted into an executable format. If not, make the file executable with the following command.
chmod +x Development

where ‘Development’ is an executable file format of the source file named ‘Development.cpp’.

➔ Navigate to the **nobackup** section and make a personalized folder name, according to the simulation job (Note: The name should not contain spaces. Eg) folder_name).

cd /nesi/nobackup/ NeSI_username

mkdir folder_name

cd folder_name

➔ Copy '*slurm*' and '*config*' files from progress folder to the new directory 'folder name' that was created in the 'nobackup' directory. Slurm files contain instructions to the supercomputer about details of running the simulation task, such as number of cores to employ, maximum time after which the simulation job should terminate and the email address to which notifications should be sent for simulation notifications. Assistance on ‘*slurm*’ files can be received from the NeSI engineers, to customize them according to user’s code requirement. ‘*Config*’ files were written in *.xml* language and contain the simulation parameters taken as input for the C++ code.

cp/nesi/project/NeSI_username**/slurm_templates**/progress.slurm/slurm_script/

cp /nesi/project/ NeSI_username **/progress/**configAD.xml ./config.xml

cp/nesi/project/NeSI_username/progress/Development.cpp ./Development.cpp

where ‘progress.slurm’ is the *slurm* file.

➔ The ‘*nano*’ program was used to change the simulation parameters in the '*config*' file and the *slurm* script.

nano config.xml

nano File.slurm

➔ The following command was used to run the simulation.

sbatch File.slurm

This line is a substitute to '**mpirun -n 4** Development config.xml ' which is used to run simulations on the local computer using 4 cores.

➔ The running status of the simulations can be checked using the following command.

squeue -u $(whoami)

The time keeps decreasing as the code runs and thus the job status can be verified. An automatic email notification is also sent out confirming the status of the computation job, if the option is enabled in the *slurm* file.

➔ To copy the simulation results from NeSI computer to local computer, the following command is used.

scp -r mahuika:/nesi/nobackup/ NeSI_username/ Development .

➔ Transferring files from the supercomputer to local computer takes longer time. Therefore the files were first compressed using the following command.

tar -cvzf Results.tgz Results

This command will make a compressed file named Results.tgz from the Results folder.

➔ To transfer the compressed **.tgz** file from *Mahuika* to local system, the following command was used

(Note: This command should be typed by navigating to the folder in the local computer, in which the data transfer should occur).

scp -r mahuika:/nesi/nobackup/ NeSI_username/ Development.tgz .

➔ To decompress the file, the following command was used.

tar -xvf Development.tgz

➔ To upload a new code to the *Mahuika* platform, the following command was used.

scp -r Development.cpp **Makefile config.xml**
mahuika:/nesi/project/nesi00494/progress/.
module load gimkl/2017a
make
ls -ltr
chmod +x Development

F. Partition coefficient of TPMS structures

Porosity	**25%**	**50%**	**80%**
Gyroid	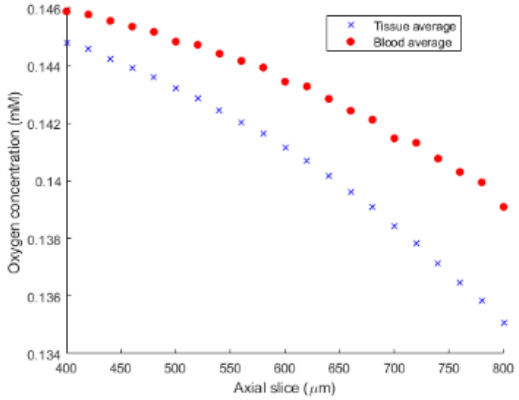	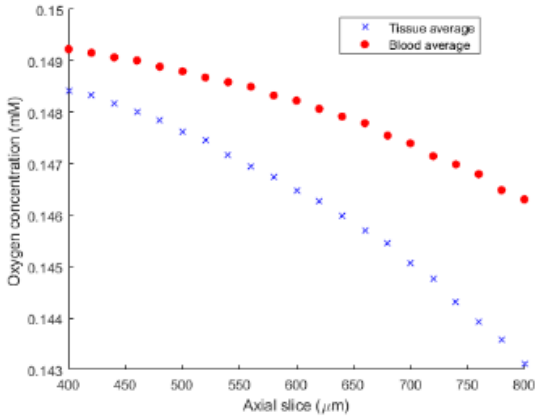	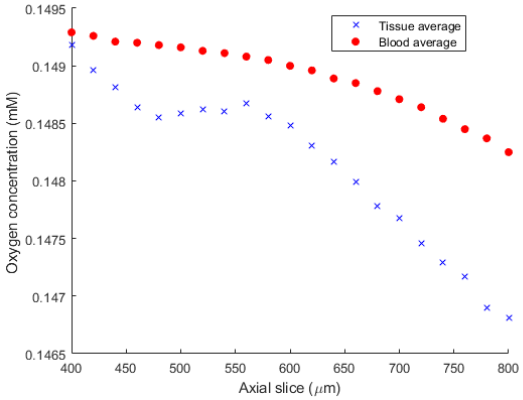

Porosity	**25%**	**50%**	**80%**
Lidinoid	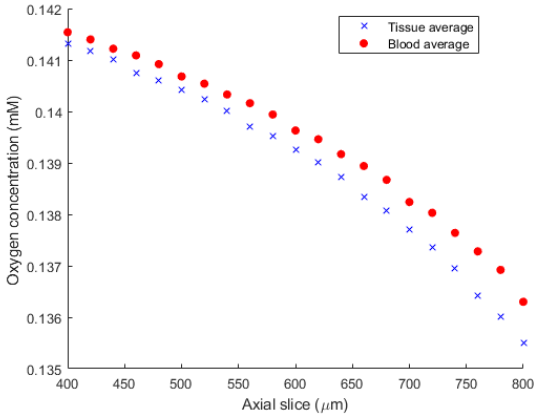	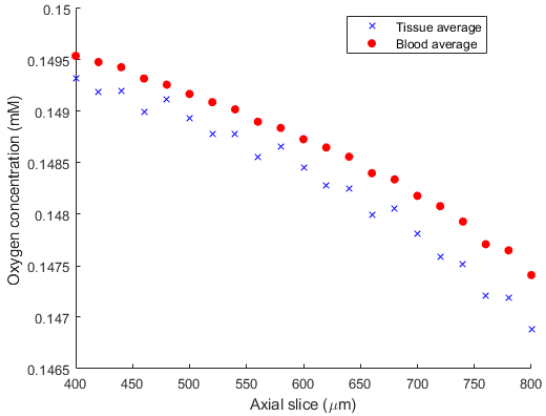	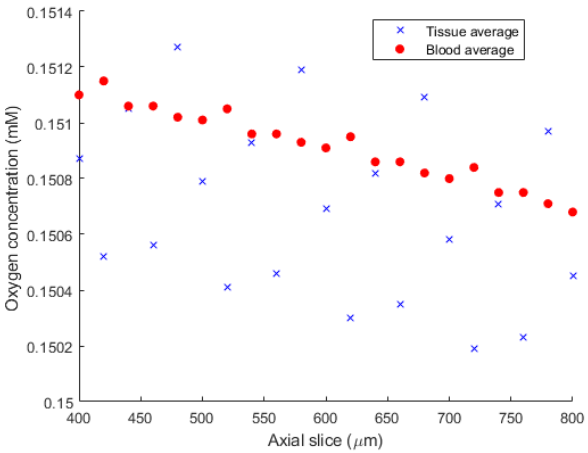

Porosity	**25%**	**50%**	**80%**
DSG	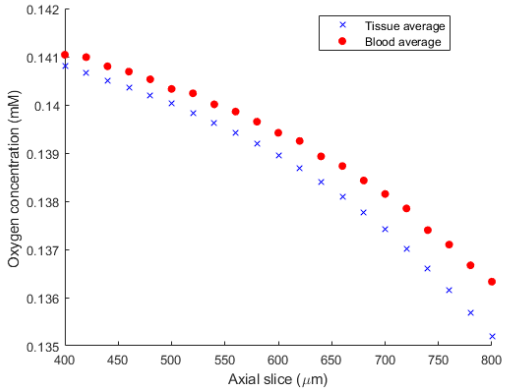	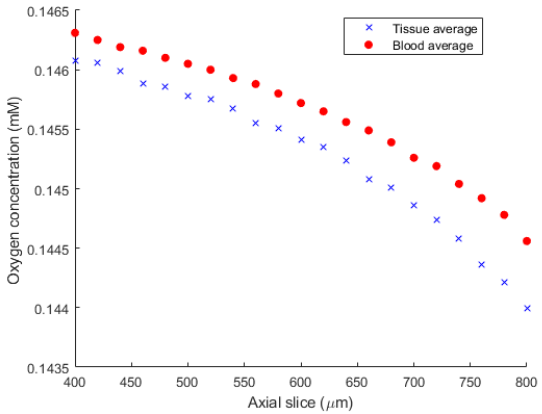	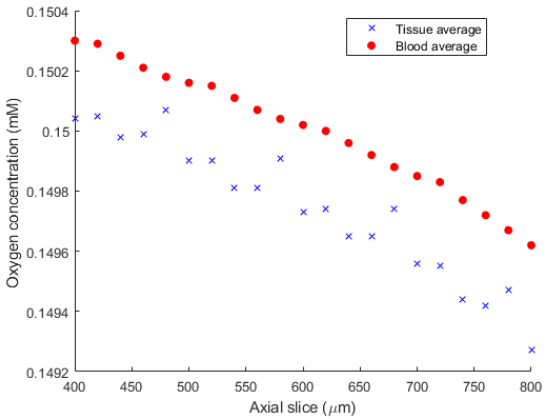
P2GD	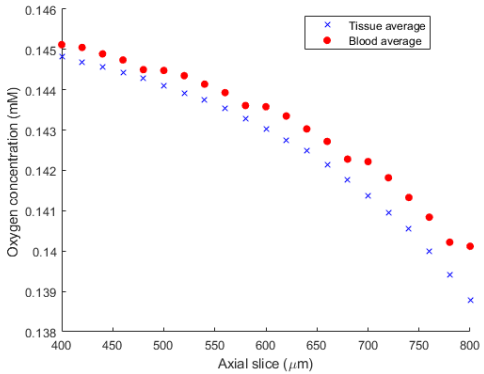	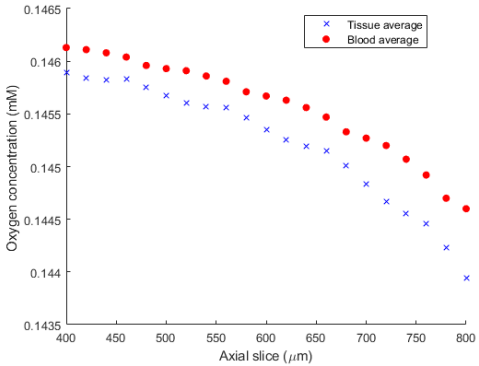	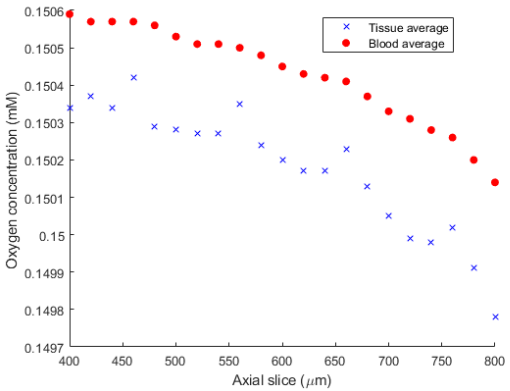

Porosity	**50%**	**80%**
FRD	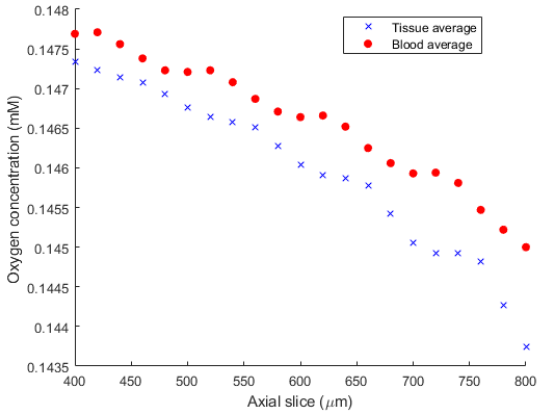	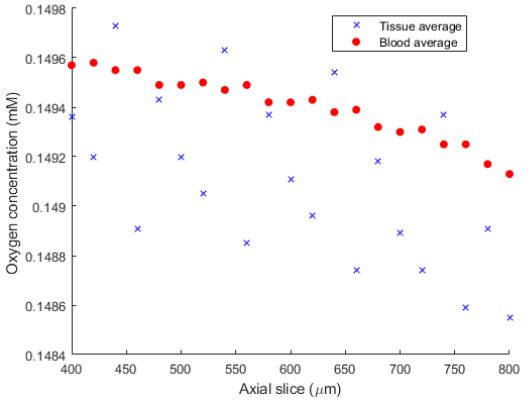
Double-Diamond	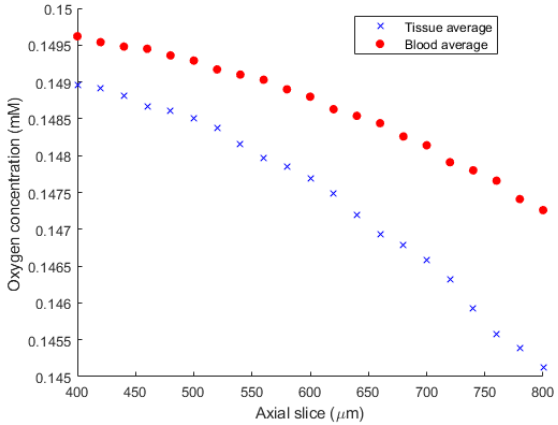	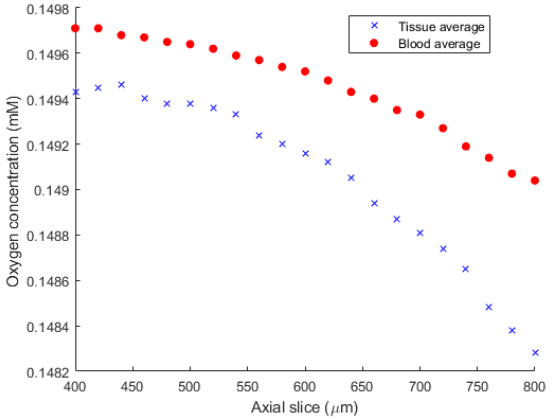

Porosity **50%**

IWP

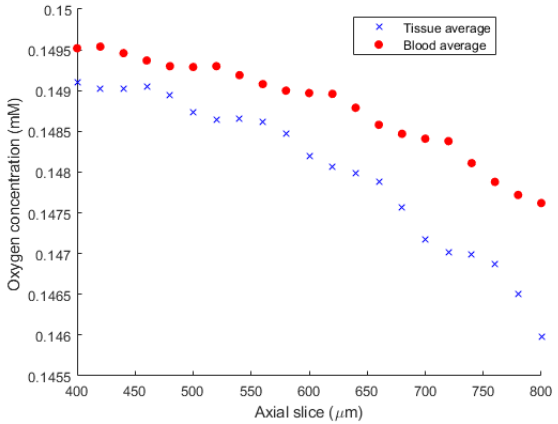

D_Dash

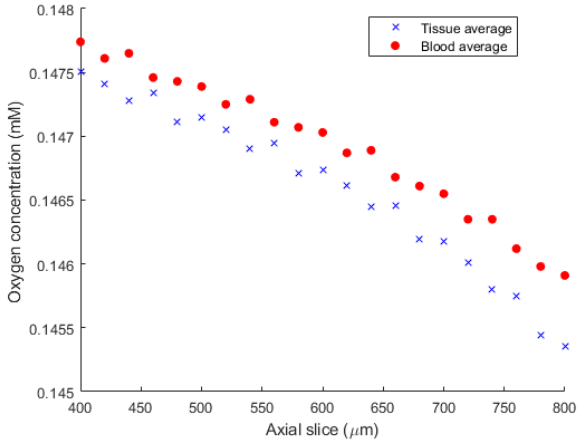

G. Linear extrapolation method to determine survival length.

The general equation for a line is given by [$y = mx + C$]

At x = 0 microns, y = 0.15 mM

$$0.15 = m(0) + C$$

$$C = 0.15$$

To determine the 'x' or the distance from the scaffold entry point, where the concentration falls to 0.005 mM, the following calculation was done

$$x = \frac{y - C}{m}$$

$$x = \frac{0.005 - 0.15}{m}$$

This 'x' was defined as survival length which was to evaluate the estimated gradient values (m) obtained from LBM simulations. However, the gradient value of the case with perfused oxygen concentration of 0.15mM was considered as a reference to approximate the survival length.

H. Anoxia

The following image distinguishes normoxic and anoxic region when the perfused oxygen concentration was more than 0.005 mM (left image) and less than 0.005 mM (right image). The presence of blue colour throughout the domain in the right image confirms anoxia.